

DEVELOPMENT AND IMPLEMENTATION OF EFFICIENT  
SEGMENTATION ALGORITHM FOR THE DESIGN OF  
ANTENNAS AND ARRAYS

ANG IRENE

(B. Eng. (*Hons.*), NUS)

A THESIS SUBMITTED

FOR THE DEGREE OF DOCTOR OF PHILOSOPHY

DEPARTEMENT OF ELECTRICAL AND COMPUTER  
ENGINEERING

NATIONAL UNIVERSITY OF SINGAPORE

2008

## **Acknowledgements**

I would like to take this opportunity to express my gratitude to my supervisors Associate Professor Ooi Ban Leong and Professor Prof. Leong Mook Seng for their invaluable guidance, constructive criticisms and encouragement throughout the course of my study. Without their kind assistance and teaching, the progress of this project would not be possible.

I would like to thank the staff from Microwave Laboratory in the Electrical and Computing Engineering (ECE) department, especially Mr Sing Cheng Hiong, Mdm Lee Siew Choo, Mr Jalil and Mr Chan for their kind assistances and support during the fabrication processes and measurement of the prototypes presented in this thesis. I would like to thank my friends in Microwave Laboratory, especially Dr Wang Ying, Miss Zhang Yaqiong, Miss Fan Yijing, Miss Nan Lan, Mr Yu Yan Tao, Mr Zhong Zheng and Mr Ng Tiong Huat for providing the laughter, encouragement and valuable help throughout my Ph.D.

Finally, I would like to thank my family and friends. I am very grateful to my parents for their everlasting supports and encouragement. I would like to express my appreciation to my mentor cum brother, Mr Chan Hock Soon for teaching me many

valuable life lessons. I wish to express my sincere thanks and appreciation to Heng Nam for his encouragement, understanding and patience during the completion of this course.

# Table of Contents

<b>ACKNOWLEDGEMENTS.....</b>	<b>I</b>
<b>TABLE OF CONTENTS.....</b>	<b>III</b>
<b>SUMMARY.....</b>	<b>VI</b>
<b>LIST OF FIGURES.....</b>	<b>IX</b>
<b>LIST OF TABLES.....</b>	<b>XV</b>
<b>LIST OF SYMBOLS.....</b>	<b>XVII</b>
<b>LIST OF ACRONYMS.....</b>	<b>XVIII</b>
<b>CHAPTER 1 INTRODUCTION.....</b>	<b>1</b>
1.1 LITERATURE REVIEW AND MOTIVATION.....	1
1.2 SCOPE OF WORK.....	8
1.3 LIST OF ORIGINAL CONTRIBUTIONS.....	10
1.4 PUBLICATIONS.....	11
<b>CHAPTER 2 NUMERICAL MODELLING OF PLANAR MULTILAYERED STRUCTURES.....</b>	<b>13</b>
2.1 INTRODUCTION.....	13
2.2 SPECTRAL DOMAIN GREEN'S FUNCTIONS [63].....	15
2.3 MIXED POTENTIAL INTEGRAL EQUATION [64].....	20
2.4 NUMERICAL EVALUATION OF THE SOMMERFELD INTEGRALS [68]-[71].....	22
2.5 DISCRETE COMPLEX IMAGE METHOD [39].....	23
2.6 THE METHOD OF MOMENTS [78]-[80].....	26
2.6.1 <i>Rooftop Basis Functions</i> .....	27
2.6.2 <i>RWG Basis Function</i> .....	28
2.7 DE-EMBEDDING OF NETWORK PARAMETERS [82].....	30
2.8 MATCHED LOAD SIMULATION [83].....	33
2.9 INTERPOLATION SCHEMES FOR THE GREEN'S FUNCTION.....	35
2.9.1 <i>Radial Basis Function [59]</i> .....	37
2.9.2 <i>Cauchy Method [60]-[61]</i> .....	38
2.9.3 <i>Generalized Pencil-of-Function Method [56]</i> .....	40
2.9.4 <i>Numerical Study of the interpolation techniques</i> .....	41
2.10 FAR-FIELD RADIATION PATTERN [86].....	44
2.11 NUMERICAL RESULT.....	45
2.12 CONCLUSION.....	47
<b>CHAPTER 3 MACRO-BASIS FUNCTION.....</b>	<b>48</b>

3.1	INTRODUCTION .....	48
3.2	MACRO-BASIS FUNCTION.....	51
3.3	SUB-DOMAIN MULTILEVEL APPROACH [50].....	52
3.4	SUB-ENTIRE-DOMAIN BASIS FUNCTION METHOD [55] .....	56
3.5	MACRO-BASIS FUNCTION WITH PROGRESSIVE METHOD.....	57
3.6	ITERATIVE REFINEMENT PROCESS.....	60
3.7	EFFICIENT EVALUATION OF MACRO-BASIS FUNCTION REACTION TERM USING ADAPTIVE INTEGRAL METHOD .....	64
3.8	NUMERICAL APPLICATIONS TO FILTER AND ANTENNA ARRAYS .....	70
3.8.1	<i>Bandpass Filter</i> .....	71
3.8.2	<i>Linear Series-fed Array</i> .....	83
3.8.3	<i>Bowtie Dipole Array</i> .....	95
3.8.4	<i>Design of 24GHz Antenna Array</i> .....	102
3.8.4.1	Design Procedure.....	103
3.8.4.2	Simulations and Measurements .....	108
3.9	CONCLUSION.....	114
<b>CHAPTER 4 DESIGN OF VARIOUS WIDEBAND PROBE-FED MICROSTRIP PATCH ANTENNAS AND ARRAYS.....</b>		<b>115</b>
4.1	INTRODUCTION .....	115
4.2	OVERVIEW OF WIDEBAND PROBE-FED MICROSTRIP PATCH ANTENNA.....	117
4.2.1	<i>Parasitic Elements [7]-[14]</i> .....	117
4.2.2	<i>Slotted Patches [15]-[22]</i> .....	118
4.2.3	<i>Shaped Probes [23]-[26]</i> .....	119
4.3	WIDEBAND SEMI-CIRCLE PROBE-FED MICROSTRIP PATCH ANTENNAS .....	120
4.3.1	<i>Semi-circle Probe-fed Rectangular Patch Antenna</i> .....	120
4.3.2	<i>Semi-circle Probe-fed Stub Patch Antenna</i> .....	123
4.3.2.1	Antenna Structure .....	123
4.3.2.2	Simulations and Measurements .....	125
4.3.2.3	Parametric Study.....	131
4.3.3	<i>Semi-circle Probe-fed Flower-shaped Patch Antenna</i> .....	136
4.3.3.1	Antenna Structure .....	136
4.3.3.2	Simulations and Measurements .....	137
4.3.4	<i>Semi-circle Probe-fed Pentagon-slot Patch Antenna</i> .....	145
4.3.4.1	Antenna Geometry .....	145
4.3.4.2	Simulations and Measurements .....	145
4.4	SEMI-CIRCLE PROBE-FED MICROSTRIP STUB ARRAY .....	153
4.4.1	<i>4 by 4 Semi-circle Probe-fed Microstrip Stub Patch Antenna Array</i> .....	154
4.4.1.1	Antenna Geometry .....	154
4.4.1.2	Simulations and Measurements .....	161
4.4.2	<i>Two-element Linearly-polarized Array</i> .....	168
4.4.2.1	Antenna Geometry .....	168
4.4.2.2	Feed Network .....	169
4.4.3	<i>4 by 4 Linearly-polarized Array</i> .....	172
4.5	CONCLUSION.....	175

<b>CHAPTER 5</b>	<b>CONCLUSIONS AND FUTURE WORK.....</b>	<b>176</b>
5.1	CONCLUSIONS .....	176
5.2	SUGGESTIONS FOR FUTURE WORK .....	179
<b>REFERENCES</b>	<b>.....</b>	<b>181</b>
<b>APPENDIX A</b>	<b>TRANSMISSION LINE GREEN'S FUNCTION .....</b>	<b>195</b>
<b>APPENDIX B</b>	<b>METHOD OF AVERAGES .....</b>	<b>200</b>

## Summary

The method of moments (MoM) is a common numerical technique for solving integral equations. However, the method generates dense matrix which is computationally expensive to solve, and this limits the complexity of problems which can be analyzed. To reduce the computational cost of the method of moments, iterative solvers are employed to solve the dense matrix. However, iterative solvers may lead to convergence difficulties in dealing with large scale objects. In order to overcome the convergence issue, segmentation techniques, which can significantly reduce the number of unknowns, are used to analyze large structures. The focus of this thesis is to develop improved segmentation method for effective simulation of large scale problems. This is achieved by combining macro-basis function with progressive method coupled with adaptive integral method.

In this thesis, spatial domain MoM is used to analyze planar structures. The spatial domain Green's functions are evaluated by the discrete complex image method. Interpolation scheme is required to further reduce the computation time to calculate the Green's function. Different interpolation schemes, namely the radial basis function, the Cauchy method and the generalized pencil-of-function method are investigated and compared. Of these, the generalized pencil-of-function interpolation scheme

provides the best accuracy with the less number of interpolation points.

In the sub-domain multilevel approach, the mutual coupling between different portions of the geometry is not directly accounted for during the construction of the macro-basis function. In turn, this will affect the accuracy of the sub-domain multilevel approach, especially for dense and complex structure. In order to improve the accuracy of the solution, a new grouping concept of near-far neighbour evaluation called the macro-basis function with progressive method (MBF-PM) is developed in this thesis. For a chebyshev bandpass filter, the relative error of the current computed from the macro-basis function with progressive method is 6.4% while the relative error of the current computed from the sub-domain multilevel approach is 22.9%. Thus, compared to the sub-domain multilevel approach, better accuracy has been achieved.

To further improve the accuracy of the solution, a new iterative refinement process, which utilizes the concept of the macro-basis function, is introduced. Compared to the reported iterative refinement process in [1], the computation complexity of the new iterative refinement process is reduced. Compared to the reported iterative refinement process in [2], better convergence is achieved.

Even though the macro-basis function with progressive method has drastically reduced the memory requirements and the computation time, the calculation of the



interactions between the macro-basis functions remains the most time-consuming part of the procedure. In order to speed up the matrix filling time, the adaptive integral method is integrated into the macro-basis function with progressive method. Some numerical examples are conducted to examine the performance of this new hybrid scheme, the macro-basis function with progressive and adaptive integral method (MBF-PM-AIM). It is demonstrated that for a 1 by 14 antenna array, MBF-PM-AIM is 10 times faster than the conventional MoM. For a 20 by 20 antenna array with 87780 unknowns, MBF-PM-AIM has achieved a reduction of computer time by a factor of approximately 60 as compared to the commercial software, IE3D.

After developing the segmentation technique, MBF-PM-AIM is applied to the design of broadband probe-fed antennas and arrays. Due to the growing demand of modern wireless communication systems, there is a need to enhance the impedance bandwidth of the antennas. In this thesis, various wideband semi-circle probe-fed antennas and arrays are developed for wireless local area network. These include the semi-circle probe-fed stub patch antenna, the semi-circle probe-fed flower-shaped patch antenna and the semi-circle probe-fed pentagonal-slot patch antenna. The antennas have been fabricated and the simulated results are in good agreement with the measured results. Among the three antennas studied, the semi-circle probe-fed stub patch antenna gives the best performance with an impedance bandwidth of 68.3%, a 3 dB gain bandwidth of 45.5% and a broadside gain of 7.07 dBi at 5.4 GHz.

## List of Figures

FIG 2.1: AN ARBITRARY SHAPED SCATTERER EMBEDDED IN LAYERED DIELECTRIC MEDIUM.....	15
FIG 2.2: ROTATED SPECTRUM-DOMAIN COORDINATE SYSTEM. ....	17
FIG 2.3: COMPARISON OF THE CALCULATION FOR $G_Q$ USING DCIM AND NUMERICAL INTEGRATION (METHOD OF AVERAGES) ON SUBSTRATE WITH $H=1.0\text{MM}$ , $E_R=12.6$ AT $F=30\text{GHZ}$ . ....	25
FIG 2.4: X-DIRECTED ROOFTOP BASIS FUNCTION WITH THE CURRENT AND CHARGE CELLS. ....	27
FIG 2.5: RWG BASIS FUNCTION. ....	29
FIG 2.6: 1 CELL ALONG THE TRANSVERSE DIRECTION OF THE FEEDLINE. ....	31
FIG 2.7: MULTIPLE CELLS ALONG THE TRANSVERSE DIRECTION OF THE FEEDLINE.....	32
FIG 2.8: ILLUSTRATION OF MATCHED LOAD TERMINATION. ....	34
FIG 2.10: COMPARISON OF THE CPU TIME USED IN THE DIRECT COMPUTATION OF THE CLOSED-FORM GREEN'S FUNCTION AND THE GPOF INTERPOLATION SCHEME WITH RESPECT TO THE NUMBER OF GREEN'S FUNCTIONS EVALUATED.....	44
FIG 2.11: MICROSTRIP PATCH ANTENNA WITH SUBSTRATE HEIGHT = 31 MILS AND $E_R= 2.33$ AT RESONANT FREQUENCY 2.5 GHz. ....	45
FIG 2.12: COMPARISON OF THE MAGNITUDE AND PHASE OF THE RETURN LOSS OF A LONG PATCH ANTENNA BETWEEN THE WRITTEN CODE AND IE3D. ....	46
FIG. 3.1: ILLUSTRATION OF SUB-DOMAIN MULTILEVEL APPROACH. (A) NON-IDENTICAL PROBLEM (B) IDENTICAL PROBLEM .....	52
FIG. 3.2: ILLUSTRATION OF SUB-ENTIRE-DOMAIN BASIS FUNCTION METHOD. ....	56
FIG.3.3: ILLUSTRATION OF MACRO-BASIS FUNCTION WITH PROGRESSIVE METHOD. ....	58
FIG.3.4: EXTENDED REGION OF THE ROOT DOMAIN.....	59
FIG.3.5: ITERATIVE REFINEMENT PROCESS. (A) ITERATIVE PROCESS A. (B) ITERATIVE PROCESS B.....	61
FIG.3.6: TRANSLATION OF ROOFTOP BASIS FUNCTION TO THE HIGHLIGHTED RECTANGULAR GRIDS. ....	65
FIG 3.7: FLOW CHART FOR ANALYZING A LARGE PROBLEM USING THE DEVELOPED ALGORITHM (MBF-PM-AIM).....	69
FIG 3.8: PHOTOGRAPH OF THE FABRICATED CHEBYSHEV BANDPASS FILTER. ....	71
FIG.3.9: CHEBYSHEV BANDPASS FILTER. (A) LAYOUT OF THE BANDPASS FILTER. (B) SMALL DOMAIN OF THE BANDPASS FILTER. $L=22.45$ , $W=1.27$ , $G_1=0.254$ , $G_2=1.17$ AND $G_3=1.32$ . ALL DIMENSIONS ARE GIVEN IN MM. ....	73
FIG.3.10: COMPARISON OF THE INITIAL CURRENT ON THE BANDPASS FILTER UNDER VARIOUS METHODS: MACRO-BASIS FUNCTION WITH PROGRESSIVE METHOD	

(MBF-PM), SUB-DOMAIN MULTILEVEL APPROACH (SMA), SUB-ENTIRE-DOMAIN (SED) AND CONVENTIONAL MoM.....	74
FIG.3.11: COMPARISON OF THE CURRENT COEFFICIENTS AMONG THE MACRO-BASIS FUNCTION WITH PROGRESSIVE METHOD (MBF-PM), THE SUB-ENTIRE-DOMAIN BASIS FUNCTION METHOD (SED), THE SUB-DOMAIN MULTILEVEL APPROACH (SMA) AND THE CONVENTIONAL MoM WITH RESPECT TO THE NUMBERING OF THE ROOFTOP BASIS FUNCTION ON THE BANDPASS FILTER AFTER 1 ITERATIVE SWEEP. ....	76
FIG.3.12: CONVERGENCE OF THE SOLUTION WITH RESPECT TO THE NUMBER OF ITERATIVE SWEEPS. ....	77
FIG.3.13: RELATIVE ERROR OF THE CURRENT WITH RESPECT TO THE NUMBER OF ITERATIVE SWEEPS. ....	78
FIG.3.14: CONDITION NUMBER OF THE BANDPASS FILTER VERSUS THE MATRIX STAGES. ....	79
FIG.3.15: SPECTRAL RADIUS OF THE BANDPASS FILTER VERSUS THE MATRIX STAGES. ....	79
FIG.3.16: REFLECTION COEFFICIENTS OF THE BANDPASS FILTER. ....	82
FIG.3.17: 1 X 5 LINEAR SERIES-FED ANTENNA ARRAYS. (A) 1 X 5 LINEAR SERIES-FED ANTENNA ARRAY WITH NO TAPERING (ARRAY A). (B) 1 X 5 LINEAR SERIES-FED ANTENNA ARRAY WITH TAPERING (ARRAY B). ALL DIMENSIONS ARE IN MM. ....	83
FIG.3.18: MESH OF THE 1 X 5 LINEAR SERIES-FED ANTENNA ARRAYS. (A) 1 X 5 LINEAR SERIES-FED ANTENNA ARRAY WITH NO TAPERING (ARRAY A). (B) 1 X 5 LINEAR SERIES-FED ANTENNA ARRAY WITH TAPERING (ARRAY B). ....	83
FIG.3.19: CUT POSITION, D FROM THE DISCONTINUITY EDGE. ....	85
FIG.3.20: RELATIVE ERROR OF THE CURRENT AS A FUNCTION OF THE CUT POSITION D FOR A 1 BY 5 ANTENNA ARRAY. ....	85
FIG.3.21: RELATIVE ERROR OF THE CURRENT VERSUS THE NUMBER OF ITERATIVE SWEEPS. ....	87
FIG.3.22: COMPARISON OF CPU TIME AMONG MBF-PM-AIM, MBF-PM AND THE CONVENTIONAL MoM.....	90
FIG.3.23: COMPARISON OF MEMORY USAGE AMONG MBF-PM-AIM, MBF-PM AND THE CONVENTIONAL MoM.....	90
FIG.3.24: COMPARISON OF THE CURRENT ALONG THE LINE AA' FOR ARRAY A AMONG MBF-PM-AIM, MBF-PM AND THE CONVENTIONAL MoM WITH THE PROPOSED ITERATIVE REFINEMENT PROCESS AFTER 1 ITERATIVE SWEEP. ....	91
FIG.3.25: REFLECTION COEFFICIENTS OF ARRAY A AND ARRAY B. ....	92
FIG.3.26: RADIATION PATTERNS OF ARRAY A (A) E-PLANE. (B) H-PLANE. ....	93
FIG.3.27: RADIATION PATTERNS OF ARRAY B (A) E-PLANE. (B) H-PLANE. ....	94
FIG.3.28: BOWTIE DIPOLE ARRAY .....	95
FIG.3.29: COMPARISON OF THE CURRENT COEFFICIENTS AMONG THE MACRO-BASIS FUNCTION WITH PROGRESSIVE METHOD (MBF-PM), THE SUB-ENTIRE-DOMAIN BASIS FUNCTION METHOD (SED), THE SUB-DOMAIN MULTILEVEL APPROACH (SMA) AND THE CONVENTIONAL MoM WITH RESPECT TO THE RWG BASIS FUNCTIONS ON ELEMENTS 28 AND 37 OF THE BOWTIE ARRAY. THE NUMBERING OF THE RWG BASIS FUNCTIONS IS SHOWN IN THE INSETS. ....	100
FIG.3.30: RADIATION PATTERNS OF THE BOWTIE ARRAY AT 150MHZ (WITHOUT ITERATIVE PROCESS) (A) XZ PLANE (B) YZ PLANE.....	101

FIG.3.31: PHOTOGRAPH OF THE 24 GHz ANTENNA ARRAY.....	102
FIG.3.32: EQUIVALENT CIRCUIT OF A SERIES-CONNECTED PATCH ARRAY. ....	105
FIG.3.33: LAYOUT OF THE 10 X 14 ANTENNA ARRAY. $D_1=85.8$ , $D_2=9.2$ , $W_1=2.57$ , $W_2=0.8324$ , $W_3=0.3$ , $W_4=1.52$ , $W_5=1.72$ , $W_6=2.253$ , $W_7=2.987$ , $W_8=1.28$ , $L_1=1.85$ , $L_2=4.25$ , $L_3=0.67$ , $L_4=5.24$ , $L_5=4.39$ , $L_6=4.2$ . ALL DIMENSIONS GIVEN IN MM. PRINTED ON SUBSTRATE WITH $\epsilon_r=2.2$ AND $H=0.254$ MM. THE DASHED BOX DEFINES HOW THE SUB-DOMAINS IS SUBDIVIDED. ....	109
FIG.3.34: MESH OF THE 10 X 14 ANTENNA ARRAY. ....	109
FIG.3.35: COMPARISON OF CPU TIME USED IN THE PROPOSED METHOD AND THE SIMULATION SOFTWARE, IE3D, FOR THE 10 X 14 ARRAY. ....	111
FIG.3.36: REFLECTION COEFFICIENT OF THE 10 X 14 ANTENNA ARRAY. ....	112
FIG.3.37: RADIATION PATTERNS OF THE 10 X 14 ANTENNA ARRAY AT $F=24$ GHz. (A) E-PLANE (B) H-PLANE.....	113
FIG. 4.1: GEOMETRY OF A PROBE FED MICROSTRIP ANTENNA WITH EDGE-COUPLED PARASITIC PATCHES. ....	118
FIG. 4.2: GEOMETRY OF A PROBE FEED STACKED MICROSTRIP ANTENNA. ....	118
FIG.4.3: GEOMETRY OF A PROBE FEED ANTENNA WITH A U-SLOT. ....	118
FIG.4.4: GEOMETRY OF PATCH ANTENNAS WITH DIFFERENT PROBE SHAPED (A) L-PROBE (B) T-PROBE. ....	119
FIG.4.5: GEOMETRY OF A SEMI-CIRCLE FED PATCH PROXIMITY COUPLED TO A RECTANGULAR PATCH.....	120
FIG.4.6: VARIATION OF THE DIAMETER OF THE SEMI-CIRCLE FED PATCH, D WITHOUT THE PARASITIC PATCH (SIMULATED).....	121
FIG.4.7: CAPACITANCE, C WITH RESPECT TO THE DIAMETER OF THE SEMI-CIRCLE AT 6.5 GHz. ....	122
FIG.4.8: VARIATION OF THE DIAMETER OF THE SEMI-CIRCLE FED PATCH, D WITH RECTANGULAR PATCH (SIMULATED).....	123
FIG.4.9: GEOMETRY OF THE SEMI-CIRCLE PROBE-FED STUB PATCH ANTENNA. ....	124
FIG.4.10: PHOTOGRAPHS OF THE FABRICATED SEMI-CIRCLE PROBE-FED STUB PATCH ANTENNA. ....	124
FIG.4.11: SIMULATED AND MEASURED RETURN LOSS OF THE SEMI-CIRCLE PROBE-FED STUB PATCH ANTENNA. ....	125
FIG.4.12: (A) MEASURED IMPEDANCE LOCUS OF THE STUB PATCH ANTENNA, RECTANGULAR PATCH ANTENNA AND SEMI-CIRCLE FED PATCH. (B) COMPARISON OF THE MEASURED RETURN LOSS OF THE STUB PATCH, THE RECTANGULAR PATCH AND THE SEMI-CIRCLE FED PATCH. ....	127
FIG.4.13: COMPARISON OF THE BROADSIDE GAIN OF THE SEMI-CIRCLE PROBE-FED STUB PATCH ANTENNA BETWEEN THE MEASUREMENT AND THE SIMULATION.....	127
FIG.4.14: MEASURED RADIATION PATTERNS OF THE SEMI-CIRCLE PROBE-FED STUB PATCH ANTENNA AT 4.2 GHz. BLACK LINES REPRESENT CO-POLARIZED PATTERN. BLUE LINES REPRESENT CROSS-POLARIZED PATTERN. ....	129
FIG.4.15: MEASURED RADIATION PATTERNS OF THE SEMI-CIRCLE PROBE-FED STUB PATCH ANTENNA AT 5.4 GHz. BLACK LINES REPRESENT CO-POLARIZED PATTERN. BLUE LINES REPRESENT CROSS-POLARIZED PATTERN. ....	129

FIG.4.16: MEASURED RADIATION PATTERNS OF THE SEMI-CIRCLE PROBE-FED STUB PATCH ANTENNA AT 7.0 GHZ. BLACK LINES REPRESENT CO-POLARIZED PATTERN. BLUE LINES REPRESENT CROSS-POLARIZED PATTERN. ....	130
FIG.4.17: SIMULATED CURRENT DISTRIBUTIONS OF THE SEMI-CIRCLE PROBE-FED STUB PATCH ANTENNA AT (A) 4.5 GHZ (B) 5.5 GHZ (C) 7 GHZ. ....	131
FIG. 4.18: VARIATION OF THE DIAMETER OF THE SEMI-CIRCLE FED PATCH, D WITH THE STUB PATCH (SIMULATED). ....	133
FIG.4.19: VARIATION OF THE GAP, G BETWEEN THE TOP PATCH AND THE FED PATCH (SIMULATED). ....	133
FIG. 4.20: VARIATION OF THE LENGTH, L1 OF THE STUB PATCH (SIMULATED). ....	134
FIG.4.21: VARIATION OF THE LENGTH, W1 OF THE STUB PATCH (SIMULATED). ....	134
FIG.4.22: RELATIVE LONGITUDINAL TRANSLATION BETWEEN THE FED PATCH AND THE STUB PATCH (SIMULATED). ....	135
FIG.4.23: VARIATION OF THE FEED POSITION, F OF THE SEMI-CIRCLE PROBE-FED STUB PATCH ANTENNA. ....	135
FIG. 4.24: (A) GEOMETRY OF SEMI-CIRCLE PROBE-FED FLOWER-SHAPED PATCH ANTENNA. (B) PHOTOGRAPHS OF THE FABRICATED SEMI-CIRCLE PROBE-FED STUB PATCH ANTENNA. ....	137
FIG.4.25: SIMULATED AND MEASURED RETURN LOSS OF SEMI-CIRCLE PROBE-FED FLOWER-SHAPED PATCH ANTENNA. ....	139
FIG.4.26: COMPARISON OF MEASURED RETURN LOSS OF FLOWER-SHAPED PATCH, DIAMOND-SHAPED PATCH AND RECTANGULAR-SHAPED PATCH. ....	139
FIG.4.27: MEASURED IMPEDANCE LOCUS OF THE RECTANGULAR PATCH, DIAMOND PATCH AND FLOWER-SHAPED PATCH. ....	140
FIG.4.28: VARIATION OF THE LENGTH L2 OF THE FLOWER-SHAPED PATCH (SIMULATED). ....	140
FIG.4.29: VARIATION OF THE LENGTH S1 OF THE FLOWER-SHAPED PATCH (SIMULATED). ....	141
FIG.4.30: COMPARISON OF THE BROADSIDE GAIN OF THE SEMI-CIRCLE PROBE-FED FLOWER-SHAPED PATCH ANTENNA BETWEEN MEASUREMENT AND SIMULATION... ..	141
FIG.4.31: MEASURED RADIATION PATTERNS FOR FLOWER-SHAPED PATCH ANTENNA AT 4.2 GHZ. BLACK LINES REPRESENT CO-POLARIZED PATTERN. BLUE LINES REPRESENT CROSS-POLARIZED PATTERN. ....	143
FIG.4.32: MEASURED RADIATION PATTERNS FOR FLOWER-SHAPED PATCH ANTENNA AT 5.4 GHZ. BLACK LINES REPRESENT CO-POLARIZED PATTERN. BLUE LINES REPRESENT CROSS-POLARIZED PATTERN. ....	143
FIG.4.33: MEASURED RADIATION PATTERNS FOR FLOWER-SHAPED PATCH ANTENNA AT 7.0 GHZ. BLACK LINES REPRESENT CO-POLARIZED PATTERN. BLUE LINES REPRESENT CROSS-POLARIZED PATTERN. ....	144
FIG.4.34: SIMULATED CURRENT DISTRIBUTION OF THE SEMI-CIRCLE PROBE-FED FLOWER-SHAPED PATCH ANTENNA AT (A) 4.5 GHZ (B) 5.5 GHZ (C) 7.0 GHZ. ....	145
FIG.4.35: (A) GEOMETRY OF THE SEMI-CIRCLE PROBE-FED PENTAGON-SLOT PATCH ANTENNA. (B) PHOTOGRAPHS OF THE FABRICATED SEMI-CIRCLE PROBE-FED PENTAGON-SLOT PATCH ANTENNA. ....	146

FIG.4.36: SIMULATED AND MEASURED RETURN LOSS OF THE PENTAGON-SLOT ANTENNA. .....	147
FIG.4.37: COMPARISON OF THE MEASURED RETURN LOSS OF THE PENTAGON SLOT PATCH, THE RECTANGULAR PATCH AND THE SEMI-CIRCLE FED PATCH. ....	148
FIG.4.38: MEASURED INPUT IMPEDANCE PLOT OF THE PENTAGON SLOT PATCH (SOLID LINE) AND THE RECTANGULAR PATCH (DASHED LINE).....	148
FIG.4.39: VARIATION OF LENGTH, S2 OF THE PENTAGON-SLOT PATCH (SIMULATED). ..	149
FIG.4.40: VARIATION OF LENGTH, S1 OF THE PENTAGON-SLOT PATCH (SIMULATED). ..	149
FIG.4.41: COMPARISON OF BROADSIDE GAIN OF THE SEMI-CIRCLE PROBE-FED PENTAGON-SLOT PATCH ANTENNA BETWEEN THE MEASUREMENT AND SIMULATION. .....	150
FIG.4.42: MEASURED RADIATION PATTERNS OF THE SEMI-CIRCLE PROBE-FED PENTAGON-SLOT ANTENNA AT 4.6 GHZ. BLACK LINES REPRESENT CO-POLARIZED PATTERN. BLUE LINES REPRESENT CROSS-POLARIZED PATTERN. ....	150
FIG.4.43: MEASURED RADIATION PATTERNS OF THE SEMI-CIRCLE PROBE-FED PENTAGON-SLOT ANTENNA AT 6.1 GHZ. BLACK LINES REPRESENT CO-POLARIZED PATTERN. BLUE LINES REPRESENT CROSS-POLARIZED PATTERN. ....	151
FIG.4.44: MEASURED RADIATION PATTERNS OF THE SEMI-CIRCLE PROBE-FED PENTAGON-SLOT ANTENNA AT 7.3 GHZ. BLACK LINES REPRESENT CO-POLARIZED PATTERN. BLUE LINES REPRESENT CROSS-POLARIZED PATTERN. ....	151
FIG.4.45: SIMULATED CURRENT DISTRIBUTIONS OF THE SEMI-CIRCLE PROBE-FED PENTAGON-SLOT PATCH ANTENNA AT (A) 4.5 GHZ (B) 5.5 GHZ (C) 7.0 GHZ. ....	152
FIG.4.46: 4 BY 4 SEMI-CIRCLE PROBE-FED MICROSTRIP STUB PATCH ANTENNA ARRAY.	155
FIG.4.47: CIRCUIT SCHEMATIC OF A POWER DIVIDER.....	156
FIG.4.48: MEASURED S-PARAMETERS OF A POWER DIVIDER. ....	157
FIG.4.49: 4 X 4 SEMI-CIRCLE PROBE-FED MICROSTRIP STUB PATCH ANTENNA ARRAY. (A) FEED NETWORK A (B) FEED NETWORK B .....	158
FIG.4.50: AVERAGE CURRENT DENSITY OF THE FEED NETWORK AT 5.4 GHZ. THE ARROWS INDICATE THE DIRECTION OF THE CURRENT (A) FEED NETWORK A (B) FEED NETWORK B.....	159
FIG.4.51: SIMULATED S-PARAMETERS OF FEED NETWORK A AND FEED NETWORK B. (A) S11 (B) S21. ....	160
FIG.4.52: PHOTOGRAPH OF THE 4 X 4 SEMI-CIRCLE PROBE-FED STUB PATCH ANTENNA ARRAY WITH FEED NETWORK A.....	160
FIG.4.53: FAR FIELD MEASUREMENT FOR THE 4 X 4 SEMI-CIRCLE PROBE-FED STUB PATCH ANTENNA ARRAY IN THE ANECHOIC CHAMBER. ....	161
FIG.4.54: MEASURED RETURN LOSS OF THE 4 X 4 SEMI-CIRCLE PROBE-FED STUB PATCH ANTENNA ARRAY WITH (A) FEED NETWORK A AND (B) FEED NETWORK B.....	162
FIG.4.55: RADIATION PATTERNS OF THE 4 X 4 SEMI-CIRCLE PROBE-FED STUB PATCH ANTENNA ARRAY AT 4.2 GHZ. (A) CO-POLARIZED PATTERN IN E-PLANE (B) CO-POLARIZED PATTERN IN H-PLANE (C) CROSS-POLARIZED PATTERN IN H-PLANE .....	165
FIG.4.56: RADIATION PATTERNS OF THE 4 X 4 SEMI-CIRCLE PROBE-FED STUB PATCH ANTENNA ARRAY AT 5.4 GHZ. (A) CO-POLARIZED PATTERN IN THE E-PLANE (B)	

CO-POLARIZED PATTERN IN THE H-PLANE (C) CROSS-POLARIZED PATTERN IN H-PLANE .....	166
FIG.4.57: RADIATION PATTERNS OF THE 4 X 4 SEMI-CIRCLE PROBE-FED STUB PATCH ANTENNA ARRAY AT 7 GHZ. (A) CO-POLARIZED PATTERN IN THE E-PLANE (B) CO-POLARIZED PATTERN IN THE H-PLANE (C) CROSS-POLARIZED PATTERN IN THE H-PLANE .....	168
FIG.4.58: 2 X 1 LINEARLY POLARIZED ARRAY. ....	168
FIG.4.59: CIRCUIT SCHEMATIC OF THE PLANAR BALUN. ....	170
FIG.4.60: MEASURED OUTPUT PORTS S-PARAMETERS OF THE PLANAR BALUN.....	170
FIG.4.61: MEASURED PHASE DIFFERENCE BETWEEN THE OUTPUT PORTS OF THE PLANAR BALUN.....	170
FIG.4.62: MEASURED RETURN LOSS OF THE 2 X 1 LINEARLY POLARIZED ARRAY.....	171
FIG.4.63: RADIATION PATTERNS OF THE 2 X 1 LINEARLY POLARIZED ANTENNA ARRAY AT 5.4 GHZ. (A) E-PLANE (B) H-PLANE.....	172
FIG.4.64: 4 X 4 LINEAR POLARIZED ANTENNA ARRAY. ....	173
FIG.4.65: RADIATION PATTERNS OF THE 4 X 4 LINEAR POLARIZED ANTENNA ARRAY AT 5.4 GHZ. (A) E-PLANE (B) H-PLANE .....	174

## List of Tables

TABLE 2.1: COMPARISON OF THE AVERAGE INTERPOLATION RELATIVE ERROR BETWEEN THE THREE INTERPOLATION SCHEMES. (K: NUMBER OF INTERPOLATION POINTS; N: NUMBER OF COEFFICIENTS REQUIRED BY THE INTERPOLATION SCHEMES; D: $\bar{r} - \bar{r}'$ .	43
Table 3.1: Specifications of the Chebyshev bandpass filter.	71
TABLE 3.2: COMPARISON OF THE RELATIVE ERRORS IN THE CURRENT DISTRIBUTION, TIME REDUCTION WITH RESPECT TO THE CONVENTIONAL MoM WITHOUT ANY ITERATIVE SWEEP. ....	75
TABLE 3.3: COMPARISON OF THE TIME REDUCTION WITH RESPECT TO CONVENTIONAL MoM AND NUMBER OF ITERATIVE SWEEPS SUBJECT TO $\xi < 0.2\%$ AND THE RELATIVE ERROR IN CURRENT, $\Delta_c$ IS 0.09%.....	78
TABLE 3.4: DEFINITION OF THE MATRIX STAGES. ....	80
TABLE 3.5: COMPARISON BETWEEN THE SPECIFICATIONS AND THE MEASUREMENTS OF THE BANDPASS FILTER. ....	82
TABLE 3.6: SPECIFICATIONS OF THE SERIES-FED ARRAY. ....	84
TABLE 3.7: COMPARISON OF THE RELATIVE ERROR AND THE CPU TIME BETWEEN SMALL DOMAINS A AND B WHEN APPLIED TO MBF-PM-AIM. ....	86
TABLE 3.8: COMPARISON OF THE RELATIVE ERROR IN THE CURRENT UNDER VARIOUS METHODS WITHOUT ITERATIVE REFINEMENT PROCESS. ....	86
TABLE 3.9: COMPARISON OF THE REDUCTION IN TIME AND MEMORY USAGE UNDER VARIOUS METHODS WITH ITERATIVE REFINEMENT PROCESS SUBJECT TO $\Delta_c \leq 1.5\%$ .	88
TABLE 3.10: COMPARISON OF THE CPU TIME, THE NUMBER OF MBFs GENERATED AND THE RELATIVE ERRORS BETWEEN MBF-PM, MBF-PM-AIM AND CHARACTERISTICS BASIS FUNCTION (CBF). ....	89
TABLE 3.11: COMPARISON OF THE RELATIVE ERROR OF THE INPUT IMPEDANCE BETWEEN MBF-PM AND MBF-PM-AIM.....	91
TABLE 3.12: SPECIFICATIONS OF THE BOWTIE DIPOLE ARRAY. ....	95
TABLE 3.13: COMPARISON OF THE RELATIVE ERRORS IN CURRENT AND TIME REDUCTION WITH RESPECT TO THE CONVENTIONAL MoM FOR THE BOWTIE ARRAY WITHOUT ITERATIVE REFINEMENT PROCESS. ....	97
TABLE 3.14: SUMMARY OF THE RADIATION PATTERNS OF THE BOWTIE ARRAY. ....	97
TABLE 3.15: ROOT MEAN SQUARE DEVIATION AND MAXIMUM DEVIATION FROM THE CONVENTIONAL MoM AFTER ONE ITERATIVE SWEEP.....	97
TABLE 3.16: SPECIFICATIONS OF THE 24 GHz ANTENNA ARRAY.....	103



TABLE 3.17: COMPARISON OF THE PERFORMANCES AMONG MBF-PM-AIM, THE SUB-DOMAIN MULTILEVEL APPROACH AND THE COMMERCIAL SOFTWARE, IE3D.	110
Table 4.1: Specifications of the antenna.	120
TABLE 4.2: SUMMARY OF THE RADIATION CHARACTERISTICS OF STUB PATCH ANTENNA. .....	128
TABLE 4.3: SUMMARY OF THE CHARACTERISTICS OF FLOWER-SHAPED PATCH ANTENNA. .....	142
TABLE 4.4: SUMMARY OF THE RADIATION CHARACTERISTICS OF PENTAGON-SLOT PATCH ANTENNA. ....	148
TABLE 4.5: SUMMARY OF THE PERFORMANCE OF THE THREE PROPOSED PROBE FED PATCH ANTENNAS. ....	153
TABLE 4.6: COMPARISON OF THE SIMULATED AND THE MEASURED GAINS OF THE 4 X 4 SEMI-CIRCLE PROBE-FED STUB PATCH ANTENNA ARRAY. ....	163
TABLE 4.7: SUMMARY OF THE RADIATION CHARACTERISTICS OF THE 4 X 4 SEMI-CIRCLE PROBE-FED STUB PATCH ANTENNA ARRAY WITH FEED NETWORK B. ....	163

## List of Symbols

$\epsilon_0$	permittivity of free space ( $8.854 \times 10^{-12}$ F/m)
$\mu_0$	permeability of free space ( $4\pi \times 10^{-7}$ F/m)
$\epsilon_r$	relative permittivity of substrate
$\mu_r$	relative permeability of substrate
$\omega$	radian frequency
$\eta$	intrinsic impedance of the medium
E	electric field intensity
H	magnetic field intensity
J	electric surface current density
M	magnetic surface current density
q	surface charge density

## List of Acronyms

AIM	Adaptive Integral Method
CBF	Characteristic Basis Function
DCIM	Discrete Complex Image Method
FFT	Fast Fourier Transform
GPOF	Generalized Pencil-of-function Method
MBF	Macro-basis Function
MBF-PM	Macro-basis Function with Progressive Method
MBF-PM-AIM	Macro-basis Function with Progressive and Adaptive Integral Method
MoM	Method of Moments
RBF	Radial Basis Function
SED	Sub-entire-domain Basis Function Method
SMA	Sub-domain Multilevel Approach
SVD	Singular Value Decomposition

# **CHAPTER 1 Introduction**

## **1.1 Literature Review and Motivation**

During recent years, there has been an enormous growth in the wireless communication industry such as cellular communications, wireless local area network and Bluetooth systems. As antennas serve as the transition between the RF front-end circuitry and the radiation and propagation of electromagnetic waves in the free space, they play a critical role in the wireless technology. As such, it is necessary to use antennas that have good impedance match and radiation pattern over the required frequency range. Moreover, if the impedance bandwidth of an antenna is wide enough to cover several operating bands, then a single antenna can be used in operating different wireless applications and this could save a lot of space in product design [3].

Antennas should be relatively cheap and easy to manufacture. They should be lightweight, low-profile and robust. One type of antenna that fulfils these requirements very well is the microstrip antenna [4]-[6]. There are four fundamental techniques to feed or excite the patch. These include the probe feed, the microstrip line feed, the aperture-coupled feed and the proximity coupled feed. The feeding

techniques have their own advantages and disadvantages. However, the probe feed has a number of characteristics that make it very suitable for application in the wireless communications field. As the feed network is separated from the patch, there is less spurious radiation from the feed network as compared to that of the microstrip-line feed and the proximity-coupled feed. In this thesis, the probe feed is used to excite the proposed antennas.

Regardless of the feeding techniques, the main drawback associated with microstrip patch antennas is that they inherently have a very narrow impedance bandwidth. This is due to the fact that the region under the patch is a cavity with a high quality factor. In most cases, the impedance bandwidth is not wide enough for the requirements of wireless communication systems. As a result, a lot of broadband techniques using probe feed have been investigated [7]-[26]. These techniques include the use of parasitic elements [7]-[14], slotted patches [15]-[22] and different probes shape [23]-[26]. Although researchers have already proposed several impedance bandwidth enhancement techniques, the bandwidth normally cannot exceed 60%. As such, the research into wideband probe-fed microstrip patch antennas is still a relevant topic.

As antennas become more complex, the use of simple analytical modeling techniques is not sufficient anymore. The use of more sophisticated numerical methods, such as full-wave modeling techniques, has therefore become inevitable. A variety of full-wave electromagnetic methods has been developed and these methods can be

divided into the partial differential equation [27]-[31] and the integral equation method [32]-[34]. The partial differential equation approach includes finite difference time domain [27]-[28] and finite element method [29]-[30]. The partial differential equation solver requires the entire computation domain to be discretized while in the integral equation method, which is solved using the method of moments, allows one to apply Green's theorem to reduce volume integrals to surface integrals, thus reducing the matrix dimension significantly. Among the existing methods, the method of moments (MoM) is one of the most popular choices to solve multilayer medium problems.

The MoM analysis can be carried out either in the spectral domain [35]-[36] or the spatial domain [37]-[38]. To generate the impedance matrix in the spectral domain formulation, the time-consuming evaluation of the double infinite integration is required. Although acceleration techniques and approximations can improve the computational efficiency of the spectral domain MoM, they impose some restrictions on the type of basis functions to be used. In contrast, for the spatial domain MoM, the adopted basis functions can be arbitrary. However, the efficiency of this approach depends on the evaluation of the spatial domain Green's function, which is expressed in terms of the Sommerfeld integral. The numerical integration of the Sommerfeld integral is time-consuming since the integrand is both highly oscillating and slowly decaying. To solve this problem, the Sommerfeld integral can be expressed in closed-form using the discrete complex image method (DCIM) [39]. Even though

DCIM provides an efficient way to evaluate the Green's function, the number of Green's functions to be evaluated is still very large. The number of Green's functions to be evaluated is proportional to  $O(N^2)$ , where  $N$  is the number of unknowns. In addition, it is expensive to evaluate the Hankel function in the closed-form expression. To circumvent these problems, interpolation scheme is employed. In this thesis, three interpolation techniques, namely the radial basis function, the Cauchy method and the generalized pencil-of-function method are studied. Among the three interpolation techniques, the generalized pencil-of-function interpolation scheme provides the best accuracy with the less number of interpolation points.

The memory requirements and computation complexity for the method of moments using direct solver is  $O(N^2)$  and  $O(N^3)$  respectively. Hence as  $N$  increases, there will be a tremendous increase in time usage and memory, rendering the method computationally expensive to solve for large structures. When an iterative solver such as the conjugate gradient method is employed for solving the MoM matrix equation, the operation count is reduced from  $O(N^3)$  to  $O(N^2)$  per iteration. However, this operation count is still too high for an efficient simulation.

To make the iterative method more efficient, it is necessary to speed up the matrix-vector multiplication. By exploiting the translational invariance of the Green's function, the matrix-vector product can be computed using the fast Fourier transform. The conjugate gradient fast Fourier transform [40]-[41] combines the conjugate

gradient method with the fast Fourier transform. The use of fast Fourier transform reduces the operation count to  $O(N \log N)$  per iteration. However, the method works only when the structure is discretized into uniform rectangular grids, which necessitates a staircase approximation in the modeling of an arbitrary geometry. This is often considered as the most serious drawback of the conjugate gradient fast Fourier transform method. To model an arbitrary geometry accurately, one has to use triangular elements. However, the triangular discretization does not allow the application of the fast Fourier transform to speed up the matrix-vector multiplication. The method to alleviate the problem is to use the fast multipole method [42]-[45]. The fast multipole method improves the time performance by accelerating the matrix-vector multiplications needed in the iterative solvers in a highly efficient manner using a spherical harmonic expansion technique. Another method is to project the triangular elements onto uniform grids using the adaptive integral method [46]-[49]. The resulting algorithm has the memory requirement proportional to  $O(N)$  and the operation count for the matrix-vector multiplication proportional to  $O(N \log N)$ .

Although the methods discussed above have reduced the computation burden, the iterative solver employs in these methods may lead to convergence difficulties when dealing with very large scale objects. As such, the search for techniques to overcome convergence issue for large structure is a very important research area. One emerging approach is based on the segmentation technique. The use of high-level basis



functions, defined over electrically large geometrical domains, can significantly reduce the number of unknowns. Recently, the sub-domain multilevel approach [50]-[54] has been proposed to handle large planar antenna arrays. However, the method does not directly account for the mutual coupling effect between different portions of the geometry during the construction of the macro-basis function. If each portion of the geometry is a strong radiator, the sub-domain multilevel approach may not be able to solve the problem accurately. The sub-entire-domain basis function method reported in [55] improves the accuracy of the solution by relying on the hypothesis that the fields on a given sub-domain in the large finite structure can be precisely described by solutions obtained for very small problems. Even though the method gives good accuracy, it is used for periodic structure. To overcome this limitation, a new grouping concept of near-far neighbour evaluation is developed. This new concept called the macro-basis function with progressive method is investigated in this thesis. The basic idea of the method is to partition a given complex geometry into several sub-domains. A small problem that is made up of a few sub-domains is first solved using the conventional method of moments. The solved solution on the subsectional basis functions of each sub-domain is merged into macro-basis function. The remaining sub-domains are then inserted into the smaller problem progressively, taking into account the mutual coupling effect of the solved currents. The macro-basis function with progressive method is tested on some numerical examples. The numerical results show that the proposed method gives a much better accuracy as compared to the sub-domain multilevel approach.

Although the macro-basis function with progressive method has improved the accuracy of the solution, iterative refinement process is still required for dense and complex structures with strong or important parasitic couplings. In [1], a block Gauss-Seidel process is applied to each macro-basis function. During the process, the macro-basis function extends over the whole structure. Thus, complete matrix-vector products must be performed for each block Gauss-Seidel process. Although the method converges very fast, its computational complexity is high. The computational complexity of the iterative refinement process can be reduced by adopting the method in [2]. However, the approach may not converge for all cases. As a solution to this problem, an improved iterative refinement process, which utilizes the concept of macro-basis function, is developed in this thesis.

In a large electromagnetic problem, where the memory occupation and the computational time have already been significantly reduced using the macro-basis function with progressive method, the interaction between different macro-basis functions remains the most time-consuming part of the procedure. This thesis introduces an efficient way of computing the interactions between different macro-basis functions. The strategy for improving the macro-basis function in terms of computational time is based on the adaptive integral method. The macro-basis functions are projected onto regular auxiliary grids. In this way, the reaction integrals take a two-dimensional convolution form and can be efficiently evaluated by means of fast Fourier transform. When the adaptive integral method is combined with the

macro-basis function with progressive method, the resulting algorithm is called the macro-basis function with progressive and adaptive integral method. The macro-basis function with progressive and adaptive integral method is tested on some numerical examples. For a 1 by 14 antenna array, the numerical result shows that the method is 10 times faster than the conventional method of moments. The macro-basis function with progressive and adaptive integral method is subsequently used for the design of three broadband probe-fed antennas and arrays in the thesis.

## 1.2 Scope of Work

This chapter presents some background information on the computational electromagnetics and microstrip patch antennas. A variety of electromagnetic methods has been investigated to solve the radiation and scattering problems. Among the methods, the method of moments is a powerful technique to analyze multilayer structure. However, the method becomes inefficient when dealing with large structures. In the present work, the objective is to develop improved segmentation method, which is called the macro-basis function with progressive and adaptive integral method, for effective simulation of large scale problems. Various wideband probe-fed microstrip antennas and arrays are then designed with the macro-basis function with progressive and adaptive integral method. The remaining chapters are organized in the following way:

Chapter 2 reviews the formulation of multilayer Green's function and magnetic field integral equation. The method of moments and the computation of antenna parameters such as scattering parameters and far-fields are discussed in detail. Three interpolation schemes are investigated to speed up the evaluation of the Green's function for large structures. They are the radial basis function [58]-[59], the Cauchy method [60]-[61] and the generalized pencil-of-function method [56]-[57].

Chapter 3 presents a hybrid macro-basis function combined with progressive and adaptive integral method to efficiently solve microstrip problems. This chapter first outlines the concept of macro-basis function. A grouping concept, which utilizes both the macro-basis function and the progressive method, to analyze microstrip structures is next introduced. An iterative refinement process that accelerates the convergence of the solution is presented. This will be followed by developing an efficient way to compute the interactions between the macro-basis functions. Finally, this chapter demonstrates the accuracy and efficiency of the macro-basis function with progressive and adaptive integral method by investigating some examples in which the proposed method is compared with the conventional MoM.

Various wideband probe-fed microstrip patch antennas are investigated in Chapter 4. This chapter rolls off by presenting an overview of various techniques that have been used thus far for the bandwidth-enhancement of probe-fed microstrip patch antennas. This is followed by the presentation of three novel semi-circle probe-fed patch

antennas in which one of the antennas is used in array configurations.

Chapter 5 contains general conclusions regarding the research findings and concludes the thesis with some recommendations for the future work.

### 1.3 List of Original Contributions

As a result of the research work, the following contributions have been achieved:

1. A comparison of different interpolation techniques, namely the radial basis function, the Cauchy method and the generalized pencil-of-function method to evaluate multilayer Green's function for large-scale structure is given. Among the interpolation techniques, the generalized pencil-of-function method provides the best accuracy with the less number of interpolation points.
2. A new grouping concept, which utilizes the macro-basis function with progressive method, is developed to analyze microstrip structures. The method reduces the matrix size and in turn, leads to considerable savings in computer memory requirements and speed when compared to the conventional method of moments.
3. A new iterative refinement method has been developed to accelerate the convergence of the iterative procedure.
4. An efficient way of filling the MoM matrix through adaptive integral method is proposed. The interaction between the macro-basis functions and the testing function is carried out using compressed representation and the computation is

speeded up using the fast Fourier transform.

5. A feeding mechanism, semi-circle probe, has been developed for probe-fed microstrip patch antennas on thick substrates, which can be used with any shape of radiating elements. Three novel semi-circle probe-fed microstrip patch antennas are then proposed to achieve wideband operation in multipath environments.

## 1.4 Publications

The research and study in this thesis are reported in the following papers:

### Journals

1. Irene Ang and B.L. Ooi, "A Broadband Semi-circle-Fed Microstrip Patch Antenna," IET Microwaves, Antennas and Propagation, Vol.1, No.3, pp. 770-775, June 2007.
2. Irene Ang and B.L. Ooi, "An Ultra-wideband Stacked Microstrip Patch Antenna," Microwave and Optical Technology Letters, Vol 49, No.7, pp. 1659-1665, July 2007.
3. Irene Ang and B.L. Ooi, "A Broadband Semi-circle fed Pentagon-Slot Microstrip Patch Antenna," Microwave and Optical Technology Letters, Vol 47, No. 5, pp. 500-505, Dec 2005
4. B.L. Ooi and Irene Ang, "A Broadband Semi-circle fed flower-shaped Microstrip Patch Antenna," IET Electronics Letters, Vol. 41, No. 17, pp. 7- 8, Aug 2005.
5. B. L. Ooi, Irene Ang, and M. S. Leong, "Improving Macro-basis function using

Insertion method and Iterative Refinement Process for Antenna Array and Filter,”  
submitted to IET Microwaves, Antennas and Propagation.

### Conferences

1. Irene Ang and B.L.Ooi, “A Broad Band Stacked Microstrip Patch Antenna,”  
Seventeenth Asia-Pacific Microwave Conference paper, Vol 2, pp.2, Dec 2005
2. Jayasanker J, B.L Ooi, Irene Ang, M.S Leong and M. K Iyer, “PEEC Model for  
Multiconductor Systems Including Dielectric Mesh,” Seventeenth Asia-Pacific  
Microwave Conference paper, Vol 2, pp. 3, Dec. 2005.
3. B. L. Ooi, M. S. Leong, H. D. Hristov, R. Feick, Irene Ang, Z. Zhong and C. H.  
Sing, “An efficient algorithm for analyzing microstrip structure using  
macro-basis-function and progressive method,” IEEE Applied Electromagnetics  
Conference, Dec 2007.
4. Irene Ang, B. L. Ooi, “A hybrid technique for combining Macro-basis Function  
and AIM approach,” Progress in Electromagnetics Research Symposium, 2008

# **CHAPTER 2      Numerical Modelling of Planar Multilayered Structures**

## **2.1      Introduction**

The analysis of microstrip structures requires efficient electromagnetic simulation [34]. Typically, the analysis can be performed using either the partial differential equation solvers [27]-[31] or the integral equation solvers [32]-[33]. The partial differential equation method requires the whole computational domain to be meshed and appropriate terminating boundary conditions to be specified which leads to a large number of unknowns to be solved. The integral equation solver uses the method of moments to solve for the unknown surface currents. Thus, only the surface of the circuit needs to be discretized, leading to a significant reduction in the number of unknowns. The method of moments (MoM) has received intense attention to tackle the multilayer medium problems. In this method, the evaluation of the Green's functions [63]-[77] and the choice of basis functions are crucial to obtaining accurate and efficient solutions.

In this chapter, the discrete complex image method (DCIM) [39] is presented to



evaluate the Green's functions. The basic idea of the DCIM is to approximate the spectral kernel of a Green's function by a sum of complex exponentials extracted using the generalized pencil-of-function method [56]-[57]. Then the Sommerfeld integral is evaluated in closed-forms via the Sommerfeld identity. Even though DCIM provides an efficient way to evaluate the Green's functions, a heavy computation is still required to analyse a large structure. The number of Green's functions to be evaluated is proportional to  $O(N^2)$  in the MoM analysis, where  $N$  is the total number of unknowns. To circumvent these problems, interpolation methods have been introduced to speed up the evaluation of the Green's function. In this thesis, three interpolation schemes, namely the radial basis function [58]-[59], the Cauchy method [60]-[61] and the generalized pencil-of-function method [56]-[57] are studied and compared.

This chapter is organized as follows. First the Green's function for the multilayered planar medium is reviewed. This will be followed by a discussion on the MoM method, the interpolation scheme for the Green's function for fast evaluation of the MoM matrix elements and the computation of the radiation patterns. Finally, a patch antenna is analyzed to demonstrate the accuracy of the algorithm.

## 2.2 Spectral Domain Green's Functions [63]

It is often more convenient to work in the spectral domain rather than in the spatial domain. This is due to the fact that in the spectral domain, the original vector problem can be reduced to the scalar transmission line problem and the dyadic Green's function for a grounded multilayered medium can be derived in closed-form.

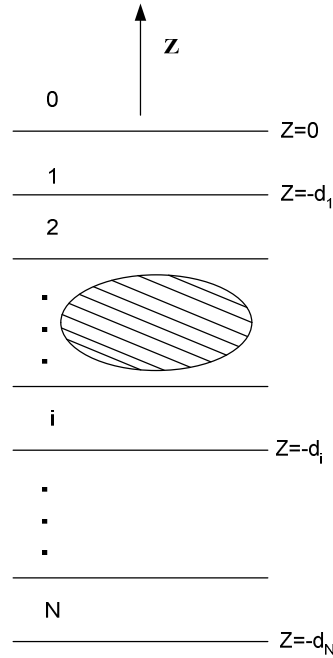


Fig 2.1: An arbitrary shaped scatterer embedded in layered dielectric medium.

Consider a general multilayer medium as shown in Fig 2.1. The medium is assumed to be homogeneous and laterally infinite. The fields ( $\mathbf{E}$ ,  $\mathbf{H}$ ) due to a specified current ( $\mathbf{J}$ ,  $\mathbf{M}$ ) are governed by Maxwell's equations:

$$\nabla \times \mathbf{E} = -j\omega\mu_0\mu_r\mathbf{H} - \mathbf{M}, \quad (2.1)$$

$$\nabla \times \mathbf{H} = j\omega\epsilon_0\epsilon_r\mathbf{E} + \mathbf{J}. \quad (2.2)$$

The problem is formulated in the transformed spectral domain, in which the

transverse and longitudinal components are decomposed with the transverse coordinate  $\boldsymbol{\rho} = \hat{\mathbf{x}}x + \hat{\mathbf{y}}y$  replaced by the spectral counterpart  $\mathbf{k}_\rho = \hat{\mathbf{x}}k_x + \hat{\mathbf{y}}k_y$  through the Fourier transform,

$$\mathfrak{F}f(\mathbf{r}) \equiv \tilde{f}(\mathbf{k}_\rho; z) = \int_{-\infty}^{+\infty} \int_{-\infty}^{+\infty} f(\mathbf{r}) e^{j\mathbf{k}_\rho \cdot \boldsymbol{\rho}} dx dy, \quad (2.3)$$

$$\mathfrak{F}^{-1}\tilde{f}(\mathbf{k}_\rho; z) \equiv f(\mathbf{r}) = \frac{1}{(2\pi)^2} \int_{-\infty}^{+\infty} \int_{-\infty}^{+\infty} \tilde{f}(\mathbf{k}_\rho; z) e^{-j\mathbf{k}_\rho \cdot \boldsymbol{\rho}} dk_x dk_y. \quad (2.4)$$

The inverse Fourier integral equation (2.4) can be expressed as the Fourier-Bessel transform pair by introducing the Bessel function,

$$J_0(k_\rho \rho) = \frac{1}{2\pi} \int_0^{2\pi} e^{-jk_\rho \rho \cos(\alpha - \zeta)} d\alpha = \int_0^{2\pi} e^{-j(k_\rho \cos(\alpha) \rho \sin(\zeta) + k_\rho \sin(\alpha) \rho \sin(\zeta))} d\alpha. \quad (2.5)$$

Given  $k_x = k_\rho \cos \alpha$ ,  $k_y = k_\rho \sin \alpha$ ,  $x - x' = \rho \cos \zeta$ ,  $y - y' = \rho \sin \zeta$ ,  $k_\rho = \sqrt{k_x^2 + k_y^2}$ ,

$\alpha = \arctan\left(\frac{k_y}{k_x}\right)$ ,  $\rho = \sqrt{(x - x')^2 + (y - y')^2}$ ,  $\zeta = \arctan\left(\frac{y - y'}{x - x'}\right)$  and

$dk_x dk_y = k_\rho d\alpha dk_\rho$ , the inverse Fourier integral also referred to as Sommerfeld integral is expressed as

$$\mathfrak{F}^{-1}\tilde{f}(\mathbf{k}_\rho) \equiv f(\boldsymbol{\rho}, z) = \frac{1}{2\pi} \int_0^\infty \tilde{f}(\mathbf{k}_\rho; z) J_0(k_\rho \rho) k_\rho dk_\rho. \quad (2.6)$$

We can rewrite Maxwell's equations [63] as follows:

$$\frac{\partial}{\partial z} \tilde{\mathbf{E}}_\rho = \frac{1}{j\omega \epsilon_0 \epsilon_r} (k_0^2 \mu_r \epsilon_r - \mathbf{k}_\rho \mathbf{k}_\rho \cdot) (\tilde{\mathbf{H}}_\rho \times \hat{\mathbf{z}}) + \frac{\mathbf{k}_\rho \tilde{J}_z}{\omega \epsilon_0 \epsilon_r} - \tilde{\mathbf{M}}_\rho \times \hat{\mathbf{z}}, \quad (2.7)$$

$$\frac{\partial}{\partial z} \tilde{\mathbf{H}}_\rho = \frac{1}{j\omega \mu_0 \mu_r} (k_0^2 \mu_r \epsilon_r - \mathbf{k}_\rho \mathbf{k}_\rho \cdot) (\hat{\mathbf{z}} \times \tilde{\mathbf{E}}_\rho) + \frac{\mathbf{k}_\rho \tilde{M}_z}{\omega \mu_0 \mu_z} - \hat{\mathbf{z}} \times \tilde{\mathbf{J}}_\rho, \quad (2.8)$$

$$-j\omega \epsilon_0 \epsilon_z \cdot \tilde{\mathbf{E}}_z = j\tilde{\mathbf{k}}_\rho \cdot (\tilde{\mathbf{H}}_\rho \times \hat{\mathbf{z}}) + \tilde{J}_z, \quad (2.9)$$

$$-j\omega \mu_0 \mu_z \cdot \tilde{\mathbf{H}}_z = j\tilde{\mathbf{k}}_\rho \cdot (\hat{\mathbf{z}} \times \tilde{\mathbf{E}}_\rho) + \tilde{M}_z. \quad (2.10)$$

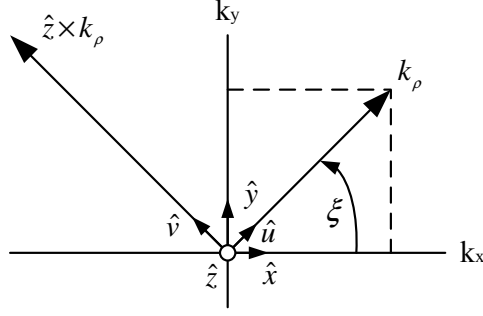


Fig 2.2: Rotated spectrum-domain coordinate system.

If the spectral domain transverse components in the  $(x, y)$  coordinate are rotated by an angle  $\xi$  to the new coordinate  $(u, v)$ , as shown in Fig 2.2. We obtain

$$\begin{bmatrix} \hat{u} \\ \hat{v} \end{bmatrix} = \begin{bmatrix} \cos \xi & \sin \xi \\ -\sin \xi & \cos \xi \end{bmatrix} \begin{bmatrix} \hat{x} \\ \hat{y} \end{bmatrix}, \quad (2.11)$$

where

$$\cos \xi = \frac{k_x}{k_\rho}, \quad \sin \xi = \frac{k_y}{k_\rho}. \quad (2.12)$$

The transverse magnetic and electric fields are expressed as

$$\tilde{\mathbf{E}}_\rho = \hat{u} \mathbf{V}^c + \hat{v} \mathbf{V}^h, \quad \tilde{\mathbf{H}}_\rho \times \hat{z} = \hat{u} \mathbf{I}^c + \hat{v} \mathbf{I}^h. \quad (2.13)$$

By projecting equations (2.7) and (2.8) on  $\hat{u}$  and  $\hat{v}$ , we obtain two decoupled sets of transmission line equations of the form,

$$\frac{dV^p}{dz} = -jk_z Z^p I^p + v^p, \quad (2.14)$$

$$\frac{dI^p}{dz} = -jk_z Y^p V^p + i^p,$$

where the superscript  $p$  assumes the values of  $e$  or  $h$ . The component of  $\tilde{\mathbf{E}}_\rho$  and  $\tilde{\mathbf{H}}_\rho$  in the  $(u, v)$  plane may be interpreted as voltages and currents on a transmission-line

analog of the medium along the  $z$  axis. The propagation wavenumbers, the characteristic impedances of the transmission line, the voltage and current sources in equation (2.14) are given as follows:

$$k_z = \sqrt{k_0^2 \epsilon_r \mu_r - k_p^2}, \quad (2.15)$$

$$Z^e = \frac{1}{Y^e} = \frac{k_z}{\omega \epsilon_0 \epsilon_r}, \quad Z^h = \frac{1}{Y^h} = \frac{\omega \mu_0 \mu_r}{k_z}, \quad (2.16)$$

$$v^e = \frac{k_p}{\omega \epsilon_0 \epsilon_r} \tilde{J}_z - \tilde{M}_v, \quad i^e = -\tilde{J}_u, \quad (2.17)$$

$$i^h = -\frac{k_p}{\omega \mu_0 \mu_r} \tilde{M}_z - \tilde{J}_v, \quad v^h = \tilde{M}_u. \quad (2.18)$$

The spectral fields may now be expressed as

$$\tilde{\mathbf{E}} = \hat{\mathbf{u}}V^e + \hat{\mathbf{v}}V^h - \hat{\mathbf{z}} \frac{1}{j\omega \epsilon_0 \epsilon_r} (jk_p I^e + \tilde{J}_z), \quad (2.19)$$

$$\tilde{\mathbf{H}} = -\hat{\mathbf{u}}I^h + \hat{\mathbf{v}}I^e + \hat{\mathbf{z}} \frac{1}{j\omega \mu_0 \mu_r} (jk_p V^e + \tilde{M}_z). \quad (2.20)$$

Let  $V_i^p(z|z')$  and  $I_i^p(z|z')$  denote the voltage and current, respectively at  $z$  due to a 1A shunt current source at  $z'$ . Let  $V_v^p(z|z')$  and  $I_v^p(z|z')$  denote the voltage and current, respectively at  $z$  due to a 1V series voltages source at  $z'$ . Then it follows from equation (2.14) that these transmission-line Green's Functions satisfy the following:

$$\begin{aligned} \frac{dV_i^p}{dz} &= -jk_z^p Z^p I_i^p, \\ \frac{dI_i^p}{dz} &= -jk_z^p Y^p V_i^p + \delta(z-z'), \end{aligned} \quad (2.21)$$

$$\begin{aligned} \frac{dV_v^p}{dz} &= -jk_z^p Z^p I_v^p + \delta(z-z'), \\ \frac{dI_v^p}{dz} &= -jk_z^p Y^p V_v^p, \end{aligned} \quad (2.22)$$

where  $\delta$  is the Dirac delta, and they possess the reciprocity properties as follows:

$$\begin{aligned}
V_i^p(z|z') &= V_i^p(z'|z), \\
I_v^p(z|z') &= I_v^p(z'|z), \\
V_v^p(z|z') &= -I_i^p(z'|z), \\
I_i^p(z|z') &= -V_v^p(z'|z).
\end{aligned} \tag{2.23}$$

The linearity of the transmission line equations allows one to obtain  $(V^p, I^p)$  at any point  $z$  via the superposition integrals:

$$\begin{aligned}
V^p &= \langle V_i^p, i^p \rangle + \langle V_v^p, v^p \rangle, \\
I^p &= \langle I_i^p, i^p \rangle + \langle I_v^p, v^p \rangle,
\end{aligned} \tag{2.24}$$

Upon substituting these equations into equation (2.19) and equation (2.20) and using equation (2.18), one obtains the spectrum-domain counterparts of

$$\begin{aligned}
\tilde{\mathbf{E}} &= \langle \tilde{\mathbf{G}}^{EJ}; \tilde{\mathbf{J}} \rangle + \langle \tilde{\mathbf{G}}^{EM}; \tilde{\mathbf{M}} \rangle, \\
\tilde{\mathbf{H}} &= \langle \tilde{\mathbf{G}}^{HJ}; \tilde{\mathbf{J}} \rangle + \langle \tilde{\mathbf{G}}^{HM}; \tilde{\mathbf{M}} \rangle,
\end{aligned} \tag{2.25}$$

where the spectral domain dyadic Green's function can be written in the  $(u, v, z)$  coordinate system as

$$\tilde{\mathbf{G}}^{EJ}(\mathbf{k}_\rho, z|z') = \begin{bmatrix} -V_i^e & 0 & \frac{k_\rho}{\omega \epsilon_0 \epsilon'_r} V_v^e \\ 0 & -V_i^h & 0 \\ \frac{k_\rho}{\omega \epsilon_0 \epsilon'_r} I_i^e & 0 & \frac{k_\rho}{j\omega \epsilon_0 \epsilon'_r} \left[ \frac{k_\rho^2}{j\omega \epsilon_0 \epsilon'_r} I_v^e - \delta(z-z') \right] \end{bmatrix}, \tag{2.26}$$

$$\tilde{\mathbf{G}}^{HJ}(\mathbf{k}_\rho, z|z') = \begin{bmatrix} 0 & I_i^h & 0 \\ -I_i^e & 0 & \frac{k_\rho}{\omega \epsilon_0 \epsilon'_r} I_v^e \\ 0 & -\frac{k_\rho}{\omega \mu_0 \mu'_r} V_i^h & 0 \end{bmatrix}, \tag{2.27}$$

$$\tilde{\mathbf{G}}^{\text{EM}}(\mathbf{k}_\rho, z|z') = \begin{bmatrix} 0 & -\mathbf{V}_v^c & 0 \\ \mathbf{V}_v^h & 0 & -\frac{k_\rho}{\omega\mu_0\mu'_r} \mathbf{I}_i^h \\ 0 & \frac{k_\rho}{\omega\epsilon_0\epsilon_r} \mathbf{I}_v^c & 0 \end{bmatrix}, \quad (2.28)$$

$$\tilde{\mathbf{G}}^{\text{HM}}(\mathbf{k}_\rho, z|z') = \begin{bmatrix} -\mathbf{I}_v^h & 0 & \frac{k_\rho}{\omega\mu_0\mu'_r} \mathbf{I}_i^h \\ 0 & -\mathbf{I}_v^c & 0 \\ \frac{k_\rho}{\omega\mu_0\mu_r} \mathbf{V}_v^h & 0 & \frac{k_\rho}{\omega\mu_0\mu'_r} \left[ \frac{k_\rho^2}{j\omega\mu_0\mu_r} \mathbf{V}_i^h - \delta(z-z') \right] \end{bmatrix}. \quad (2.29)$$

To solve the integral equation in the spatial domain, the spectral domain Green's functions have to be transformed to the spatial domain.

### 2.3 Mixed Potential Integral Equation [64]

The fields can be expressed in terms of vector and scalar potential by the following equations:

$$\mathbf{E} = -j\omega\mathbf{A} - \nabla\phi, \quad (2.30)$$

$$\mathbf{H} = \frac{1}{\mu_0\mu_r} \nabla \times \mathbf{A}. \quad (2.31)$$

Using Green's function, we have the following equations:

$$\mathbf{H} = \langle \mathbf{G}^{\text{HJ}}; \mathbf{J} \rangle, \quad (2.32)$$

$$\mathbf{A} = \mu_0 \langle \mathbf{G}^{\text{A}}; \mathbf{J} \rangle, \quad (2.33)$$

where the notation  $\langle ; \rangle$  is used for integrals of products of two functions separated by a comma over their common spatial support, with a dot over the comma indicating

vector dot product. Hence, the Green's function for vector potential is associated with the magnetic field by

$$\mathbf{G}^{\text{HJ}} = \frac{1}{\mu_r} \nabla \times \mathbf{G}^{\text{A}}. \quad (2.34)$$

$\mathbf{G}^{\text{A}}$  is not uniquely defined in layered medium problems as discussed in [64]. Here, the traditional form of  $\tilde{\mathbf{G}}^{\text{A}}$  is chosen as

$$\tilde{\mathbf{G}}^{\text{A}} = \begin{bmatrix} \tilde{\mathbf{G}}_{\text{xx}}^{\text{A}} & 0 & 0 \\ 0 & \tilde{\mathbf{G}}_{\text{xx}}^{\text{A}} & 0 \\ \frac{k_x}{k_\rho} \tilde{\mathbf{G}}_{\text{zx}}^{\text{A}} & \frac{k_y}{k_\rho} \tilde{\mathbf{G}}_{\text{zx}}^{\text{A}} & \tilde{\mathbf{G}}_{\text{zz}}^{\text{A}} \end{bmatrix}. \quad (2.35)$$

In the spectral domain, the nabla operation is  $\tilde{\nabla} = -jk_\rho \hat{\mathbf{u}} + \hat{\mathbf{z}}d/dz$ .  $\tilde{\mathbf{G}}^{\text{HJ}}$  can be derived from equation (2.27). Thus, the components of  $\tilde{\mathbf{G}}^{\text{A}}$  can be expressed as

$$j\omega\mu_o \tilde{\mathbf{G}}_{\text{xx}}^{\text{A}} = \mathbf{V}_i^{\text{h}}, \quad (2.36)$$

$$j\omega \tilde{\mathbf{G}}_{\text{zz}}^{\text{A}} = \frac{\mu_r}{\epsilon_o \epsilon'_z} \mathbf{I}_v^{\text{e}}, \quad (2.37)$$

$$j\tilde{\mathbf{G}}_{\text{zx}}^{\text{A}} = \frac{\mu_r}{k_\rho} (\mathbf{I}_i^{\text{h}} - \mathbf{I}_i^{\text{e}}). \quad (2.38)$$

The Lorentz gauge is taken as

$$\nabla \cdot \mathbf{A} = -j\omega\mu_r\mu_o\epsilon_r\epsilon_o\phi. \quad (2.39)$$

To arrive at the mixed-potential form of  $\mathbf{E}$ , we have

$$\frac{1}{\epsilon_r\mu_r} \nabla \cdot \mathbf{G}^{\text{A}} = -\nabla' \mathbf{G}^\phi + \mathbf{C}^\phi \hat{\mathbf{z}}, \quad (2.40)$$

where  $\mathbf{G}^\phi$  is the scalar potential kernel and  $\mathbf{C}^\phi$  is the correction factor, which arises in general when both horizontal and vertical current components are present. From this relation, we can find  $\mathbf{G}^\phi$  and  $\mathbf{C}^\phi$  by substituting equation (2.35) in the



spectrum-domain counterpart of equation (2.40), obtaining

$$-\frac{\tilde{\mathbf{G}}^\phi}{j\omega\epsilon_0} = \frac{1}{k_p^2} (\mathbf{V}_i^h - \mathbf{V}_i^c), \quad (2.41)$$

$$-\frac{\tilde{\mathbf{C}}^\phi}{j\omega\epsilon_0} = \frac{j\omega\mu_0\mu'_r}{k_p^2} (\mathbf{V}_v^h - \mathbf{V}_v^c). \quad (2.42)$$

The space domain counterparts of the spectral kernels derived above can be expressed in terms of the Sommerfeld integrals. By substituting equations (2.39) and (2.40) into equation (2.30), the electric field can be expressed as

$$\mathbf{E} = -j\omega\mu_0 \langle \mathbf{G}^A; \mathbf{J} \rangle + \frac{1}{j\omega\epsilon_0} \nabla \left( \langle \mathbf{G}^\phi, \nabla \cdot \mathbf{J} \rangle + \langle \mathbf{C}^\phi \hat{\mathbf{z}}; \mathbf{J} \rangle \right). \quad (2.43)$$

The formulations for  $\tilde{\mathbf{G}}_{xx}^A$ ,  $\tilde{\mathbf{G}}_{zx}^A$ ,  $\tilde{\mathbf{G}}_{zz}^A$  and  $\tilde{\mathbf{G}}^\phi$  depend on  $\mathbf{V}_i^p$ ,  $\mathbf{V}_v^p$ ,  $\mathbf{I}_i^p$  and  $\mathbf{I}_v^p$  and the derivation can be found in Appendix A.

## 2.4 Numerical Evaluation of the Sommerfeld Integrals [68]-[71]

From the inverse Fourier-Bessel transform, we can write the spatial domain Green's function as

$$\mathbf{G}(\boldsymbol{\rho}, z | z') = \frac{1}{2\pi_0} \int_0^\infty \mathbf{G}(\mathbf{k}_p, z | z') J_0(k_p \rho) k_p dk_p. \quad (2.44)$$

That is a well-known Sommerfeld integral. Therefore,  $\tilde{\mathbf{G}}_{xx}^A$ ,  $\tilde{\mathbf{G}}_{zx}^A$ ,  $\tilde{\mathbf{G}}_{zz}^A$  and  $\tilde{\mathbf{G}}^\phi$  can be written in the form of Sommerfeld Integral. Evaluation of Sommerfeld Integral [71] is essential for the spatial domain approach. The integration interval is divided into three subsections,  $[0, k_0]$ ,  $[k_0, k_0\sqrt{\epsilon_r}]$  and  $[k_0\sqrt{\epsilon_r}, \infty]$ . In the region  $[0, k_0]$ , the infinite derivative in  $k_0$  is eliminated with a change of variables  $k_p = k_0 \cos t$ . The

resulting smooth function is integrated numerically. In the interval  $[k_0, k_0\sqrt{\epsilon_r}]$ , the singularity is first extracted. There is still an infinite derivative at  $k_p = k_0$ . With a change of variable  $k_p = k_0 \cosh t$ , a smooth function is obtained. For the first two intervals which are bounded, Simpson rule is used for the integration. Finally, in the region  $[k_0\sqrt{\epsilon_r}, \infty]$  the integral is a slowly convergent oscillating function. A special procedure known as the method of averages [68]-[70] has been developed to combat the oscillation. The method of averages is discussed in Appendix B.

## 2.5 Discrete Complex Image Method [39]

Numerical integration of the Sommerfeld Integral is very time consuming because of the highly oscillating and slowly decaying behavior of the integrand. The discrete complex image method (DCIM) alleviates the numerical evaluation of the Sommerfeld integral and represents the Sommerfeld integral in a closed-form. In DCIM, the quasi-static and surface-wave contributions are first extracted from the spectral domain kernel, so the remaining kernel is approximated by a sum of complex exponentials by the generalized pencil of function method (GPOF). The spatial domain Green's function can then be obtained analytically using the Sommerfeld identity. We obtain

$$G_{a,q} = G_{a,q}^{(qd)} + G_{a,q}^{(sw)} + G_{a,q}^{ci}, \quad (2.45)$$

where  $G^{(qd)}$  represents the contribution from the quasi-dynamic images dominating in the near-field region. The quasi dynamic image is extracted from the Green's

function by using the approximation  $k_{z0} \approx k_{z1}$  when the frequency is very low.  $G^{(sw)}$  represents the contribution from the surface waves dominating in the far-field region.  $G^{(ci)}$  represents the contribution from the complex images which dominates in the intermediate region and is approximated by the summation of exponential functions using GPOF method. The specific forms of  $G_a$  and  $G_q$  for a single-layer microstrip problem can be written as

$$G_a = G_a^{(qd)} + G_a^{(sw)} + G_a^{ci}, \quad (2.46)$$

where

$$G_a^{qd} = \frac{\mu_0}{4\pi} \left( \frac{e^{-jk_0 r_0}}{r_0} - \frac{e^{-jk_0 r_1}}{r_1} \right), \quad (2.47)$$

$$G_a^{sw} = \frac{\mu_0}{4\pi} (-j2\pi) \sum_{n=1}^{N_{TE}} \text{Res}_{(n)} \cdot H_0^2(k_{pp(n)} \rho) k_{pp(n)}, \quad (2.48)$$

$$G_a^{(ci)} = \frac{\mu_0}{4\pi} \sum_{i=1}^N a_i \frac{e^{-jk_0 r_i}}{r_i}, \quad (2.49)$$

$$G_q = G_q^{(qd)} + G_q^{(sw)} + G_q^{ci}, \quad (2.50)$$

$$G_q^{(qd)} = \frac{1}{4\pi\epsilon_0} \left[ \frac{e^{-jk_0 r_0}}{r_0} + K \frac{e^{-jk_0 r''_0}}{r''_0} + \sum_{n=1}^{\infty} K^{n-1} (K^2 - 1) \frac{e^{-jk_0 r_n}}{r_n} \right], \quad (2.51)$$

and

$$G_q^{(sw)} = \frac{1}{4\pi\epsilon} (-j2\pi) \sum_{n=1}^{N_{TE} + N_{TM}} \text{Res}_{(n)} \cdot H_0^2(k_{pp(n)} \rho) k_{pp(n)}, \quad (2.52)$$

$$G_q^{(ci)} = \frac{1}{4\pi\epsilon_0} \sum_{i=1}^N a'_i \frac{e^{-jk_0 r'_i}}{r'_i}. \quad (2.53)$$

In the above,  $r_n = \sqrt{\rho^2 + (2nh)^2}$  with  $h$  being the thickness of the substrate,  $r_i = \sqrt{\rho^2 - b_i^2}$  and  $r'_i = \sqrt{\rho^2 - b_i'^2}$  where  $b_i$ ,  $b_i'$ ,  $a_i$  and  $a'_i$  by GPOF method, and  $K = \frac{1-\epsilon_r}{1+\epsilon_r}$  with  $\epsilon_r$  being the relative permittivity of the substrate.  $k_{pp}$  is the surface wave pole located on the real axis of the complex  $k_p$  plane, and the symbol  $\text{Res}$  denotes the residues of the integrand at the pole  $k_p = k_{pp}$ . For the single-layer Green's function expressions, one can refer to Appendix A.2 for detail derivation.

A single-layer microstrip substrate with  $\epsilon_r = 12.6$  and  $h=1$  mm is examined at two different frequencies ( $f=10$  GHz, 30 GHz). The closed-form Green's function is then compared with the numerical integration as shown in Fig 2.3.

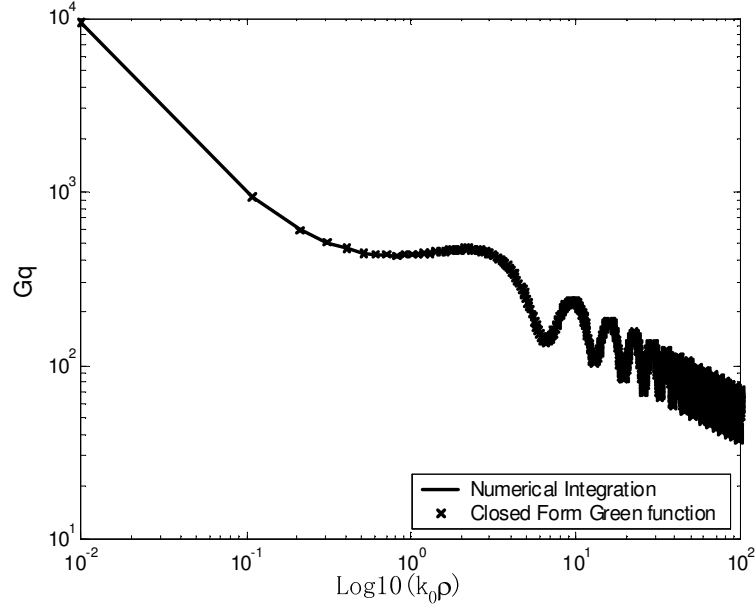


Fig 2.3: Comparison of the calculation for  $G_q$  using DCIM and numerical integration (Method of Averages) on substrate with  $h=1.0$ mm,  $\epsilon_r=12.6$  at  $f=30$ GHz.

For  $\log_{10}(k_0\rho) > 1$ , the closed-form Green's function gives an error that is less than 1% as compared with the numerical integration of the Sommerfeld integrals. It can be seen that the difference between the closed-form Green's function and the numerical integration is nearly unobservable. Hence, instead of using numerical integration, which is often time consuming, the closed-form equations can be used to evaluate the spatial Green's function.

## 2.6 The Method of Moments [78]-[80]

In order to apply the mixed potential integral equation (MPIE) to irregular microstrip shapes, the method of moments (MoM) has been selected. This numerical technique, which is among the most widely used numerical techniques in electromagnetics, transforms the integral equation into a matrix algebraic equation that can be easily solved on a computer.

For subsectional basis functions approach in the method of moments, the structure is decomposed into smaller elementary cells and each defines simple approximations for the surface current on each cell. The most commonly adopted shapes for the elementary cells are mainly the triangle and the rectangular. Even though the triangular shape is more flexible, rectangular cells involve simpler calculations and are sufficient for many microstrip problems. Depending on the structure, either RWG basis functions [78]-[79] or Rooftop basis functions [80] are used for the analysis in

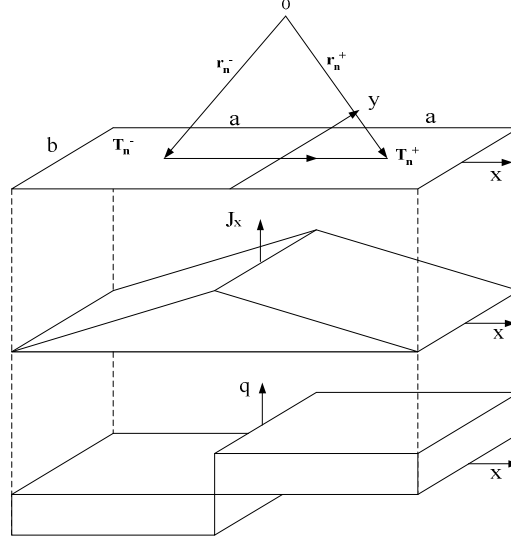


Fig 2.4: X-directed rooftop basis function with the current and charge cells.

this thesis.

### 2.6.1 Rooftop Basis Functions

Let us define  $\mathbf{f}_n$  as the vector rooftop function associated with two adjacent cells  $T_n^+$  and  $T_n^-$ . The union of these two cells will be simply denoted by  $T_n$ . In general, we need to consider  $N_x$  x-directed functions and  $N_y$  y-directed functions. The total number of basis functions is  $N = N_x + N_y$ .  $\mathbf{f}_n$  and  $\nabla_s \cdot \mathbf{f}_n$  are given as

$$\mathbf{f}_n = \begin{cases} \hat{\mathbf{x}} f_{nx} = \hat{\mathbf{x}} \left( 1 - \frac{|x|}{a} \right) & , \quad n = 1, \dots, N_x, \\ \hat{\mathbf{y}} f_{ny} = \hat{\mathbf{y}} \left( 1 - \frac{|y|}{b} \right) & , \quad n = N_x + 1, \dots, N, \end{cases} \quad (2.54)$$

$$\nabla_s \cdot \mathbf{f}_n = \begin{cases} -\frac{|x|}{a} , & n = 1, \dots, N_x, \\ -\frac{|y|}{a} , & n = N_x + 1, \dots, N. \end{cases} \quad (2.55)$$

The current shown in Fig 2.4 is expanded as

$$\mathbf{J} = \sum_{n=1}^N I_n \mathbf{f}_n , \quad (2.56)$$

where  $I_n$  are the unknown coefficients and the surface charge density is related to the surface divergence of  $\mathbf{J}$  through the equation of continuity:

$$q = -\nabla \cdot \mathbf{f}_n / j\omega . \quad (2.57)$$

After applying the Galerkin's procedure to equation (2.43), we achieve the matrix equation

$$\mathbf{Z}\mathbf{I} = \mathbf{V} , \quad (2.58)$$

with the elements of the matrix given by

$$z_{nm} = A_{nm} + \phi_{nm} , \quad (2.59)$$

where the contribution of vector potential  $A$  and scalar potential  $\phi$  are respectively

$$A_{nm} = j\omega\mu_0 \int_{S_n} \mathbf{f}_n(\mathbf{r}) \cdot \int_{S_m} \bar{\mathbf{G}}^A(\mathbf{r}|\mathbf{r}') \cdot \mathbf{f}_m(\mathbf{r}') dS' dS, \quad (2.60)$$

$$\phi_{nm} = \frac{1}{j\omega\epsilon_0} \int_{S_n} \nabla \cdot \mathbf{f}_n(\mathbf{r}) \int_{S_m} \bar{\mathbf{G}}^\phi(\mathbf{r}|\mathbf{r}') \nabla \cdot \mathbf{f}_m(\mathbf{r}') dS' dS. \quad (2.61)$$

The element  $V_n$  of the vector is

$$V_n = \int_{S_n} \mathbf{f}_n(\mathbf{r}) \cdot \mathbf{E}^e(\mathbf{r}) dS. \quad (2.62)$$

## 2.6.2 RWG Basis Function

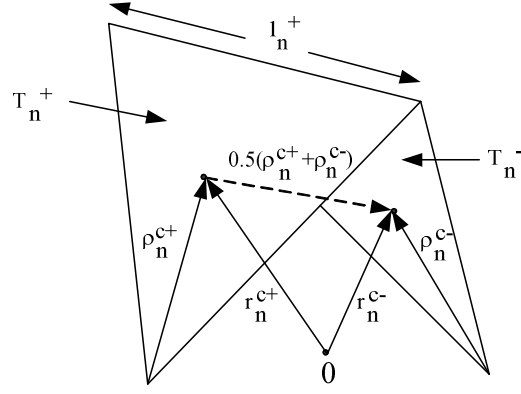


Fig 2.5: RWG basis function.

Let define  $\mathbf{f}_n(\mathbf{r})$  as the vector basis function defined on the adjacent triangles associated with the nth edge as shown in Fig 2.5, and is expanded as

$$\mathbf{f}_n(\mathbf{r}) = \begin{cases} \mathbf{f}_n^+ = \frac{l_n}{2A_n^+} \rho_n^+, \mathbf{r} \text{ in } T_n^+, \\ \mathbf{f}_n^- = \frac{l_n}{2A_n^-} \rho_n^-, \mathbf{r} \text{ in } T_n^-, \\ 0, & \text{otherwise,} \end{cases} \quad (2.63)$$

where  $l_n$  is the length of the edge,  $A_n^\pm$  is the area of triangle  $T_n^\pm$  and  $\rho_n^\pm$  is the position vector. The surface charge divergence  $\mathbf{f}_n(\mathbf{r})$ , which is proportional to the surface charge density  $\Pi_n = -\nabla \cdot \mathbf{f}_n / j\omega$  is given by

$$\nabla_s \cdot \mathbf{f}_n = \begin{cases} \frac{l_n}{A_n^+}, \mathbf{r} \text{ in } T_n^+, \\ -\frac{l_n}{A_n^-}, \mathbf{r} \text{ in } T_n^-, \\ 0, & \text{otherwise.} \end{cases} \quad (2.64)$$

The currents are expanded as in equation (2.56). After applying the Galerkin's procedure, we will get the matrix equations.



## 2.7 De-Embedding of Network Parameters [82]

The current induced on the structure can be solved by an excitation such as a voltage source. The delta-gap generator is used. In this model, the port is assumed to be excited by a voltage source of magnitude  $V$ , applied within an infinitesimal small gap. We have assumed a break as a voltage source to induce the current. With the current distribution, one can obtain the network parameters such as the admittance or scattering matrices. However, the admittance obtained in this manner contains a capacitance of unknown nature, due to the physical nature of a gap. Their contribution to the calculated input impedance must be removed. One way to avoid this problem is to characterize a microstrip discontinuity by the reflection and transmission waves, of the scattering parameters on the microstrip.

Numerical results [81] reveal that the evaluated current distribution along the feedline of a typical microstrip circuit or antenna is very close to a sinusoidal function along the feed-line just 0.1-0.2 wavelength away from junctions and other discontinuities. Therefore, we can assume the current distribution along the feed-line as

$$I(z) = a \exp(-\gamma z) - b \exp(\gamma z), \quad (2.65)$$

where  $a$  and  $b$  are the amplitudes of the incident wave and reflected wave in a port.  $\gamma = \alpha + j\beta$  is the complex propagation constant.

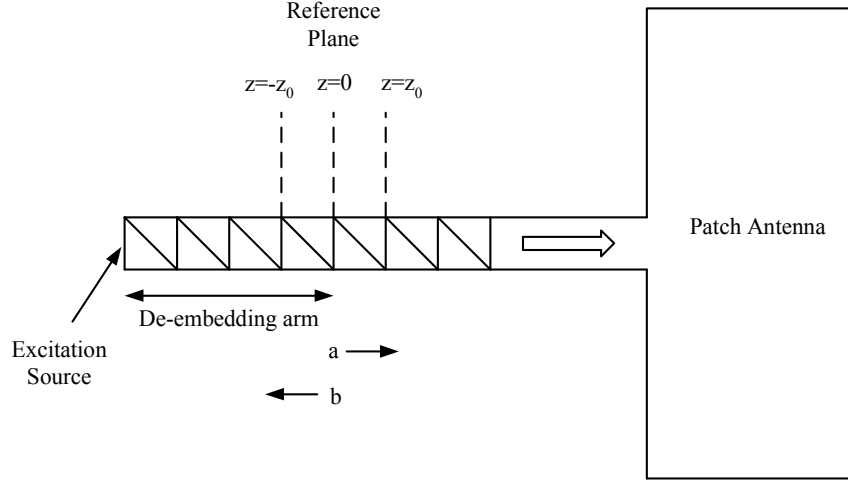


Fig 2.6: 1 cell along the transverse direction of the feedline.

The process of solving  $a$ ,  $b$  and  $\gamma$  leading to the S-parameters is called de-embedding.

Fig 2.6 shows the typical configuration of the one port device. The current distribution at three uniformly-spaced points is detected with the center point coincident with the reference plane at  $z=0$  to provide three equations [82]:

$$I(z = -z_0) = a \exp(\gamma z_0) - b \exp(-\gamma z_0), \quad (2.66)$$

$$I(z = 0) = a - b, \quad (2.67)$$

$$I(z = z_0) = a \exp(-\gamma z_0) - b \exp(\gamma z_0). \quad (2.68)$$

Summating equations (2.66) and (2.68) yields

$$2(a - b) \cosh(\gamma z_0) = I(z = -z_0) + I(z = z_0). \quad (2.69)$$

Substituting equation (2.67) into equation (2.69) yields

$$\cosh(\gamma z_0) = \frac{I(z = -z_0) + I(z = z_0)}{2I(z = 0)}. \quad (2.70)$$

A unique  $\gamma$  can be solved as long as  $\beta z_0 < \frac{\pi}{2}$ . Then the incident and reflected waves can be obtained from either two of equations (2.66), (2.67) and (2.68) provided.

We avoid the situation where  $|I(z=0)| \ll |I(z=-z_0)|$  and  $|I(z=z_0)|$ . The

S-parameter at the reference plane is computed from  $S_{ij} = \frac{b_i}{a_j}$ .

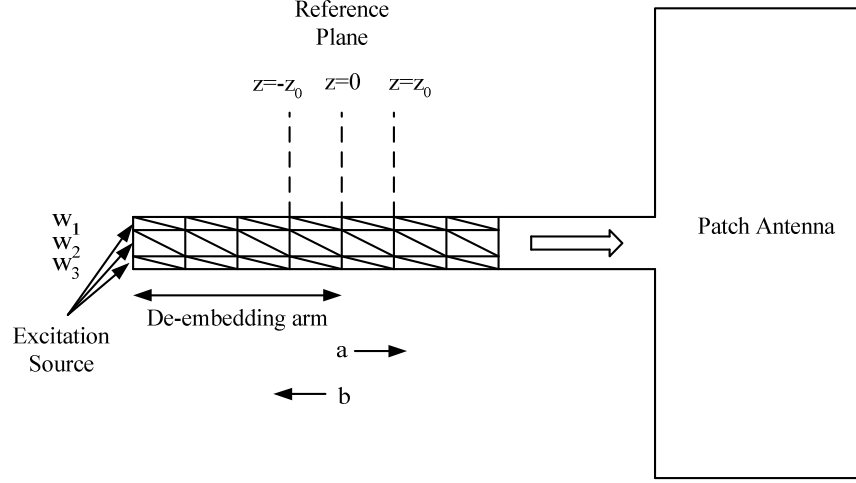


Fig 2.7: Multiple cells along the transverse direction of the feedline.

Sometimes the feedline is divided into a number of cells in the transverse direction as shown in Fig 2.7. The width of the cells in the transverse direction are  $w_1$ ,  $w_2$  and  $w_3$ . The longitudinal currents  $I_{w_1}(z=-z_0)$ ,  $I_{w_1}(z=0)$ ,  $I_{w_1}(z=z_0)$ ,  $I_{w_2}(z=-z_0)$ ,  $I_{w_2}(z=0)$ ,  $I_{w_2}(z=z_0)$ ,  $I_{w_3}(z=-z_0)$ ,  $I_{w_3}(z=0)$  and  $I_{w_3}(z=z_0)$  are sampled along the microstrip feedline. The sampled longitudinal currents are related to  $I(z=-z_0)$ ,  $I(z=0)$  and  $I(z=z_0)$  by

$$I(z=-z_0) = \frac{w_1 I_{w_1}(z=-z_0) + w_2 I_{w_2}(z=-z_0) + w_3 I_{w_3}(z=-z_0)}{w_1 + w_2 + w_3}, \quad (2.71)$$

$$I(z=0) = \frac{w_1 I_{w_1}(z=0) + w_2 I_{w_2}(z=0) + w_3 I_{w_3}(z=0)}{w_1 + w_2 + w_3}, \quad (2.72)$$

$$I(z=z_0) = \frac{w_1 I_{w_1}(z=z_0) + w_2 I_{w_2}(z=z_0) + w_3 I_{w_3}(z=z_0)}{w_1 + w_2 + w_3}. \quad (2.73)$$

The  $S_{11}$  can be de-embedded using the same method in the case where the feedline has only a single cell in the transverse direction.

The process described above can only be used to de-embed the reflection coefficient of a one-port network. For N-port network, N different excitation states have to be provided to solve for a, b and  $\gamma$  for each port in each state in order to extract the S-matrix.

## 2.8 Matched Load Simulation [83]

As mentioned in Section 2.7, for N-port network, N linearly independent excitations are required using open load simulation. However, if matched load termination is adopted, only one port needs to be excited as shown in Fig 2.8. Thus, the time taken to solve the problem is reduced. The matched load termination [83] can be achieved by enforcing in the spatial domain a unidirectional current travelling wave propagating along each of the output lines in the direction away from the discontinuities. The simulation is based on a simple manipulation of the matrix equation (2.58).

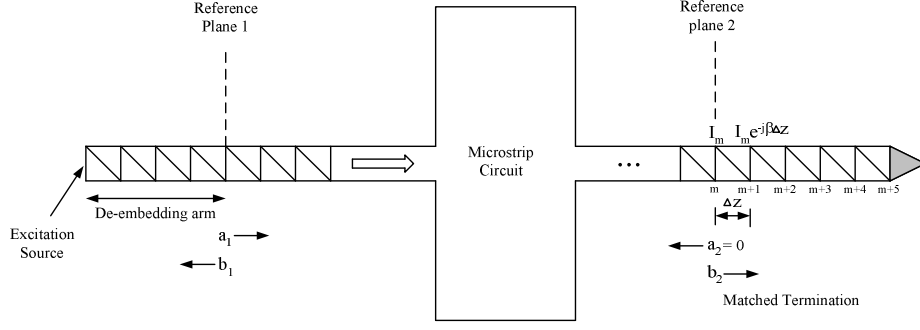


Fig 2.8: Illustration of matched load termination.

The mutual relationship of the current coefficients along the various output lines is enforced by introducing new linear equations into the matrix equation

$$I_{m+1} - I_m e^{-j\beta_g \Delta z} = 0, \quad (2.74)$$

where  $\beta_g$  is the pre-computed propagation constant for the output line and  $\Delta z$  is the distance between the locations of the centers of successive rooftop basis functions.

This equation enforces a uniform magnitude and a uniform progressive phase lag constraint on the coefficients  $I_m$  and  $I_{m+1}$  on any particular output line. A typical  $m^{\text{th}}$  row in  $Z_{ij}$  can now be expressed as

$$[0 \quad \dots \quad 0 \quad -e^{-j\beta_g \Delta z} \quad 1 \quad 0 \quad \dots \quad 0]. \quad (2.75)$$

The shaded triangle face shown in Fig 2.8 is added to the end of the terminating line in order to make boundary edge,  $m+5$  into internal edges. However, we do not take the shaded triangle into account when evaluating the  $Z$  matrix, the end result being that unknown charges accumulate on the triangle. A simple physical explanation of the match-termination is that the forward-travelling current wave on the terminating line carries all the charges onto the shaded face. This, however, has no effect on the current distribution in the microstrip circuit.

It is noted that constant-amplitude, constant phase-lag current conditions should only be enforced for coefficients associated with current cells that are physically located far from the discontinuity at the junction between the output line and the device. This ensures that all effects due to the discontinuity will have become negligible and that the enforcement of a simple outgoing quasi-TEM mode is then justified.

Once the current distribution of a matched multi-port structure has been obtained, the extraction of S-parameters involves can be obtained by using the three-point curve-fitting de-embedding techniques discuss earlier.

## 2.9 Interpolation Schemes for the Green's function

For a large structure, the evaluation of the matrix in (2.58) requires a large amount of computation even though DCIM is used to evaluate the Green's function. For a rectangular patch divided into 10 by 10 rectangular cells, the order of the matrix is 180, hence the number of elements in it is  $180^2=32400$ . Even when a simple 4 X 4 Gaussian quadrature method is used in equations (2.60) and (2.61), the number of Green's functions to be evaluated would exceed half a million.

For a given structure, the Green's function only depends upon the distance from source to observer. Thus, it is possible to use interpolation schemes to evaluate the Green's function. Since the Green's function at the source point has a singularity, the

observation points in the vicinity of the source point are needed to be calculated accurately with the region classified as the near field. However, as the distance between the source and the observation point increases, the Green's function becomes a smooth function of distance which enables the possibility of developing interpolation approach. The Green's function can be evaluated over a finite set of  $N$  points located between two bounds, namely,  $d_{\min} \leq \bar{r} - \bar{r}' \leq d_{\max}$ . The upper bound is the largest linear dimension of the antenna, whereas the lower bound depends on the numerical method used for the integration. The Green's function in the near field region, between 0 to  $d_{\min}$ , is evaluated using the direct computation. As it is mentioned in [85], the dominating term of the Green's function in the near-field of the source is the quasi-static term. For both the vector and the scalar potential Green's functions, the quasi-static terms attenuate as  $1/\rho$  in the near field and as  $1/\rho^3$  in the far field of the source. However, the quasi-static part of the scalar Green's function may be obscured by the leaky wave and surface wave contributions at high frequencies, since the region that these two terms contribute move close to the source with the increasing frequency, resulting in a rapid drop of the quasi-static contribution from  $1/\rho$  to  $1/\rho^3$ . Thus, the field in the near field of the source changes abruptly and needs to be evaluated using direct approach.

Between  $d_{\min} \leq \bar{r} - \bar{r}' \leq d_{\max}$ , the phase terms of the Green's function vary rapidly with distance between the source and field points. To ensure interpolation accuracy, one should divide the region into two parts, namely the intermediate and the far field

regions. The near field region is determined by the distance  $d_{\min} < 0.1\lambda_0$  where  $\lambda_0$  is the free-space wavelength, the immediate region  $0.1\lambda_0 \leq \bar{r} - \bar{r}' < 2\lambda_0$  and the far field region  $2\lambda_0 \leq \bar{r} - \bar{r}' < d_{\max}$ . These regions are obtained after carrying out extensive numerical experiments. Three interpolation techniques, namely, the radial basis function using inverse multiquadric basis function [59], the Cauchy method [60]-[61] and the generalized pencil-of-function method [56]-[57] are adopted for the investigation of the Green's function interpolation within the intermediate and far field regions. The three interpolation techniques are briefly discussed in the following sections.

### 2.9.1 Radial Basis Function [59]

The conventional radial basis function (RBF) interpolation is expressed as

$$Y(\mathbf{k}) = \sum_{i=1}^P \beta_i \varphi_i(\mathbf{k}), \quad (2.76)$$

where  $\{\varphi_i\}_{i=1}^P$  a set of radial basis functions,  $\{\beta_i\}_{i=1}^P$  is their corresponding unknown coefficients and  $P$  is the number of interpolation points. Given a function  $Y(\mathbf{k})$  and a set of radial basis functions  $\{\varphi_i\}_{i=1}^P$ , one can solve equation (2.76) using the collocation method to obtain the coefficient set  $\{\beta_i\}_{i=1}^P$ . Inverse multiquadric basis function is chosen and is expressed as

$$\varphi_i(\mathbf{k}) = \frac{1}{\sqrt{\|\mathbf{k} - \mathbf{k}_i\|^2 + c^2}}, \quad (2.77)$$

where  $\|\bullet\|$  denotes the distance norm,  $\mathbf{k}_i$  is the interpolation point and  $c$  is the shape parameter. One drawback of the method is that no analytical expression for  $c$  is



available. Optimized  $c$  can be determined by performing some numerical experiments. After conducting numerous numerical experiments, it is found that the optimal  $c$  is closed to the distance between interpolation points.

### 2.9.2 Cauchy Method [60]-[61]

$Y(k)$  is approximated by a ratio of two polynomials  $A(k)$  and  $B(k)$  where  $k=0,1, \dots, N-1$ . The Cauchy method is used to evaluate the order of the polynomials and their coefficients,  $a_0, \dots, a_p$  and  $b_1, \dots, b_q$ .  $Y(k)$  is expressed as

$$Y(k) = \frac{A(k)}{B(k)} = \frac{a_0 + a_1k + a_2k^2 + \dots}{b_0 + b_1k + b_2k^2 + \dots} = \frac{a_0 + \sum_{n=1}^p a_n k^n}{b_0 + \sum_{n=1}^q b_n k^n}. \quad (2.78)$$

The unknowns  $a_n$  and  $b_n$  in equation (2.78) can be put in the following form:

$$[\mathbf{A} - \mathbf{B}] \begin{bmatrix} \mathbf{a} \\ \mathbf{b} \end{bmatrix} = \mathbf{M} \begin{bmatrix} \mathbf{a} \\ \mathbf{b} \end{bmatrix} = 0, \quad (2.79)$$

$$[\mathbf{a}] = [a_0, a_1, a_2, \dots, a_p]^T, \quad (2.80)$$

$$[\mathbf{b}] = [b_0, b_1, b_2, \dots, b_p]^T. \quad (2.81)$$

$\mathbf{M}$  is of order  $N \times (P+Q+2)$ . A singular value decomposition (SVD) of the matrix  $\mathbf{M}$  will give us a gauge of the required values of  $P$  and  $Q$ . A SVD results in the equation

$$[\mathbf{U}][\Sigma][\mathbf{V}]^H \begin{bmatrix} \mathbf{a} \\ \mathbf{b} \end{bmatrix} = 0. \quad (2.82)$$

The matrices  $\mathbf{U}$  and  $\mathbf{V}$  are unitary matrices and  $\Sigma$  is a diagonal matrix with the singular values of  $\mathbf{M}$  in descending order as its entries. The columns of  $\mathbf{U}$  are the left singular vectors of  $\mathbf{M}$  or the eigenvectors of  $\mathbf{M}\mathbf{M}^H$ . The columns of  $\mathbf{V}$  are the right

singular vectors of  $\mathbf{M}$  or the eigenvectors of  $M^H M$ . The singular values are the square roots of the eigenvalues of the matrix  $M^H M$ . Therefore the singular values of any matrix are real and positive. The number of nonzero singular values is the rank of the matrix in equation (2.79) and so gives one an idea of the information in this system of simultaneous equations. If  $R$  is the number of nonzero singular values, the dimension of the right null space of  $\mathbf{M}$  is  $P+Q+2-R$ . The solution vector belongs to the null space. Therefore, to make this solution unique, one needs to make the dimension of this null space 1 so that only one vector defines this space. Hence,  $P$  and  $Q$  must satisfy the relation

$$R + 1 = P + Q + 2. \quad (2.83)$$

To estimate  $R$ ,  $P$  and  $Q$  must be chosen to be much higher than the expected system. Using equation (2.83) better estimates for  $P$  and  $Q$  are obtained. Letting  $P$  and  $Q$  stand for these new estimates of the polynomial orders, one can recalculate the matrices  $\mathbf{A}$  and  $\mathbf{B}$ . Therefore one comes back to the relation equation (2.79).

The Total Least Squares method is used to solve equation (2.79). A QR decomposition of the matrix results in

$$\begin{bmatrix} \mathbf{R}_{11} & \mathbf{R}_{12} \\ 0 & \mathbf{R}_{22} \end{bmatrix} \begin{bmatrix} \mathbf{a} \\ \mathbf{b} \end{bmatrix} = 0 \Rightarrow \mathbf{R}_{22} \mathbf{b} = 0. \quad (2.84)$$

A SVD of  $\mathbf{R}_{22}$  is needed to solve  $\mathbf{b}$ .  $\mathbf{R}_{22} \mathbf{b}$  can be expressed as

$$\mathbf{R}_{22} \mathbf{b} = [\mathbf{U}][\Sigma][\mathbf{V}]^H \mathbf{b} = 0. \quad (2.85)$$

The solution of  $\mathbf{b}$  is proportional to the last column of the matrix  $\mathbf{V}$ . The numerator coefficients  $a_n$  can be solved from equation (2.84).

### 2.9.3 Generalized Pencil-of-Function Method [56]

Using the generalized pencil-of-function method (GPOF),  $y_k$  can also be expressed as

$$y_k = \sum_{i=1,M} b_i \exp(s_i \delta t k), \quad (2.86)$$

where  $k=0,1, \dots, N-1$ ,  $b_i$  are the complex residues,  $s_i$  are the complex poles, and  $\delta t$  is the sampling interval. We can let  $z_i = \exp(s_i \delta t)$ . The purpose of utilizing pencil-of-function method [56] is to find a set of poles  $s_i$  that can represent the sample points in equation (2.86). We consider the following set of information vectors:  $\mathbf{y}_0, \mathbf{y}_1, \dots, \mathbf{y}_L$  where

$$\mathbf{y}_i = [y_i, y_{i+1}, \dots, y_{i+N-L-1}]^T. \quad (2.87)$$

Based on these vectors, we define the matrices  $\mathbf{Y}_1$  and  $\mathbf{Y}_2$  as

$$\mathbf{Y}_1 = [\mathbf{y}_0, \mathbf{y}_1, \dots, \mathbf{y}_{L-1}], \quad (2.88)$$

$$\mathbf{Y}_2 = [\mathbf{y}_1, \mathbf{y}_2, \dots, \mathbf{y}_L]. \quad (2.89)$$

Denoting  $\mathbf{Y}_1^+$  as the (Moore-Penrose) pseudo-inverse of  $\mathbf{Y}_1$ ,  $z_i$  can be easily derived as follows:

$$\begin{bmatrix} z_1 \\ z_2 \\ \vdots \\ z_M \end{bmatrix} = \text{eig}[\mathbf{Y}_1^+ \mathbf{Y}_2]. \quad (2.90)$$

From  $z_i$ , one can obtain the poles  $s_i$ . To compute the pseudo-inverse  $\mathbf{Y}_1^+$ , one can use the singular value decomposition of  $\mathbf{Y}_1$  as follows:

$$\mathbf{Y}_1 = \sum_{i=1,M} \sigma_i \mathbf{u}_i \mathbf{v}_i^H = \mathbf{U} \mathbf{D} \mathbf{V}^H, \quad (2.91)$$

$$\mathbf{Y}_1^+ = \mathbf{V} \mathbf{D}^{-1} \mathbf{U}^H, \quad (2.92)$$

where  $U = [\mathbf{u}_1, \dots, \mathbf{u}_M]$ ,  $V = [\mathbf{v}_1, \dots, \mathbf{v}_M]$ , and  $D = \text{diag}[\sigma_1, \dots, \sigma_M]$ . The superscript  $H$  denotes the conjugate transpose of a matrix. The residues  $b_i$  can be obtained by using the least square method to best-fit the sampled points. The residues  $b_i$  and  $z_i$  can be put in the following form:

$$\begin{bmatrix} 1 & 1 & \cdots & 1 \\ z_1 & z_2 & \cdots & z_M \\ \vdots & \vdots & \cdots & \vdots \\ z_1^{N-1} & z_2^{N-1} & \cdots & z_M^{N-1} \end{bmatrix} \begin{bmatrix} b_1 \\ b_2 \\ \vdots \\ b_M \end{bmatrix} = \begin{bmatrix} y_0 \\ y_1 \\ \vdots \\ y_{N-1} \end{bmatrix}. \quad (2.93)$$

#### 2.9.4 Numerical Study of the interpolation techniques

To test the accuracy of these interpolation techniques, a 1-dimensional simulation on the Green function conducted on a substrate of  $\epsilon_r=2.2$  and height=1.59 mm at 9.4 GHz, and varying between  $0.1\lambda_0 \leq \bar{r} - \bar{r}' \leq 15\lambda_0$  are performed. Table 2.1 lists the average interpolation errors for the different regions and the different numbers of interpolation points. The errors in the shadowed region of this table are greater than 0.02. The constant shape parameter for the radial basis function within the interval  $0.1\lambda_0 \leq \bar{r} - \bar{r}' \leq 2\lambda_0$  and  $2\lambda_0 \leq \bar{r} - \bar{r}' \leq 15\lambda_0$  are taken to be at 0.0058 and 0.01 respectively. The constant shape parameter is determined by performing numerical experiments. For the same distance, when the number of interpolation points is small, GPOF interpolation scheme is noted to be more accurate than both the radial basis function and the Cauchy method. However, the simulation results show that the accuracy of GPOF deteriorates when the number of interpolation points increases. As the number of interpolation points increases, the condition number in equation (2.93) increases accordingly and consequently causes a lower accuracy in matrix inversion.

On the other hand, the Cauchy method and the radial basis function give better accuracy as the number of interpolation points gets larger. However, this comes at the expense of slower simulation time. To improve the accuracy of GPOF interpolation scheme, two distinct regions, namely,  $2\lambda_o \leq \bar{r} - \bar{r}' \leq 7\lambda_o$  and  $7\lambda_o \leq \bar{r} - \bar{r}' \leq 15\lambda_o$  are adopted. Smaller errors are observed in the two regions. Thus, one can conclude that GPOF interpolation scheme achieves a higher accuracy with the less number of interpolation points as compared to the Cauchy method and the radial basis function.

Fig 2.9 shows the CPU time consumption for the evaluation of the Green's functions. The simulation was performed on a PC with Pentium 4 of 3.2 GHz and 2 GB RAM. We observed that GPOF interpolation scheme is much faster than the direct computation of the closed-form Green's function. To evaluate 500000 number of Green's functions, GPOF interpolation scheme takes approximately 3.3 seconds while the direct computation of the closed-form Green's function takes about 3000 seconds.

Table 2.1: Comparison of the average interpolation relative error between the three interpolation schemes. (K: Number of Interpolation Points; N: Number of coefficients required by the interpolation schemes; d:  $\bar{r} - \bar{r}'$ ).

Interp. method	$0.1\lambda_0 \leq d \leq 2\lambda_0$			$2\lambda_0 \leq d \leq 15\lambda_0$			$2\lambda_0 \leq d \leq 7\lambda_0$			$7\lambda_0 \leq d \leq 15\lambda_0$		
	K	N		K	N		K	N		K	N	
Cauchy	40	41	9.64E-9	140	141	1.49E-6	60	61	3.94E-11	80	81	1.8E-7
	20	21	1.72E-7	70	71	4.2E-5	30	31	1.56E-7	40	41	1.85E-5
	10	11	0.0033	28	29	0.258	12	13	0.16	20	21	0.0339
RBF	40	40	0.0111	140	140	1.10E-4	60	60	1.70E-04	80	80	2.1E-4
	20	20	0.0404	70	70	0.0025	30	30	0.0035	40	40	0.0044
	10	10	0.2722	28	28	0.529	12	12	0.37	20	20	0.31
GPOF	40	12	0.0072	140	12	0.42	60	10	0.0025	80	8	3.03E-4
	20	12	1.6E-4	70	12	0.0757	30	10	3.78E-4	40	8	1.55E-4
	10	10	0.0024	28	12	6E-4	12	10	4.32E-7	20	8	3.43E-5

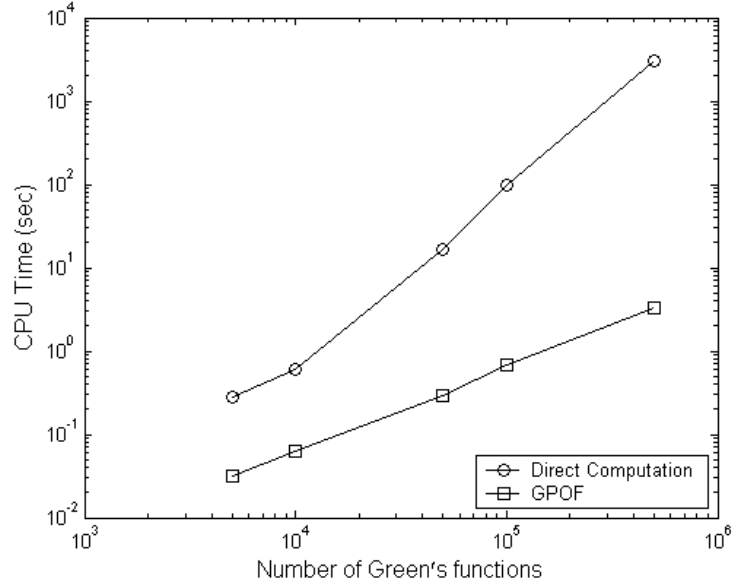


Fig 2.9: Comparison of the CPU time used in the direct computation of the closed-form Green's function and the GPOF interpolation scheme with respect to the number of Green's functions evaluated.

## 2.10 Far-field Radiation Pattern [86]

The radiation pattern can be computed using the reciprocity theorem [86]. In accordance with the reciprocity theorem, the electric field  $\mathbf{E}^{\text{rad}}$  radiated by  $\mathbf{J}$  in the presence of multilayer media is related to  $\mathbf{J}$  by

$$\iiint_V \mathbf{E}^{\text{rad}}(\mathbf{r}, \theta, \phi) \cdot \mathbf{J}_2(\mathbf{r}, \theta, \phi) dV = \iint_S \mathbf{E}_2(\mathbf{r}', \theta', \phi') \cdot \mathbf{J}(\mathbf{r}') ds', \quad (2.94)$$

$\mathbf{J}_2$  denotes an arbitrary current and  $\mathbf{E}_2$  is the field radiated by  $\mathbf{J}_2$ . Choosing an infinitesimal electric current dipole with either the  $\phi$  or  $\theta$  orientation and placing it at the observation point in the far zone, we can compute the electric field  $\mathbf{E}_2(\mathbf{r}', \theta', \phi')$  in the presence of multilayer media without the microstrip antenna. We can obtain

$$\mathbf{E}^{\text{rad}}(\mathbf{r}, \theta, \phi) = \iint_S \mathbf{E}_2(\mathbf{r}', \theta', \phi') \cdot \mathbf{J}(\mathbf{r}') ds'. \quad (2.95)$$

## 2.11 Numerical Result

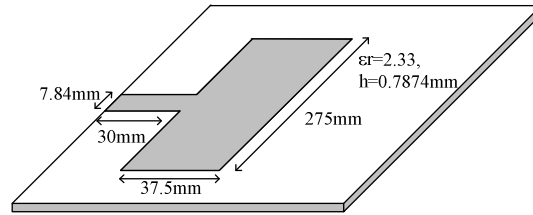
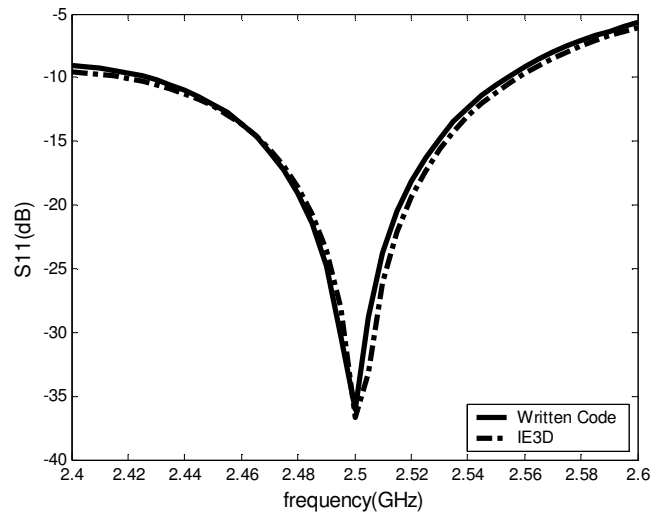


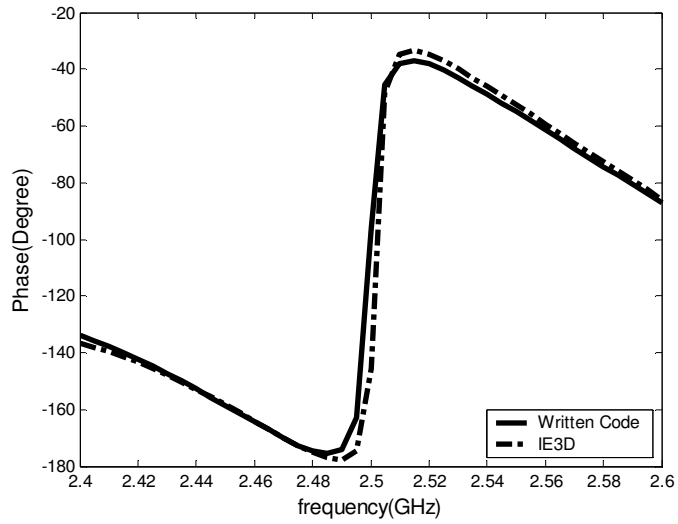
Fig 2.10: Microstrip patch antenna with substrate height = 31mils and  $\epsilon_r = 2.33$  at resonant frequency 2.5 GHz.

We consider a long rectangular patch antenna as shown in Fig 2.10. As the input impedance of a long patch is low, a quarter-wave transmission line section is used in order to match the antenna with a 50 ohm cable. The width and length of the transmission line are 37.5 mm and 275 mm respectively. The patch antenna is excited at one end by a SMA connector. Fig 2.11 shows the comparison of the magnitude and phase of the return loss of a long patch antenna. The measured result can be found in the literature report [87]. The simulated result shows good agreement with those obtained from commercial software IE3D [62]. The norm-2 error of the input impedance between the written code and the IE3D is 3.2%.





(a)



(b)

Fig 2.11: Comparison of the magnitude and phase of the return loss of a long patch antenna between the written code and IE3D.

## 2.12 Conclusion

This chapter presents a detailed exposition of the theoretical formulation that is implemented for the analysis of microstrip structure. It starts off with an overview of the spectral domain Green's functions for a structure that is embedded within a grounded multilayered medium. The spatial domain Green's functions in the form of Sommerfeld Integrals are then evaluated by DCIM, which obviates the time-consuming numerical integration. GPOF interpolation scheme is employed to further reduce the computation time to evaluate the Green's function of a large structure. For example, to evaluate 500000 number of Green's functions, GPOF interpolation scheme takes approximately 3.3 seconds while the direct computation of the closed-form Green's function takes about 3000 seconds. The chapter also includes how S-parameters and far fields can be calculated.

## CHAPTER 3    **Macro-basis Function**

### 3.1    Introduction

The MoM analysis in the previous chapter requires  $O(N^3)$  computation complexity, where  $N$  is the number of unknowns and  $O(N^2)$  memory to solve a structure. As the number of unknowns becomes very large, there will be a tremendous increase in the computation time usage and memory requirements, giving rise to dense matrices that are expensive to store and evaluate. To manage large problems, iterative solvers are usually employed in the fast methods such as the adaptive integral method [46]-[49] and the fast multipole method [42]-[45]. However, iterative solvers may lead to convergence difficulties when dealing with very large scale objects. Another emerging approach for solving large problems is based on the segmentation techniques, which can significantly reduce the number of unknowns. Various segmentation techniques for solving microstrip problems are given in the next paragraph.

Allen Taflove [2] presents a spatial decomposition technique whereby the method of moments is sequentially implemented on each sub-domain of the original target. The spatial decomposition technique is useful for the solution of scatterer problems, but

has not yet been extended to large radiation problems. S. Ooms and D. De Zutter [1] introduce an iterative Diakoptics-based multilevel moment method to analyze large planar microwave structures. Even though the method converges very fast, its computational complexity is high. A recursive technique called sub-domain multilevel approach [50]-[54], where the macro-basis function is constructed from the solution of the sub-domain in isolation has been developed by J. R. Mosig to handle large antenna arrays. The main drawback of the method is that it does not directly consider the mutual coupling effect between different portions of the geometry. This will affect the accuracy of the solution especially for dense and complex structure. In order to account for the mutual coupling effect of the neighboring sub-domains, the sub-entire-domain basis function method reported in [55] introduces dummy sub-domains to an observation sub-domain. Even though the method gives good accuracy, it is more efficient for periodic structures.

The above methods attempt to correct the mutual coupling terms through iterative refinement process. R. Mittra [96]-[99] proposed a method called the characteristic basis function that does not require iterative refinement process. This technique includes the mutual coupling effects directly by using a new type of high-level basis function, referred to as primary and secondary characteristic basis functions. Even though the characteristic basis function does not require iterative process, the number of characteristic basis functions generated will depend on the order of the coupling instead of the number of sub-domains as in the case of the above methods. If one only

considers the primary and the second-order coupling, there will be  $N_b$  characteristic basis functions for each single sub-domain where  $N_b$  is the number of sub-domains. This will lead to  $N_b^2$  characteristic basis functions for the entire problem. The number of characteristic basis functions generated will increase with the order of the coupling, resulting in a larger matrix size as compared to the above methods.

In this chapter, we present a grouping concept, which utilizes the macro-basis function with the progressive method, to analyze microstrip structures. This new concept of near-far neighbour evaluation gives a better accuracy as compared to the sub-domain multilevel approach and the sub-entire-domain basis function method. Besides, the number of macro-basis functions generated will be lesser than those generated from the characteristic basis function. A new iterative refinement process is then developed to further improve the accuracy of the solution, especially for dense and complex structures. In addition, we employ the fast matrix-vector properties of the adaptive integral method to accelerate the matrix filling time.

This chapter is organized as follows. We will first discuss the macro-basis function. Two reported methods, namely the sub-domain multilevel approach [50]-[54] and the sub-entire-domain basis function method [55] to determine the macro-basis function (MBF) will be illustrated. This will be followed by the introduction of the macro-basis functions with progressive method. A new iterative method is then described. The strategy to accelerate the matrix filling time is presented to further reduce the

computation time. Finally, some examples are analyzed to demonstrate the accuracy and efficiency of the developed algorithm.

### 3.2 Macro-basis Function

In the segmentation technique, the MoM impedance matrix is made up of blocks named  $Z_{mn}$ , standing for basis and testing functions on sub-domains  $n$  and  $m$ , respectively. The unknown current coefficients, as well as the right-hand side of the system of equations, can be segmented into vectors, named  $I_m$  and  $v_m$ , respectively, associated with the successive sub-domains that can be put in the following form:

$$\begin{bmatrix} Z_{11} & \cdots & Z_{1M} \\ & \ddots & \\ Z_{M1} & \cdots & Z_{MM} \end{bmatrix} \begin{bmatrix} I_1 \\ \vdots \\ I_M \end{bmatrix} = \begin{bmatrix} v_1 \\ \vdots \\ v_M \end{bmatrix}. \quad (3.1)$$

If Galerkin testing functions are applied, macro-testing functions and macro-basis functions applied are the same. Thus, a reduced system of equations can be written with the help of the following primed quantities:

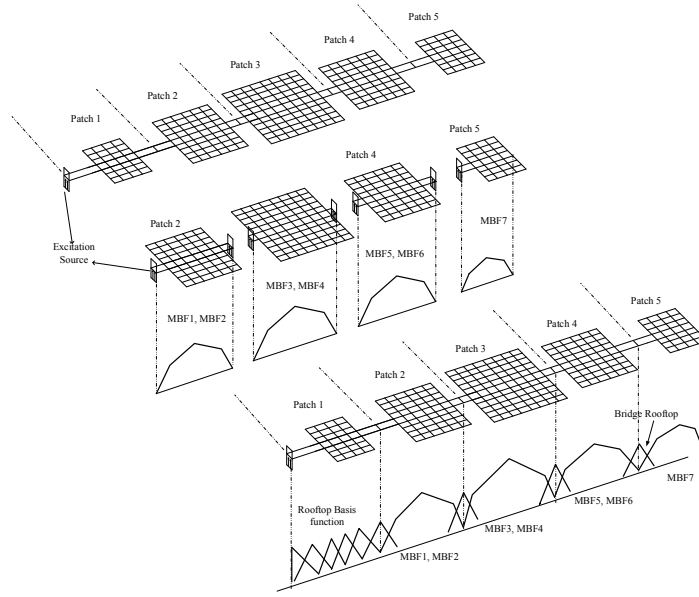
$$Z'_{mn} = \beta^T Z_{mn} \beta, \quad (3.2)$$

$$I_n = \beta I'_n, \quad (3.3)$$

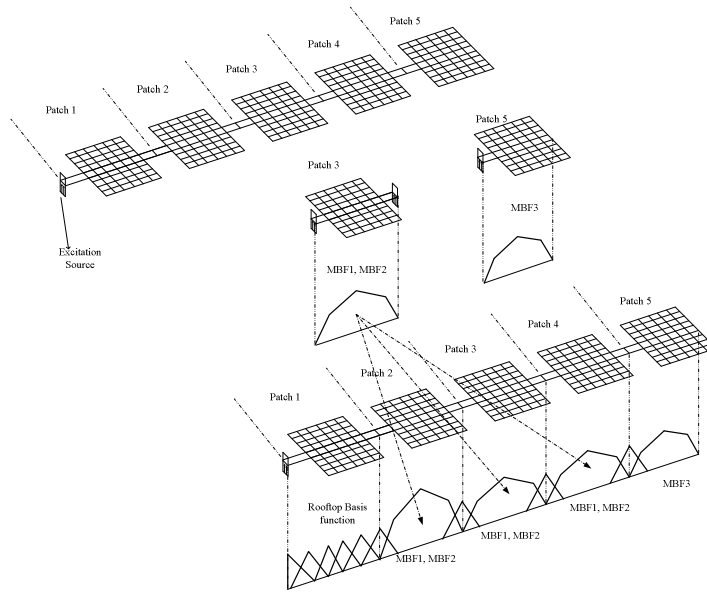
$$v'_n = \beta^T v_n. \quad (3.4)$$

With an adequate choice of macro-basis functions (MBF) (which are taken identical to the macro testing functions), relatively fast and accurate solutions can be obtained for the problem.

### 3.3 Sub-domain Multilevel Approach [50]



(a)



(b)

Fig. 3.1: Illustration of sub-domain multilevel approach. (a) Non-identical problem (b) Identical problem

We will illustrate the sub-domain multilevel approach (SMA) using linear 1 by 5

series-fed arrays. Fig. 3.1 (a) describes the procedure for non-identical patches while Fig. 3.1 (b) describes the procedure for identical patches. In sub-domain multilevel approach, large computation is broken down into several smaller sub-problems. The series-fed array is divided into five sub-domains where Patch 1, Patch 2, ..., Patch 5, serve to distinctly label each sub-domain. A basis function called the bridge rooftop is connected between each sub-domain. Since Patches 2, 3 and 4 have two cutting point, they are analyzed as a two-port device, alternately exciting one port with the voltage generator and leaving the other port open circuit. Thus, two MBFs are required to describe the sub-domain. Since Patch 5 has only one cut point, a voltage generator is introduced at the cut position while the end is an open stub. For non-identical problems (Fig. 3.1(a)), each isolated sub-domain is solved using the conventional MoM, resulting in 7 MBFs for a 1 by 5 non-identical linear array. On the other hand, for identical problem (Fig. 3.1(b)), only two sub-domains, Patch 3 and Patch 5, need to be computed as one can take the advantage of patches that are replicas of already computed sub-domains. However, the sub-domains must have exactly the same mesh and the same basis function numbering scheme. The MBFs for Patch 3 can be used for Patch 2 and Patch 4, resulting in 3 MBFs for a 1 by 5 identical linear array. Substituting the solved coefficients  $[\hat{\alpha}_k^p]$  into (2.56), the individual rooftops on the isolated domains are merged into macro-basis function that is defined as [10]

$$\mathbf{m}_p(\mathbf{r}) = \sum_k \hat{\alpha}_k^p \mathbf{f}_k^p(\mathbf{r}), \quad (3.5)$$

where  $\mathbf{f}_k^p$  is the basis function associated with the  $k^{\text{th}}$  interior edge of the mesh on the sub-domain  $S_p$ .



The MBF  $\mathbf{m}_p$  is in turn grouped into the global MoM system, taking into account the symmetries and mutual coupling. The global current is expanded using the remaining individual basis functions,  $[\alpha_k]$  on the root domain and the MBFs  $[\beta_p]$  defined over the sub-domains. The root domain is defined as the sub-domain that is represented by the original basis function and where no MBFs will be formed. The global current is defined as

$$\mathbf{J} = \sum_k \alpha_k \mathbf{f}_k + \sum_p \beta_p \mathbf{m}_p. \quad (3.6)$$

Applying the Galerkin testing functions, a compressed MoM system of equations for the global problem with a significantly reduced number of unknowns is obtained. For the case of four MBFs, the MoM equation is expressed as

$$\begin{bmatrix} \langle \mathbf{f}_1, \mathcal{L}\mathbf{f}_1 \rangle & \cdots & \langle \mathbf{f}_1, \mathcal{L}\mathbf{m}_1 \rangle & \langle \mathbf{f}_1, \mathcal{L}\mathbf{m}_2 \rangle & \langle \mathbf{f}_1, \mathcal{L}\mathbf{m}_3 \rangle & \langle \mathbf{f}_1, \mathcal{L}\mathbf{m}_4 \rangle \\ \vdots & \cdots & \vdots & \vdots & \vdots & \vdots \\ \langle \mathbf{m}_1, \mathcal{L}\mathbf{f}_1 \rangle & \cdots & \langle \mathbf{m}_1, \mathcal{L}\mathbf{m}_1 \rangle & \langle \mathbf{m}_1, \mathcal{L}\mathbf{m}_2 \rangle & \langle \mathbf{m}_1, \mathcal{L}\mathbf{m}_3 \rangle & \langle \mathbf{m}_1, \mathcal{L}\mathbf{m}_4 \rangle \\ \langle \mathbf{m}_2, \mathcal{L}\mathbf{f}_1 \rangle & \cdots & \langle \mathbf{m}_2, \mathcal{L}\mathbf{m}_1 \rangle & \langle \mathbf{m}_2, \mathcal{L}\mathbf{m}_2 \rangle & \langle \mathbf{m}_2, \mathcal{L}\mathbf{m}_3 \rangle & \langle \mathbf{m}_2, \mathcal{L}\mathbf{m}_4 \rangle \\ \langle \mathbf{m}_3, \mathcal{L}\mathbf{f}_1 \rangle & \cdots & \langle \mathbf{m}_3, \mathcal{L}\mathbf{m}_1 \rangle & \langle \mathbf{m}_3, \mathcal{L}\mathbf{m}_2 \rangle & \langle \mathbf{m}_3, \mathcal{L}\mathbf{m}_3 \rangle & \langle \mathbf{m}_3, \mathcal{L}\mathbf{m}_4 \rangle \\ \langle \mathbf{m}_4, \mathcal{L}\mathbf{f}_1 \rangle & \cdots & \langle \mathbf{m}_4, \mathcal{L}\mathbf{m}_1 \rangle & \langle \mathbf{m}_4, \mathcal{L}\mathbf{m}_2 \rangle & \langle \mathbf{m}_4, \mathcal{L}\mathbf{m}_3 \rangle & \langle \mathbf{m}_4, \mathcal{L}\mathbf{m}_4 \rangle \end{bmatrix} \begin{bmatrix} \alpha_1 \\ \vdots \\ \beta_1 \\ \beta_2 \\ \beta_3 \\ \beta_4 \end{bmatrix} = \begin{bmatrix} \langle \mathbf{f}_1, -\mathbf{E}_t^a \rangle \\ \vdots \\ \langle \mathbf{m}_1, -\mathbf{E}_t^a \rangle \\ \langle \mathbf{m}_2, -\mathbf{E}_t^a \rangle \\ \langle \mathbf{m}_3, -\mathbf{E}_t^a \rangle \\ \langle \mathbf{m}_4, -\mathbf{E}_t^a \rangle \end{bmatrix}. \quad (3.7)$$

The interaction integrals between two MBFs  $\mathbf{m}_p$  and  $\mathbf{m}_q$  can be done using vector-matrix-vector multiplication as follows:

$$\begin{aligned}
\langle \mathbf{m}_p, \mathcal{L}\mathbf{m}_q \rangle &= j\omega\mu_0 \iint_{S_p} \iint_{S_q} \left[ \begin{array}{c} \mathbf{m}_p(\mathbf{r}) \cdot \mathbf{G}_a(\mathbf{r}, \mathbf{r}') \cdot \mathbf{m}_q(\mathbf{r}') \\ -\frac{1}{k_0^2} \nabla \cdot \mathbf{m}_p(\mathbf{r}) \nabla' \cdot \mathbf{m}_q(\mathbf{r}') G_q(\mathbf{r}, \mathbf{r}') \end{array} \right] dS' dS \\
&= \sum_k \hat{\alpha}_k^p \sum_i \hat{\alpha}_i^q j\omega\mu_0 \iint_{S_p} \iint_{S_q} \left[ \begin{array}{c} \mathbf{f}_k^p \cdot \mathbf{G}_a(\mathbf{r}, \mathbf{r}') \cdot \mathbf{f}_i^q \\ -\frac{1}{k_0^2} \nabla \cdot \mathbf{f}_k^p \nabla' \cdot \mathbf{f}_i^q G_q(\mathbf{r}, \mathbf{r}') \end{array} \right] dS' dS \quad (3.8) \\
&= [\hat{\alpha}_k^p]^T [Z_{k,i}^{pq}] [\hat{\alpha}_i^q].
\end{aligned}$$

The interaction integrals between the testing function on the root domain,  $\mathbf{f}_p$  and the MBF  $\mathbf{m}_q$  can be done using matrix-vector multiplication as follows:

$$\begin{aligned}
\langle \mathbf{f}_p, \mathcal{L}\mathbf{m}_q \rangle &= j\omega\mu_0 \iint_{S_p} \iint_{S_q} \left[ \begin{array}{c} \mathbf{f}_k^p(\mathbf{r}) \cdot \mathbf{G}_a(\mathbf{r}, \mathbf{r}') \cdot \mathbf{m}_q(\mathbf{r}') \\ -\frac{1}{k_0^2} \nabla \cdot \mathbf{f}_k^p(\mathbf{r}) \nabla' \cdot \mathbf{m}_q(\mathbf{r}') G_q(\mathbf{r}, \mathbf{r}') \end{array} \right] dS' dS \\
&= \sum_k \sum_i \hat{\alpha}_i^q j\omega\mu_0 \iint_{S_p} \iint_{S_q} \left[ \begin{array}{c} \mathbf{f}_k^p \cdot \mathbf{G}_a(\mathbf{r}, \mathbf{r}') \cdot \mathbf{f}_i^q \\ -\frac{1}{k_0^2} \nabla \cdot \mathbf{f}_k^p \nabla' \cdot \mathbf{f}_i^q G_q(\mathbf{r}, \mathbf{r}') \end{array} \right] dS' dS \quad (3.9) \\
&= [Z_{k,i}^{pq}] [\hat{\alpha}_i^q].
\end{aligned}$$

The mutual coupling between different sub-domains is accounted for through these MoM elements. The final MoM matrix is reduced in size, but is still fully populated. Finally, the solution for each MBF is recovered by a simple expansion from the compressed solution.

Sub-domain multilevel approach can be applied to the non-radiating component or the weak coupling of the current in any structure. One example is the printed antenna array. The antenna's structure includes beamforming networks of complex shape, which contribute heavily to the final MoM matrix size, but very weakly to the overall antenna radiation.

### 3.4 Sub-entire-domain Basis Function Method [55]

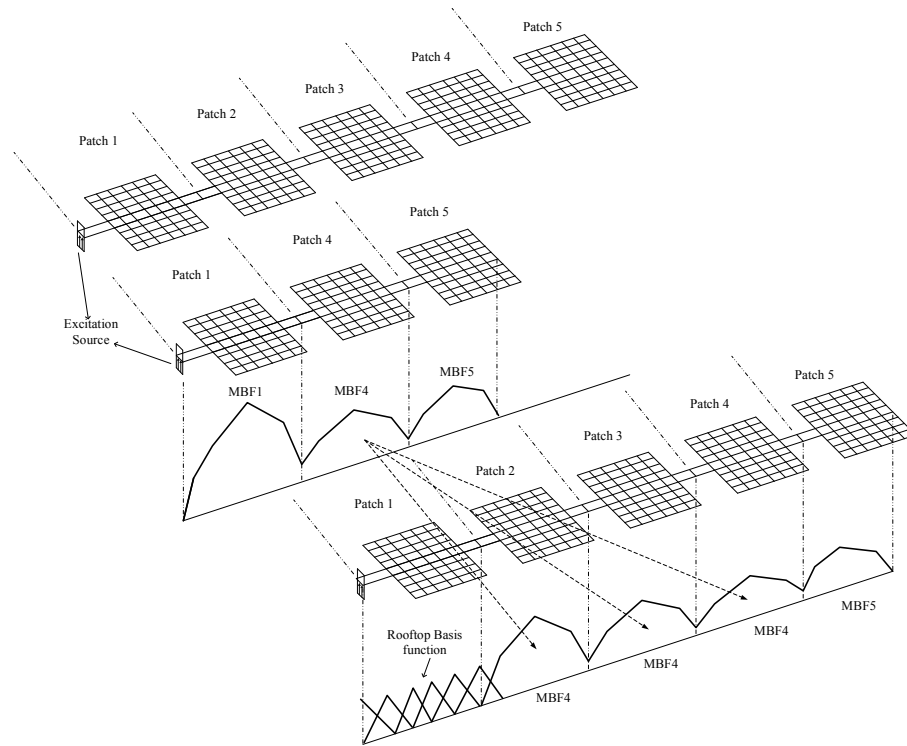


Fig. 3.2: Illustration of sub-entire-domain basis function method.

In order to obtain an accurate macro-basis function with a small computational load, sub-entire-domain basis function method introduces dummy cells to an observation cell to capture the most important mutual coupling. Sub-entire-domain (SED) basis function method is applied to periodic structure. An identical 1 by 5 series-fed array is used here to illustrate the sub-entire-domain basis function method and the procedure is shown in Fig. 3.2. A smaller domain is required for the sub-entire-domain basis function method. In this example, it is made up of Patch 1, Patch 4 and Patch 5 depicted in Fig. 3.2. The solved currents on Patch 4 are then used on Patch 2 and Patch 3 in the original problem. The currents on Patch 2 to Patch 5 are merged into

MBFs. The overall coupling of the patches is then considered in equation (3.7). The technique is more efficient for a periodic structure.

### 3.5 Macro-basis Function with Progressive Method

In this section, we present a new grouping concept of near-far neighbour evaluation, which utilizes both the macro-basis function and progressive method (MBF-PM), to analyze microstrip structures. We start with a smaller problem that is made up of the first few and the last few sub-domains. The purpose of having the first few sub-domains is to create an incident wave and the purpose of having the last few sub-domains is to create an artificial reflection from the end of the structure for the next sub-domain to be added to the problem. The remaining sub-domains are then inserted into the smaller problem progressively. In this way, the newly inserted sub-domain will take into account the mutual coupling effect of the solved current which aid in improving the accuracy of the MBFs. The proposed method emulates the transmission and reflection phenomenon of a wave travelling on the structure through the successive near-far neighbour coupling simulations.

We will illustrate our approach by using a linear series-fed microstrip antenna array as shown in Fig. 3.3. The procedure can be summarized in the following steps:

1. The array is divided into smaller patches where the sub-domains are distinctly labeled from Patches 1 to 5.

2. A smaller domain consisting of Patches 1, 4 and 5 is first solved using the conventional MoM.
3. Patch 3 is next inserted between Patches 1 and 4. The currents on Patches 4 and 5 are merged into MBFs using equation (3.5) while the current on Patch 1 serves as the new excitation source for the remaining sub-domain. By solving the new problem through MoM, it leads to a compressed matrix. The interaction between the MBFs on Patches 4 and 5 can be obtained from the previous matrix formed in Step 2. The computed current on Patch 3 is merged into MBF and the MBF of Patches 4 and 5 are updated. The interaction,  $V$  between the MBFs of Patches 3, 4 and 5 can be evaluated as

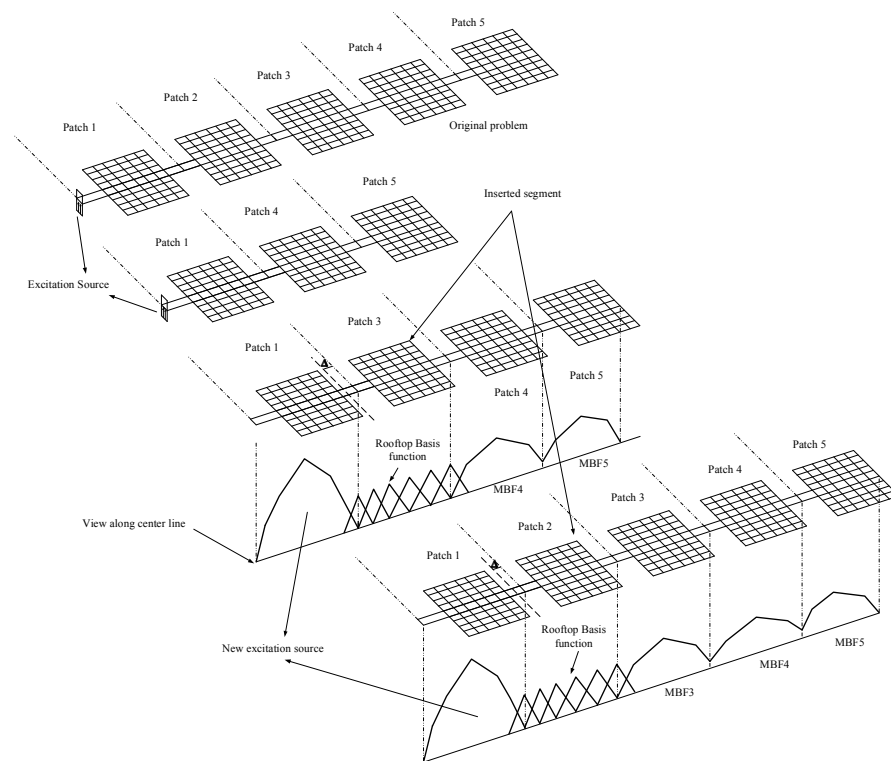


Fig.3.3: Illustration of macro-basis function with progressive method.

$$V = \begin{bmatrix} \sum_L \sum_k \alpha_k \langle f_k, \mathcal{L}f_L \rangle \alpha_L & \sum_k \alpha_k \langle f_k, \mathcal{L}m_4 \rangle \beta_4 & \sum_k \alpha_k \langle f_k, \mathcal{L}m_5 \rangle \beta_5 \\ \sum_L \beta_4 \langle m_4, \mathcal{L}f_L \rangle \alpha_L & \beta_4 \langle m_4, \mathcal{L}m_4 \rangle \beta_4 & \beta_4 \langle m_4, \mathcal{L}m_5 \rangle \beta_5 \\ \sum_L \beta_5 \langle m_5, \mathcal{L}f_L \rangle \alpha_L & \beta_5 \langle m_5, \mathcal{L}m_4 \rangle \beta_4 & \beta_5 \langle m_5, \mathcal{L}m_5 \rangle \beta_5 \end{bmatrix}. \quad (3.10)$$

4. The process continues until the initial currents on Patches 2 to 5 are solved and merged into MBFs. The first sub-domain is now the root domain (refer to page 56 for the definition of root domain). The overall coupling of the patches is then considered in equation (3.7)

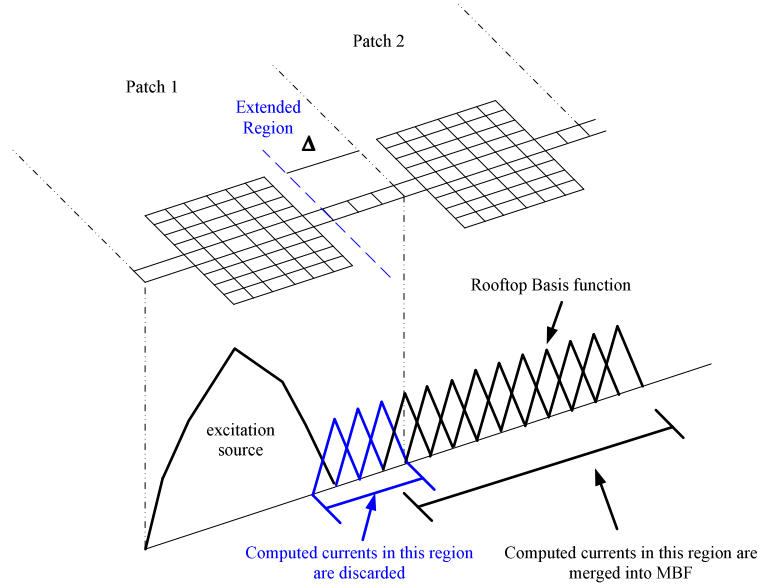


Fig.3.4: Extended region of the root domain.

In the above process (refer to Fig.3.3), the root domain is extended by a distance of  $\Delta$  on the side of the excitation source to improve the accuracy of the solution as illustrated in Fig.3.4. The extended root domain (Patch 2) shares some of the unknowns with the excitation source (Patch 1). We identify and eliminate these source locations. Once the currents on the root domain are found, we discard the currents on

the extended region and retain the rest, merging them into MBFs.

### 3.6 Iterative Refinement Process

Through our numerical simulations, it is found that for strong coupling of the current on the structure, the computed error in the current distribution using the sub-domain multilevel approach, the sub-entire-domain basis function method and the macro-basis function with progressive method can amount to more than 10 percent as compared to the rigorous solution of the conventional MoM (refer to Table 3.8). Thus we have to apply a further iterative refinement process. If the number of iterative sweeps is large, the computation time increases.

The strong coupling perturbation can be explicitly included as a source term in the first iteration solution as reported in [1]. During the first stage of the MoM simulation, only the sub-domain connected to the considered artificial port is taken into account while leaving the rest of the port open. The current on the sub-domain will excite currents on the rest of the sub-domains by (first-order) field coupling. During the first iteration, these first-order coupling currents are calculated. These currents will, in turn, excite (second-order) coupling currents on all the other sub-domains. These are calculated in the second iteration. These currents will again excite currents on all the other sub-domains. The actual current is the sum of the first stage MoM current (zeroth-order coupling current) and the currents from the different iterations (the  $n$ th

order coupling currents). During this process, all the sub-domains are considered which leads to the entire domain basis function. Although this method converges very fast, it exhibits several disadvantages [92]. Since the entire domain basis function extends over the whole structure, complete matrix vector products must be performed during the iterative refinement process as well as in the global problem. This has to be done for each sub-domain which increases the computational complexity

In this thesis, two simpler iterative process A and iterative process B (the proposed method) are studied. The iterative process A, resembles the iterative steps proposed in

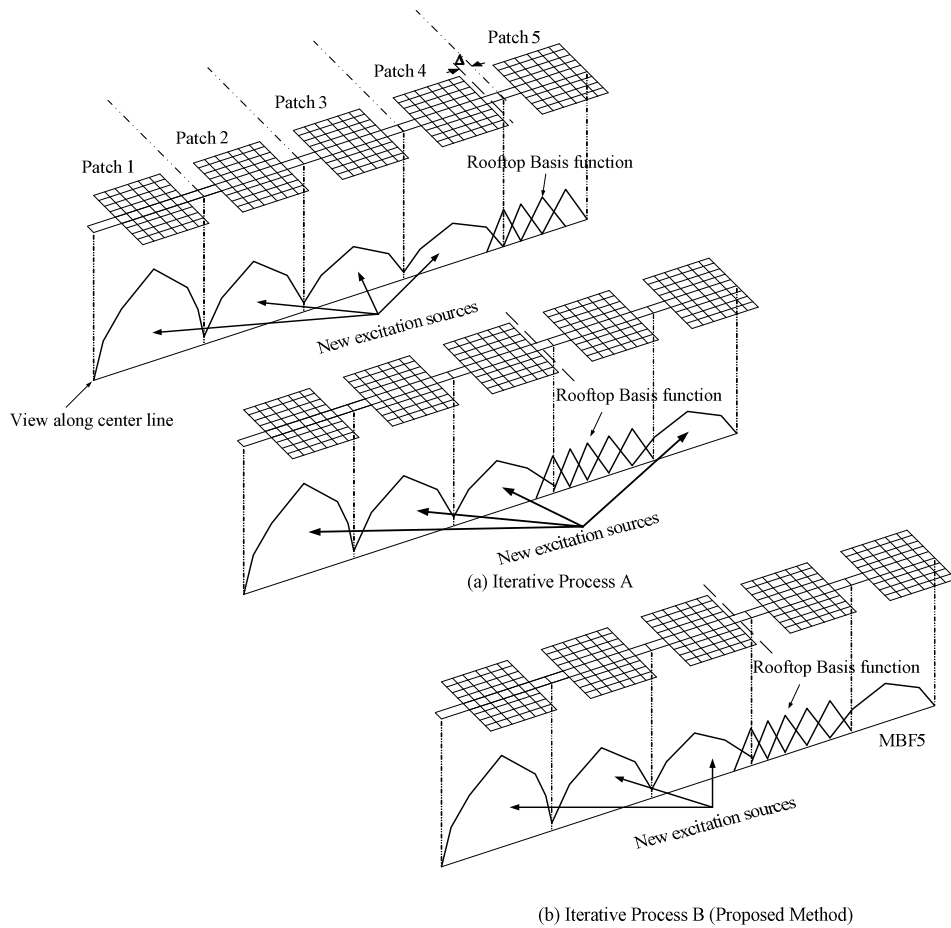


Fig.3.5: Iterative Refinement Process. (a) Iterative process A. (b) Iterative process B



Spatial Decomposition Technique [2]. The problem is divided into a number of sub-domains. The excitation of the first sub-domain consists of the original excitation source and additional excitation due to currents residing on the surfaces on the remaining sub-domains. The initial currents on the sub-domains can be computed with the sub-domain multilevel approach, the sub-entire-domain basis function or the macro-basis function with progressive method. The MoM is then applied to calculate each sub-domain. Fig.3.5 (a) illustrates the iterative process A. The analysis starts with Patch 5. The excitation for Patch 5 is given by the excitation due to Patches 1 to 4. The analysis is now shifted to the next adjacent sub-domain, Patch 4. The excitation for this sub-domain consists of the excitation due to Patches 1, 2, 3 and 5. In this manner, the procedures can be implemented for each sub-domain from one end of the structure to the other end, always using the surface currents as the excitation for the sub-domain of interest. This iterative process continues until the desired tolerance level in equation (3.11) is met.

Under our numerical experimentation, we find that iterative process A does not converge for all cases. Thus, we propose an improved iterative process B that would result in a better convergence of the solution. Instead of using the latest surface currents as the excitation for the sub-domain of interest, we merged the latest surface currents into MBF.

The proposed method is summarized in the following steps using the same example:

1. The initial currents on Patches 1 to 4 excite coupling currents on Patch 5, which currently becomes the root domain (refer to page 56 for the definition of root domain). The new current on Patch 5 is solved and merged into MBF.
2. The initial current on Patch 4 is removed and new unknown basis functions are inserted. Patches 1 to 3 become the new excitation source for the MoM (See Fig.3.5 (b)).
3. Update the MBF on Patch 5 and merged the solved current on Patch 4 into MBF.
4. The process is repeated until Patch 1 is solved. The completed process is considered as the first iterative sweep.

The iterative process is stopped when the number of iterative sweeps exceeds a specified maximum or if the iterative error becomes smaller than a tolerance (e.g. 0.1%). We can define the iterative error  $\xi$  as

$$\xi = \frac{\|I_n - I_{n-1}\|_2}{\|I_{n-1}\|_2}, \quad (3.11)$$

where  $\|I_{n-1}\|_2$  is the norm 2 of the previous current  $I$ . Another condition for the iterative process to stop is

$$\psi = \|Z_n I_n - Z_{n-1} I_{n-1}\|_2 \approx 0, \quad (3.12)$$

where  $Z_{n-1}$  is the previous MoM impedance matrix.

### 3.7 Efficient evaluation of Macro-basis Function Reaction Term using Adaptive Integral Method

In order to speed up the MoM matrix filling in the macro-basis function with progressive method, we present an efficient hybrid macro-basis function with progressive and adaptive integral method (MBF-PM-AIM). The interactions between the testing functions on the root domain (refer to page 56 for the definition of root domain) and MBFs within the near field are computed in the customary MoM manner. In the far field region, the interactions are carried out by using its compressed representation through the AIM method.  $\langle \mathbf{f}_n, \mathcal{L}\mathbf{m}_p \rangle$  in equation (3.7) can be split into two part,

$$\langle \mathbf{f}_n, \mathcal{L}\mathbf{m}_p \rangle = \mathbf{Z}^{\text{near}} + \mathbf{Z}_{\text{np}}^{\text{far}}, \quad (3.13)$$

where  $\mathbf{Z}^{\text{near}}$  denotes the interaction among the nearby elements within a threshold distance, the subscript n stand for the testing functions on the root domain and  $p^{\text{th}}$  macro-basis function. The MBFs are projected onto the regular auxiliary grid. The projection of the MBF is done by first finding the smallest 2D rectangular boxes of grid nodes that totally encloses each of the basis functions that form the MBF. The projection of the basis functions onto the grid nodes are accomplished by means of multipole moment matching in equation (3.15). For example, in Fig.3.6 (a) the highlighted rooftop basis function is approximated by  $(M+1)^2=9$  rectangular grids (highlighted grids nodes) where  $M$  is the order of translation. In Fig.3.6 (b), the highlighted rooftop basis function is approximated by  $(M+1)^2=16$  rectangular grids. Once the translation matrix has been found, it is multiplied by the coefficient,  $\hat{\alpha}_j^p$  so

as to project the MBF onto the grids. In this way, one does not need to compute the MoM matrix. The memory requirement will be reduced.

The MBF-PM-AIM procedures can be summarized as follows:

1. All the sub-domains are enclosed in identical rectangular grids.
2. The MBF and the testing functions on the root domain are projected to the surrounding grids.
3. The grid potential (interactions between the testing functions on the root domain and MBFs) is then computed with the aid of fast Fourier transform.
4. The computed potential is interpolated back to the basis functions on the root domain. The same multipole coefficient used to project the basis functions to the grid nodes can be used as the interpolating functions.
5. Compute the correct near-field interaction.

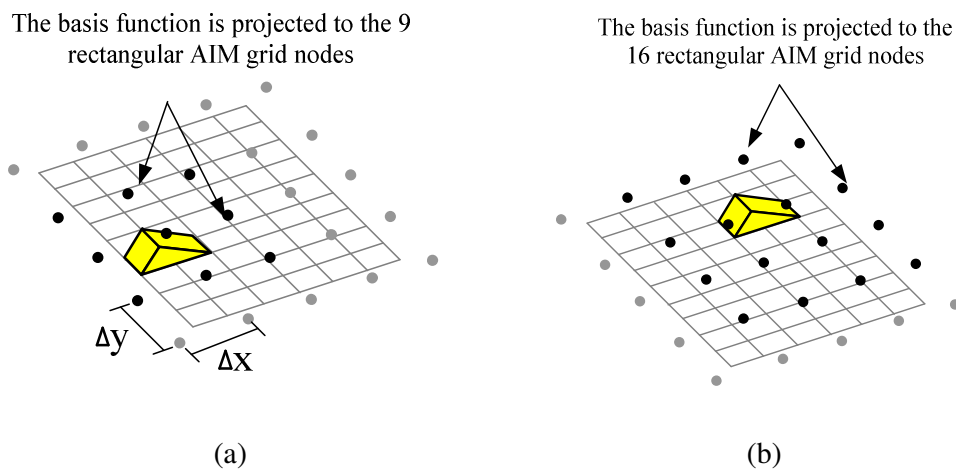


Fig.3.6: Translation of rooftop basis function to the highlighted rectangular grids.

Let  $\varphi_n(\mathbf{r})$  denote either  $\mathbf{f}_n(\mathbf{r})$  or  $\nabla \cdot \mathbf{f}_n(\mathbf{r})$  which can be approximated as a combination of the Dirac delta functions on the rectangular grids, namely:

$$\varphi_n(\mathbf{r}) = \hat{\varphi}_n(\mathbf{r}) = \sum_{u=1}^{(M+1)^2} \Lambda_{nu} \delta(\mathbf{r} - \mathbf{r}_{nu}), \quad (3.14)$$

where  $\Lambda_{nu}$  is the translation coefficient for the basis function  $\varphi_n(\mathbf{r})$ ,  $M$  is the order of the translation and  $\mathbf{r}_{nu} = (x_{nu}, y_{nu})$  is the coordinate of the grid. The subscript  $n$  denotes the  $n^{\text{th}}$  basis function. The translation coefficient can be found based on the criterion that the translated basis function produces the same multipole moments as the original basis function i.e.

$$\sum_{u=1}^{(M+1)^2} (x_{nu} - x_0)^{q_1} (y_{nu} - y_0)^{q_2} \Lambda_{nu} = \iint_{T_n} \varphi_n(\mathbf{r}) (x - x_0)^{q_1} (y - y_0)^{q_2} ds \quad (3.15)$$

$$\text{for } 0 \leq q_1, q_2 \leq M,$$

where the reference point  $\mathbf{r}_0 = (x_0, y_0)$  is chosen as the center of the basis function.

By adopting different combination values of  $q_1$  and  $q_2$ , we can form  $M$  equations to solve for the  $M$  unknowns  $\Lambda_{nu}$ . Thus if  $M=1$ , we have the following equations:

$$\sum_{u=1}^{(M+1)^2} \Lambda_{nu} = \iint_{T_n} \varphi_n(\mathbf{r}) ds \quad \text{for } q_1=0 \text{ and } q_2=0, \quad (3.16)$$

$$\sum_{u=1}^{(M+1)^2} (x_{nu} - x_0) \Lambda_{nu} = \iint_{T_n} \varphi_n(\mathbf{r}) (x - x_0) ds \quad \text{for } q_1=1 \text{ and } q_2=0, \quad (3.17)$$

$$\sum_{u=1}^{(M+1)^2} (y_{nu} - y_0) \Lambda_{nu} = \iint_{T_n} \varphi_n(\mathbf{r}) (y - y_0) ds \quad \text{for } q_1=0 \text{ and } q_2=1, \quad (3.18)$$

$$\sum_{u=1}^{(M+1)^2} (x_{nu} - x_0)(y_{nu} - y_0) \Lambda_{nu} = \iint_{T_n} \varphi_n(\mathbf{r}) (x - x_0)(y - y_0) ds \quad \text{for } q_1=1 \text{ and } q_2=1. \quad (3.19)$$

To compute  $\Lambda_{nu}$ , it is possible to form a system of equations as shown:

$$\begin{aligned}
& \begin{bmatrix} 1 & 1 & 1 & 1 \\ (x_{n1} - x_0) & (x_{n2} - x_0) & (x_{n3} - x_0) & (x_{n4} - x_0) \\ (y_{n1} - y_0) & (y_{n2} - y_0) & (y_{n3} - y_0) & (y_{n4} - y_0) \\ (x_{n1} - x_0)(y_{n1} - y_0) & (x_{n2} - x_0)(y_{n2} - y_0) & (x_{n3} - x_0)(y_{n3} - y_0) & (x_{n4} - x_0)(y_{n4} - y_0) \end{bmatrix} \begin{bmatrix} \Lambda_{n1} \\ \Lambda_{n2} \\ \Lambda_{n3} \\ \Lambda_{n4} \end{bmatrix} \\
& = \begin{bmatrix} \iint_{T_n} \varphi_n(\mathbf{r}) ds \\ \iint_{T_n} \varphi_n(\mathbf{r})(x - x_0) ds \\ \iint_{T_n} \varphi_n(\mathbf{r})(y - y_0) ds \\ \iint_{T_n} \varphi_n(\mathbf{r})(x - x_0)(y - y_0) ds \end{bmatrix}.
\end{aligned} \tag{3.20}$$

With the translation formulation,  $Z_{np}^{\text{far}}$  can be approximated as

$$Z_{np}^{\text{far}} = j\omega\mu_0 \left[ \Lambda_{n_x} G_a \Lambda_{j_x}^{p(T)} \hat{\alpha}_j^p + \Lambda_{n_y} G_a \Lambda_{j_y}^{p(T)} \hat{\alpha}_j^p - \frac{1}{k_0^2} \Lambda_{n_d} G_q \Lambda_{j_d}^{p(T)} \hat{\alpha}_j^p \right], \tag{3.21}$$

where  $\Lambda_x$ ,  $\Lambda_y$ , and  $\Lambda_d$  denote the translation coefficients for the x-component, y-component, and the divergence of the basis function, respectively. The subscript, j and the superscript, p refer to the j<sup>th</sup> subsectional basis function on the p<sup>th</sup> MBF. The superscript T stands for the transpose operation. The translation coefficients are sparse matrices with each row containing only  $(M+1)^2$  nonzero elements.

Similarly, the interaction between two MBFs can be expressed as

$$\langle \mathbf{m}_q, \mathcal{L} \mathbf{m}_p \rangle = Z^{\text{near}} + j\omega\mu_0 \begin{bmatrix} \hat{\alpha}_i^{q(T)} \Lambda_{i_x}^q G_a \Lambda_{j_x}^{p(T)} \hat{\alpha}_j^p + \hat{\alpha}_i^{q(T)} \Lambda_{i_y}^q G_a \Lambda_{j_y}^{p(T)} \hat{\alpha}_j^p \\ -\frac{1}{k_0^2} \hat{\alpha}_i^{q(T)} \Lambda_{i_d}^q G_q \Lambda_{j_d}^{p(T)} \hat{\alpha}_j^p \end{bmatrix}. \tag{3.22}$$

The translational invariance of  $G_a$  and  $G_q$  enables the use of FFT to accelerate the computation of the product of  $G$  (either  $G_a$  or  $G_q$ ) with the vector grid sources,  $\Lambda_j^{p(T)} \hat{\alpha}_j^p$ . Due to the circular convolution nature of FFT, the number of grid nodes has to be approximately twice the original size,  $(2N-1)$  where  $N$  is the number of nodes in

one direction. For the grid sources, the extended grid nodes are zero padded. For the case of 3 by 3 grid nodes, the extended grid sources,  $[\Lambda_j^{p(T)} \hat{\alpha}_j^p]_e$  in equation (3.25) can be expressed in the following matrix form:

$$[\Lambda_j^{p(T)} \hat{\alpha}_j^p]_e = \begin{bmatrix} 0 & 0 & 0 & 0 & 0 \\ 0 & 0 & 0 & 0 & 0 \\ (\Lambda_j^{p(T)} \hat{\alpha}_j^p)(7) & (\Lambda_j^{p(T)} \hat{\alpha}_j^p)(8) & (\Lambda_j^{p(T)} \hat{\alpha}_j^p)(9) & 0 & 0 \\ (\Lambda_j^{p(T)} \hat{\alpha}_j^p)(4) & (\Lambda_j^{p(T)} \hat{\alpha}_j^p)(5) & (\Lambda_j^{p(T)} \hat{\alpha}_j^p)(6) & 0 & 0 \\ (\Lambda_j^{p(T)} \hat{\alpha}_j^p)(1) & (\Lambda_j^{p(T)} \hat{\alpha}_j^p)(2) & (\Lambda_j^{p(T)} \hat{\alpha}_j^p)(3) & 0 & 0 \end{bmatrix}, \quad (3.23)$$

where  $(\Lambda_j^{p(T)} \hat{\alpha}_j^p)(u)$  corresponds to the grid source associated with the  $u^{\text{th}}$  grid node on the  $p^{\text{th}}$  MBF. If the 1<sup>st</sup> grid node on the root domain is at a distance of  $x$  from the 1<sup>st</sup> grid node on the MBF of interest, the extended  $G_e$  in equation (3.25) is expressed as

$$[G]_e = \begin{bmatrix} G(x+2\Delta x, 2\Delta y) & G(x+\Delta x, 2\Delta y) & G(x, 2\Delta y) & G(x-\Delta x, 2\Delta y) & G(x-2\Delta x, 2\Delta y) \\ G(x+2\Delta x, \Delta y) & G(x+\Delta x, \Delta y) & G(x, \Delta y) & G(x-\Delta x, \Delta y) & G(x-2\Delta x, \Delta y) \\ G(x+2\Delta x, 0) & G(x+\Delta x, 0) & G(x, 0) & G(x-\Delta x, 0) & G(x-2\Delta x, 0) \\ G(x+2\Delta x, \Delta y) & G(x+\Delta x, \Delta y) & G(x, \Delta y) & G(x-\Delta x, \Delta y) & G(x-2\Delta x, \Delta y) \\ G(x+2\Delta x, 2\Delta y) & G(x+\Delta x, 2\Delta y) & G(x, 2\Delta y) & G(x-\Delta x, 2\Delta y) & G(x-2\Delta x, 2\Delta y) \end{bmatrix}, \quad (3.24)$$

where  $\Delta x$  and  $\Delta y$  are the distance between the AIM grid nodes in the  $x$  and  $y$  directions respectively as shown in Fig.3.6 (a). The computed potential,  $\mathfrak{S}^{-1}[\mathfrak{S}[G]_e \cdot \mathfrak{S}[\Lambda_j^{p(T)} \hat{\alpha}_j^p]_e]$ , is then interpolated back to the testing function.

With FFT,  $Z_{np}^{\text{far}}$  in equation (3.21) can be evaluated as

$$Z_{np}^{\text{far}} = j\omega\mu_0 \left[ \Lambda_{n_x} \mathfrak{S}^{-1}[\mathfrak{S}[G_a]_e \cdot \mathfrak{S}[\Lambda_{j_x}^{p(T)} \hat{\alpha}_j^p]_e] + \Lambda_{n_y} \mathfrak{S}^{-1}[\mathfrak{S}[G_a]_e \cdot \mathfrak{S}[\Lambda_{j_y}^{p(T)} \hat{\alpha}_j^p]_e] \right] - \frac{1}{k_0^2} \Lambda_{n_d} \mathfrak{S}^{-1}[\mathfrak{S}[G_q]_e \cdot \mathfrak{S}[\Lambda_{j_d}^{p(T)} \hat{\alpha}_j^p]_e], \quad (3.25)$$

where  $\mathfrak{S}[\bullet]$ ,  $\mathfrak{S}^{-1}[\bullet]$ ,  $[\Lambda_{j_x}^{p(T)} \hat{\alpha}_j^p]_e$ ,  $[G_a]_e$  and  $[G_q]_e$  stand for FFT, inverse FFT,

the extended grid sources, the extended vector Green's function and scalar Green's function.

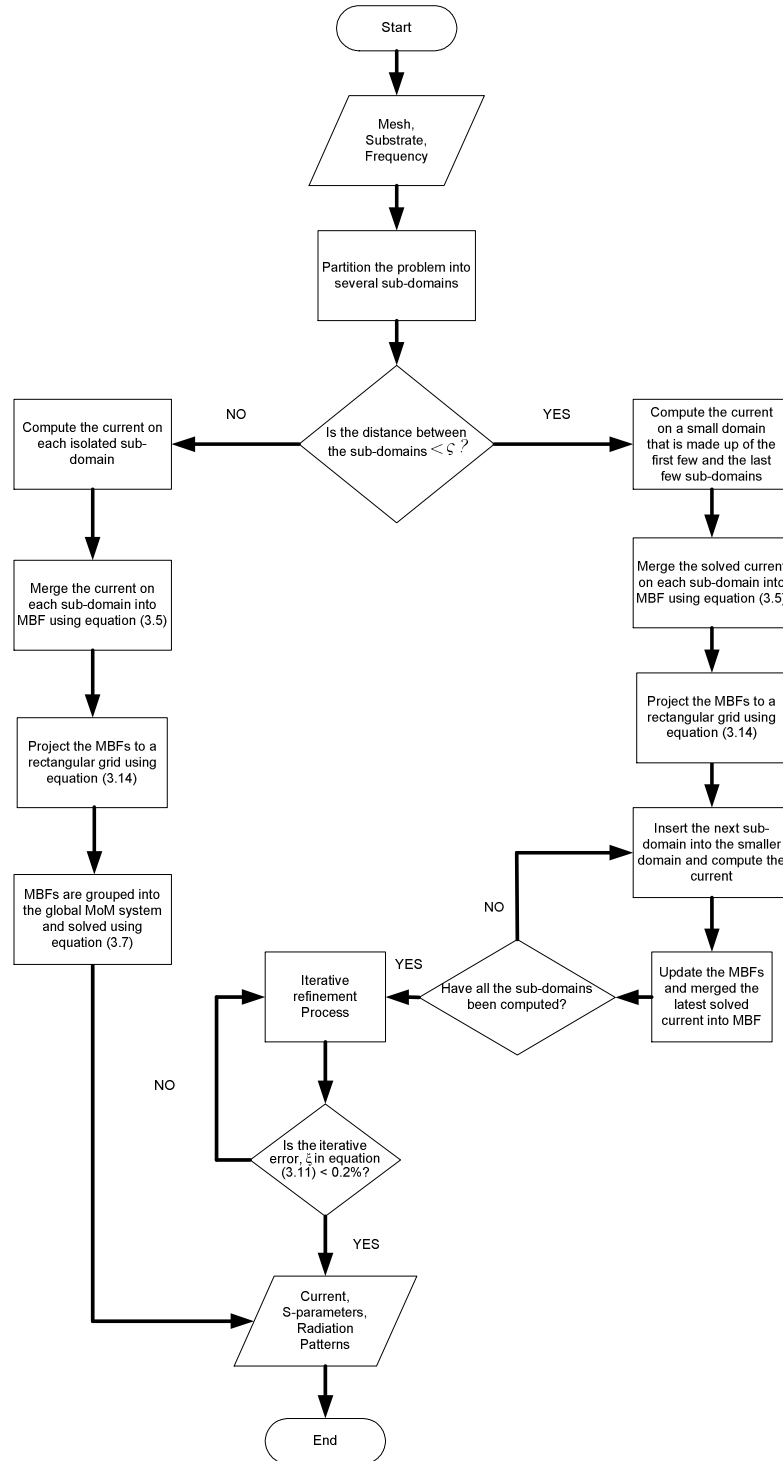


Fig 3.7: Flow chart for analyzing a large problem using the developed algorithm (MBF-PM-AIM).



When the distance between the sub-domains is greater than  $\zeta$ , the macro-basis function will be constructed from the solution of the sub-domain in isolation. The effect of the distance,  $\zeta$  on the shape of the current on the isolated sub-domain and the actual current varies for different structures. Since there is no unique way to determine  $\zeta$  for a given structure, simple numerical experiments can be performed. We can vary the distance between two sub-domains to observe the currents on both the sub-domains and compared with the currents obtained under isolated case. In general, we can take  $\zeta$  to be  $0.5\lambda_0$ . Fig. 3.7 shows the simple flow chart for analyzing a radiation problem using the developed algorithm (MBF-PM-AIM). The methods were coded in MATLAB 6.5 and were performed on a PC with Pentium 4 of 3.2 GHz and 2 GB RAM.

### 3.8 Numerical Applications to Filter and Antenna Arrays

In this section, several examples will be tested to verify the accuracy of the macro-basis function with progressive method and the proposed iterative refinement process. In addition, the computational gain obtained by combining the macro-basis function and the adaptive integral method is described.

In some examples, the relative error of the input impedance and the current of the various methods will be computed with respect to the conventional MoM. As the measure of the relative error  $\Delta_e$  in the computed input impedance,  $Z_{in}$ , we take the

ratio

$$\Delta_e = \frac{\|Z_{in} - Z_{in}^{MoM}\|_2}{\|Z_{in}^{MoM}\|_2}. \quad (3.26)$$

To find the relative error in the current, we just need to replace  $Z$  with  $I$ .

The reduction in time taken for the simulation with respect to the conventional MoM, denoted in here as  $\Delta_t$  will also be studied and is given as

$$\Delta_t = \frac{T^{MoM} - T}{T^{MoM}}, \quad (3.27)$$

where  $T^{MoM}$  is the time taken to compute a problem using conventional MoM.

### 3.8.1 Bandpass Filter

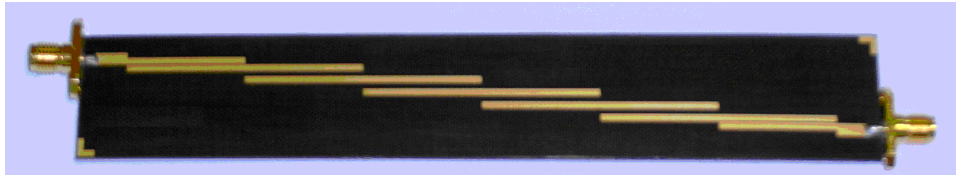


Fig 3.8: Photograph of the fabricated Chebyshev bandpass filter.

Table 3.1: Specifications of the Chebyshev bandpass filter.

Center frequency	2.4 GHz
3 dB bandwidth	240 MHz
Maximum ripple	< 0.1 dB
S21 at center frequency	As high as possible

In order to verify the accuracy of the macro-basis function with progressive method

and show that the proposed iterative refinement process converges to the correct solution, we first consider a Chebyshev bandpass filter where the smallest gap between the coupled lines is 10 mil. The specifications of the microstrip Chebyshev Bandpass filter are given in Table 3.1:

The photograph of the fabricated Chebyshev bandpass filter is shown in Fig 3.8. The dimensions of the filter are given in Fig.3.9. The substrate has permittivity  $\epsilon_r=2.31$  with a loss tangent of 0.001 and a thickness of 31.5 mil. Rooftop basis function is used to discretize the bandpass filter with 850 unknowns. For 2 port circuit problems, 2 linearly independent excitations are required for 2 port network if the filters are analyzed with open load simulation. However if matched load termination is adopted, only one port needs to be excited. Thus the time taken to solve the problem is reduced.

The dash lines in Fig.3.9 (a) show one possible way of dividing the filter into seven elements. For the bandpass filter, the strongest coupling is between the coupled lines. In order to verify that the macro-basis function with progressive method can calculate the coupling accurately, the elements are purposely chosen to separate the strongest coupling. A small domain consists of  $S_1$ ,  $S_6$  and  $S_7$  is depicted in Fig.3.9 (b). The interactions among the sub-domains are first computed and stored in a matrix which is then used repeatedly during the computation process.

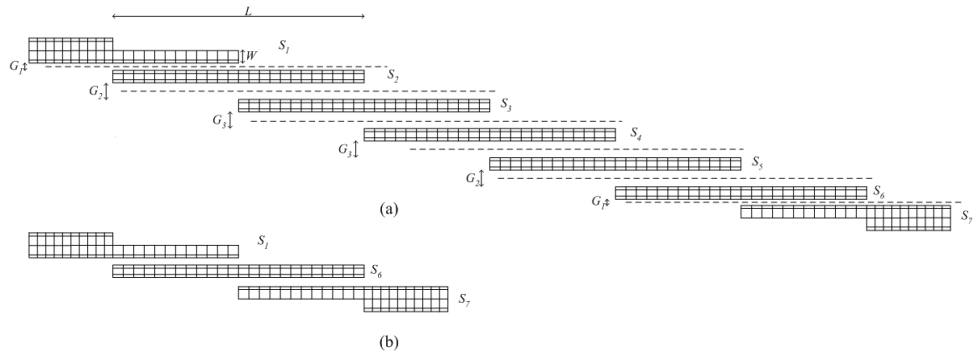
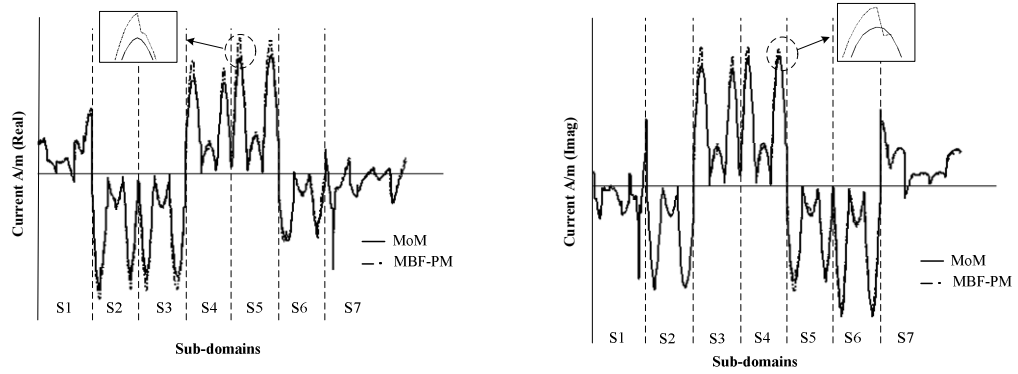
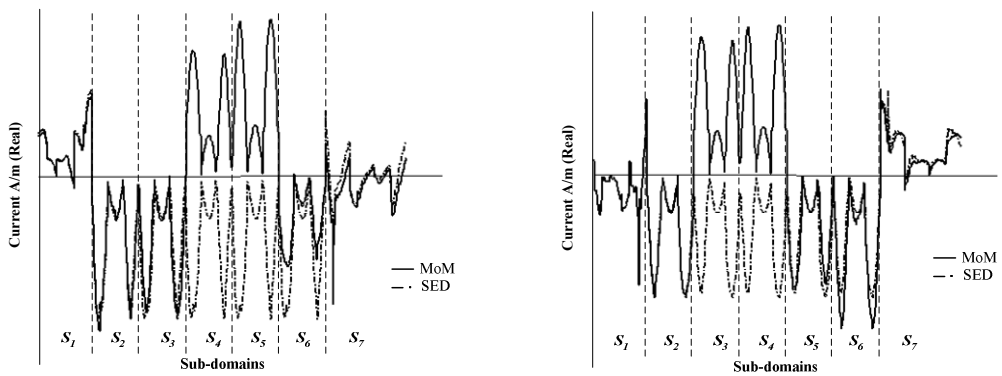


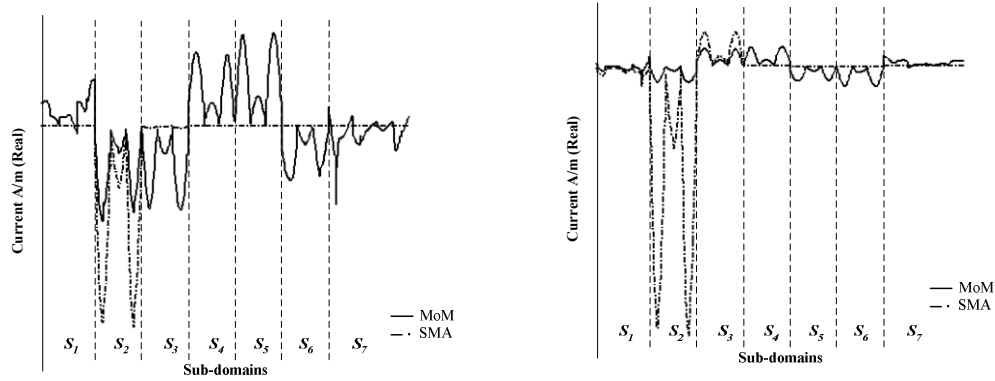
Fig.3.9: Chebyshev Bandpass Filter. (a) Layout of the bandpass filter. (b) Small domain of the bandpass filter.  $L=22.45$ ,  $W=1.27$ ,  $G_1=0.254$ ,  $G_2=1.17$  and  $G_3=1.32$ . All dimensions are given in mm.



(a) Initial current on the sub-domains computed from MBF-PM.



(b) Initial current on the sub-domains computed from SED.



(c) Initial current on the sub-domains computed from SMA.

Fig.3.10: Comparison of the initial current on the bandpass filter under various methods: macro-basis function with progressive method (MBF-PM), sub-domain multilevel approach (SMA), sub-entire-domain (SED) and conventional MoM.

Fig.3.10 (a) compares the initial currents computed from the macro-basis function with progressive method (MBF-PM) and the conventional MoM at 2.4 GHz. It is observed that the shape of the initial currents on the sub-domains resembles the correct current (computed from the conventional MoM) except at the sharp variations as depicted in the inset of Fig.3.10 (a) which can be corrected in the iterative refinement process. As the initial currents are already very close to the correct current with a relative error of 10.1%, less iterative sweeps are expected to yield the needed accuracy. For SED method, the current on  $S_6$  (computed from the small domain in Fig.3.9 (b)) will be used for  $S_2$  to  $S_5$  as depicted in Fig.3.10 (b). In SMA method, the initial current on the isolated sub-domain  $S_1$  is first computed and the current on the rest of the sub-domains are generated from this solved current. The initial current obtained from SMA method is shown in Fig.3.10 (c). It is noted in Fig.3.10 that among the three methods, MBF-PM gives the best accuracy for the initial current

which is attributed to the new grouping concept of near-far neighbour evaluation.

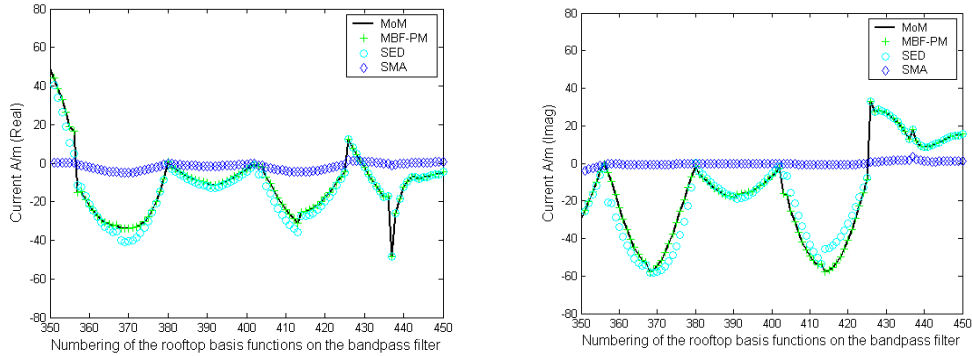
Table 3.2: Comparison of the relative errors in the current distribution, time reduction with respect to the conventional MoM without any iterative sweep.

	MBF-PM	SED [55]	SMA [50]
$\Delta_c = \frac{\ I - I^{\text{MoM}}\ _2}{\ I^{\text{MoM}}\ _2}$	6.4%	12.8%	22.9%
$\Delta_t = \frac{T^{\text{MoM}} - T}{T^{\text{MoM}}}$	56.2%	56.4%	56.9%

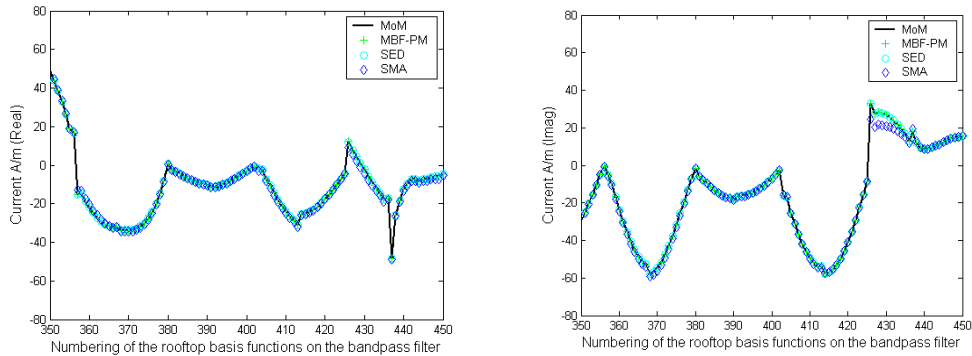
Table 3.2 summarizes the relative errors in the currents,  $\Delta_c$  and the time reduction  $\Delta_t$  computed from MBF-PM, SED and SMA without iterative refinement process. Even though MBF-PM has the slowest computational time, it gives the best accuracy with a relative error of 6.4%. For SED and SMA, the relative errors are larger than 10%. Thus, iterative refinement process is required to improve the accuracy.

Iterative process A and iterative process B discussed in Section 3.7 are investigated in this example. In order to demonstrate the effectiveness of the iterative processes, they are applied directly to the initial current (refer to Fig.3.10). Fig.3.11 shows the current coefficients with respect to the numbering of the basis functions on the bandpass filter after one iterative sweep using iterative process A and iterative process B. For the proposed iterative process B, the curves computed from MBF-PM, SED and SMA converge to the correct current (conventional MoM) after one iterative sweep. However, for iterative process A, the deviation between SMA and the correct current is approximately 99%. The accuracy of the proposed iterative process B is better than

iterative process A.



(a) Iterative Process A



(b) Iterative Process B

Fig.3.11: Comparison of the current coefficients among the macro-basis function with progressive method (MBF-PM), the sub-entire-domain basis function method (SED), the sub-domain multilevel approach (SMA) and the conventional MoM with respect to the numbering of the rooftop basis function on the bandpass filter after 1 iterative sweep.

The performances of the two iterative processes are further studied on MBF-PM and SMA. Fig.3.12 shows how the iterative error in (3.11) diminishes with increasing number of iterative sweeps for iterative process A and iterative proces B on MBF-PM and SMA. Iterative process A seems to work better when the initial current is closer to

the actual value. For a 1 by 5 linear series-fed array investigated in Section 3.8.2, we find that iterative process A does not converge even after 30 iterative sweeps.

Fig.3.13 shows the accuracy of the current during iterative process A and iterative process B. Generally MBF-PM only requires one iterative sweep from iterative process B to give a relative error of about 0.1%. Table 3.3 summarizes the performance of iterative process A and iterative process B. Since more iterative sweeps are required for iterative process A, its computational time will be slower than iterative process B. Hence, iterative process B is chosen to perform the iterative refinement process.

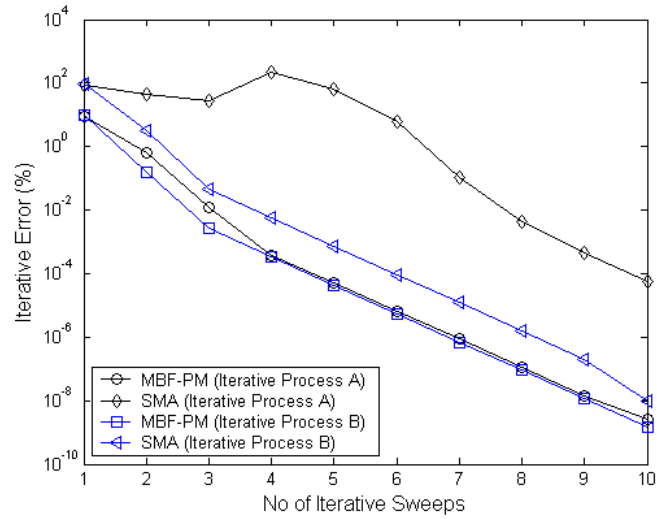


Fig.3.12: Convergence of the solution with respect to the number of iterative sweeps.



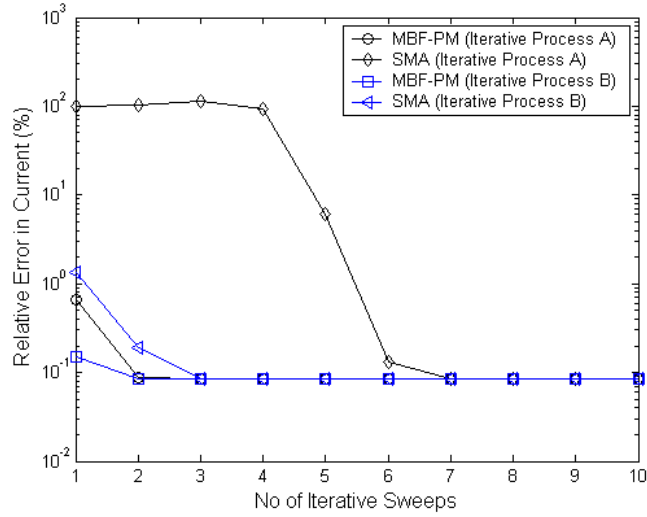


Fig.3.13: Relative error of the current with respect to the number of iterative sweeps.

Table 3.3: Comparison of the time reduction with respect to conventional MoM and number of iterative sweeps subject to  $\xi < 0.2\%$  and the relative error in current,  $\Delta_e$  is 0.09%

	Iterative Process A		Iterative Process B (Proposed)	
	MBF-PM	SMA [50]	MBF-PM	SMA [50]
No. of iterative sweep subject to $\xi < 0.2\%$	3	7	2	3
$\Delta_t = \frac{T^{\text{MoM}} - T}{T^{\text{MoM}}}$	53.4%	50.4%	54.4%	54.1%

Figs 3.14 and 3.15 show the condition number and the spectral radius of the matrix stages respectively. The definition of the matrix stages are depicted in Table 3.4. When no iterative refinement process is carried out, the condition number for SMA is approximately  $1e8$  with spectral radius of 0.37 while the condition number for MBF-PM is around  $1e5$  with spectral radius of 0.029. At the start of each iterative sweep, large condition number of approximately  $3.69e7$  and spectral radius of 1 are

observed for both SMA and MBF-PM. This is because matched load termination (refer to equation (2.75)) is employed to analyze the bandpass filter. For SMA, the initial current on  $S_3$  to  $S_5$  (refer to Fig.3.10 (c)) is closed to zero. Thus, it does not have significant effect on the matrix. As a result, the condition number for matrix stages 3 and 4 are small. It is observed that the condition number and the spectral radius of MBF-PM converge after one iterative sweep as indicated by the repetition of the curve in iterative sweeps 2 and 3. Thus, one can conclude that MBF-PM gives a better convergence.

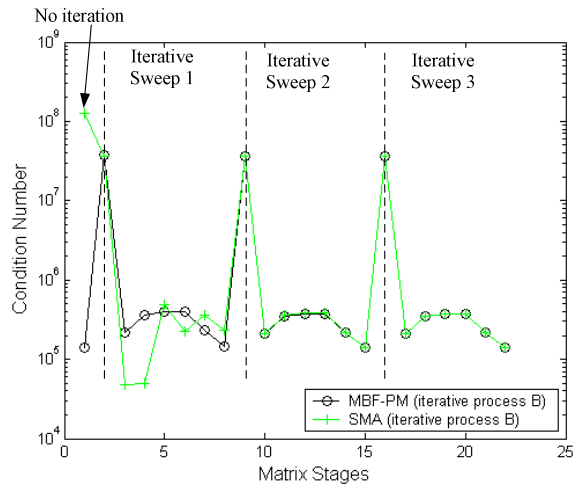


Fig.3.14: Condition number of the bandpass filter versus the matrix stages.

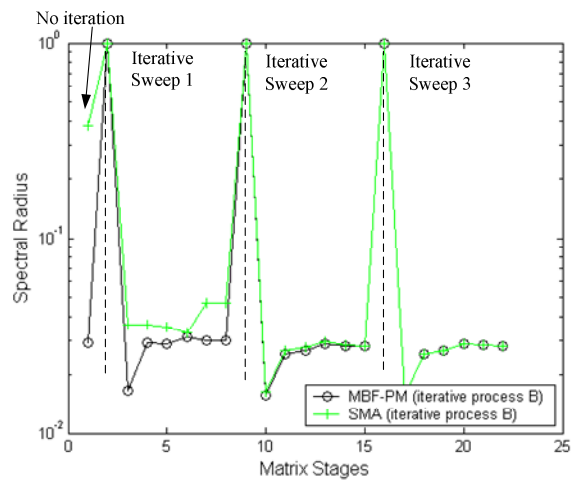


Fig.3.15: Spectral radius of the bandpass filter versus the matrix stages.

Table 3.4: Definition of the matrix stages.


Matrix Stages				Matrixes	Diagrams
	Iterative Process B (Refer to Fig for the procedure)				
No Iteration	Iterative sweep 1	Iterative sweep 2	Iterative sweep 3		
1	9	17	25	$\begin{bmatrix} Z_{11} & Z_1M_2 & Z_1M_3 & Z_1M_4 & Z_1M_5 & Z_1M_6 & Z_1M_7 \\ M_2Z_1 & M_{22} & M_{23} & M_{24} & M_{25} & M_{26} & M_{27} \\ M_3Z_1 & M_{32} & M_{33} & M_{34} & M_{35} & M_{36} & M_{37} \\ M_4Z_1 & M_{42} & M_{43} & M_{44} & M_{45} & M_{46} & M_{47} \\ M_5Z_1 & M_{52} & M_{53} & M_{54} & M_{55} & M_{56} & M_{57} \\ M_6Z_1 & M_{62} & M_{63} & M_{64} & M_{65} & M_{66} & M_{67} \\ M_7Z_1 & M_{72} & M_{73} & M_{74} & M_{75} & M_{76} & M_{77} \end{bmatrix}$	
	2	10	18	$[Z_{77}]$	
	3	11	19	$\begin{bmatrix} Z_{66} & Z_6M_7 \\ M_7Z_6 & M_{77} \end{bmatrix}$	
	4	12	20	$\begin{bmatrix} Z_{55} & Z_5M_6 & Z_5M_7 \\ M_6Z_5 & M_{66} & M_{67} \\ M_7Z_5 & M_{76} & M_{77} \end{bmatrix}$	
	5	13	21	$\begin{bmatrix} Z_{44} & Z_4M_5 & Z_4M_6 & Z_4M_7 \\ M_5Z_4 & M_{55} & M_{56} & M_{57} \\ M_6Z_4 & M_{65} & M_{66} & M_{67} \\ M_7Z_4 & M_{75} & M_{76} & M_{77} \end{bmatrix}$	

	6	14	22	$\begin{bmatrix} Z_{33} & Z_3M_4 & Z_3M_5 & Z_3M_6 & Z_3M_7 \\ M_4Z_3 & M_{44} & M_{45} & M_{46} & M_{47} \\ M_5Z_3 & M_{54} & M_{55} & M_{56} & M_{57} \\ M_6Z_3 & M_{64} & M_{65} & M_{66} & M_{67} \\ M_7Z_3 & M_{74} & M_{75} & M_{76} & M_{77} \end{bmatrix}$	
	7	15	23	$\begin{bmatrix} Z_{22} & Z_2M_3 & Z_2M_4 & Z_2M_5 & Z_2M_6 & Z_2M_7 \\ M_3Z_2 & M_{33} & M_{34} & M_{35} & M_{36} & M_{37} \\ M_4Z_2 & M_{43} & M_{44} & M_{45} & M_{46} & M_{47} \\ M_5Z_2 & M_{53} & M_{54} & M_{55} & M_{56} & M_{57} \\ M_6Z_2 & M_{63} & M_{64} & M_{65} & M_{66} & M_{67} \\ M_7Z_2 & M_{73} & M_{74} & M_{75} & M_{76} & M_{77} \end{bmatrix}$	

$Z_{ij}$  refers to the sub-matrix that is associated with the subsectional basis functions on sub-domains  $S_i$  and  $S_j$ .

$Z_iM_j$  refers to the sub-matrix that is associated with the subsectional basis functions on sub-domain  $S_i$  and the macro-basis function on sub-domain  $S_j$

$M_{ij}$  refers to the sub-matrix that is associated with macro-basis function on sub-domain  $S_i$  and the macro-basis function on sub-domain  $S_j$

 Shaded sub-domain indicates that the current on the sub-domain is merged into MBF.

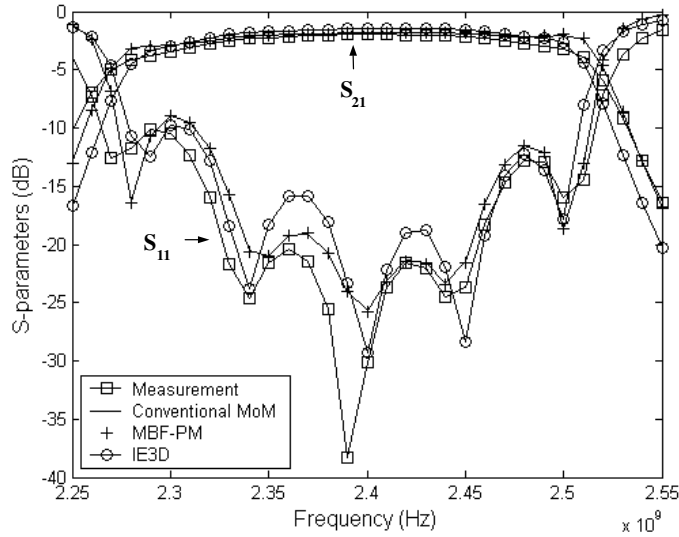


Fig.3.16: Reflection coefficients of the bandpass filter.

The structure has been analyzed using the commercial software, IE3D [62], the conventional MoM and MBF-PM. The S-parameters obtained are shown in Fig.3.16. The results computed from the conventional MoM agree very well with those computed from MBF-PM. The slight discrepancy between the results obtained from MBF-PM and the measured results is mainly attributed to the number of quadrature points used in the evaluation of the MoM matrix. Overall, the trend of the results is in good agreement with the measured results. A summary table comparing the specifications and the measurements of the bandpass filter is given below in Table 3.5.

Table 3.5: Comparison between the specifications and the measurements of the bandpass filter.

	Unit	Specifications	Measurements
BW %	%	10	10
Center Freq	GHz	2.4	2.4
S21 at 2.4 GHz	dB	As high	-1.96
Ripple	dB	<0.1dB	0.005

### 3.8.2 Linear Series-fed Array

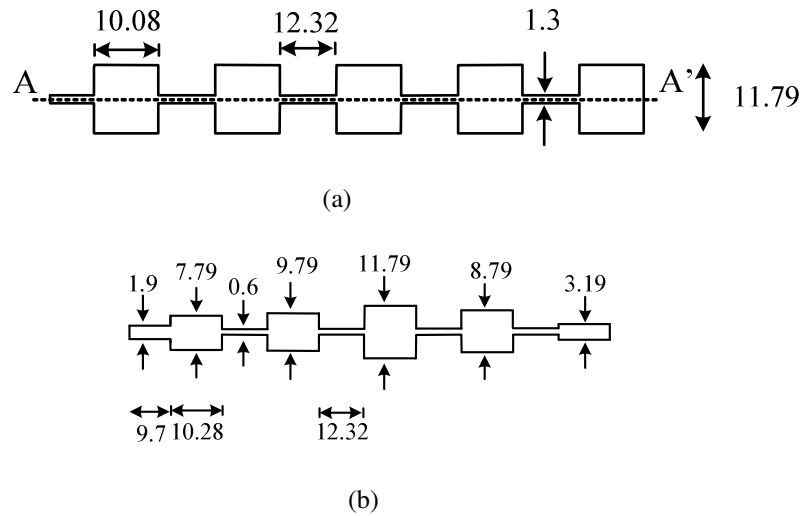


Fig.3.17: 1 X 5 linear series-fed antenna arrays. (a) 1 X 5 linear series-fed antenna array with no tapering (Array A). (b) 1 X 5 linear series-fed antenna array with tapering (Array B). All dimensions are in mm.

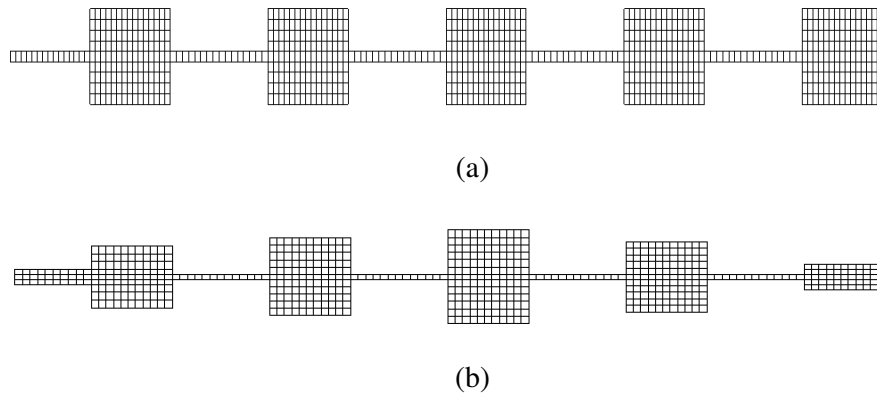


Fig.3.18: Mesh of the 1 X 5 linear series-fed antenna arrays. (a) 1 X 5 linear series-fed antenna array with no tapering (Array A). (b) 1 X 5 linear series-fed antenna array with tapering (Array B).

We will next investigate a 1 by 5 linear series-fed array with uniform excitation (Array A) and a 1 by 5 linear series-fed array with non-uniform excitation (Array B) as shown in Fig.3.17 (a) and (b) respectively. The arrays are implemented on substrate with permittivity  $\epsilon_r=2.2$  and a thickness of 1.59 mm. The arrays are densely meshed as depicted in Fig.3.18. The number of unknowns for Arrays A and B are 1334 and

1025 respectively. The design of the linear series-fed array is discussed in Section 3.8.4. The specifications of the arrays are in Table 3.6.

Table 3.6: Specifications of the series-fed array.

Center frequency	9.25 GHz (Radiolocation System)
Impedance Bandwidth for VSWR < 2	5%
Gain at the center frequency	13 dBi
Side-lobes	< -13 dB
3 dB Beamwidth	< 20°

In this example, we integrate the adaptive integral method described in Section 3.8 into the macro-basis function with progressive method. The new hybrid method is called the macro-basis function with progressive and adaptive integral method (MBF-PM-AIM). The AIM grid spacing is  $\lambda/10$ .

The first step in employing segmentation methods is to partition a problem into several sub-domains. The macro-basis function with progressive and adaptive integral method is carried out for 7 different cut positions along the feed line at a distance,  $d$ , from the discontinuity edge, where  $d = 0.16 \lambda, 0.18 \lambda, 0.21 \lambda, 0.24 \lambda, 0.26 \lambda, 0.29 \lambda$  and  $0.32 \lambda$  as shown in Fig.3.19. In Fig.3.20, the relative errors of the current at different cut positions are shown. The current is computed from MBF-PM-AIM with one iterative sweep. The minimum error of 1.5% occurs at  $0.21\lambda$ . The error increases as the cut position approaches the discontinuity edges. Thus, one should avoid cutting the problem near discontinuity junction.

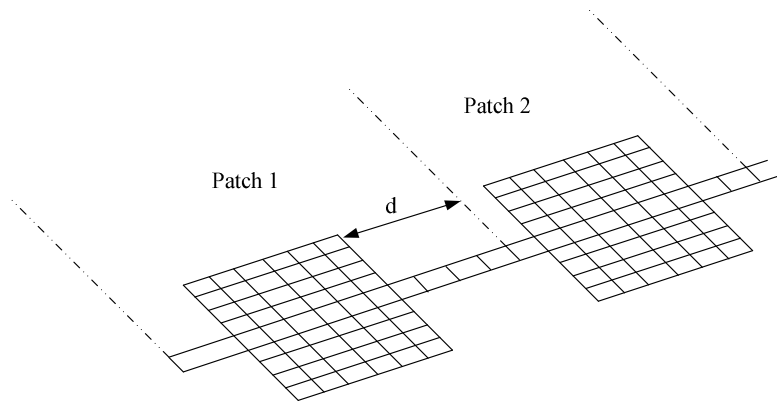


Fig.3.19: Cut Position,  $d$  from the discontinuity edge.

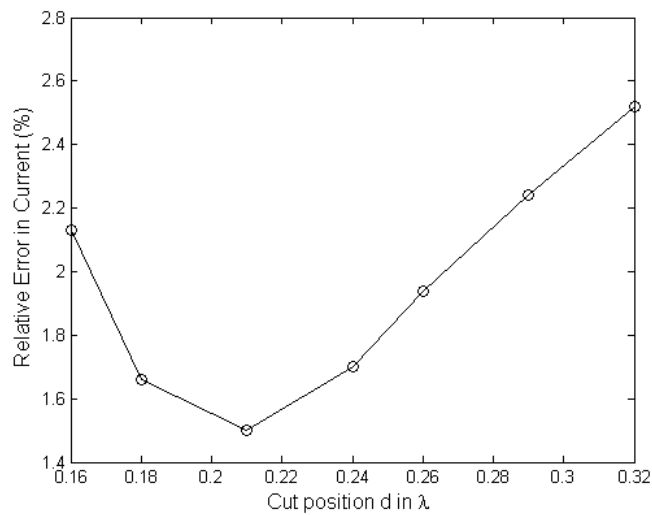


Fig.3.20: Relative error of the current as a function of the cut position  $d$  for a 1 by 5 antenna array.

When implementing MBF-PM-AIM, one has to consider how many sub-domains to use for the construction of the small domain. Two small domains, A and B, for Array A are studied. Small domain A consists of Patches 1 and 2 while small domain B is made up of Patches 1, 4 and 5. The rest of the sub-domains are then inserted into the small domain progressively as described in Section 3.5. Table 3.7 shows the comparison of the relative errors and the CPU time for the two small domains when implemented in MBF-PM-AIM. Even though small domain B gives a better accuracy



than small domain A, its computation time is faster than small domain A by 7.2 seconds. After one iterative sweep, the deviation in the relative error between small domains, A and B is only 0.08%. Hence, it is more efficient to carry out MBF-PM-AIM with small domain A.

Table 3.7: Comparison of the relative error and the CPU time between small domains A and B when applied to MBF-PM-AIM.

	MBF-PM-AIM	
	Small Domain A (Patches 1, 5)	Small Domain B (Patches 1, 4, 5)
Array A (without iterative refinement process)		
$\Delta_e = \frac{\ \mathbf{I} - \mathbf{I}^{\text{MoM}}\ _2}{\ \mathbf{I}^{\text{MoM}}\ _2}$	12.81%	10.1%
CPU Time	109.1 sec	116.3 sec
Array A (with 1 iterative sweep)		
$\Delta_e = \frac{\ \mathbf{I} - \mathbf{I}^{\text{MoM}}\ _2}{\ \mathbf{I}^{\text{MoM}}\ _2}$	1.5%	1.42%
CPU Time	114.6 sec	121.8 sec

Table 3.8: Comparison of the relative error in the current under various methods without iterative refinement process.

Arrays	Relative error, $\Delta_e = \frac{\ \mathbf{I} - \mathbf{I}^{\text{MoM}}\ _2}{\ \mathbf{I}^{\text{MoM}}\ _2}$			
	MBF-PM	MBF-PM-AIM	SED [55]	SMA [50]
Linear Series-fed array with uniform excitation				
1314 (1 X 5)	11.9%	12.8%	28.1%	71.2%
3737 (1 X 14)	17.6%	18.4%	40.1%	80%
Linear Series-fed array with non-uniform excitation				
1080 (1 X 5)	14.69%	15.4%	-	71.1%

(\* For linear series-fed array with non-uniform excitation, SED method is not applicable.)

Tables 3.8 shows the relative error among MBF-PM, MBF-PM-AIM, SED and SMA respectively. There is a tremendous improvement in the accuracy of MBF-PM as compared to SED and SMA. By inspecting the tables, we observe that SMA has the largest relative errors of 71.2% and 80% for a 1 by 5 antenna array with uniform excitation and a 1 by 14 antenna array with uniform excitation respectively. MBF-PM gives a slightly better accuracy than MBF-PM-AIM by approximately 1%. Even though the proposed methods give better accuracy, the relative errors are still larger than 10%.

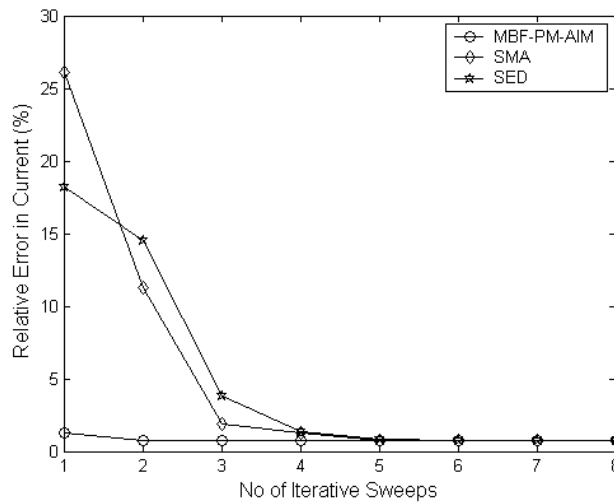


Fig.3.21: Relative error of the current versus the number of iterative sweeps.

In order to improve the accuracy, iterative refinement process is required. Fig.3.21 shows the relative error of the current during the iterative process for a 1 by 14 antenna array. It is observed that MBF-PM-AIM requires only one iterative sweep to give a relative error of the current less than 1.4% while SMA and SED require at least 4 iterative sweeps to give the same error.

Table 3.9 summarizes the performance of MBF-PM-AIM, SED and SMA with

iterative process B. We observe that MBF-PM-AIM has the fastest computational time as compared to the other two methods. For a 1 by 14 antenna array with uniform excitation, MBF-PM-AIM has an improvement of around 56% in the computational time as compared to SMA. For a 1 by 5 antenna array with non-uniform excitation, the computational time for MBF-PM-AIM is faster than SMA by 29.3%. It is expected that as more non-identical patches are added to the array, the time saved for MBF-PM-AIM will be greater. MBF-PM-AIM has demonstrated a less memory usage as compared to the other two reported method. Thus, we can conclude that MBF-PM-AIM is a very competitive approach to solve large and non-identical structure and its gain in computational time increases with the number of unknowns.

Table 3.9: Comparison of the reduction in time and memory usage under various methods with iterative refinement process subject to  $\Delta_e \leq 1.5\%$ .

Arrays	Time reduction, $\Delta_t = \frac{T^{\text{MoM}} - T}{T^{\text{MoM}}}$ subject to $\Delta_e \leq 1.5\%$		
	MBF-PM-AIM	SED [55]	SMA [50]
Linear Series-fed array with uniform excitation			
1314 (1 X 5)	57.3%	51.4%	51.5%
No of iterative sweeps	1	2	2
Memory (MB)	66	71	71
CPU Time	114.6 sec	130.4 sec	130.2 sec
3737 (1 X 14)	90.7%	78.8%	78.9%
No of iterative sweeps	1	4	4
Memory (MB)	66	92	92
CPU Time	137.3 sec	313 sec	311.5 sec
Linear Series-fed array with non-uniform excitation			
1025 (1 X 5)	30.3%	-	1.2%
No of iterative sweeps	1	-	2
Memory (MB)	67	-	72
CPU Time	92.7 sec	-	131.2 sec

(\* For linear series-fed array with non-uniform excitation, SED method is not applicable.)

Table 3.10: Comparison of the CPU time, the number of MBFs generated and the relative errors between MBF-PM, MBF-PM-AIM and characteristics basis function (CBF).

1 X 14 Array (3737 unknowns)			
	MBF-PM	MBF-PM-AIM	CBF [96]
CPU Time			
Block matrices	287.5 sec	N. A	287.5 sec
Generation of MBFs and solving the reduced matrix	12.18 sec	137.3 sec	65.03 sec
Total Time	299.68 sec	137.3 sec	352.56 sec
Number of MBFs generated	13	13	169
$\Delta_e = \frac{\ I - I^{MoM}\ _2}{\ I^{MoM}\ _2}$	1.1%	1.18%	2%

(\* For MBF-PM-AIM, one does not need to generate the block matrices.)

Table 3.10 shows the comparison of the results computed from MBF-PM, MBF-PM-AIM and the characteristic basis function (CBF) [98] for a 1 by 14 antenna array. The antenna is partitioned into 14 sub-domains. In the characteristic basis function, the primary CBF, the second-order and third-order coupling (secondary CBFs) are generated which lead to 169 CBFs while MBF-PM only generates 13 MBFs. The computational time involved in the methods are examined. For MBF-PM and CBF, there are two main stages in the methods, namely, the interaction of the sub-domains and the generation and solving of the reduced matrix. The CPU times for these stages are presented in the table. It is observed that the total CPU time for MBF-PM is 52.88 seconds faster than CBF. For MBF-PM-AIM, the total CPU time is approximately 40% faster than CBF.

Fig.3.22 gives the comparison of the CPU time using MBF-PM-AIM, MBF-PM and the conventional MoM. We note that the CPU time for MBF-PM-AIM becomes more efficient as the number of unknowns increases. Their memory requirements are

illustrated in Fig.3.23. For 3737 unknowns, MBF-PM-AIM has demonstrated 71.3% less memory usage as compared to conventional MoM.

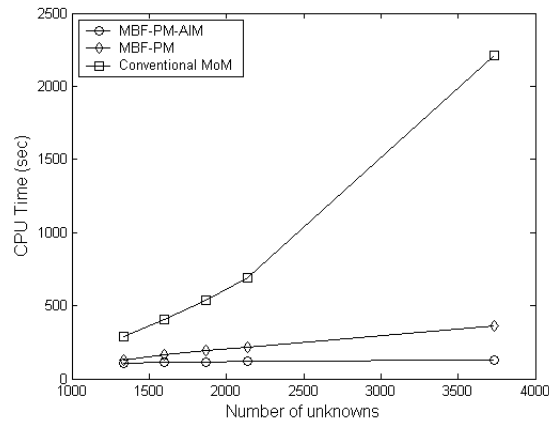


Fig.3.22: Comparison of CPU time among MBF-PM-AIM, MBF-PM and the conventional MoM.

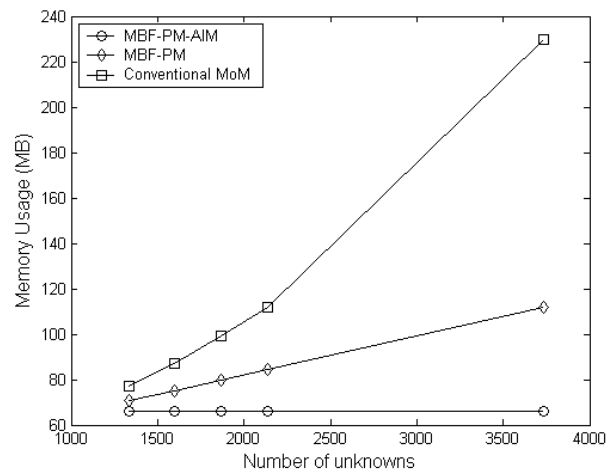


Fig.3.23: Comparison of Memory Usage among MBF-PM-AIM, MBF-PM and the conventional MoM.

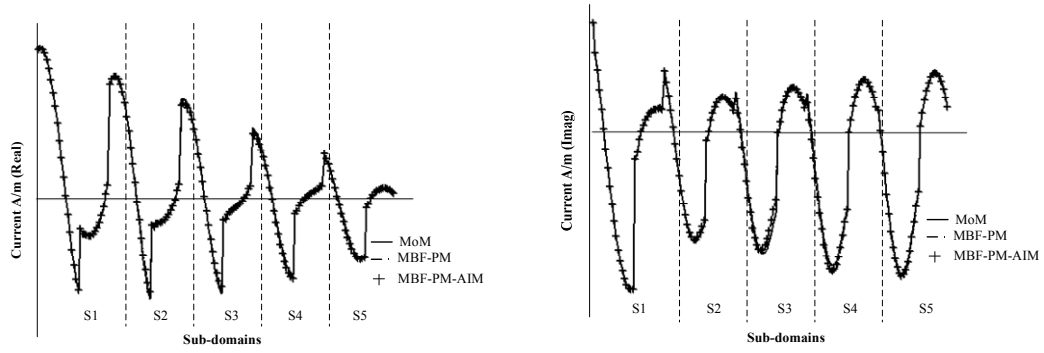


Fig.3.24: Comparison of the current along the line AA' for Array A among MBF-PM-AIM, MBF-PM and the conventional MoM with the proposed iterative refinement process after 1 iterative sweep.

Fig.3.24 compares the computed current obtained from MBF-PM-AIM and the conventional MoM for Array A at 9.25 GHz. The current shown is along the center of the Array A, AA' (refer to Fig.3.17 (a)). After one iterative sweep, the three curves practically give the same result as shown in Fig.3.24.

Table 3.11: Comparison of the relative error of the input impedance between MBF-PM and MBF-PM-AIM.

Series-fed array (N)	Relative error, $\Delta_e = \frac{\ Z_{input} - Z_{input}^{MoM}\ _2}{\ Z_{input}^{MoM}\ _2} \times 100$	
	MBF-PM	MBF-PM-AIM
1334 (1 X 5)	0.66%	0.84%
1620 (1 X 6)	0.39%	0.86%
1868 (1 X 7)	0.46%	0.64%
2135 (1 X 8)	0.56%	0.83%
3737 (1 by 14)	0.72%	0.87%

Table 3.11 shows a comparison of the relative error of the input impedance between

MBF-PM and MBF-PM-AIM. MBF-PM-AIM yields satisfactory results with relative errors below 0.9%.

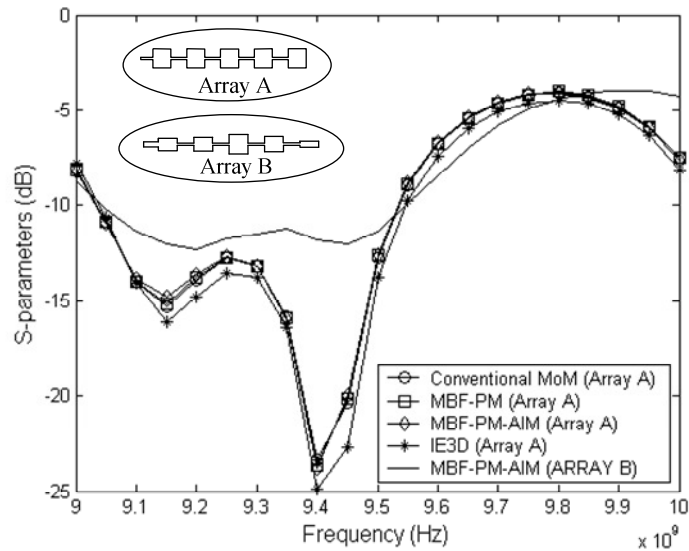
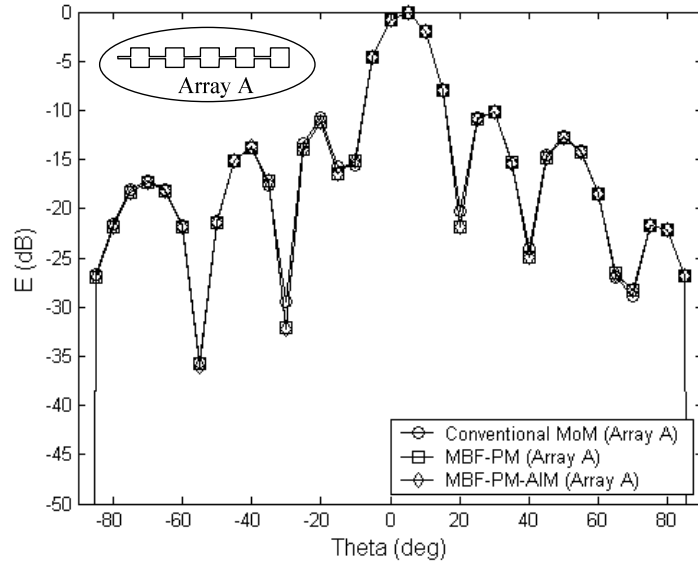


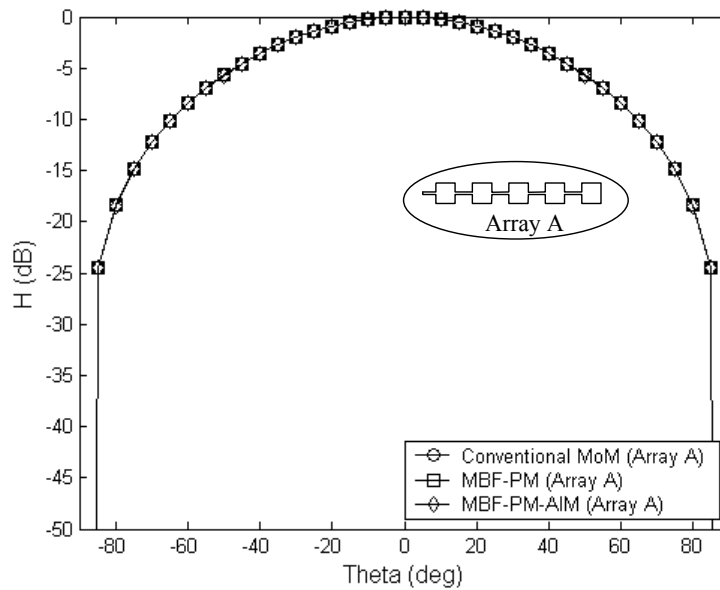
Fig.3.25: Reflection coefficients of Array A and Array B.

Fig.3.25 depicts the return loss of Array A using the conventional MoM, MBF-PM, MBF-PM-AIM and IE3D. The result obtained under MBF-PM is practically the same as in the case of the result obtained under the conventional MoM. The return loss of Array B computed with MBF-PM-AIM is also depicted in the figure. Both arrays have an impedance bandwidth of approximately 5.4%. Fig.3.26 (a) and (b) show the computed radiation patterns in the E-plane and H-plane of Array A respectively. Fig.3.27 (a) and (b) show the computed radiation patterns in the E-plane and H-plane of Array B respectively. From Fig.3.26, it is observed that the results obtained from MBF-PM-AIM are in good agreement with the results computed from the conventional MoM. The slight discrepancy between the results obtained from MBF-PM-AIM and those from the commercial software, IE3D is mainly attributed to the number of quadrature points used in the evaluation of the MoM matrix. Array A has a 3 dB beamwidth of  $13^{\circ}$  in the E-plane, a side-lobe level of -10 dB and a

broadside gain of 14 dBi at 9.25 GHz. Array B has a 3 dB beamwidth of  $18.3^\circ$  in the E-plane with a side-lobe level of -15 dB and a broadside gain of 13.6 dBi at 9.25 GHz. Compared to Array A, the lowering of the side-lobe levels and the broadening of the beamwidth for Array B are attributed to the tapering of the amplitude distribution of the antenna elements.



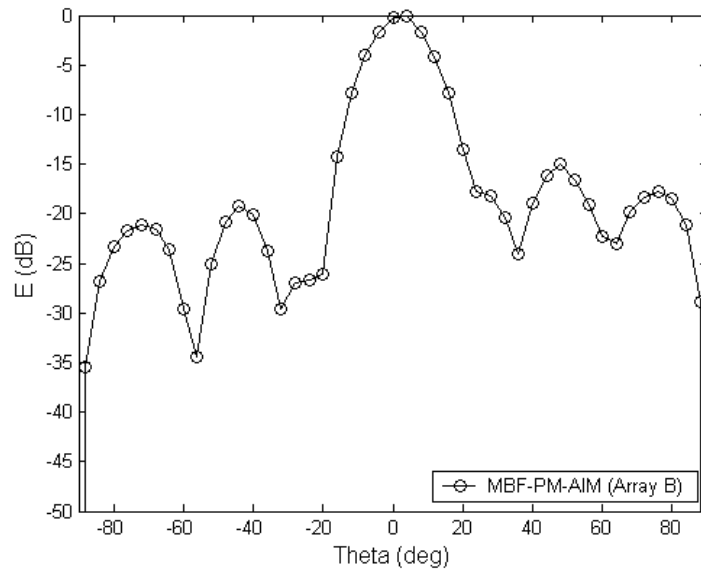
(a)



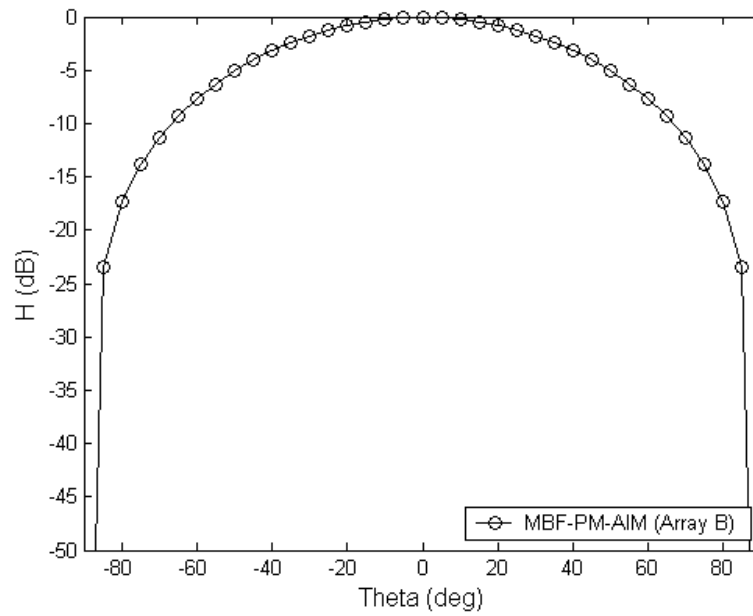
(b)

Fig.3.26: Radiation Patterns of Array A. (a) E-plane (b) H-plane





(a)



(b)

Fig.3.27: Radiation Patterns of Array B. (a) E-plane (b) H-plane

### 3.8.3 Bowtie Dipole Array

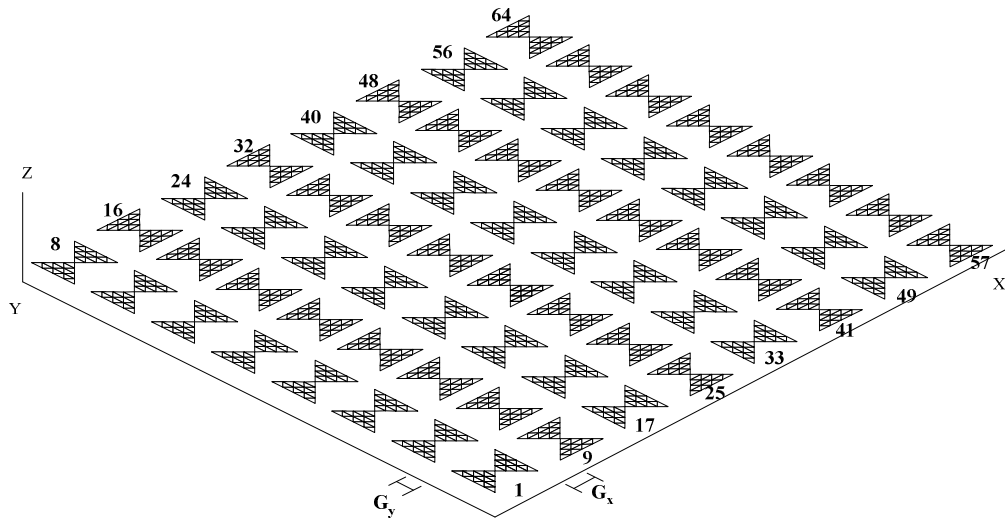


Fig.3.28: Bowtie dipole array

We next consider an 8 by 8 dual polarized bowtie dipole array as shown in Fig.3.28 with the spacing of  $G_x=0.075 \lambda$  and  $G_y=0.075 \lambda$ , where the coupling among all the elements are strong. The specifications of the array are given in Table 3.12.

Table 3.12: Specifications of the bowtie dipole array.

Center frequency	150 MHz
Gain at the center frequency	13 dBi
Side-lobes	< -13 dB
3 dB Beamwidth	< $25^0$

The size of the bowtie array element is 0.45 X 0.5 m with flare angle at  $90^0$ . Each bowtie is discretized into 30 sub-triangles with the help of RWG basis function leading to 2240 unknowns. There are 35 unknowns for each bowtie. The bowtie is center-fed, with a feeding edge located exactly in the middle junction. The elements

are numbered from one corner of the array to the opposite corner, first along y then along x.

An 8 by 4 array problem is first carried out directly using the conventional MoM. The rest of the elements are then inserted into the problems. The solved currents on each element are then merged into MBFs. In the patterns shown below, uniform excitation is considered. The results are compared with those from the conventional MoM.

Fig.3.29 shows the comparison of the current coefficients computed using the conventional MoM, the macro-basis function with progressive method (MBF-PM), the sub-entire-domain (SED) basis function method and the sub-domain multilayer approach (SMA) at 150 MHz with respect to the basis function on elements 28 and 37. In this example, a small domain made up of a 4 by 4 antenna array is used for SED. The current on the internal elements of the small domain is then used to represent the current on the interior elements of the array while the current on the edge and corner are used as the corresponding edge and corner of the array. By inspecting the current on elements 28 and 37, it is observed that MBF-PM is able to capture the trend of the current more accurately than SED and SMA. Table 3.13 compares the relative errors in the current and the time reduction with respect to the conventional MoM computed using the three methods without any iterative refinement techniques. In this example, only the interactions between the first sub-domain and other sub-domains need computing. The interactions are then stored in a matrix and used repeatedly to express the interactions among other blocks. The time for generating the MBFs is reduced dynamically. Although MBF-PM has the slowest computation time, it has the smallest relative error (13.72%). SED has the largest relative error of 35.24%. Thus, for brevity,

we will only study the radiation patterns computed from MBF-PM and SMA as they give lower relative errors in current.

Table 3.13: Comparison of the relative errors in current and time reduction with respect to the conventional MoM for the bowtie array without iterative refinement process.

	MBF-PM	SED [55]	SMA [50]
$\Delta_c = \frac{\ I - I^{\text{MoM}}\ _2}{\ I^{\text{MoM}}\ _2}$	13.72%	35.24%	24.83%
$\Delta_t = \frac{T^{\text{MoM}} - T}{T^{\text{MoM}}}$	94.3%	95.4%	97.8%

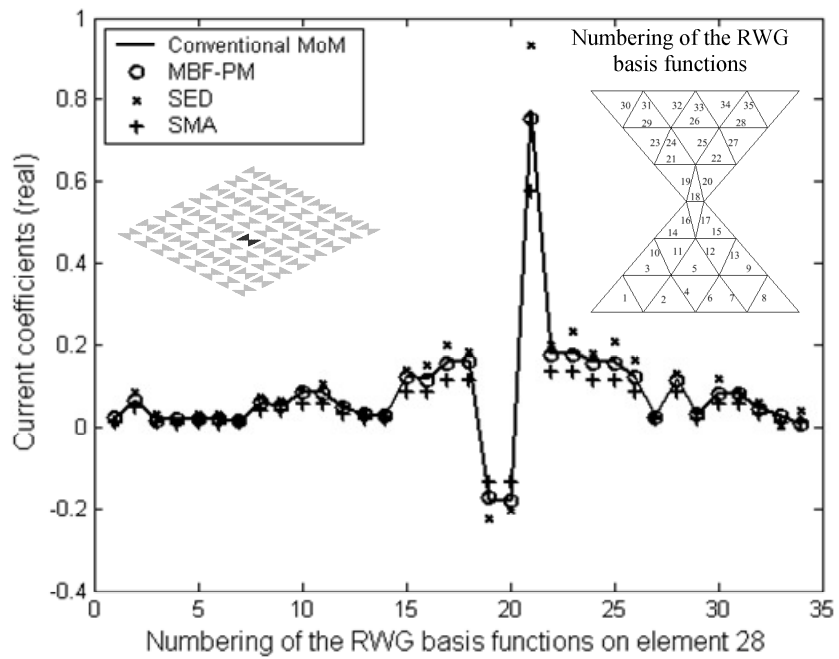
Table 3.14: Summary of the radiation patterns of the bowtie array.

	MoM	MBF-PM	SMA [50]
Broadside Gain (dBi)			
XZ-plane	14.48	14.66	13.9
YZ-plane	14.18	14.32	14.85
3 dB Beamwidth			
XZ-plane	25 <sup>0</sup>	25 <sup>0</sup>	23.6 <sup>0</sup>
YZ-plane	22 <sup>0</sup>	22 <sup>0</sup>	24.6 <sup>0</sup>
Root mean square deviation (dB)			
XZ-plane	0	1.03	3.72
YZ-plane	0	0.92	3.08
Maximum deviation(dB)			
XZ-plane	0	3.4	26
YZ-plane	0	2.36	8.06

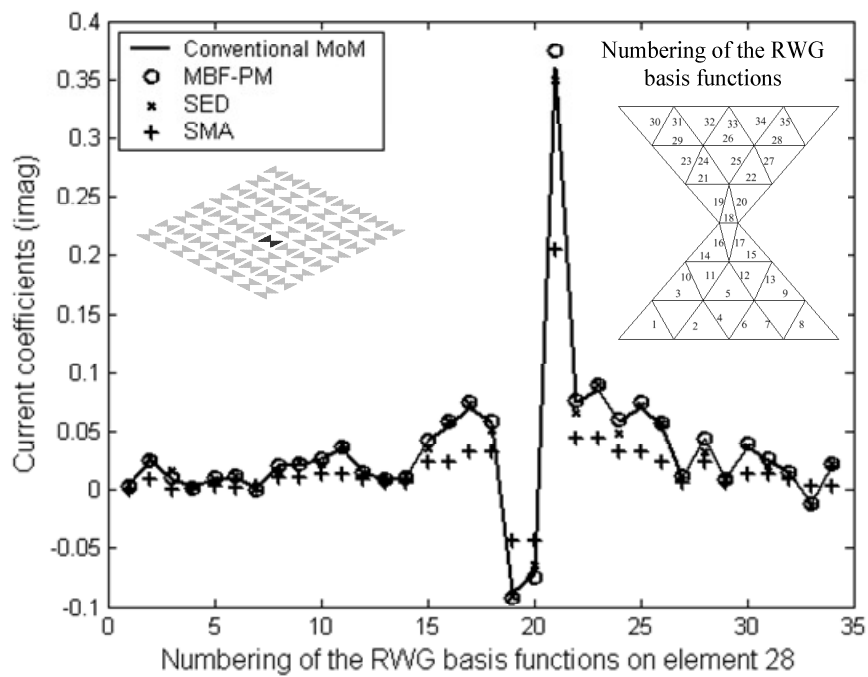
Table 3.15: Root mean square deviation and maximum deviation from the conventional MoM after one iterative sweep.

	MBF-PM	SMA [50]
Root mean square deviation (dB)		
XZ-plane	0.53	0.82
YZ-plane	0.64	1.87
Maximum deviation (dB)		
XZ-plane	2.5	6.52
YZ-plane	1.21	4.52

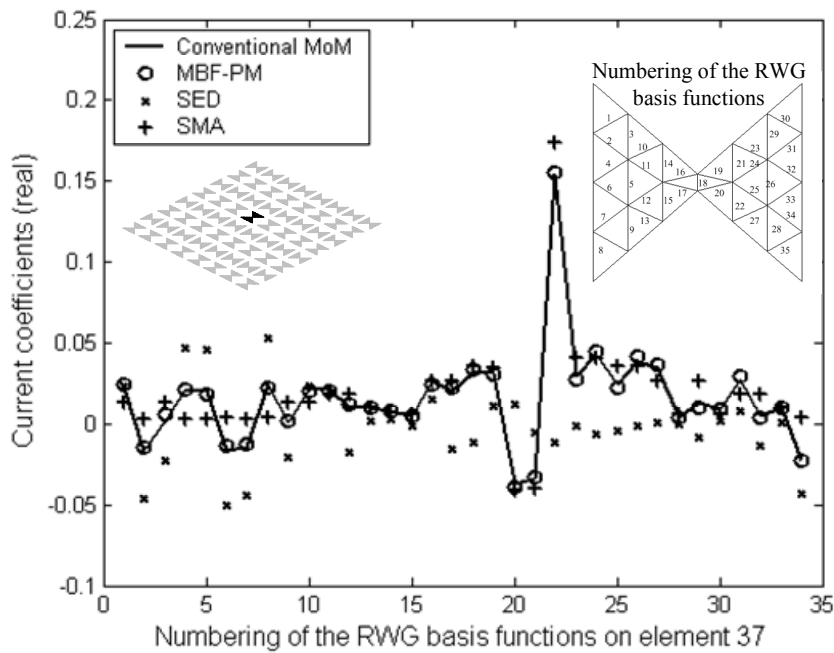
Fig.3.30 (a) and (b) show the radiation patterns of the array at 150MHz in the XZ-plane and YZ-plane respectively. By inspecting Fig.3.30 (b), it is observed that the side-lobe level computed from SMA deviates from the conventional MoM by approximately 46%. Table 3.14 summarizes the performance of the radiation patterns computed from the conventional MoM, MBF-PM and SMA. The root mean square deviations of the radiation patterns from the conventional MoM are also included in the table. Generally, MBF-PM and SMA give good predictions on the broadside gain and the 3 dB beamwidth with a maximum relative error of 4.7% with respect to the conventional MoM. However, MBF-PM gives a smaller root mean square deviation of the radiation patterns with a maximum deviation of 3.4 dB than SMA, which has a maximum deviation of 26 dB. The accuracy of MBF-PM is better than SMA by approximately 3 times. Even though the accuracy for both MBF-PM and SMA has improved after one iterative sweep as shown in Table 3.15, MBF-PM still gives smaller errors. Our proposed method provides accuracy comparable to the conventional MoM and yields more than 90% reduction in time.



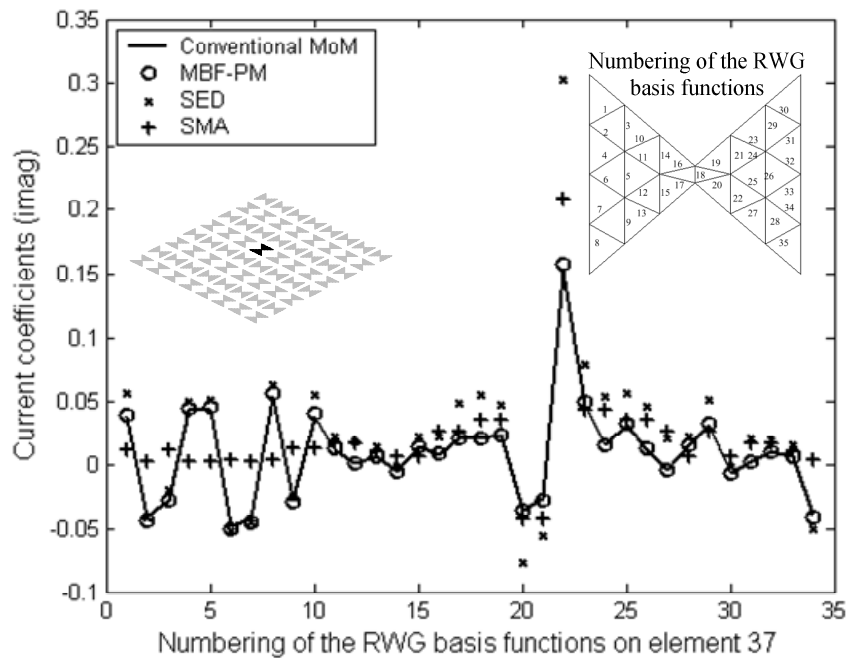
(a)



(b)



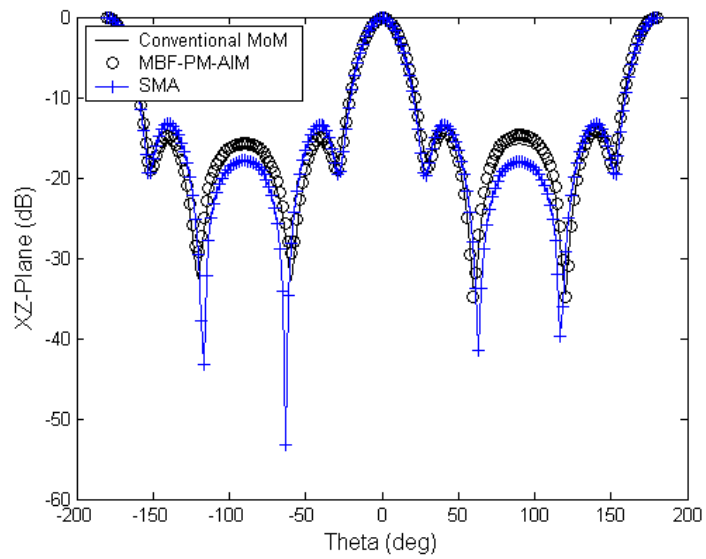
(c)



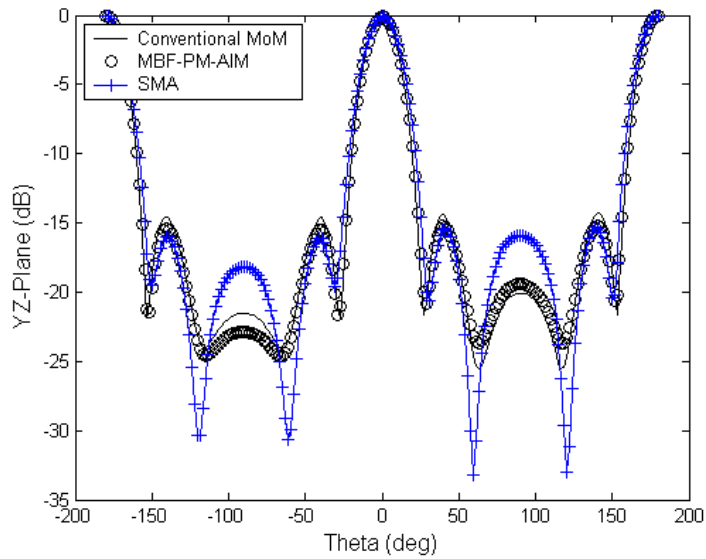
(d)

Fig.3.29: Comparison of the current coefficients among the macro-basis function with progressive method (MBF-PM), the sub-entire-domain basis function method (SED), the sub-domain multilevel approach (SMA) and the conventional MoM with respect

to the RWG basis functions on elements 28 and 37 of the bowtie array. The numbering of the RWG basis functions is shown in the insets.



(a)



(b)

Fig.3.30: Radiation patterns of the bowtie array at 150MHz (without iterative process) (a) XZ-plane (b) YZ-plane.



### 3.8.4 Design of 24GHz Antenna Array

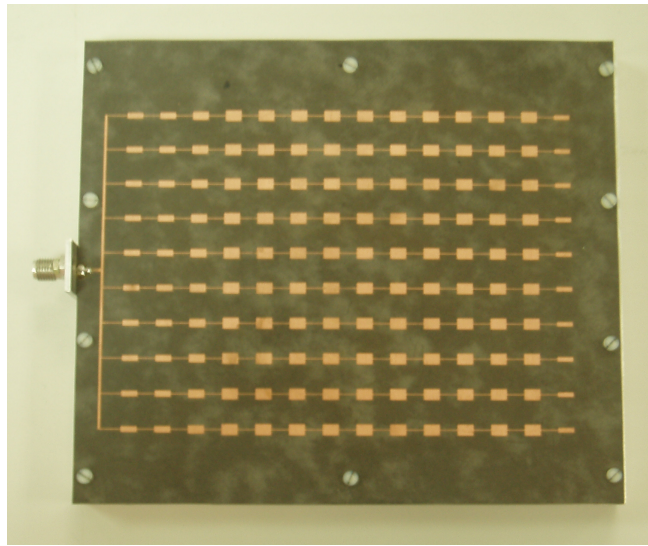


Fig.3.31: Photograph of the 24 GHz antenna array.

As a final example, a 24 GHz antenna array is studied. Based on the most recent standard of ETSI EN 302 288-1 V1.1.1 (2005-01) defined in January 2005 [103], the 24 GHz antenna can be used in automotive industry. MBF-PM-AIM is used to design a 24 GHz antenna array.

The initial dimensions of the array were obtained using a CAD program [102]. With the initial values, the 24 GHz antenna array was optimized with proposed method and verified by the commercial software, IE3D. The antenna was then fabricated on a RT/Duroid 5880 substrate as shown in Fig.3.31. The substrate has a permittivity of 2.2, a loss tangent of 0.0004 and a thickness of 10 mil. The results of our method are compared with IE3D and the measured results.

### 3.8.4.1 Design Procedure

The specifications of the antenna array are given in Table 3.16.

Table 3.16: Specifications of the 24 GHz antenna array.

Center frequency	24 GHz (Automotive System)
Impedance Bandwidth for VSWR < 2	2%
Gain at the center frequency	24 dBi
Side-lobes	< -13 dB
3 dB Beamwidth	< 15

The design procedure is described as follows:

#### (i) Patch dimension and feed line width

The patch dimension is calculated using the well known equations for rectangular patch antennas [104]. For patch width,

$$W = \frac{c}{2f_0} \left( \frac{\epsilon_r + 1}{2} \right)^{-0.5}, \quad (3.28)$$

where  $c$  is the velocity of light in free space.

For patch length,

$$L = \frac{c}{2f_0\sqrt{\epsilon_e}} - 2\Delta L, \quad (3.29)$$

where  $\epsilon_e$  is the effective permittivity and is given by

$$\epsilon_e = \frac{\epsilon_r + 1}{2} + \frac{(\epsilon_r - 1) \left( 1 + 10 \frac{h}{W} \right)^{-0.5}}{2}, \quad (3.30)$$

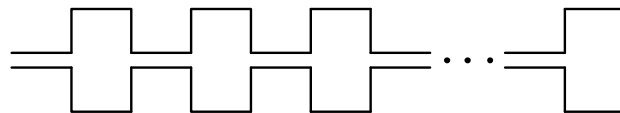
and  $\Delta L$  is the line extension due to the fringing fields given as

$$\Delta L = \frac{0.412h(\epsilon_c + 0.3)\left(\frac{W}{h} + 0.264\right)}{(\epsilon_c - 0.3)\left(\frac{W}{h} + 0.8\right)}. \quad (3.31)$$

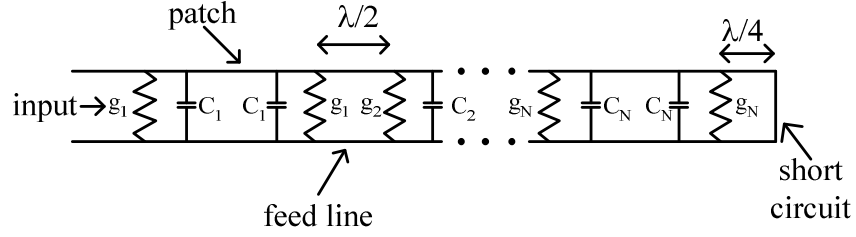
In order for the patches to operate like antennas, the feed line width should be a small fraction of the antenna width. Otherwise, significant blockage of the radiating edges occurs. The feed line must be small compared to the narrowest patch. On the other hand, extremely narrow lines suffer from high losses. Some compromise is necessary. In this case, a  $90\Omega$  line will be used.

(ii) Linear series-connected array

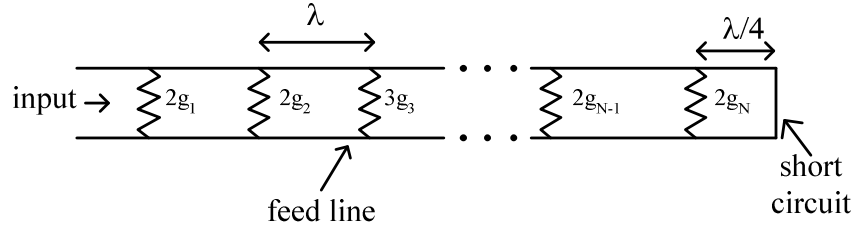
An array with a uniform excitation produces the narrowest possible beamwidth along with the highest side-lobe level. Sometimes it is necessary to reduce the side-lobe level. High side-lobe level can increase interference or result in spurious signal reception. The side-lobe level is reduced by introducing a taper in the amplitudes of the elements. When tapering the amplitude distribution, the excitation is highest at the center of the array and then decreases toward the edge. For series-mounted patches, the amplitude of the element excitation is controlled by varying the patch width. The patch width can be determined by finding the excitation coefficients. From the excitation coefficients, one can obtain element conductances, leading to the patch width values. The method used in the CAD [102] is briefly discussed below.



(a)



(b)



(c)

Fig.3.32: Equivalent circuit of a series-connected patch array.

The equivalent circuit of the series-connected patch array (refer to Fig.3.32 (a)) is shown in Fig.3.32 (b). The feed line consists of alternating sections. One is the narrow line connecting adjacent patches, and the other is the patch itself. The patch edges have a shunt capacitance associated with the fringing fields. Each patch places two conductances and capacitors across the feed line. The closed-form expression for the edge conductance,  $g$  [105] is

$$g = \frac{1}{\pi^2 \eta_0} \left\{ \begin{array}{l} \left( w \text{Si}(w) + \frac{\sin(w)}{w} + \cos(w) - 2 \right) \left( 1 - \frac{s^2}{24} \right) \\ + \frac{s^2}{12} \left( \frac{1}{3} + \frac{\cos(w)}{w^2} - \frac{\sin(w)}{w^3} \right) \end{array} \right\}, \quad (3.32)$$

where  $s = k_0 W$ ,  $W$  is the patch width,  $\text{Si}(w)$  is the sine integral, and  $s = k_0 \Delta L$ . Since the patch is nominally a half-wavelength long, the line in between patches is also a half-wavelength long. The characteristic impedance of the patch line is much lower

than that of the interconnect. The capacitors can be removed by replacing the physical length of the patch with an equivalent length that includes the end-effect extensions. The voltages across the input and output edge conductances are equal but out of phase. Each edge absorbs essentially the same power. The equivalent circuit can be further simplified by combining the edge conductances as in Fig.3.32 (c). The patches are now represented by a shunt conductance of twice the edge value. A fictitious line connects the patches. It must be emphasized that Fig.3.32 (c) is an extremely simplified representation that should only be used to find the element conductances.

The voltage across all the elements is the same because of the wavelength spacing. The power absorbed by the  $n$ th element is

$$P_n = V^2 g_n , \quad (3.33)$$

where  $V$  is the voltage across each element. The far field radiated by the  $n^{\text{th}}$  element is

$$E_n = E_0 a_n \cos \left[ \frac{(2n-1)}{2} kd \cos \theta \right]. \quad (3.34)$$

The power radiated by the element is proportional to the field squared, for example,

$$P_n \propto E_n^2 \propto a_n^2 . \quad (3.35)$$

This power is related to the amplitude excitation distribution,  $a_n$ . The absorbed power must equal the power radiated, ignoring the usually negligible losses in the antenna. From this conservation of power argument, the element conductance,  $g_n$  must be proportional to the amplitude distribution squared expressed as

$$g_n = K a_n^2 , \quad (3.36)$$

where  $K$  is the constant of proportionality. Since the elements are spaced a wavelength apart and the conductances are normalized, the input conductance to the array is the sum of all the element conductances,

$$g_{in} = \sum_{n=1}^N g_n = 1. \quad (3.37)$$

K is found by combining equation (3.36) with equation (3.37) as

$$K = \frac{1}{\sum_{n=1}^N a_n^2}. \quad (3.38)$$

The excitation amplitudes distribution can be determined with Dolph-Chebyshev distributions [4]. The relative current distribution for an array with  $2N+1$  elements is

$$I_n = \sum_{p=n}^N (-1)^{N-p} \frac{N}{N+p} \binom{N+p}{2p} \binom{2p}{p-n} u_0^{2p}, \quad (3.39)$$

and for an array with  $2N$  elements is

$$I_n = \sum_{p=n}^N (-1)^{N-p} \frac{2N-1}{2(N+p-1)} \binom{N+p-1}{2p-1} \binom{2p-1}{p-n} u_0^{2p-1}, \quad (3.40)$$

where  $u_0$  is determined from  $T_m(u_0)=b$  in equation (3.41), with  $b$  fixed by the desired side-lobe level. The order  $m$  of the Chebyshev polynomial,  $T_m$  is always one less than the total number of elements and is given by

$$\begin{aligned} T_m(u) &= \cos(m \cos^{-1} u) & -1 \leq u \leq 1 \\ &= \cosh(m \cosh^{-1} u) & |u| \geq 1. \end{aligned} \quad (3.41)$$

Finally, the amplitude excitation distribution for  $2N$  and  $2N+1$  elements are given by

$a_n = \frac{I_n}{I_1}$  and  $a_n = \frac{I_n}{I_0}$  respectively. Substituting  $a_n$  into equation (3.38), one can

determine  $K$ . After  $K$  has been found, it is possible to find the required element conductance. The conductance can then be linked to the patch width.

### (iii) Planar series-connected array

For a larger two dimensional array, the vertical feed line does not have to be as high in impedance as for the linear series-fed array. There is no concern about blockage of the

radiating element. The feed line length between rows of arrays is equal to a wavelength in the feed line.

#### 3.8.4.2 Simulations and Measurements

The array is densely meshed at 24 GHz, which leads to a large number of  $N=31,087$  basis functions. The final dimensions of the array are shown in Fig.3.33. The mesh of the array is depicted in Fig.3.34. Since the distance between each row of arrays is approximately a wavelength, the structure can be split into eleven parts: the feed network (root domain) and ten rows of arrays with each row merging into MBF. Each row is further decomposed into fourteen sub-domains in which the MBF on each row is solved by adopting macro-basis function with progressive and integral adaptive method. The small domain requires by the MBF-PM-AIM consists of the first three and the last sub-domains. To speed up the computation of the MBF reaction terms, the MBF on each row is projected to its corresponding rectangular grid. By exploiting the translational invariance of the Green's function, the interaction between the MBFs can be efficiently computed using fast Fourier transform.

The computational time per frequency point is about 4.74 min when the proposed approach was applied to solve a 10 by 14 antenna array. For the commercial software, IE3D using AIMS II solver, the computational time for the same problem is 171.8 min per frequency and approximately 7 iterations are required for each frequency point.

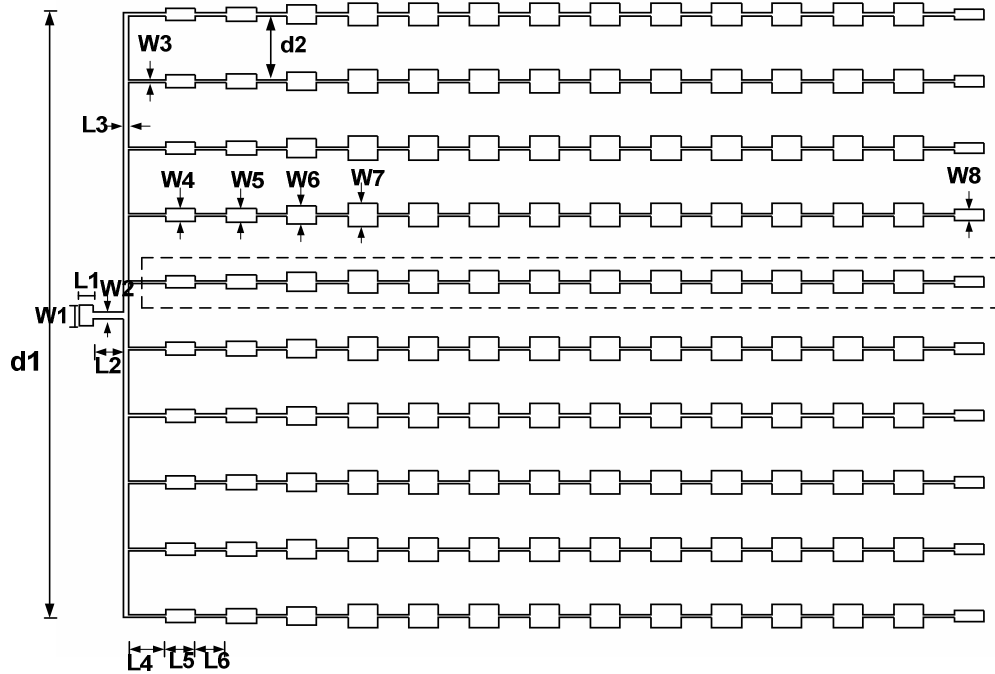


Fig.3.33: Layout of the 10 X 14 antenna array.  $d1=85.8$ ,  $d2=9.2$ ,  $W1=2.57$ ,  $W2=0.8324$ ,  $W3=0.3$ ,  $W4=1.52$ ,  $W5=1.72$ ,  $W6=2.253$ ,  $W7=2.987$ ,  $W8=1.28$ ,  $L1=1.85$ ,  $L2=4.25$ ,  $L3=0.67$ ,  $L4=5.24$ ,  $L5=4.39$ ,  $L6=4.2$ . All dimensions given in mm. Printed on substrate with  $\epsilon_r=2.2$  and  $h=0.254$  mm. The dashed box defines how the sub-domains is subdivided.

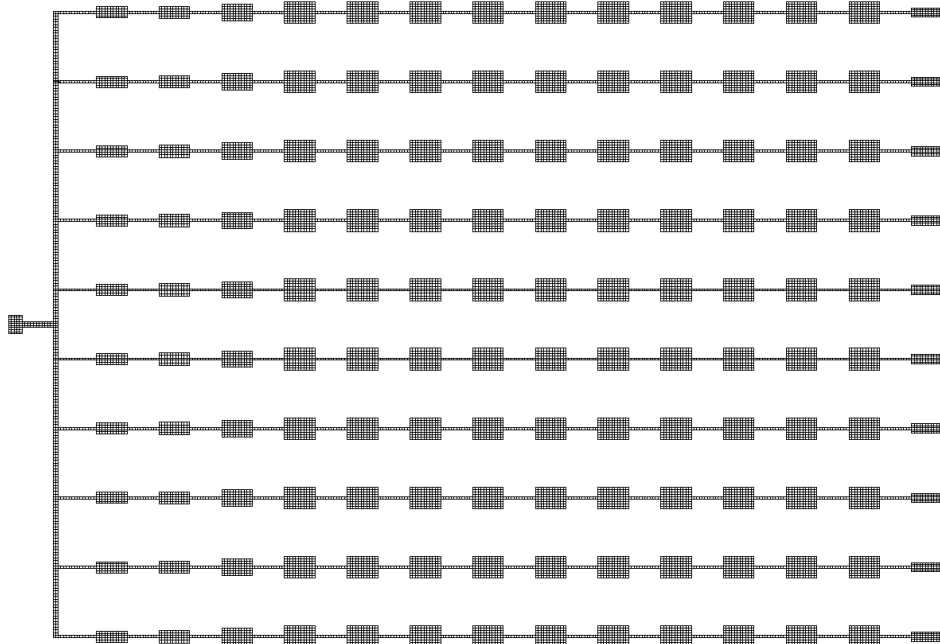


Fig.3.34: Mesh of the 10 X 14 antenna array.



Table 3.17: Comparison of the performances among MBF-PM-AIM, the sub-domain multilevel approach and the commercial software, IE3D.

No of elements	10X14		10X20	
No of unknowns	31,087		44,628	
<b>MBF-PM-AIM</b>				
	Time (s)	RAM (MB)	Time (s)	RAM (MB)
MBF on each row				
Small domain	137	73	137	73
MBF-PM-AIM	3.39	60	8	61
1 iteration	12.16	60	24.95	63
Feed Network (Root domain)				
	98	62	98	62
Whole Structure (Root domain + 10 MBFs)				
	33.85	69	48.4	69
Total Time and Peak Ram Required				
Total Time (s)	284.4		316.35	
Peak Ram (MB)	73		73	
<b>Sub-domain Multilevel Approach [50]</b>				
Total Time (s)	3177.2		3978.2	
Peak Ram (MB)	90		90	
<b>IE3D (Solver: AIMII)</b>				
Total Time (s)	10310		17850	

Table 3.17 shows the breakdown in computational time and RAM usage of the MBF-PM-AIM. The small domain for each row and the feed network are solved using the conventional MoM with direct solver. It is noted that most of the computation time is dominated by the small domain and the feed network. If the number of elements in each row is increased to 20, forming a 10 by 20 antenna array, the time taken to solve the array is 5.27 min, 0.53 min slower than the previous array. The RAM required for the MBF-PM-AIM is 73 Mb. The computational time for MBF-PM-AIM is 3661.85 seconds faster than the sub-domain multilevel approach. Fig.3.35 shows the CPU time consumption for the MBF-PM-AIM and IE3D versus the number of unknowns. The numbers of unknowns are 17870, 31087, 44628, 87780 and 87780, which correspond to 4 by 20, 10 by 14, 10 by 20, 20 by 20 and 30 by 20

antenna arrays, respectively. For 87780 unknowns, the CPU time for MBF-PM-AIM is faster than the time taken for IE3D by 98.4% even though MBF-PM-AIM was coded in MATLAB 6.5 and direct solver was used instead of iterative solver.

The reflection coefficients of the 10 by 14 antenna array (see Fig.3.36) computed by the various methods are shown in Fig.3.36. MBF-PM-AIM and IE3D show a good agreement with MBF-PM-AIM being in more advantageous computational time. These results are then verified by the measured data. The measured impedance bandwidth according to the 10 dB return loss is approximately 2.3% (23.6 GHz ~24.15 GHz).

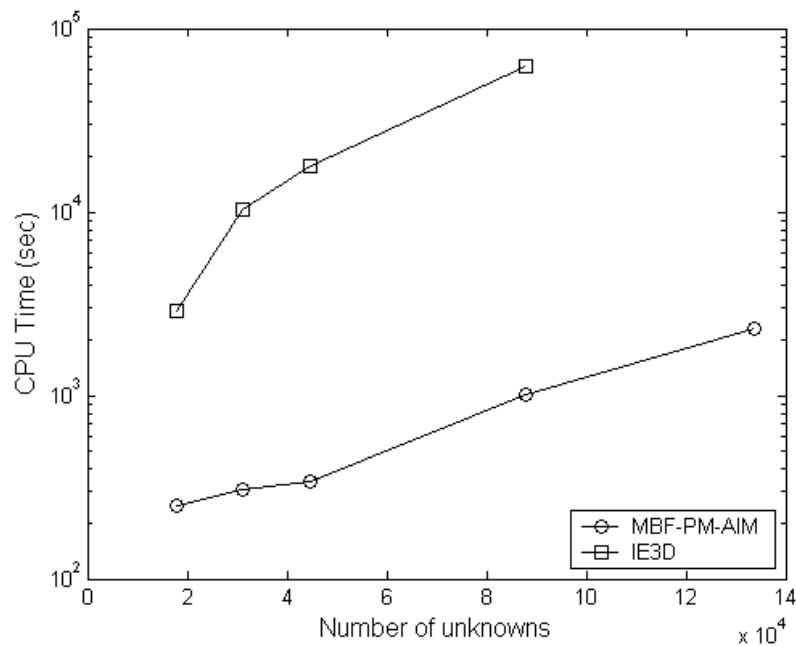


Fig.3.35: Comparison of CPU time used in the proposed method and the simulation software, IE3D, for the 10 X 14 array.

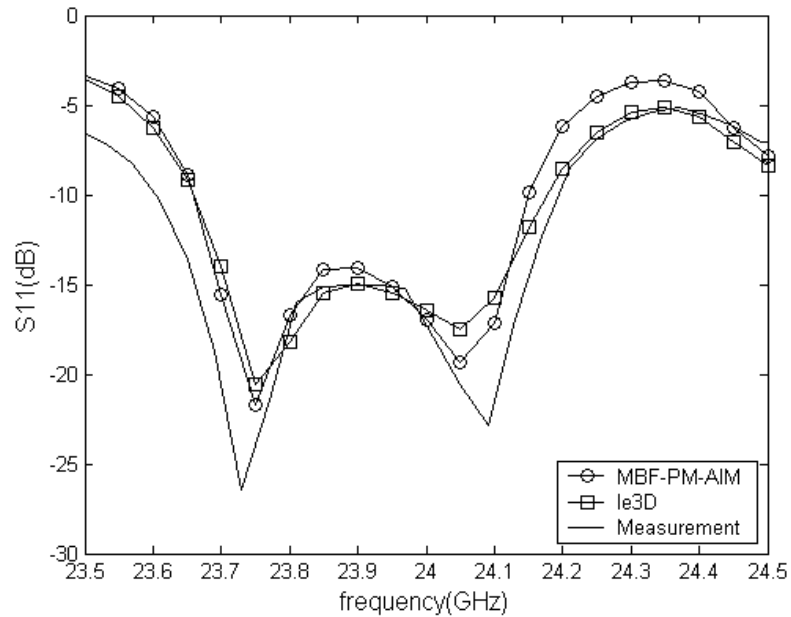
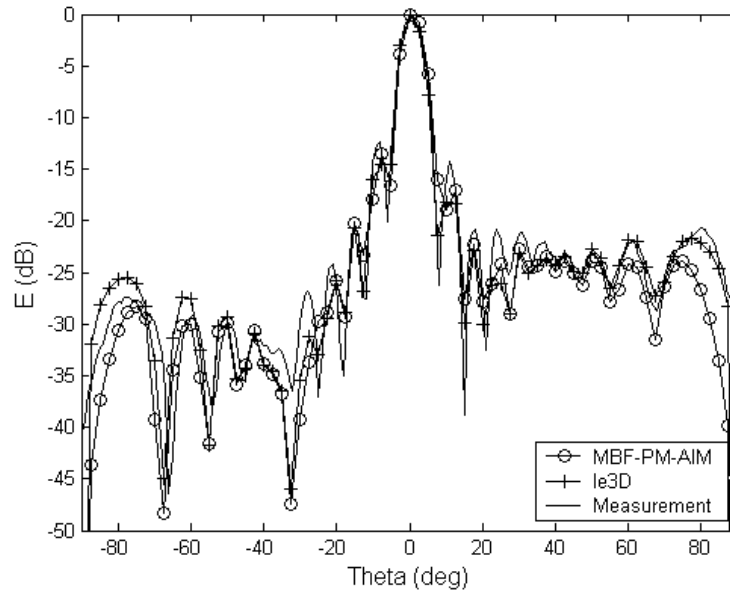


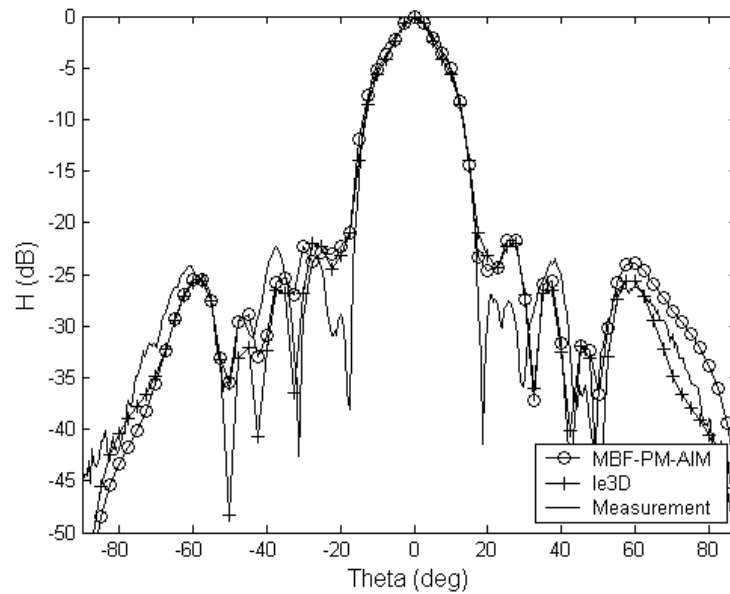
Fig.3.36: Reflection coefficient of the 10 X 14 antenna array.

Finally, we compare the computed and the simulated (IE3D) radiation patterns in the E-plane and H-plane to the measured data in Fig.3.37 (a) and Fig.3.37 (b) respectively. The far-field radiation patterns are measured in anechoic chamber. The computed and the simulated patterns show good agreement with the measured results. The half power beamwidths in the E-plane and H-plane are  $5.5^\circ$  and  $14^\circ$  respectively. The peak side-lobe levels are -13.5 dB for the E-plane and -20 dB for the H-plane. The measured peak gain is 24.4 dBi. As an end-fed array is used in the design and the array is not symmetrical along the horizontal directions, the side-lobe level in the E-plane is not balanced. When theta is between  $-90^\circ$  to  $-20^\circ$ , the side-lobe level is approximately -27 dB. When theta is between  $20^\circ$  to  $90^\circ$ , a side-lobe level of around -22 dB is achieved. More symmetrical pattern is observed in the H-plane. The slight deviation between the simulated and the measured results is due to the connector effect that is not taken into account in the simulation. As the antenna array is mounted

on the finite ground plane, the edge diffraction will affect the radiation pattern. In our simulation, an infinite ground plane is used in the simulation model.



(a)



(b)

Fig.3.37: Radiation patterns of the 10 X 14 antenna array at  $f=24$  GHz. (a) E-plane (b) H-plane

### 3.9 Conclusion

In this chapter, a grouping concept of near-far neighbour evaluation, which utilizes the macro-basis function with progressive method, is introduced to analyze microstrip structures. The macro-basis function with progressive method gives a better accuracy as compared to the sub-domain multilevel approach and the sub-entire-domain basis function. To further improve the accuracy of the solution, an iterative refinement process is developed.

In a large electromagnetic problem, where the memory requirements and the computational time have already been significantly reduced using the macro-basis function with progressive method, the calculation of the MBF reaction terms remains the most time-consuming part of the procedure. Therefore, an efficient way of computing MBF reaction terms is introduced. The strategy for improving the computational time is based on translating the MBFs to grid nodes using multipole moments through the adaptive integral method. Fast Fourier transform is utilized to carry out the matrix-vector multiplication, leading to an improvement of around 56.5% in MoM fill-in time as compared to the macro-basis function with progressive method for a 1 by 14 series fed array with 3737 unknowns.

Examples given have shown that the computational time of the macro-basis function with progressive and adaptive integral method is faster than the conventional MoM. The gain in CPU time increases with the number of unknowns. It has been shown that for a 20 by 20 antenna array with 87780 unknowns, the CPU time computed from MBF-PM-AIM is 98.4% faster than the commercial software IE3D. In terms of accuracy, the proposed method compares well with the conventional MoM and IE3D

# **CHAPTER 4      Design of Various Wideband Probe-Fed Microstrip Patch Antennas and Arrays**

## **4.1      Introduction**

Microstrip antennas have been widely used due to its distinct advantages like light weight and small size [5]-[6]. However, it is well known that the bandwidth of the microstrip antenna is very narrow. Antenna designers are constantly finding a way to fulfill the bandwidth requirements without affecting the other features of patch antennas, including their compactness. Many techniques [7]-[26] such as using thick and air-filled substrate have been developed to improve the bandwidth. However, the modern wireless communication systems significantly increase the bandwidth demand and new solutions have to be found. The goal of satisfying these new bandwidth requirements is usually accompanied by the practical requestment to keep the antenna overall dimensions compact.

In the multipath environments, typical of mobile and cellular communication systems, the polarization purity of antennas mounted in terminal equipments does not represent a strong design constraint as the signal polarization on the receiving antenna is difficult to predict. Based on the statistical consideration, the channel's impulse

response is virtually independent of the states of polarization of the transmitting and receiving antennas if there is no line-of-sight path between them [106]-[107]. Therefore high cross-polarization levels for the antenna do not worsen the radio-link performances. Instead, they represent a good choice for polarization diversity purposes. This opens the possibilities of improving the impedance bandwidth of the antenna by exciting higher order modes, whose resonant frequencies are closed together while keeping the antenna size compact. Every current mode by itself would produce an almost purely polarized radiated field. However, the strong coupling between two (or more) of them may represent a way to extend the impedance matching, at the tradeoff between polarization purity and impedance bandwidth. In the communication systems where polarization purity does not represent a constraint, exciting higher order mode can be enhanced which has led to current interest in employing polygonal patch for the design of compact antennas in multipath environments [107]-[108].

In this chapter, three new wideband probe-fed microstrip patch antennas based on polygonal shapes are studied. A wideband feeding mechanism, semi-circle probe feed is introduced. As multiple resonance technique is employed to improve the bandwidth of the antennas, the antennas have high cross-polarization. The designs can be extended to low cross-polarized applications through array configuration where elements are positioned in a back-to-back configuration. A probe-fed stub patch array with low cross-polarized is presented.

The design of the antenna elements is carried out with the developed code and verified with the commercial software, IE3D. Both results give good agreement. For

the array design, in which the number of unknowns is large, our developed code had to be used. The standard we employ to characterize the operating bandwidth is the frequency range that is less than 10 dB return loss. The S-parameters are measured using an HP8510A network analyzer. The field radiation pattern and gain are obtained by measurements in a compact antenna test range with N5230A Antenna Measurement System.

The chapter begins by briefly introducing the background of the development of probe-fed patch antennas. This will be followed by the design of wideband probe-fed patch antennas. Finally two probe-fed arrays are discussed.

## 4.2 Overview of Wideband Probe-fed Microstrip Patch Antenna

The microstrip patch antenna is basically a leaky cavity and therefore has narrow bandwidth, impeding their application in many systems. Hence the discussion on bandwidth-enhancement techniques will focus on input impedance. There are a number of ways in which the impedance bandwidth of probe-fed microstrip patch antennas can be enhanced. In this section, the approaches based on multiple resonances are characterized in terms of the antenna structures which include parasitic elements, slotted patches and shaped probes.

### 4.2.1 Parasitic Elements [7]-[14]

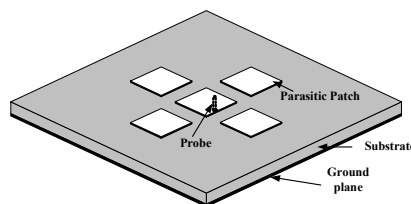




Fig. 4.1: Geometry of a probe fed microstrip antenna with edge-coupled parasitic patches.

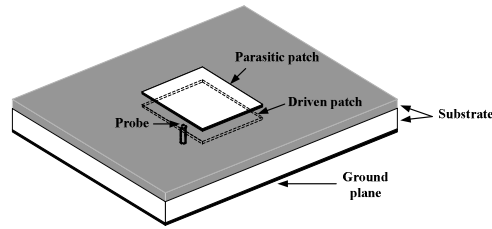


Fig. 4.2: Geometry of a probe feed stacked microstrip antenna.

In order to enhance the impedance bandwidth of a patch antenna, multiple resonance technique has been employed. By adding parasitic elements either in the same layer [7] or different layer [8]-[14], the impedance bandwidth of a patch antenna can be increased to about 20-30% for  $VSWR < 2$ . The basic idea is to introduce additional resonant patches to provide two or more closely spaced resonance. By doing so, a few closely-spaced resonances can be created. Fig. 4.1 shows a probe-fed antenna with edge-coupled parasitic patches. The designs of coplanar parasitic subarrays improve the impedance bandwidth and gain at the expense of size. They are simple to design and fabricate. Fig. 4.2 shows a stacked geometry consisting of one fed patch and a parasitic patch on another layer. The method has the advantages of small projection size, wide impedance bandwidth and relatively stable radiation pattern over the frequency range.

#### 4.2.2 Slotted Patches [15]-[22]

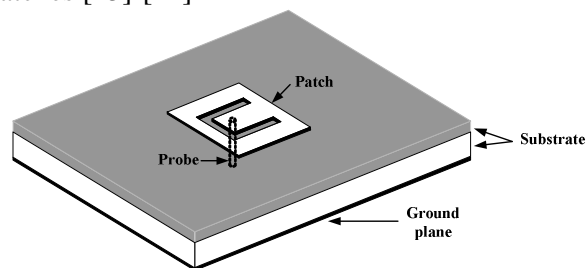


Fig.4.3: Geometry of a probe feed antenna with a U-slot.

It is important to keep the size of an antenna as small as possible while maintaining its performance. Coplanar parasitic subarray geometry has the disadvantage of increasing the size of the antenna, while stacked geometry has the disadvantage of increasing the thickness of the antenna. Hence it would be preferable to use a single-layer single-patch antenna with wideband and stable radiation pattern. One way is to modify the patch. An example is a U-slot patch antenna [15]-[19] as shown in Fig.4.3. This antenna has no additional parasitic elements. An impedance bandwidth of about 30% for VSWR <2 can be achieved. The shape of U slot can be modified to V-shaped [20]-[21] or E-shaped [22] and similar impedance bandwidth can be obtained.

#### 4.2.3 Shaped Probes [23]-[26]

Besides modifying the patch shape, another method to keep the size of the antenna small and still maintain its performance is to modify the probe-fed [23]-[26]. Fig.4.4 shows the geometry of patch antennas with different probe shaped. The L-Probe antenna and T-Probe antenna can achieve a bandwidth of 36% and 40% respectively.

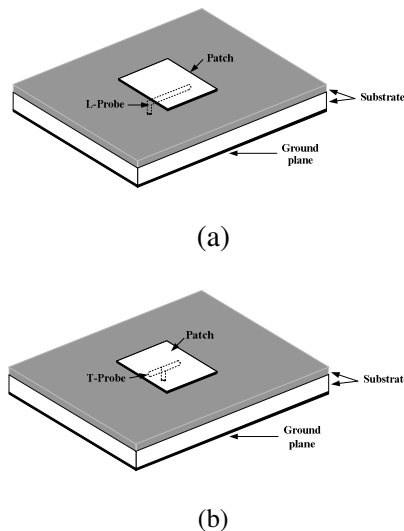


Fig.4.4: Geometry of patch antennas with different probe shaped (a) L-Probe (b) T-Probe.

### 4.3 Wideband Semi-circle Probe-fed Microstrip Patch Antennas

This section is devoted to the design of wideband semi-circle probe-fed microstrip patch antennas. The specification is listed in Table 4.1

Table 4.1: Specifications of the antenna.

Center frequency	5.4 GHz (WLAN application)
Impedance Bandwidth for VSWR < 2	>45%
Gain at the center frequency	7 dBi
3 dB gain bandwidth	>45%

#### 4.3.1 Semi-circle Probe-fed Rectangular Patch Antenna

A study on the semi-circle fed patch is first carried out followed by its effect on a rectangular patch. The geometry of a semi-circle fed patch proximity coupled to a rectangular patch is shown in Fig.4.5. The patch dimensions are obtained using equations (3.22) and (3.23). The structure depicts in Fig.4.5 actually corresponds to the stub patch antenna with  $W_1=0$ .

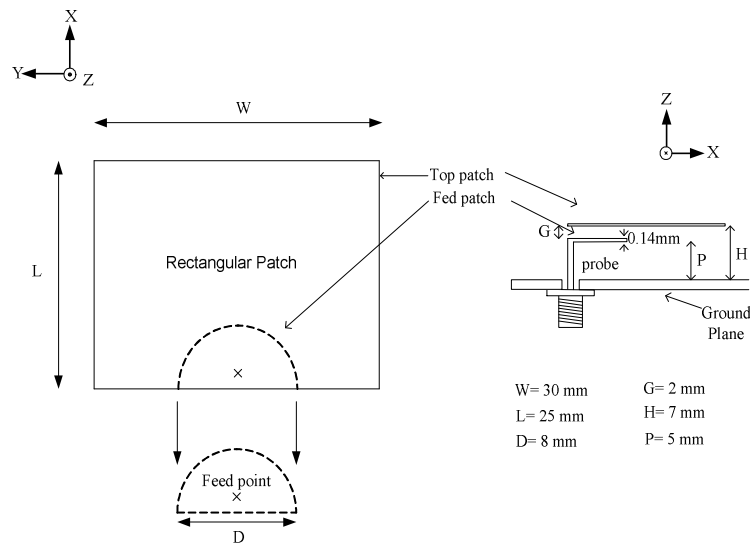


Fig.4.5: Geometry of a semi-circle fed patch proximity coupled to a rectangular patch.

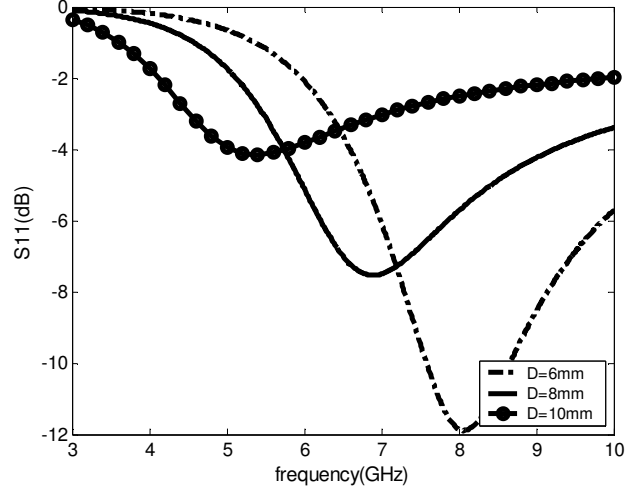


Fig.4.6: Variation of the diameter of the Semi-circle Fed Patch, D without the parasitic patch (Simulated).

Fig.4.6 displays the return loss of the semi-circle fed patch without any parasitic patch with respect to its diameter, D. It is observed that the diameter of the semi-circle fed patch is inversely proportional to the impedance matching at the higher frequency range. This implies that the inherent inductance of the probe can be compensated by the semi-circle fed patch. The inductor  $X_p$  produced by the probe is given by [109]:

$$X_p = \frac{\eta}{\pi} \tan(0.5k_0h) \ln(2.25/k_0d), \quad (4.1)$$

where h is the height of the substrate,  $\eta$  is the intrinsic resistance, d is the diameter of the probe and  $k_0$  is the wave number. The matching condition to compensate the inductive probe effectively is given by

$$\omega_r C X_p = 1. \quad (4.2)$$

The capacitance of the semi-circle fed patch, C can be approximately given by [110]

$$C = \frac{1}{2} \frac{\epsilon_0 \epsilon_r r^2 \pi}{h} \left\{ 1 + \frac{2h}{\pi \epsilon_r r} \left[ \ln\left(\frac{r}{2h}\right) + (1.41\epsilon_r + 1.77) + \frac{h}{r} (0.268\epsilon_r + 1.65) \right] \right\}, \quad (4.3)$$

where r is the radius of the semi-circle. The initial dimension of the semi-circle, r can be obtained from equations (4.1) to (4.3). One possible way of finding r is to locate

the intersection point between the capacitance value determined from equations (4.2) and (4.3) as indicated in Fig.4.7. At 6.5 GHz, a diameter of 7.6mm is required to compensate the inductive effect of the probe. Although there is significant fringing at the edges of the semi-circle disk, through our experimentation, equation (4.3) is found to give a relatively good approximation for the capacitance.

Because of the finite probe width and the technical constraint of soldering the thin connector pin on the semi-circle disk, the feed is maintained at 1mm away from the horizontal edge of the semi-circle disk for all the antennas adopted. The design of our proposed structure is an incremental approach whereby the semi-circle resonant structure is first designed at its optimum matching position and followed by the addition of parasitic patch for tuning.

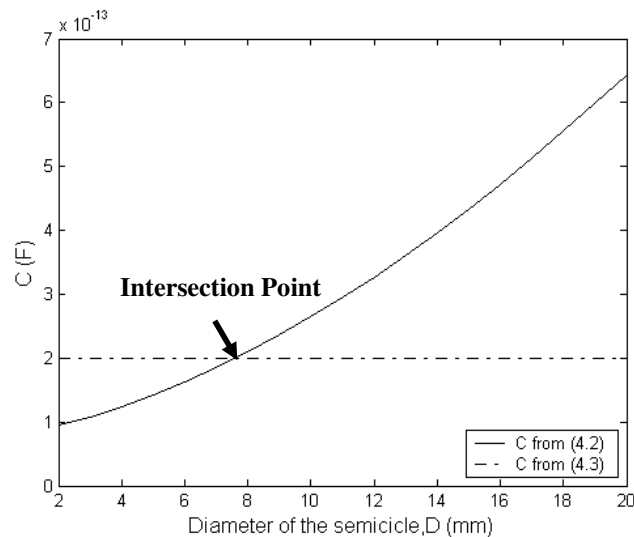


Fig.4.7: Capacitance, C with respect to the diameter of the semi-circle at 6.5 GHz.

Fig.4.8 exhibits the return loss of the semi-circle fed patch proximity coupled to a rectangular patch with respect to its diameter, D. The centre frequency of the rectangular patch is designed at around 5.4 GHz. It is noted that when D= 10 mm, the

impedance bandwidth below -10 dB is approximately 35%, centre at 4.6 GHz. However, when  $D=6$  mm, the impedance matching improves at higher frequencies but deteriorate at lower frequencies. When  $D=8$  mm, the return loss between 4 GHz to 8 GHz ripples around -7.5 dB. Therefore, if the impedance matching within this range of frequency can be further improved, wideband can be realized.

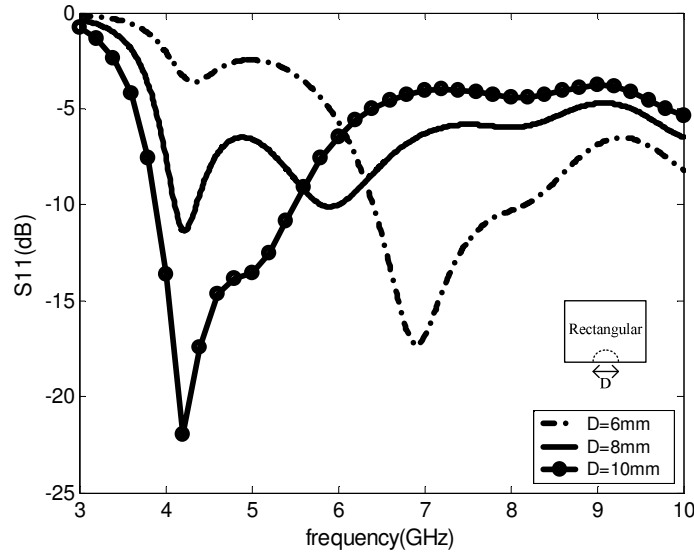


Fig.4.8: Variation of the diameter of the Semi-circle Fed Patch, D with rectangular patch (Simulated).

#### 4.3.2 Semi-circle Probe-fed Stub Patch Antenna

##### 4.3.2.3 Antenna Structure

In this section, a stub patch antenna, which is originated from stub matching concept, will be investigated to achieve wideband operation. Fig.4.9 shows the geometry of the proposed antenna. The antenna comprises of 3 layers; a main stub patch in the top layer, a semi-circle fed patch in the second layer and a ground plane. The main stub patch has two stubs, one at each side of the patch, to improve the impedance matching of the antenna. Since an air-filled dielectric is used, the main plate is separated from the ground plane by means of basswoods and proximity fed via a semi-circle probe

where the vertical section is made from the 50  $\Omega$  coaxial connector with an inner diameter of 1.25 mm and the horizontal section (semi-circle plate) is etched from a 0.14 mm thick copper sheet. The basswoods used are noticed experimentally to have no effect on the antenna. The centre frequency is designed at around 5.4GHz and the height of the substrate is approximately  $0.1\lambda$ . Fig.4.10 shows the photographs of the fabricated proposed antenna.

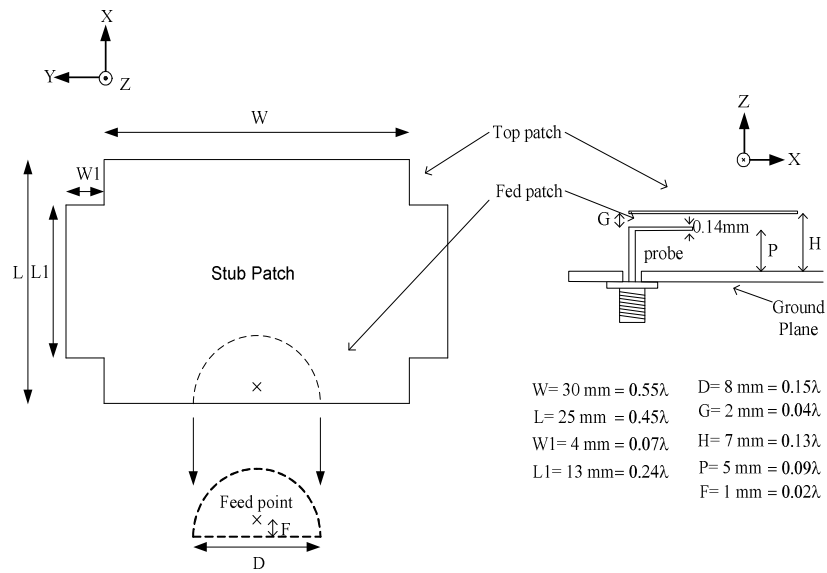


Fig.4.9: Geometry of the semi-circle probe-fed stub patch antenna.



Fig.4.10: Photographs of the fabricated semi-circle probe-fed stub patch antenna.

#### 4.3.2.2 Simulations and Measurements

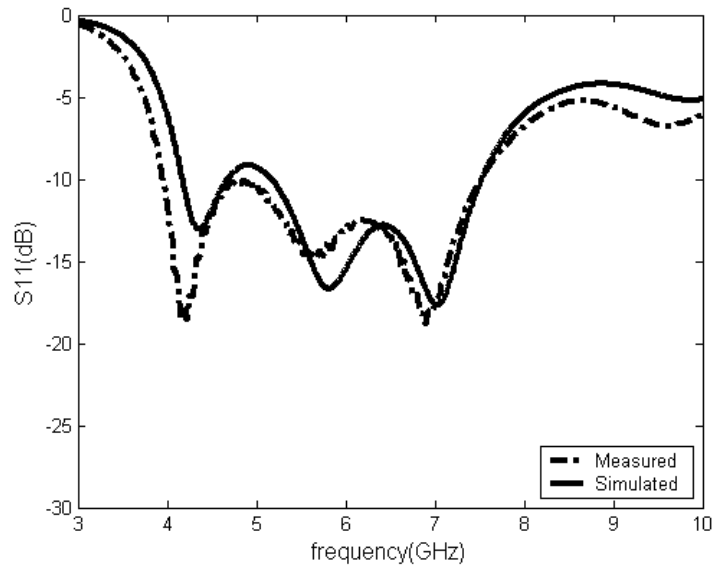


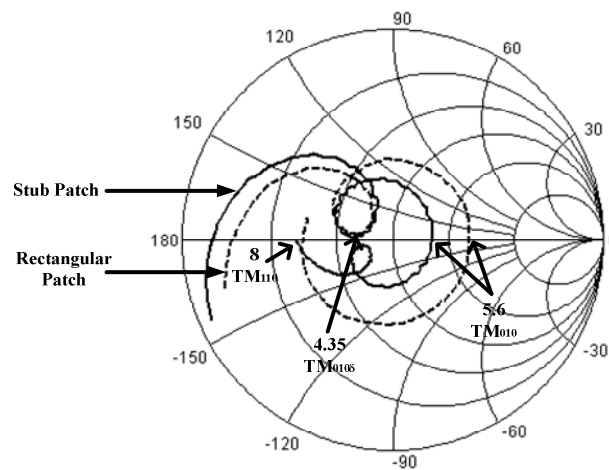
Fig.4.11: Simulated and measured return loss of the semi-circle probe-fed stub patch antenna.

The proposed stub patch antenna is first simulated. After which, a prototype was fabricated and measured. Fig.4.11 displays the simulated and measured return loss results. The measured impedance bandwidth, which corresponds to the level of -10 dB return loss, is approximately 62.3% (3.95 GHz ~ 7.50 GHz). The simulated and measured results are in relatively good agreement. The deviations between the simulated and the measured results are caused by the inaccurate modeling of the semi-circle probe-fed. In here, a thin-strip model for modeling the vertical probe is adopted.

A comparison of the measured impedance locus of the stub patch and the rectangular patch is depicted in Fig.4.12 (a). As shown from the figure, three distinct resonances are observed. The fundamental mode,  $TM_{01}$  of the antenna patch is located at about 5.6 GHz. Another resonance mode which corresponds to a delta mode is located at 4.35 GHz. This added mode is generated by the combined effort of the probe, the



semi-circle disk and the patch, and this is clearly evident by the sharp dip in Fig.4.8 and Fig.4.11. The inductance of the vertical probe together with the capacitance of the semi-circle disk and the stub patch acts as a series-resonant element to create a resonant frequency close to that of the  $TM_{01}$  mode of the antenna patch. A third resonance is also observed at 6.86 GHz. This mode, which is absent from the proximity coupled rectangular patch, is mainly due to the effect of the added stubs on the patch and this fact is clearly evident by the sharp dip shown in Fig. 4.20. A resonant mode is defined to be the frequency at which the input impedance is real. It is noted that by adding two stubs to the rectangular patch, it aids in shifting in the impedance loop towards the centre, thus, improving the overall matching. It is observed that the added open circuit stubs have capacitive effect on the antenna before 5.6 GHz. Beyond 5.6 GHz, the added stubs have inductive effect on the antenna. Fig.4.12(b) shows the return loss of the stub patch, rectangular patch and semi-circle fed patch. The stub patch has demonstrated a tremendous improvement in the impedance bandwidth.



(a)

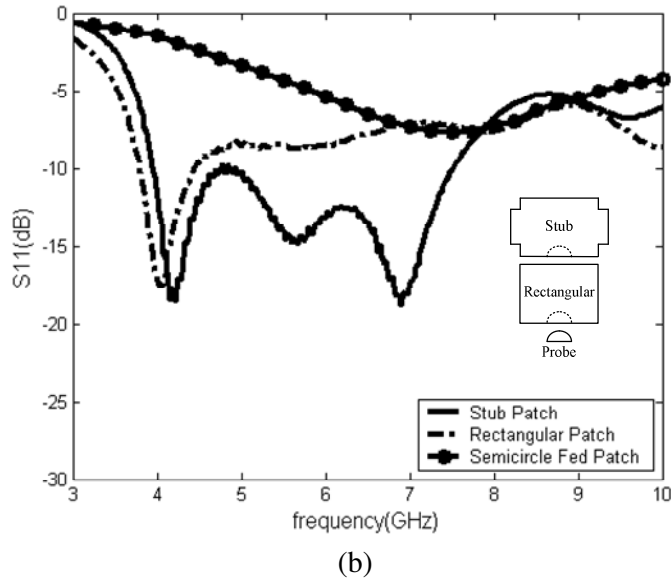


Fig.4.12: (a) Measured Impedance Locus of the stub patch antenna, rectangular patch antenna and semi-circle fed patch. (b) Comparison of the measured return loss of the stub patch, the rectangular patch and the Semi-circle Fed Patch.

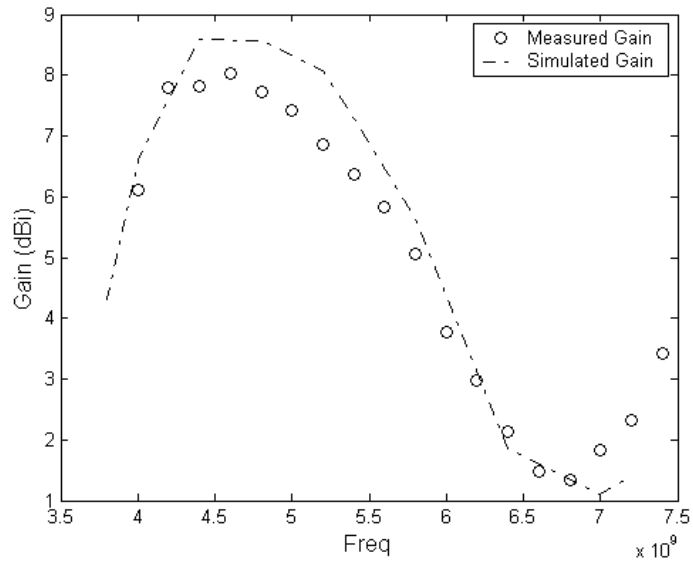


Fig.4.13: Comparison of the broadside gain of the semi-circle probe-fed stub patch antenna between the measurement and the simulation.

Fig.4.13 shows the measured and the simulated gains at  $\theta=0^\circ$  and  $\phi = 0^\circ$ . The measured peak gain is 8.02 dBi. The simulated and measured gains are found to be in good agreement with the exception that the measured gain is typically 0.5-1.5 dB

below the simulated gain. This is ascribed to the conductor loss that is not modelled in the simulation. Due to the excitation of higher order modes, there is a drop in gain at higher frequencies. The 3 dB gain bandwidth is 39.2% (3.9 GHz-5.8 GHz). The gain of the antenna can be increased by implementing an array.

Figs 4.14 to 4.16 plot the measured radiation patterns of the semi-circle probe-fed stub patch antenna at 4.2 GHz, 5.4 GHz and 7.0 GHz respectively. As observed, the patterns look very similar to a rectangular patch. The cross-polarized pattern in the E-plane of the antenna is relatively low throughout the frequency band. However, it can be seen that the cross-polarized pattern in the H-plane increases with frequencies. The high cross-polarized radiation is mainly contributed from the horizontal section of the sub patch. The asymmetrical E-plane pattern is due to the asymmetric structure of the antenna. The measured results of the half power beamwidth and the cross polarization level extracted from the H-plane radiation patterns are summarized in Table 4.2.

Table 4.2: Summary of the radiation characteristics of stub patch antenna.

Frequency (GHz)	4.2	5.4	7.0
Half power beamwidth (H-plane)	64 <sup>o</sup>	52 <sup>o</sup>	42 <sup>o</sup>
X-polar Level (dB)	-13.2	-1.31	3.83

Fig.4.17 shows the current distribution at 4.5 GHz, 5.5 GHz and 7.0 GHz. It is observed that at 4.5 GHz and 5.5 GHz, current mainly flows in the vertical direction. This mode physically corresponds closely to the TM<sub>01</sub> mode. However as the frequency increases, the current splits in the centre and flows towards the left and the right sides of the patch. From these current distributions, one can deduce that the

radiation patterns at 4.5 GHz and 5.5 GHz have a maximum gain at the broadside. However as frequency increases, the maximum gain is shifted away from the broadside.

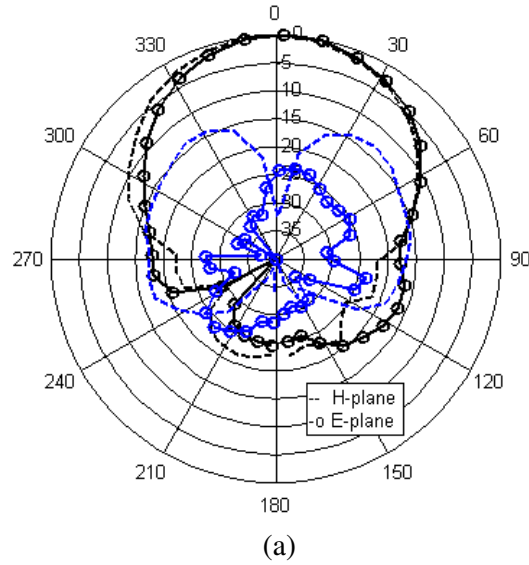


Fig.4.14: Measured radiation patterns of the semi-circle probe-fed stub patch antenna at 4.2 GHz. Black lines represent co-polarized pattern. Blue lines represent cross-polarized pattern.

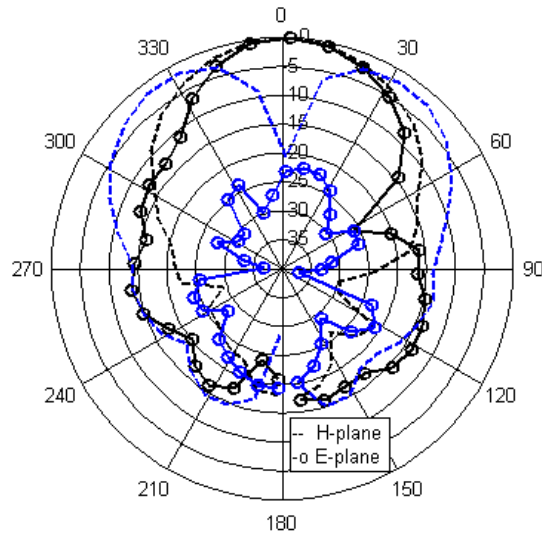


Fig.4.15: Measured radiation patterns of the semi-circle probe-fed stub patch antenna at 5.4 GHz. Black lines represent co-polarized pattern. Blue lines represent cross-polarized pattern.

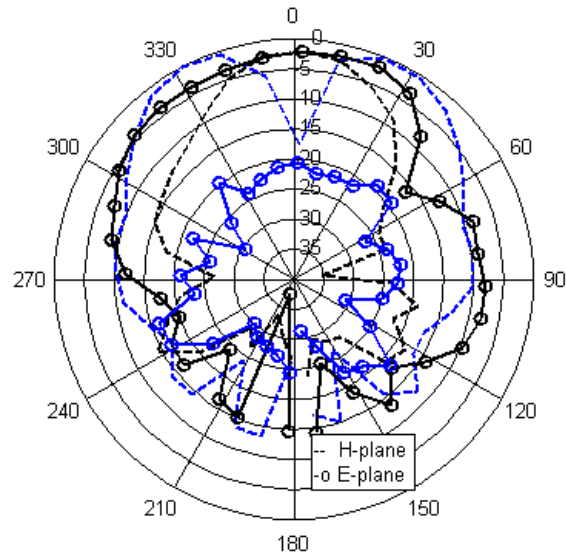
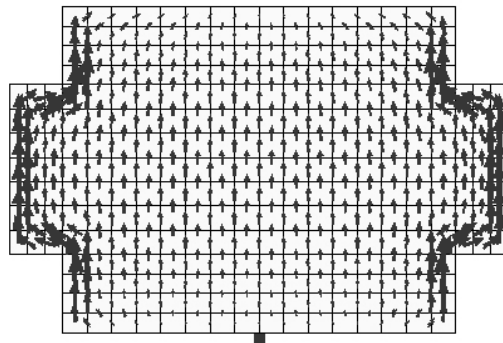
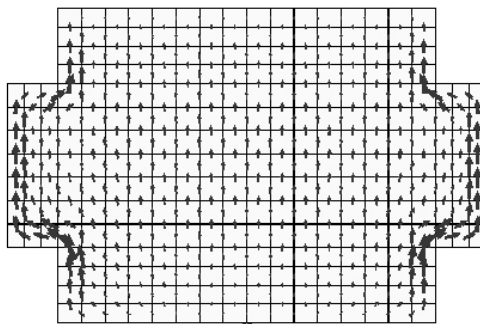


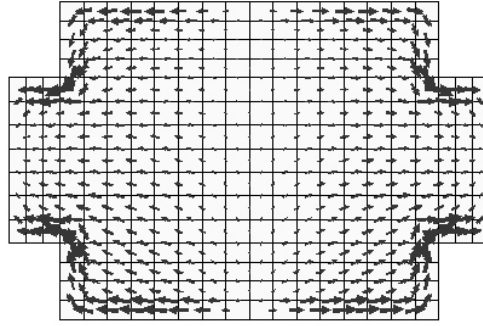
Fig.4.16: Measured radiation patterns of the semi-circle probe-fed stub patch antenna at 7.0 GHz. Black lines represent co-polarized pattern. Blue lines represent cross-polarized pattern.



(a)



(b)



(c)

Fig.4.17: Simulated current distributions of the semi-circle probe-fed stub patch antenna at (a) 4.5 GHz (b) 5.5 GHz (c) 7 GHz.

#### 4.3.2.3 Parametric Study

In order to better understand the antenna's characteristics, some key parameters are varied to analyze the structure through simulation. The first variation is performed by adjusting the diameter of the semi-circle fed patch of the proposed antenna. As mentioned above, this parameter plays a crucial role in matching. It is prominent in Fig. 4.18 that slight variation in the diameter of the semi-circle can affect the antenna's performance significantly. Increasing the diameter from 8 mm to 10 mm improves the impedance matching at the lower frequencies. Inversely, when the diameter of the semi-circle is reduced to 6 mm, it will deteriorate the matching at the lower frequencies but enhance the impedance bandwidth at the higher frequencies. Hence, one can conclude that there exists an optimum diameter where the impedance bandwidth is the largest.

It is observed from Fig.4.19 that the impedance matching of the antenna is sensitive to the gap,  $G$ , between the stub patch and the fed patch. Increasing the gap will improve the matching at higher frequencies while deteriorating the matching at lower

frequencies. On the other hand, decreasing the gap will enhance the matching at the centre frequencies and reduce the matching at the sides.

It is observed in Fig. 4.20 that as the length,  $L_1$  increases, a dip is introduced at the higher frequencies but at the expense of a narrow bandwidth. The dip becomes prominent when the length,  $L_1$  is increased to the same length as the patch (25 mm) (i.e. to form a rectangular patch). However the overall impedance bandwidth (5.1 GHz~7.22 GHz) deteriorates. Thus, there exists an optimum length,  $L_1$  where the impedance bandwidth is the largest.

The width,  $W_1$  of the stub plays a significant role in matching at the higher frequencies as depicted in Fig.4.21. By progressively increasing  $W_1$  from 3 mm to 5 mm, the matching at the higher frequencies improves but the overall impedance bandwidth reduces. It is observed that there is tradeoff in impedance matching at the higher frequencies. To achieve a very good matching, the overall impedance bandwidth will suffer. In fact, the rectangular patch in Fig.4.12(b), which corresponds to the case of  $W_1=0$ , clearly indicates that  $W_1$  plays a crucial role in ensuring a wide impedance matching.

As noted from Fig.4.22, a relative shift in positions between the top patch and the fed patch will also affect the antenna impedance matching performance. Progressively offset the position from -1 mm to 1 mm will improve the matching at lower frequencies while deteriorating the frequencies at the higher frequencies.

Fig.4.23 shows the variation of the probe feed position from 0.5 mm to 1.5 mm from

the edge of the semi-circle in the presence of the parasitic patch plus. As noted from the figure, there is minor change in the frequency response and this implies that the proposed feed position of the semi-circle is already at its best matching position.

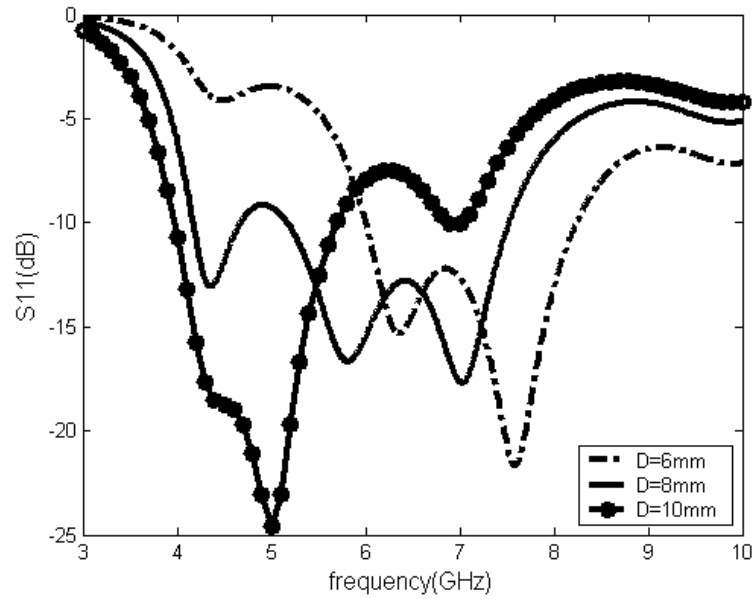


Fig. 4.18: Variation of the diameter of the Semi-circle Fed Patch,  $D$  with the stub patch (Simulated).

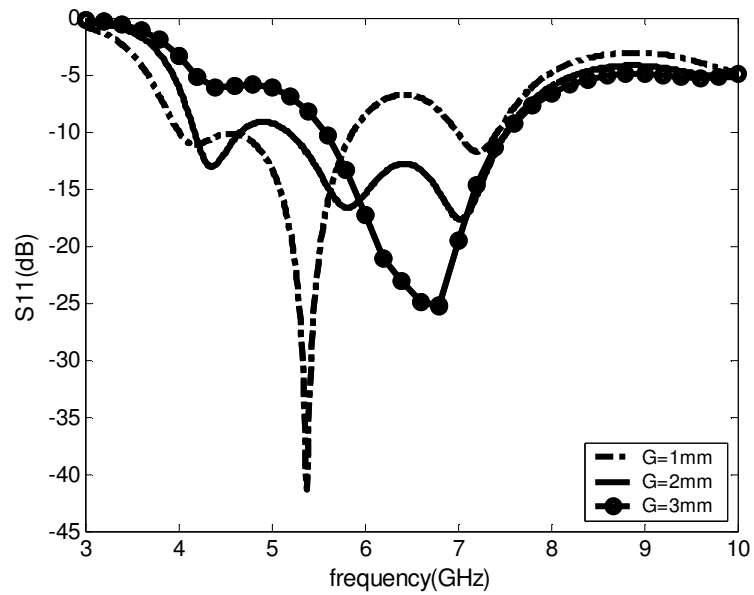


Fig.4.19: Variation of the gap,  $G$  between the top patch and the fed patch (Simulated).



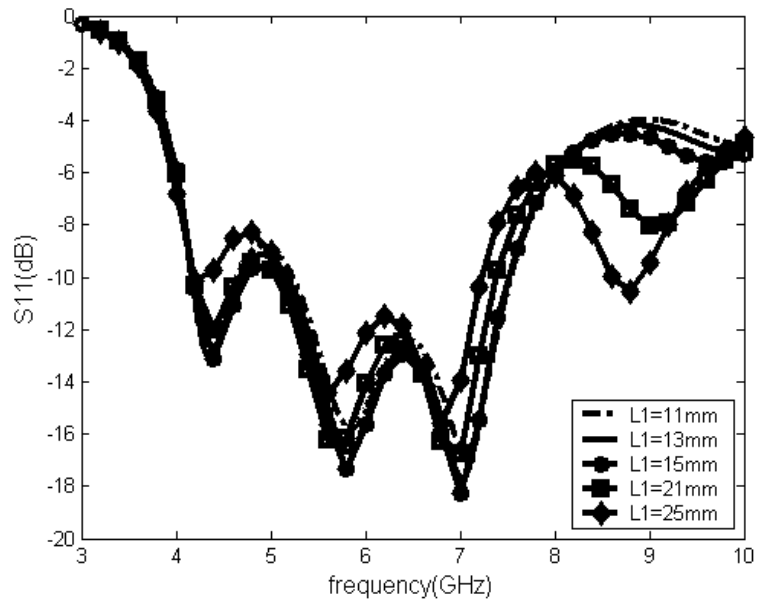


Fig. 4.20: Variation of the length,  $L1$  of the stub patch (Simulated).

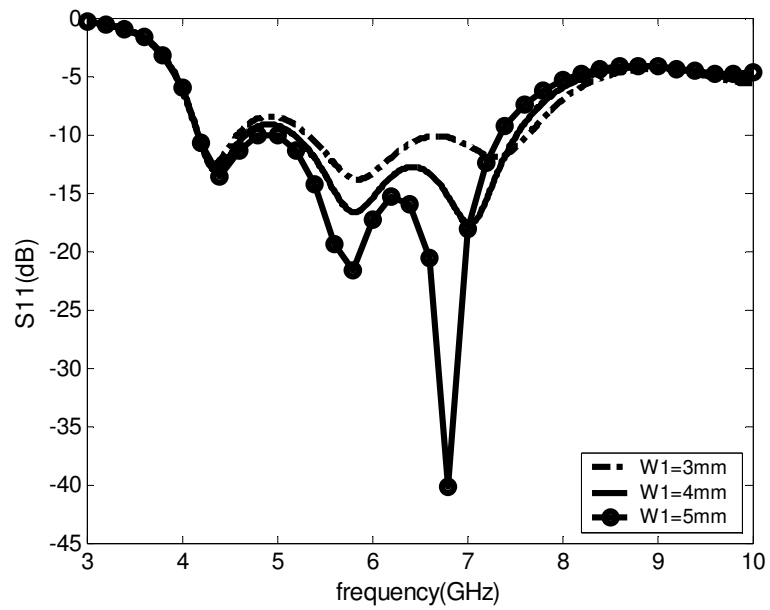


Fig.4.21: Variation of the length,  $W1$  of the stub patch (Simulated).

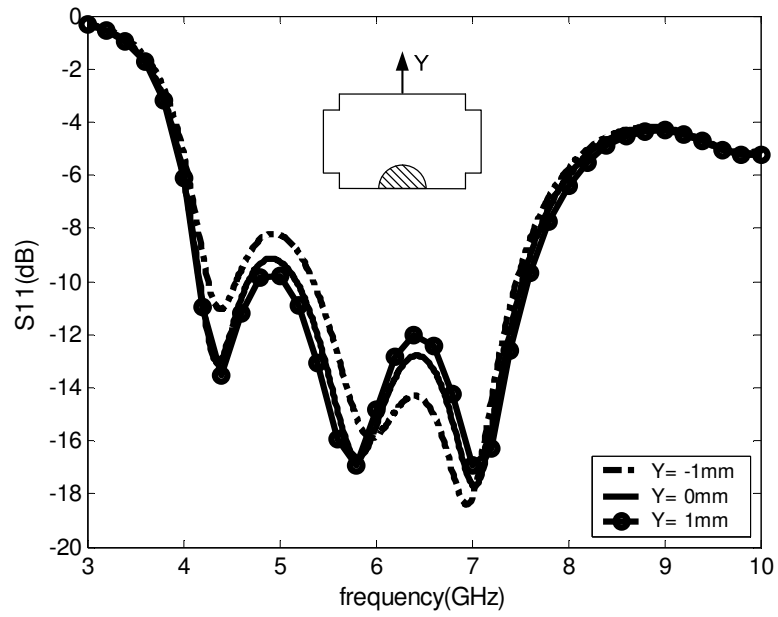


Fig.4.22: Relative longitudinal translation between the fed patch and the stub patch (Simulated).

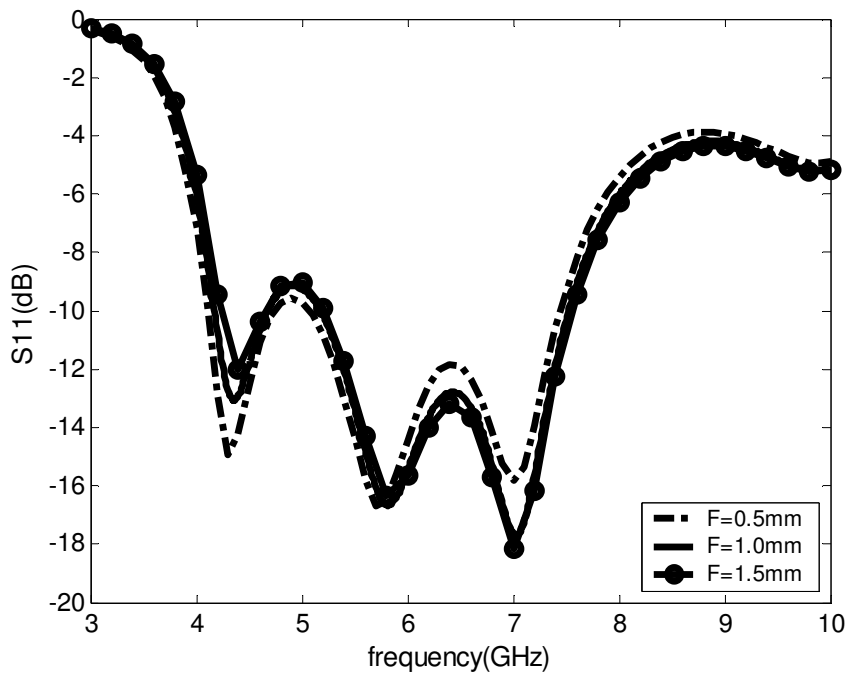


Fig.4.23: Variation of the feed position, F of the semi-circle probe-fed stub patch antenna.

After studying the effects of the various parameters on the impedance matching, a

reliable design guideline for the stub-patch antenna is developed. The following procedures are recommended to design the antenna:

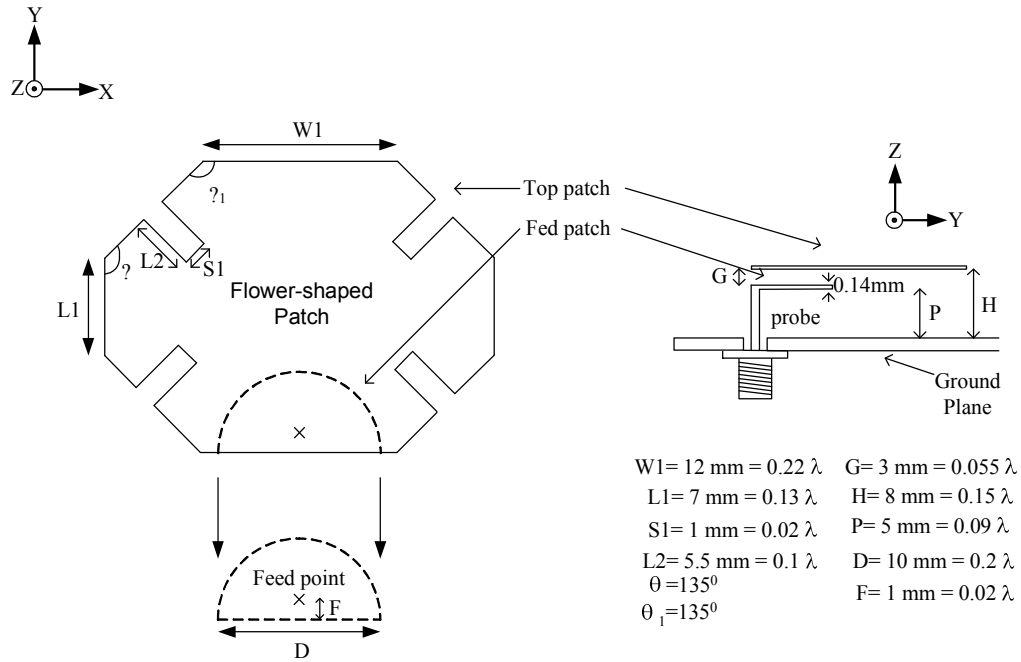
- Step 1: Calculate the resonant length of the rectangular patch  $W$  and  $L$  with equation (3.28) and equation (3.29).
- Step 2: Choose a probe height. Determine the diameter of the semi-circle using equation (4.1) to equation (4.3).
- Step 3: Add two stubs at the side of the rectangular patch with length,  $L1 \approx 0.24\lambda$  and width  $W1 \approx 0.07\lambda$ .
- Step 4: Determine the gap,  $g$  with  $g \approx 0.04\lambda$  between the patch and the semi-circle probe.

#### 4.3.3 Semi-circle Probe-fed Flower-shaped Patch Antenna

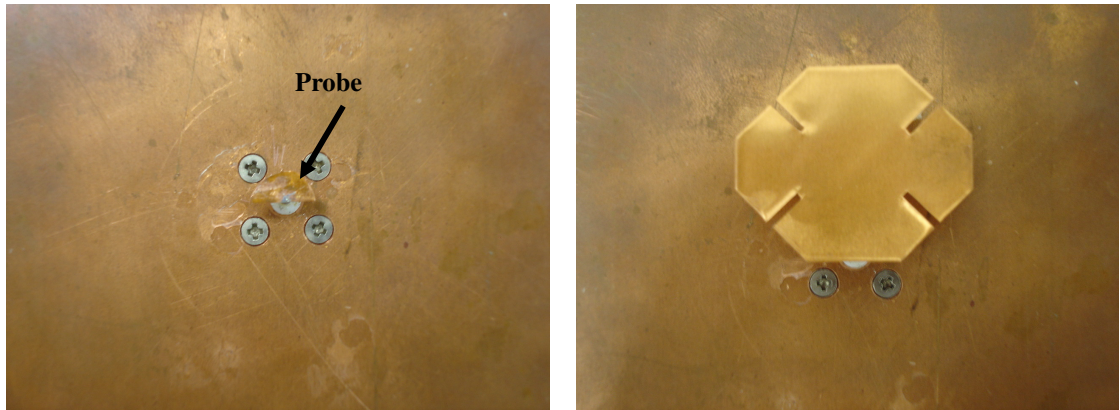
Besides feeding a stub patch, the semi-circle probe is also able to feed patch antenna with different patch shapes. A flower-shaped patch is next used in the study. The antenna has center frequency around 5.4 GHz and the height of the substrate is approximately  $0.1\lambda$ . The flower-shaped antenna made use of higher order modes to achieve wideband performance.

##### 4.3.3.3 Antenna Structure

Fig. 4.24 shows the geometry and photographs of the fabricated flower-shaped microstrip patch antenna. The antenna comprises a flower-shaped microstrip patch in the first layer, a semi-circle-fed patch in the second layer and a ground plane. The exact dimensions of the antenna are given in Fig. 4.24(a).



(a)



(b)

Fig. 4.24: (a) Geometry of semi-circle probe-fed flower-shaped patch antenna. (b) Photographs of the fabricated semi-circle probe-fed stub patch antenna.

#### 4.3.3.3 Simulations and Measurements

Fig.4.25 compares the simulated and measured return loss of the semi-circle probe-fed flower-shaped patch antenna. The measured impedance bandwidth for our proposed antenna is approximately 63% (3.875 GHz - 7.45 GHz). The deviations

between the simulated and measured results are caused by the inaccurate modeling of the semi-circle probe-fed.

Fig.4.26 shows a comparison of impedance bandwidth performance between the flower-shaped, a rectangular patch antenna and a diamond-shaped (using a similar-size rectangular patch but with the four corners being chipped off) antenna. All three antennas are subjected to the same excitation. From the results given in Fig.4.26, we observed that the diamond-shaped antenna has an impedance bandwidth of 47.9%. The slanted edge of the diamond-shaped antenna helps to introduce another resonance dip at 6 GHz by exciting the next higher-order mode, which is absent from the response due to the rectangular patch antenna. By further introducing the flower-shaped patch antenna, we observed that this resonance dip is pushed outwards to 7 GHz, thus producing an extension to the impedance bandwidth (63%). From the smith chart shown in Fig.4.27, it is observed that by modifying the rectangular patch antenna into a diamond patch antenna, an inductive shift occurs at the higher frequencies. The gap between the flower petals acts as a series capacitor, giving capacitive coupling as indicated by a downward shift in the impedance locus of the flower-shaped patch antenna from the diamond patch at the higher and lower frequencies. As noted from Fig.4.28 and 4.29, the length of L2 and S1 play significant roles in controlling the higher frequencies response, with minor effect on the lower frequencies. Through the parametric study of the variable L2 and S1, it is found that the optimal length for L2 and S1 are  $0.09 \lambda$  and  $0.001 \lambda$  respectively.

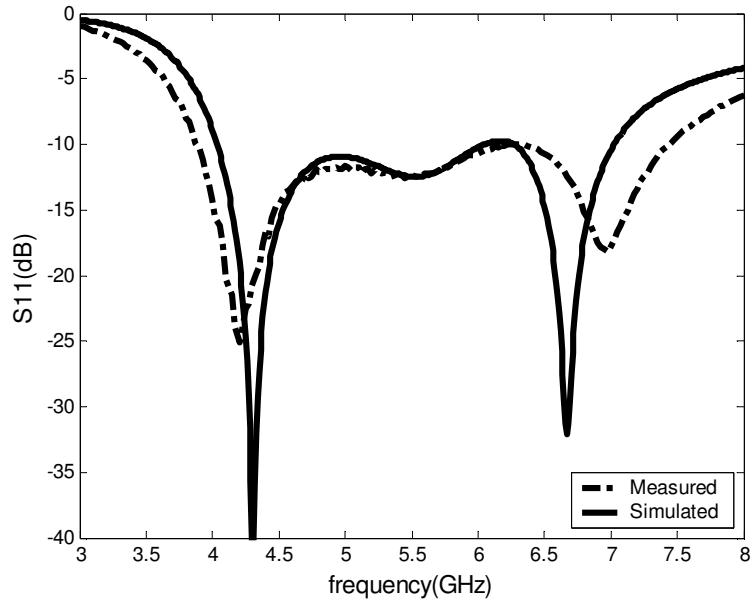


Fig.4.25: Simulated and measured return loss of semi-circle probe-fed flower-shaped patch antenna.

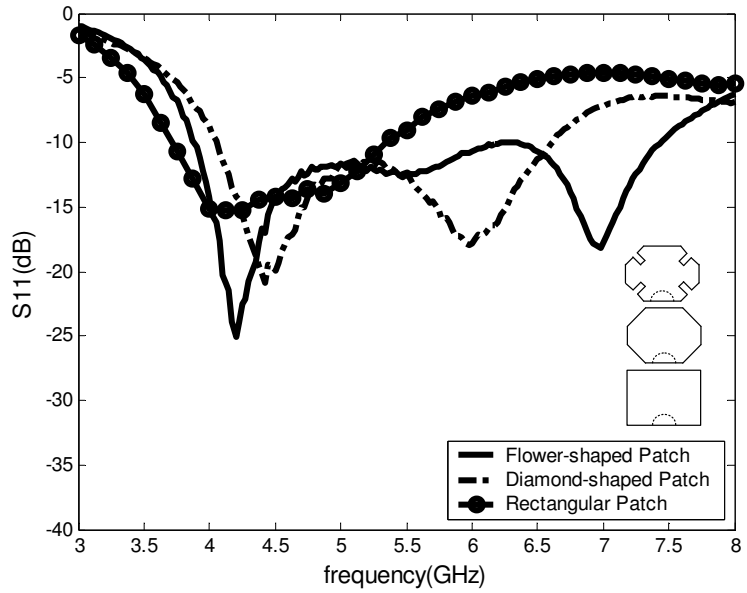


Fig.4.26: Comparison of measured return loss of flower-shaped patch, diamond-shaped patch and rectangular-shaped patch.

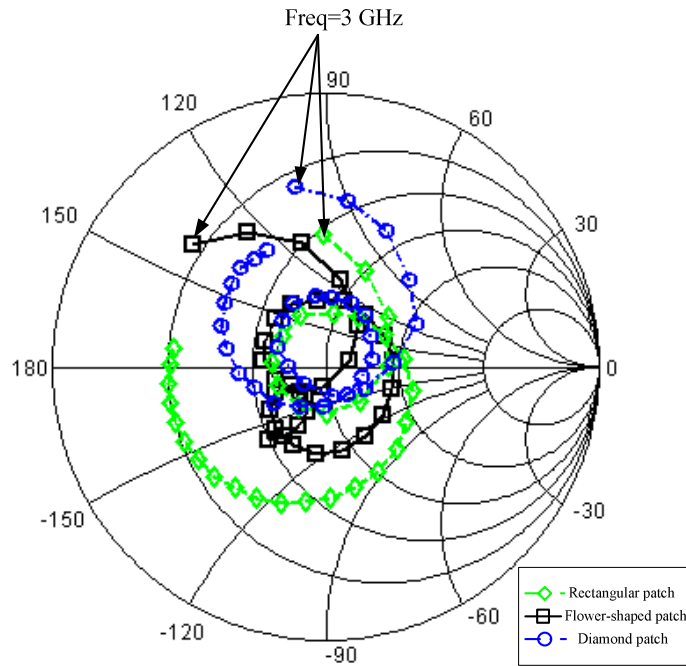


Fig.4.27: Measured impedance locus of the rectangular patch, diamond patch and flower-shaped patch.

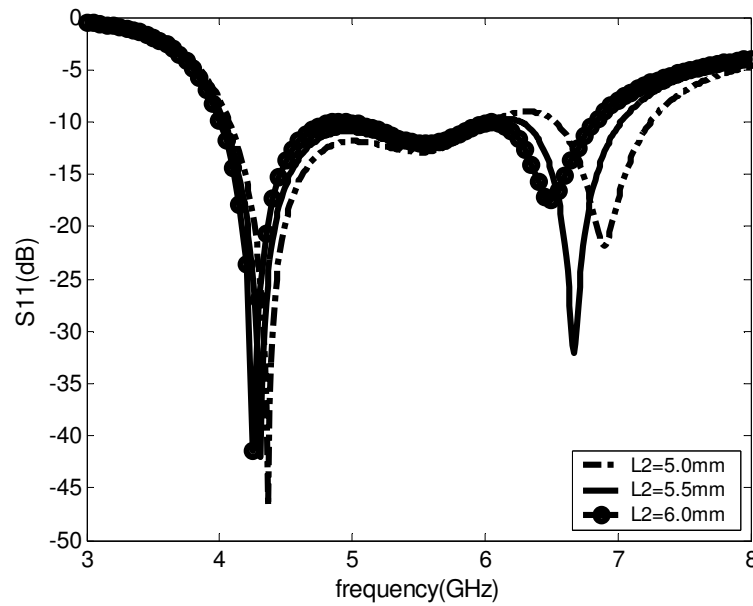


Fig.4.28: Variation of the length  $L_2$  of the flower-shaped patch (simulated).

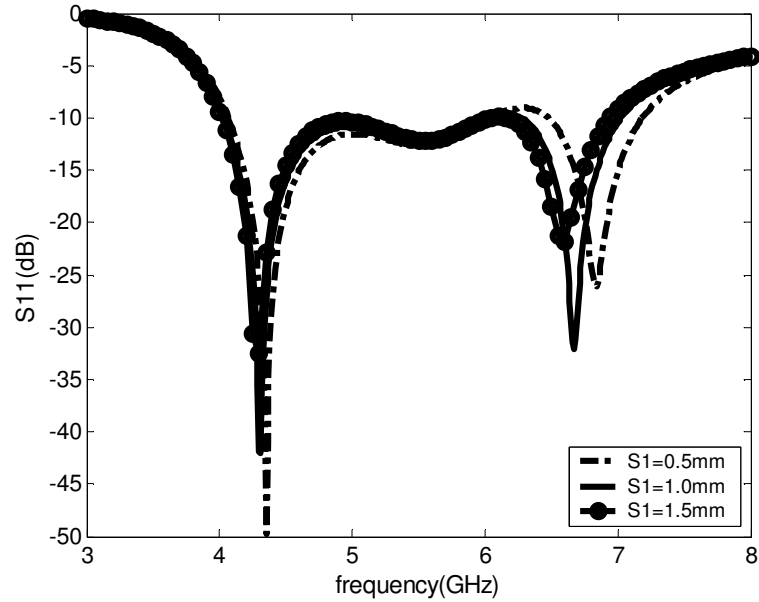


Fig.4.29: Variation of the length S1 of the flower-shaped patch (simulated).

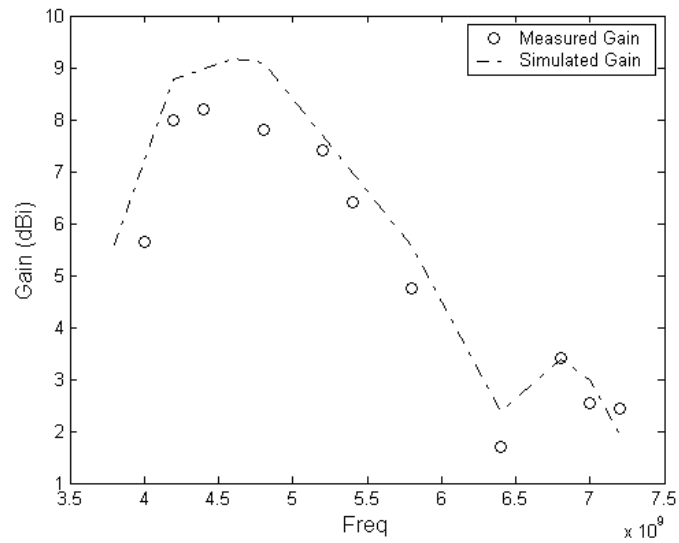


Fig.4.30: Comparison of the broadside gain of the semi-circle probe-fed flower-shaped patch antenna between measurement and simulation.

The measured broadside gain is plotted against the frequency and is represented by circles in Fig.4.30. The maximum measured gain is 8.2 dBi. The 3 dB bandwidth for gain is 31.6%. There is a drop of 7.6% in the 3 dB bandwidth as compared to semi-circle probe-fed stub patch antenna. As the flower-shaped patch increases the



overall length, higher order modes are excited. By inspecting the simulated current distribution in Fig.4.34, it is observed that strong current (indicated by the intensity of the arrow) is created along the 4 slots at the corners of the flower-shaped patch, preventing it to radiate strong vertical polarized field as frequencies increase, leading to a faster drop in gain as compared to stub patch antenna.

Figs 4.31 to 4.33 plot respectively, the measured radiation patterns at 4.2 GHz, 5.4 GHz and 7.0 GHz of the proposed antenna. Similar to probe-fed antenna, there is a beam tilt in the E-plane copolar radiation patterns, which increases with frequency. This is again due to the asymmetric antenna structure. It is observed that a broadside beam is switch to a double beam at an angle  $30^{\circ}$  from the broadside beam at 7.0 GHz. The measured results of the half power beamwidth and the cross polarization level in H-plane radiation pattern are summarized in Table 4.3.

Table 4.3: Summary of the characteristics of flower-shaped patch antenna.

Frequency (GHz)	4.2	5.4	7.0
Half power beamwidth (H-plane)	$71^{\circ}$	$71^{\circ}$	$80^{\circ}$
X-polar Level (dB)	-10.6	-3.25	2.95

Fig.4.34 plots the simulated current distribution of the antenna at 4.5 GHz, 5.5 GHz and 7.0 GHz. At 4.5 GHz and 5.5 GHz, it is observed that currents mainly flow in a vertical direction at the center of the patch while the current follows the shape of the antenna at the sides of the patch, resulting in a lower cross-polarized level than stub patch antenna at 5.4 GHz. As the frequency increases, the current along the upper and lower vertical portion of the patch flows in opposite direction and splits towards the left and the right sides of the patch, having a pattern that is close to  $TM_{11}$  mode.

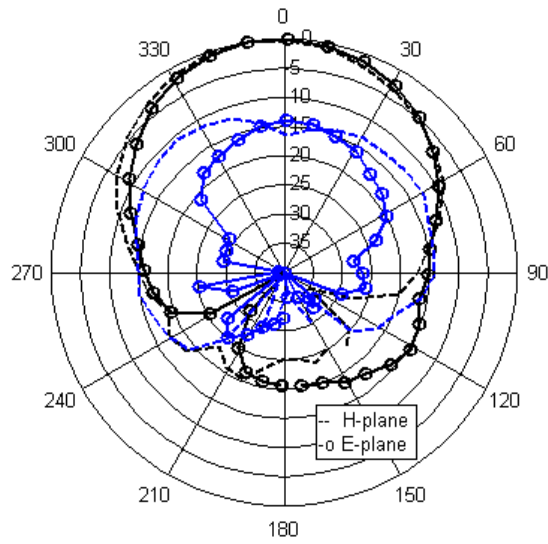


Fig.4.31: Measured radiation patterns for flower-shaped patch antenna at 4.2 GHz. Black lines represent co-polarized pattern. Blue lines represent cross-polarized pattern.

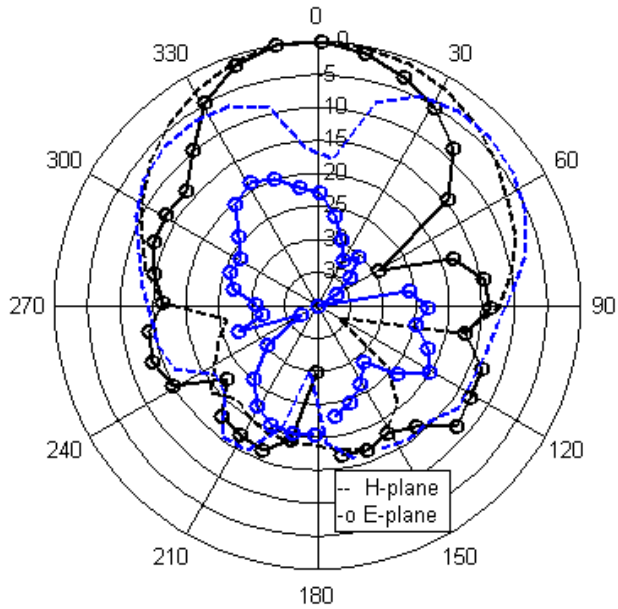


Fig.4.32: Measured radiation patterns for flower-shaped patch antenna at 5.4 GHz. Black lines represent co-polarized pattern. Blue lines represent cross-polarized pattern.

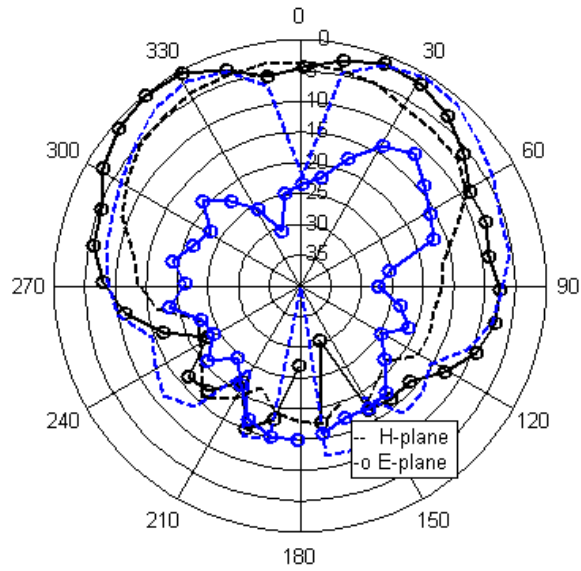
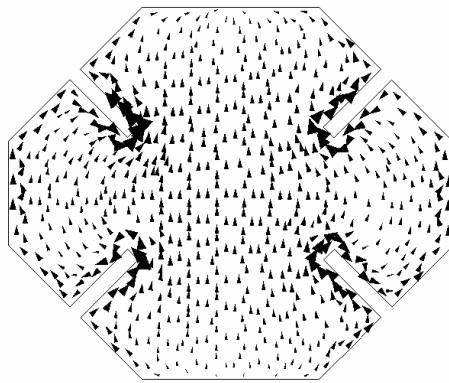
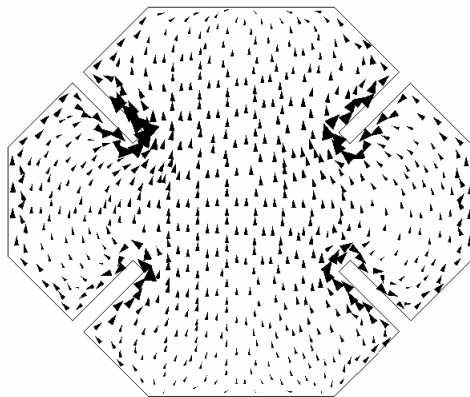


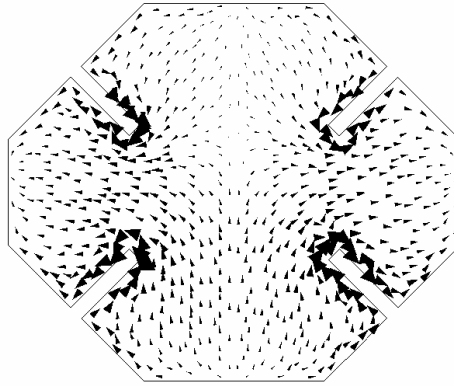
Fig.4.33: Measured radiation patterns for flower-shaped patch antenna at 7.0 GHz. Black lines represent co-polarized pattern. Blue lines represent cross-polarized pattern.



(a)



(b)



(c)

Fig.4.34: Simulated current distribution of the semi-circle probe-fed flower-shaped patch antenna at (a) 4.5 GHz (b) 5.5 GHz (c) 7.0 GHz.

#### 4.3.4 Semi-circle Probe-fed Pentagon-slot Patch Antenna

##### 4.3.4.1 Antenna Geometry

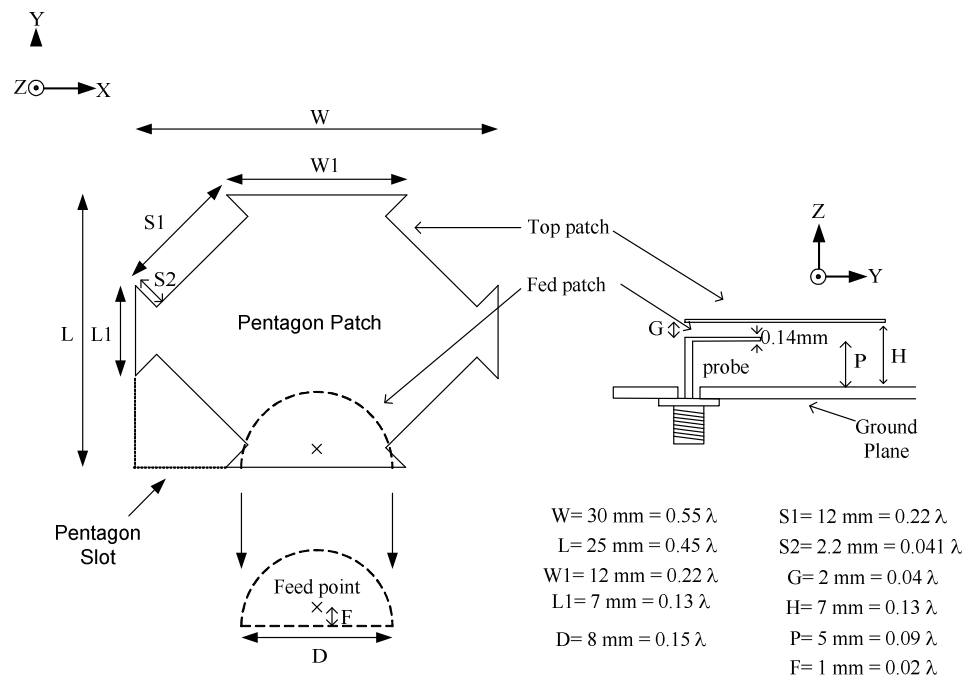
Besides flower-shaped patch antenna, a pentagon-slot patch antenna can also achieve a wideband operation with the semi-circle feeding mechanism. Fig.4.35 shows the geometry of the pentagon-slot patch antenna. The antenna is composed of the pentagon-slot patch in the first layer, a semi-circle-fed patch in the second layer and a ground plane. A pentagon slot is cut at each corner of a rectangular patch (denoted by dotted lines in Fig.4.35 (a)). Fig.4.35 (b) shows the photographs of the fabricated proposed antenna.

##### 4.3.4.2 Simulations and Measurements

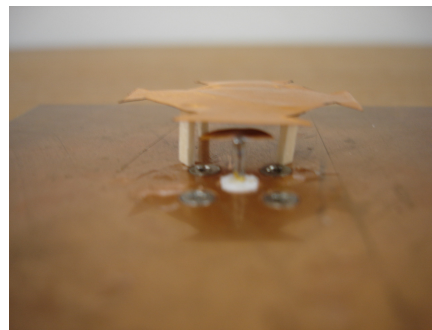
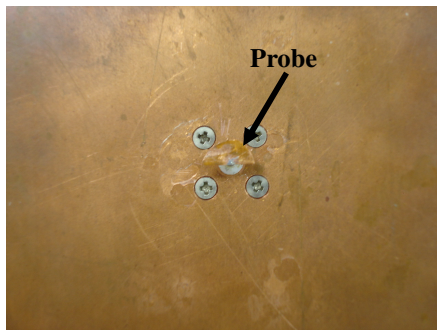
Fig.4.36 displays the simulated and measured return loss results. The measured impedance bandwidth according to the -10 dB return loss is approximately 68.3% (4.125 GHz - 8.4 GHz). The simulated and measured results are in good agreement.

Fig.4.37 shows the measured return loss of the pentagon slot patch, rectangular patch

and semi-circle-fed patch. By cutting a pentagon slot at the four corner of the rectangular patch, the impedance bandwidth improves tremendously. From the smith chart (Fig.4.38), it is observed that a pentagonal-slot patch antenna has five resonant modes at 4.4 GHz, 4.85 GHz, 6.1 GHz, 6.9 GHz and 7.5 GHz while a rectangular antenna has only two resonant modes at 4.2 GHz and 5.65 GHz. Similar to the flower-shaped antenna, the higher frequencies response is controlled by the length  $s_1$  and  $s_2$  as shown in Fig.4.39 and Fig.4.40.



(a)



(b)

Fig.4.35: (a) Geometry of the semi-circle probe-fed pentagon-slot patch antenna. (b) Photographs of the fabricated semi-circle probe-fed pentagon-slot patch antenna.

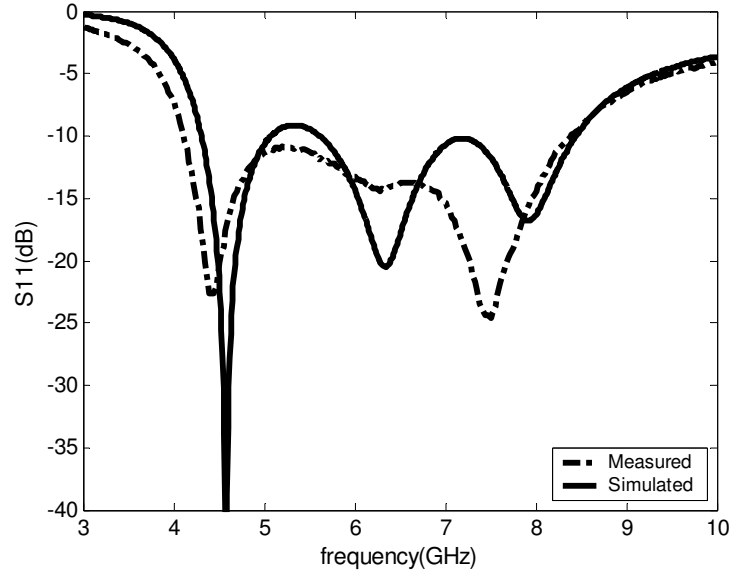


Fig.4.36: Simulated and measured return loss of the pentagon-slot antenna.

The simulated and the measured gains of the antenna at  $\theta=0^{\circ}$  and  $\varphi=0^{\circ}$  were investigated and shown in Fig.4.41. The maximum measured gain is 7.5 dBi, occurring at 5 GHz. The 3 dB gain bandwidth is approximately 45.5% from 4.15 GHz to 6.6 GHz. Among the three designs, this antenna displays the largest 3 dB gain bandwidth. This phenomenon is attributed to the shape of the antenna. The pentagonal slot patch increases its length, thereby exciting higher-order mode. However because of the reduction in the patch length and width toward the end, the excitation of the higher order mode is not very strong and the patch still radiates a strong vertically polarized field as shown in Fig.4.45.

Figs 4.42 to 4.44 plot the measured co-polarized H-plane and E-plane radiation patterns at 4.3 GHz, 6.1 GHz and 7.3 GHz respectively. Table 4.4 summarizes the measured radiation patterns in the H-plane. The half power beamwidth in the H-plane at 4.6 GHz, 6.4 GHz and 7.3 GHz is  $70^{\circ}$ . At 6.1 GHz, the cross-polarized level is -4.31 dB. Fig.4.45 shows the current distributions of the antenna at 4.5 GHz, 5.5 GHz

and 7.0 GHz.

Table 4.4: Summary of the radiation characteristics of pentagon-slot patch antenna.

Frequency (GHz)	4.6	6.1	7.3
Half power beamwidth (H-plane)	$70^{\circ}$	$70^{\circ}$	$70^{\circ}$
X-polar Level (dB)	-15.2	-4.31	1.56

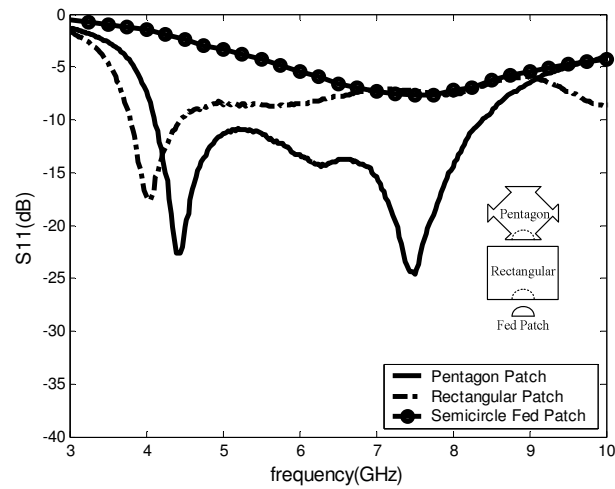


Fig.4.37: Comparison of the measured return loss of the pentagon slot patch, the rectangular patch and the semi-circle fed patch.

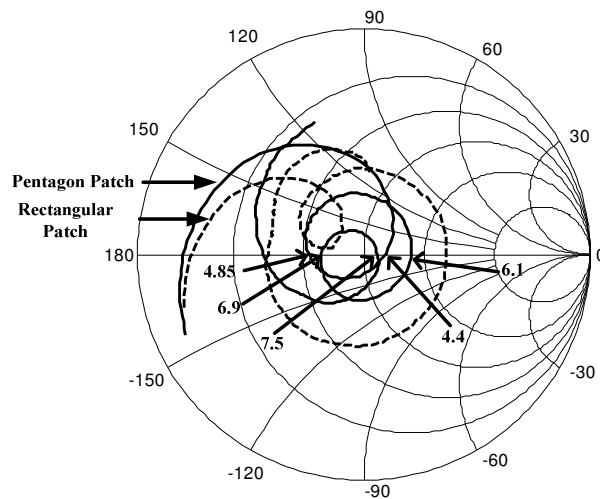


Fig.4.38: Measured input impedance plot of the pentagon slot patch (solid line) and the rectangular patch (dashed line).

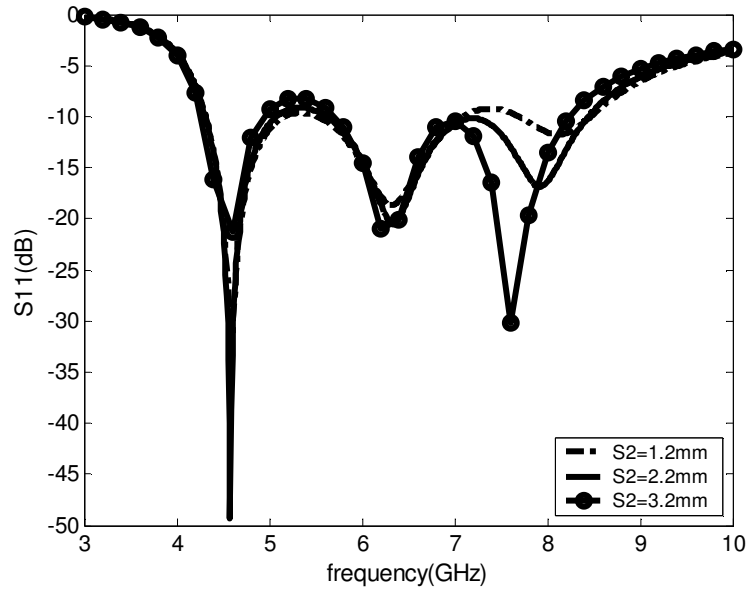


Fig.4.39: Variation of length,  $S_2$  of the pentagon-slot patch (Simulated).

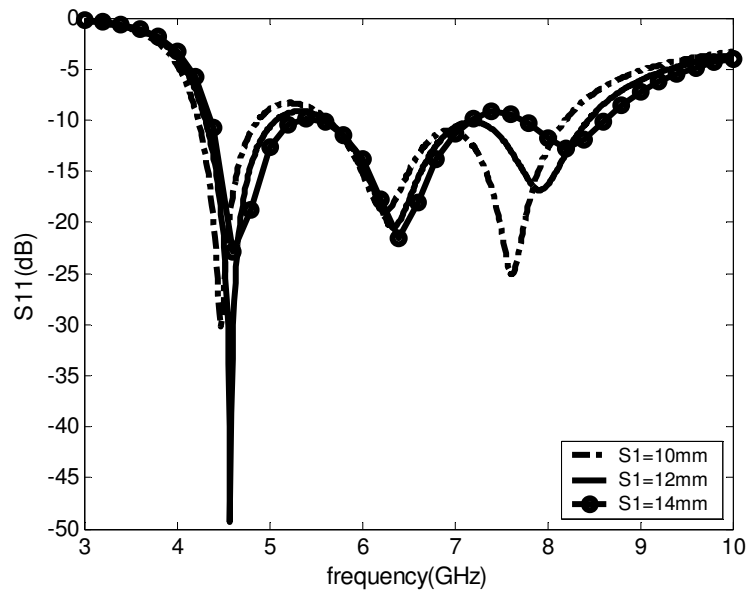


Fig.4.40: Variation of length,  $S_1$  of the pentagon-slot patch (Simulated).



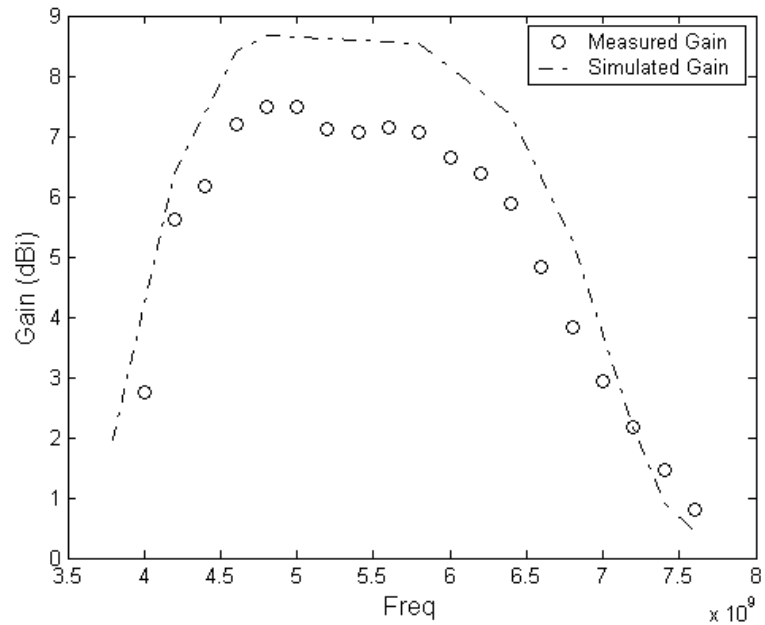


Fig.4.41: Comparison of broadside gain of the semi-circle probe-fed pentagon-slot patch antenna between the measurement and simulation.

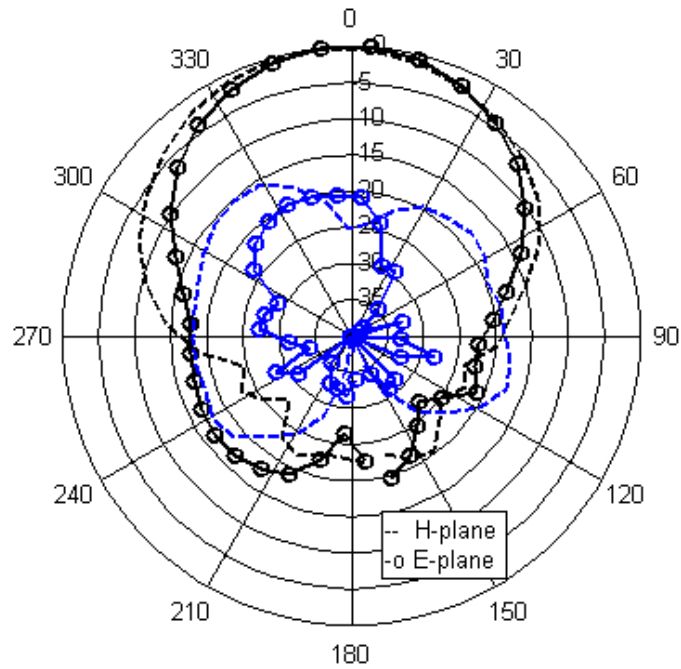


Fig.4.42: Measured radiation patterns of the semi-circle probe-fed pentagon-slot antenna at 4.6 GHz. Black lines represent co-polarized pattern. Blue lines represent cross-polarized pattern.

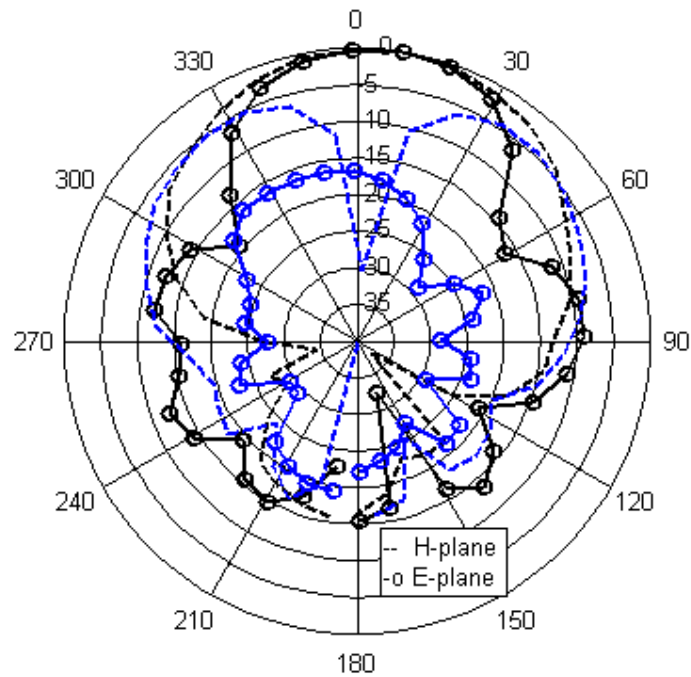


Fig.4.43: Measured radiation patterns of the semi-circle probe-fed pentagon-slot antenna at 6.1 GHz. Black lines represent co-polarized pattern. Blue lines represent cross-polarized pattern.

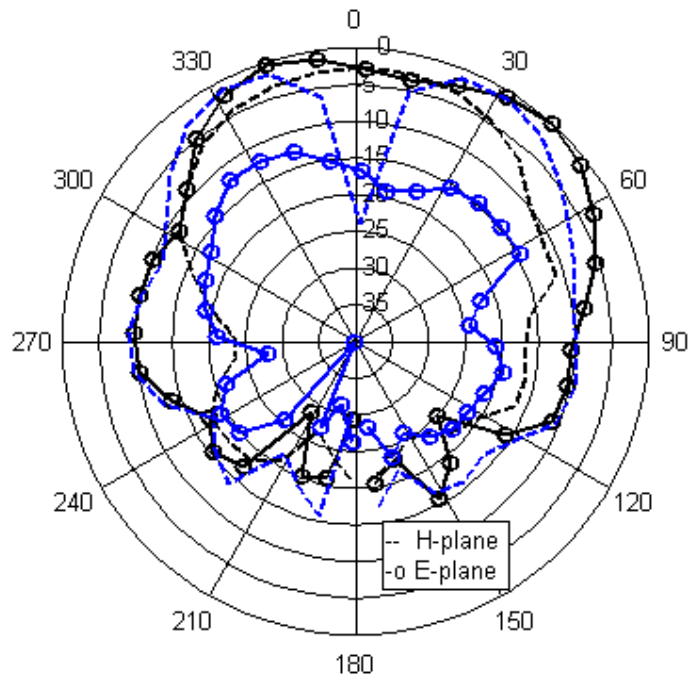
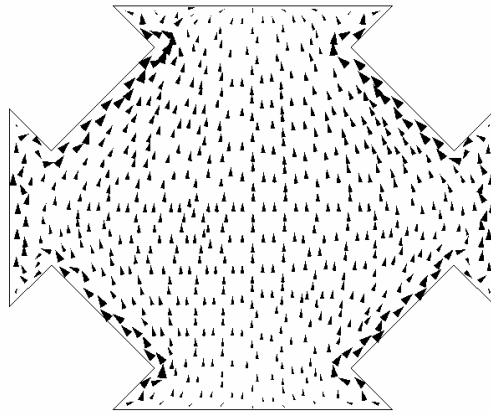
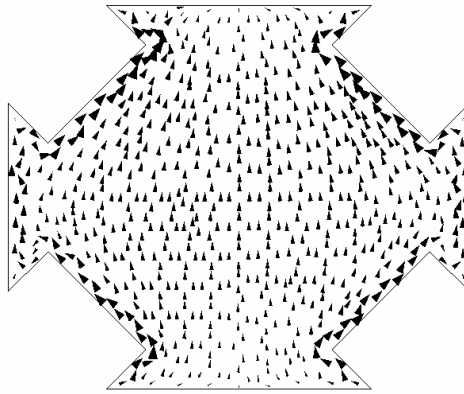


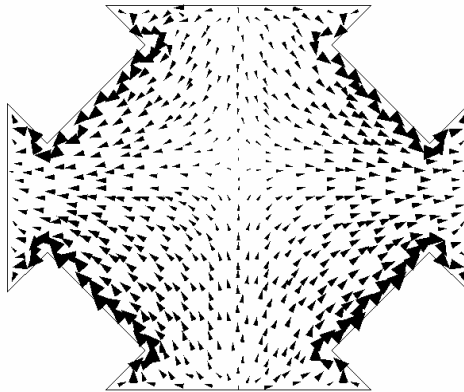
Fig.4.44: Measured radiation patterns of the semi-circle probe-fed pentagon-slot antenna at 7.3 GHz. Black lines represent co-polarized pattern. Blue lines represent cross-polarized pattern.



(a)



(b)



(c)

Fig.4.45: Simulated current distributions of the semi-circle probe-fed pentagon-slot patch antenna at (a) 4.5 GHz (b) 5.5 GHz (c) 7.0 GHz.

Table 4.5 shows a summary of the performance of the three proposed probe-fed patch

antennas. Among the three proposed antennas, the pentagonal slot patch antenna gives the best performance with an impedance bandwidth of 68.3% and a 3 dB broadside gain bandwidth of 45.5%. In addition, it has the lowest cross-polarized level of -7.1 dB at 5.4 GHz. All the three antennas have impedance bandwidth greater than 45%. However, only pentagon slot patch antenna meets all the specifications stated earlier in Table 4.1.

Table 4.5: Summary of the performance of the three proposed probe fed patch antennas.

	Impedance BW	3 dB BW (gain)	Broadside Gain at 5.4 GHz	X-polar level at 5.4 GHz
Stub patch	62.3%	39.2%	6.36 dBi	-1.31 dB
Flower-shaped patch	63%	31.6%	6.4 dBi	-3.25 dB
Pentagon Slot patch	68.3%	45.5 %	7.07 dBi	-7.1 dB

#### 4.4 Semi-circle Probe-fed Microstrip Stub Array

Microstrip patch antennas are very often used in array configurations where there might be specific requirements in terms of antenna gain, beamwidth and polarization. Among the three proposed antenna elements, the stub antenna has the simplest structure and the highest cross-polarized level at 5.4 GHz. Hence, this antenna element is used to develop an antenna array. In this section, two applications for mobile communication system are addressed where stub patch antennas with semi-circle probes can be very useful. The first application is for system in which polarization purity does not represent a constraint and the second application is for linearly polarized system. To increase antenna efficiency and gain, a low loss material should be used to fabricate the feed network. However, due to the size limitation of

our fabrication equipment in the microwave laboratory, the feed networks are etched on a FR4 substrate with relative permittivity 4.4, thickness 1.6mm and loss tangent of approximately 0.02 instead of low loss materials such as Duroid or Rogers. It has been reported in [115] that FR4 is quite lossy at 5 GHz. A typical 50  $\Omega$  transmission line on FR4 has a loss of about 0.2 dB/ cm at 5 GHz. Thus, it is important to keep the transmission lines short. In this thesis, we will investigate two different feed networks (a longer feed network and a shorter feed network) and study their effects on the gain of the antenna array.

#### 4.4.1 4 by 4 Semi-circle Probe-fed Microstrip Stub Patch Antenna Array

##### 4.4.1.1 Antenna Geometry

The geometry of the antenna array for the first application is shown in Fig.4.46. It consists of 16 antenna elements and they are separated by a distance  $G_x=15$  mm and  $G_y=15$  mm. Each antenna element has the same dimension given in Fig 4.8. The size of the ground plane is 26 by 28 cm. The total number of basis functions for the 4 by 4 array is 12520. Each antenna element is excited with uniform excitation. The feed network is not included in the simulation. Since the feed network is separated from the array elements by a ground plane, it is possible to perform separate simulations on both the feed network and the array elements as the spurious radiation from the feed network will not have significant effect on the broadside radiation.

After the design of the array has been completed, we will next consider the design of the feed network that provides the required excitations for the semi-circle probe-fed stub patch antenna elements. Since the antenna element is excited with uniform excitation, a feed network that is made up of identical power dividers is developed.

The power divider is connected to the semi-circle probe through a small circular hole formed in the ground plane.

The power divider is made up of quarter-wavelength impedance transformer to match  $100 \Omega$  input to  $50 \Omega$  antenna element as shown in Fig.4.47. The insert in Fig.4.48 shows the layout of the power divider. The quarter-wavelength impedance transformer is bent to optimize the space. The measured S-parameters response of a power divider is shown in Fig.4.48.

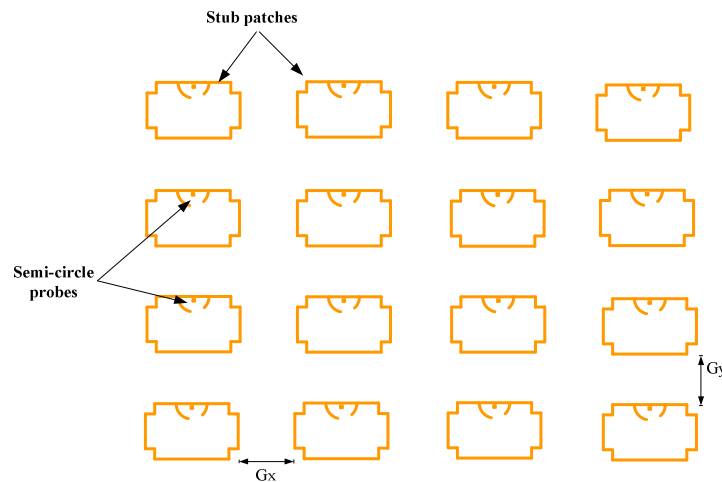


Fig.4.46: 4 by 4 semi-circle probe-fed microstrip stub patch antenna array.

In this thesis, two different feed networks, A and B are designed as depicted in Fig.4.49 (a) and (b) respectively. Feed network A is approximately 70 cm longer than feed network B. The average current density of the two feed networks is shown in Fig.4.50. It is observed that there is no distinct color difference among the output Ports 2 to 17 for both the feed networks, implying that the difference among the current density at the output ports is not large. The arrows in the diagram indicate the direction of the current. It is observed that as long as the symmetry of the geometry is maintained, and as long as the port excitation is uniform in amplitude and phase, the

cancellation of the cross-coupling contributions from the feed network occurs. For feed network B only the vertical section of the transmission line from Port 1 and the small horizontal sections of the transmission line towards the output ports are susceptible to the cross-coupling. Fig.4.51 shows the simulated S-parameters (S11 and S21) of feed network A and feed network B from 3.5 GHz to 7.5 GHz. The return loss (S11) of feed network B is below -10dB throughout the frequency range while the return loss of feed network A hover around -10 dB at the higher frequency range. At 5.4 GHz, the S21 of feed network B is around -17 dB while that of feed network A is around -23.9 dB. There is an additional loss of around -6.9 dB for a longer feed network as compared to the shorter feed network. The high losses in the feed networks are due to the lossy material used as explained above. The feed network is simulated independently from the array elements. The voltage at each port where the element is fed by the feed network is computed and stored. The radiation pattern from the elements is determined using the excitation voltage obtained from the feed network. Fig.4.52 shows a prototype of the fabricated antenna array and Fig.4.53 shows the far field measurement for the antenna array in the anechoic chamber.

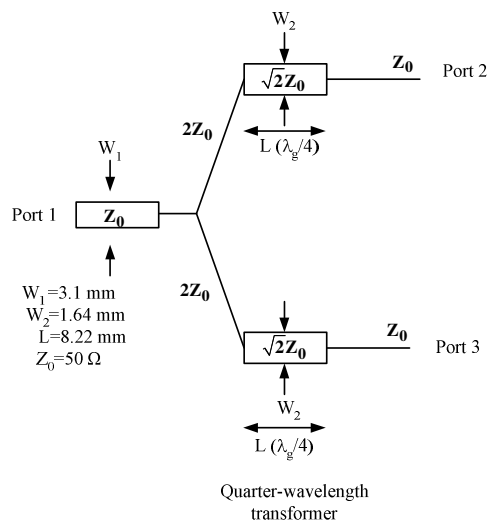


Fig.4.47: Circuit schematic of a Power Divider.

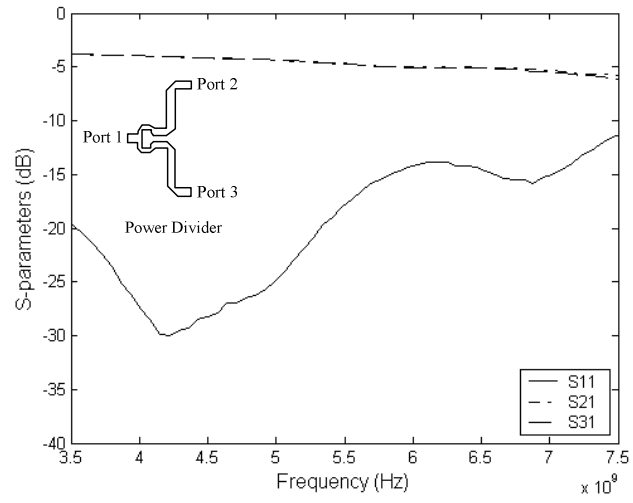
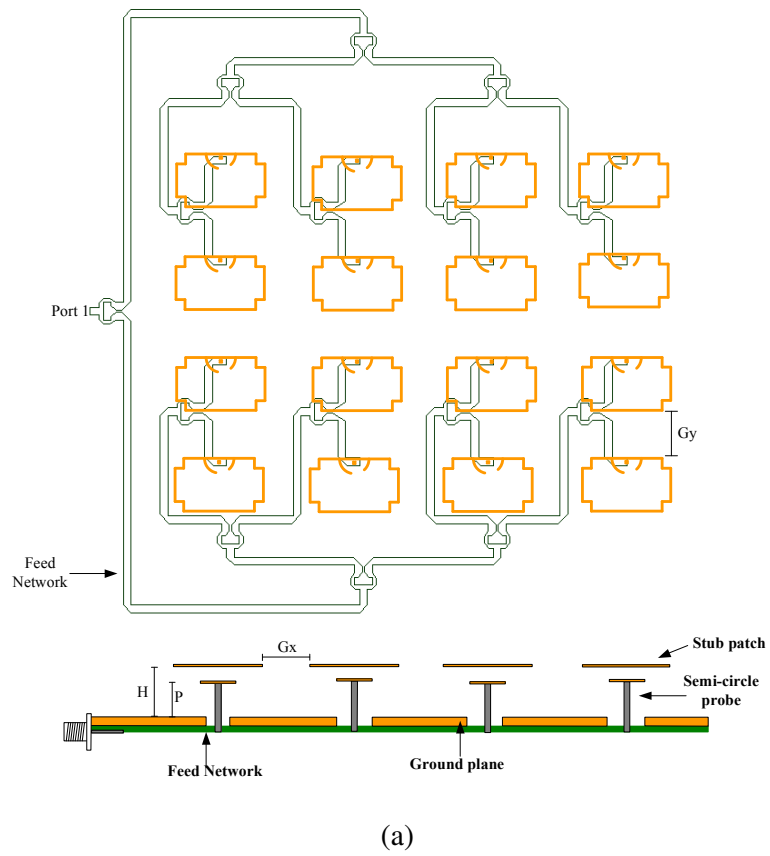
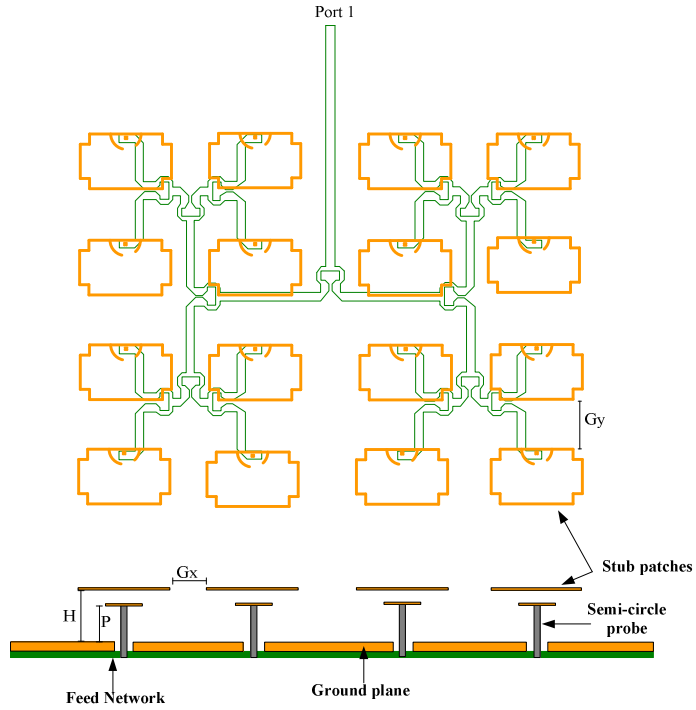


Fig.4.48: Measured S-parameters of a power divider.

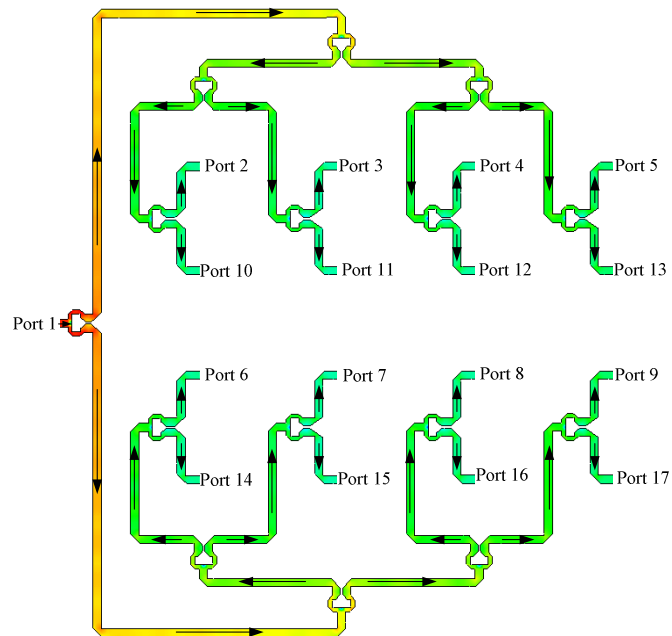




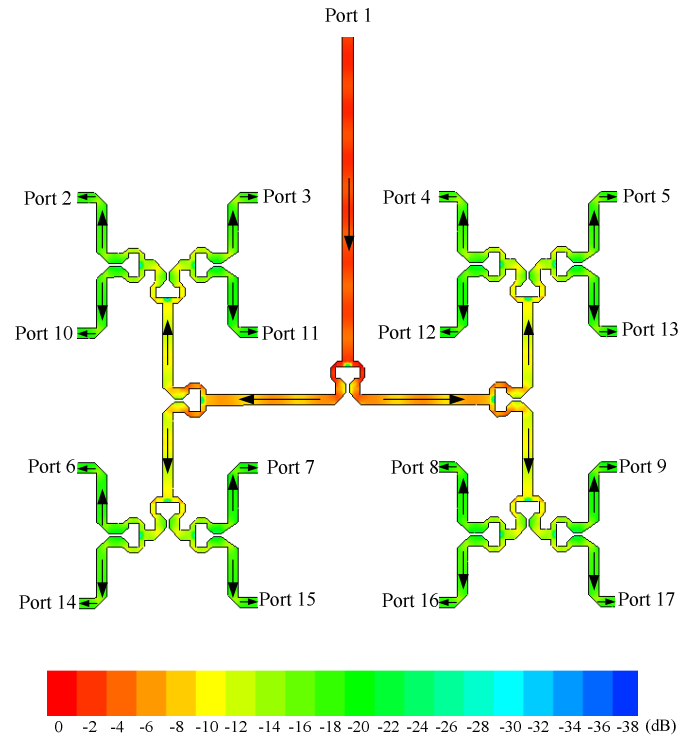


(b)

Fig.4.49: 4 X 4 semi-circle probe-fed microstrip stub patch antenna array. (a) Feed Network A (b) Feed Network B

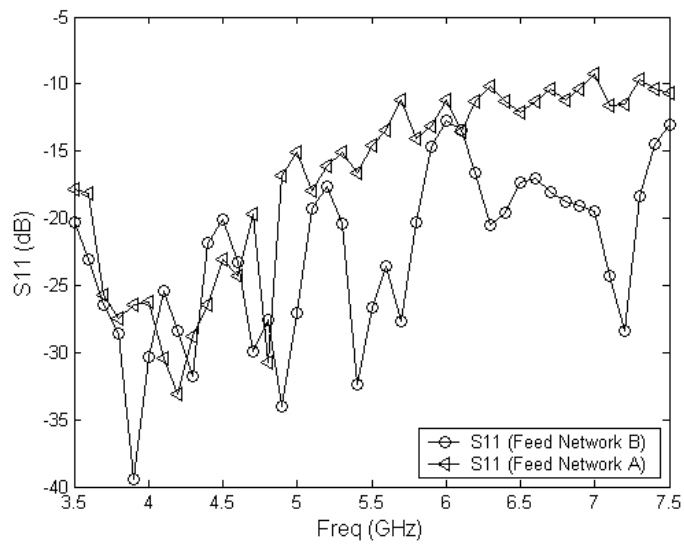


(a)

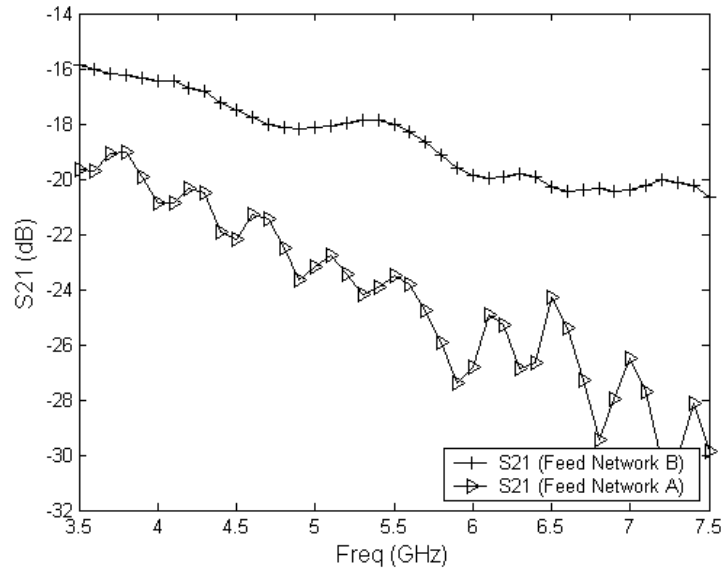


(b)

Fig.4.50: Average current density of the feed network at 5.4 GHz. The arrows indicate the direction of the current (a) Feed network A (b) Feed network B.



(a)



(b)

Fig.4.51: Simulated S-parameters of feed network A and feed network B. (a) S11 (b) S21.

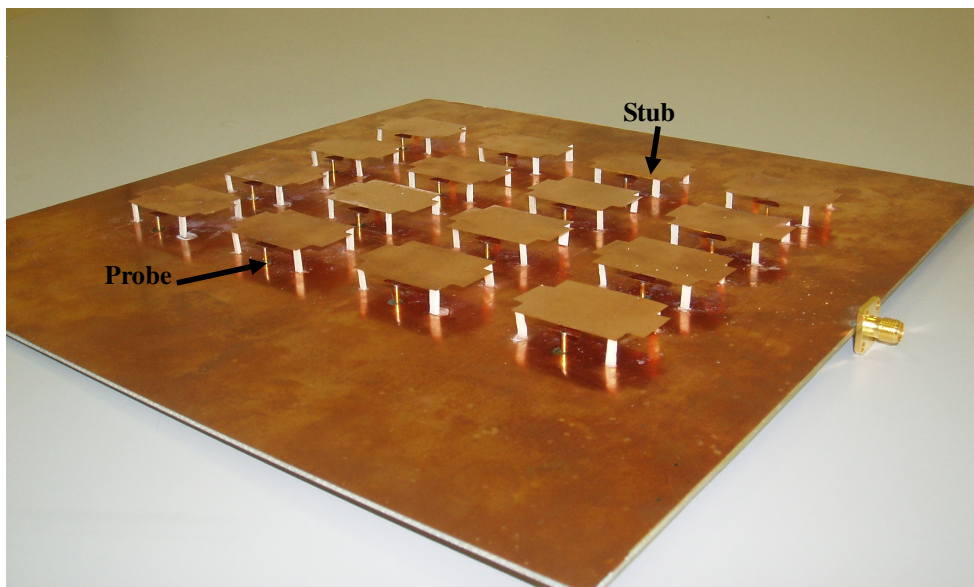


Fig.4.52: Photograph of the 4 X 4 semi-circle probe-fed stub patch antenna array with feed network A.

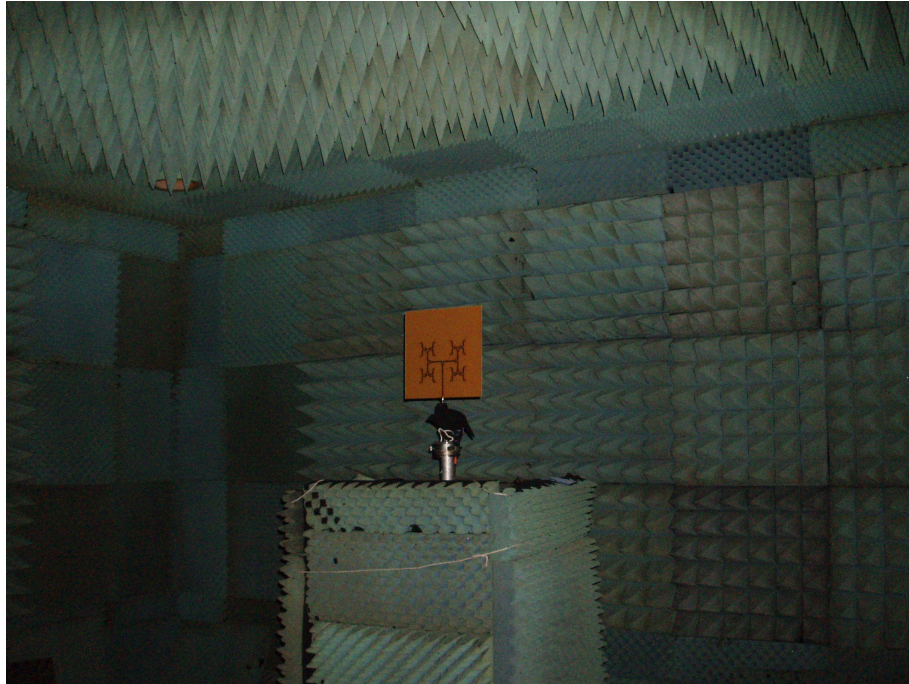
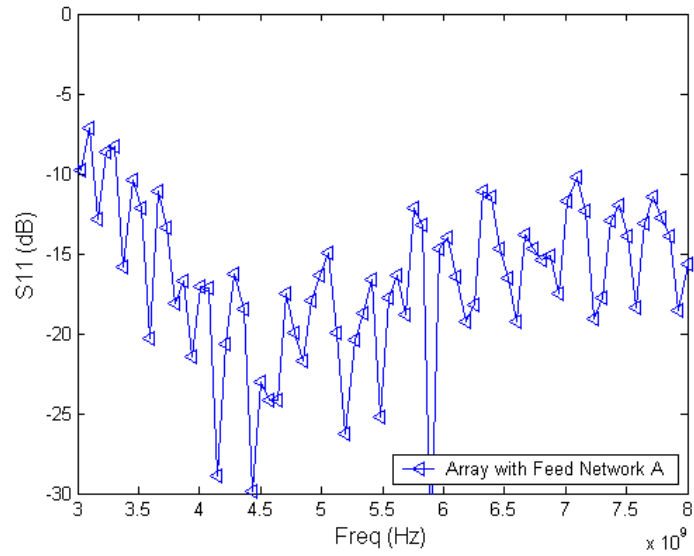


Fig.4.53: Far field measurement for the 4 X 4 semi-circle probe-fed stub patch antenna array in the anechoic chamber.

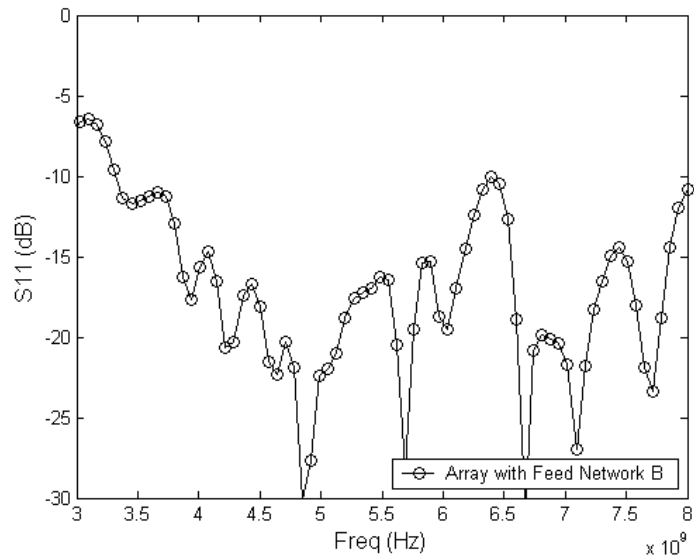
#### 4.4.1.2 Simulations and Measurements

Fig.4.54 (a) and (b) show the measured return loss of a 4 by 4 antenna array with feed network A and feed network B respectively. The antenna has a wide bandwidth. As indicated in the figure, within the frequency range (3 GHz to 8 GHz), the return loss of the antenna is approximately below -10 dB from 3.5 GHz onwards for both feed network A and feed network B..

Table 4.6 shows a summary of the simulated broadside gain without the effect of the feed network and the measured broadside gain with feed network A and feed network B. We observe that the losses due to the transmission lines have significant effect on the overall gain. There is an improvement of around 2.4 dBi to 4.35 dBi in gain when shorter feed network B is used instead of feed network A.



(a)



(b)

Fig.4.54: Measured return loss of the 4 X 4 semi-circle probe-fed stub patch antenna array with (a) Feed Network A and (b) Feed Network B.

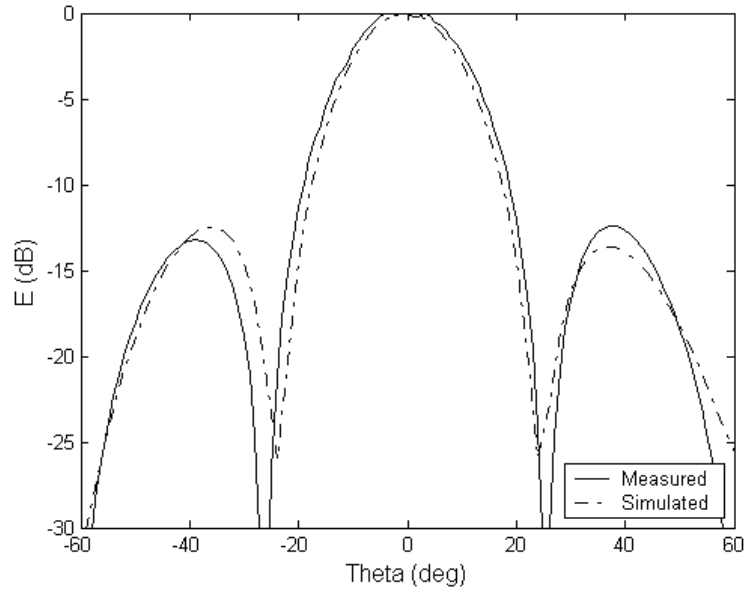
Table 4.6: Comparison of the simulated and the measured gains of the 4 X 4 semi-circle probe-fed stub patch antenna array.

Freq (GHz)	Simulated Gain (dBi) without feed network	Measured Gain (dBi)	
		With Feed Network A	With Feed Network B
4.2 GHz	19	13.2	15.6
5.4 GHz	18.13	10.1	13.1
7.0 GHz	14.83	2.0	6.95

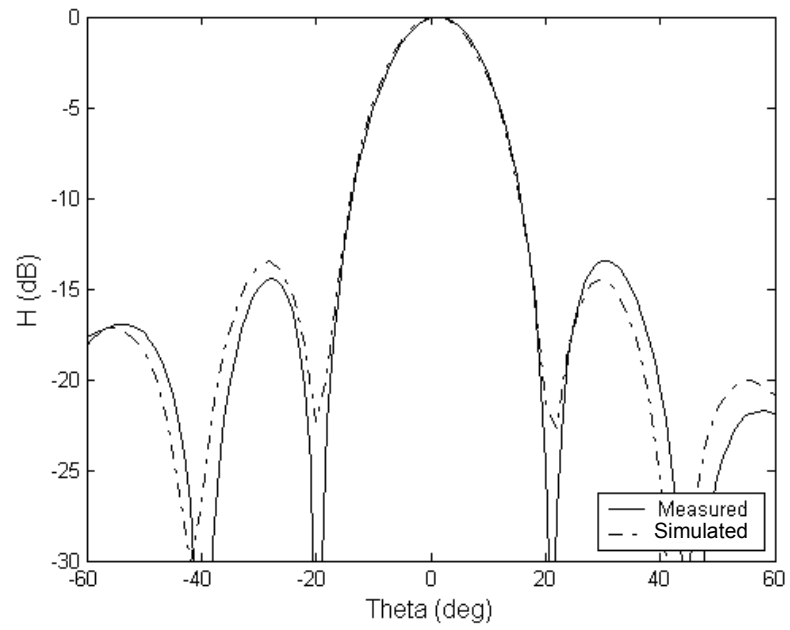
Figs 4.55 to 4.57 show the radiation patterns at 4.2 GHz, 5.4 GHz and 7.0 GHz respectively. Since the cross-polarized levels in the E-plane are below -25 dB for the three frequencies, their patterns are not shown for brevity. Generally there is a good agreement between the simulated and the measured results. The difference is possibly due to experimental tolerance and the radiation from the feed network that is not taken into account in the simulation. At 7.0 GHz, there is a 2 degree beam tilt in the E-plane copolar radiation pattern. The measured half-power beamwidths and the cross-polarized level in the H-plane are summarized in Table 4.7. At 5.4 GHz, the 3 dB beamwidth in the H-plane and the E-plane are  $15^{\circ}$  and  $14^{\circ}$  respectively.

Table 4.7: Summary of the radiation characteristics of the 4 X 4 semi-circle probe-fed stub patch antenna array with feed network B.

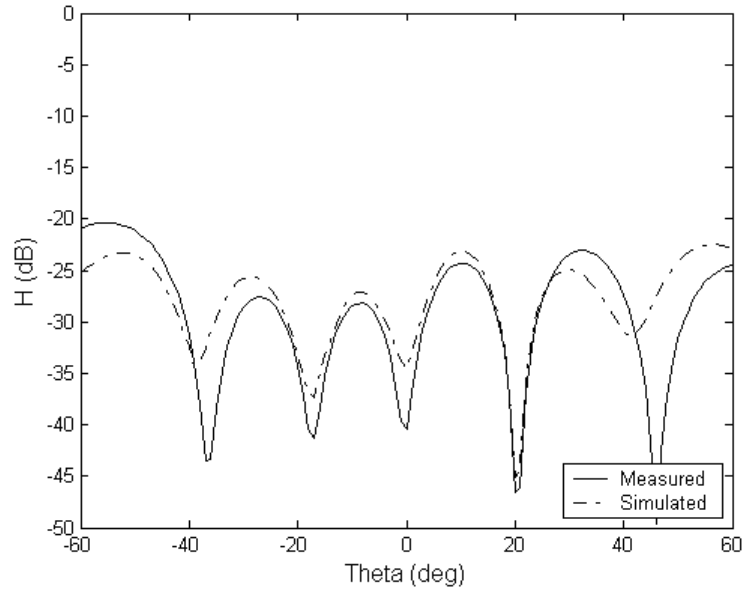
Freq (GHz)	Half-power beamwidth		X-polar level (dB)
	E-plane	H-plane	
4.2 GHz	$22.5^{\circ}$	$18^{\circ}$	-20.3
5.4 GHz	$15^{\circ}$	$14^{\circ}$	-11.05
7.0 GHz	$12^{\circ}$	$10.5^{\circ}$	2.51



(a)

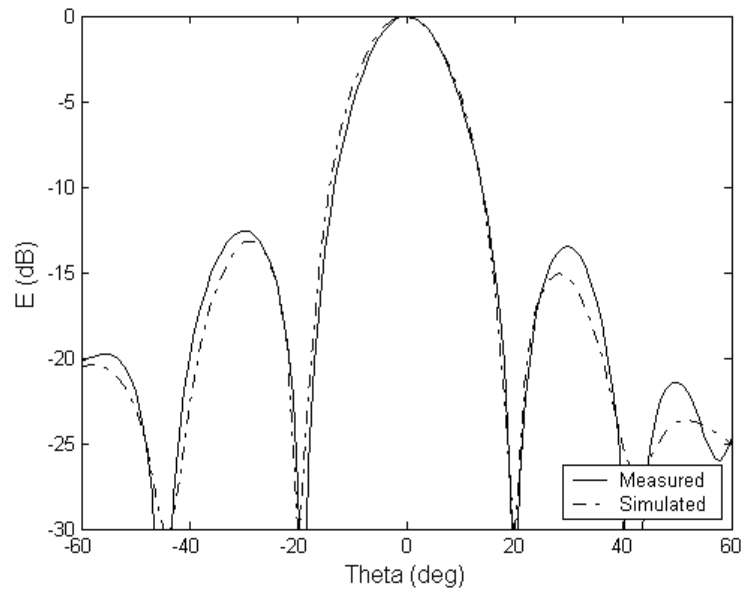


(b)



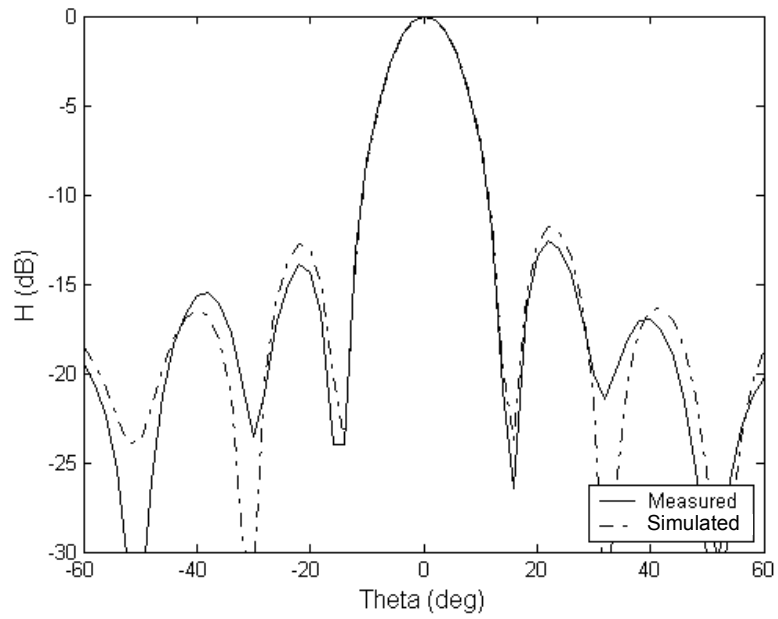
(c)

Fig.4.55: Radiation patterns of the 4 X 4 semi-circle probe-fed stub patch antenna array at 4.2 GHz. (a) Co-polarized pattern in E-plane (b) Co-polarized pattern in H-plane (c) Cross-polarized pattern in H-plane

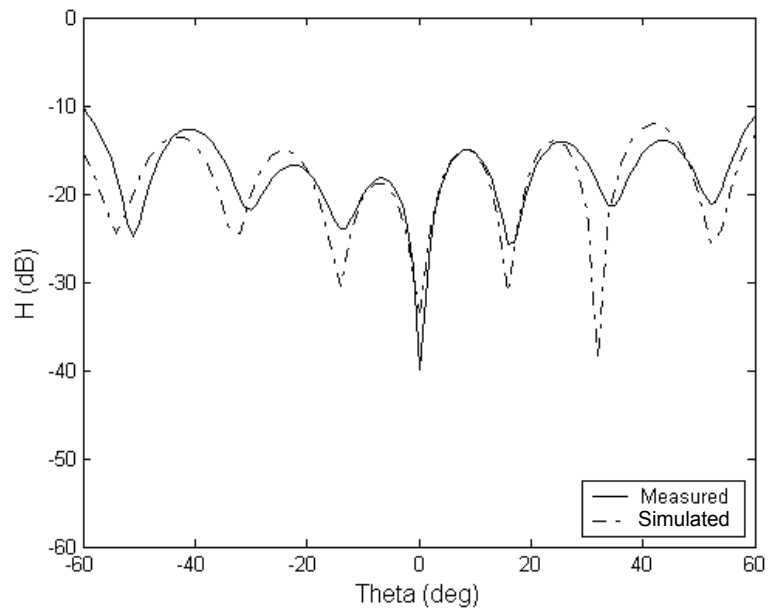


(a)



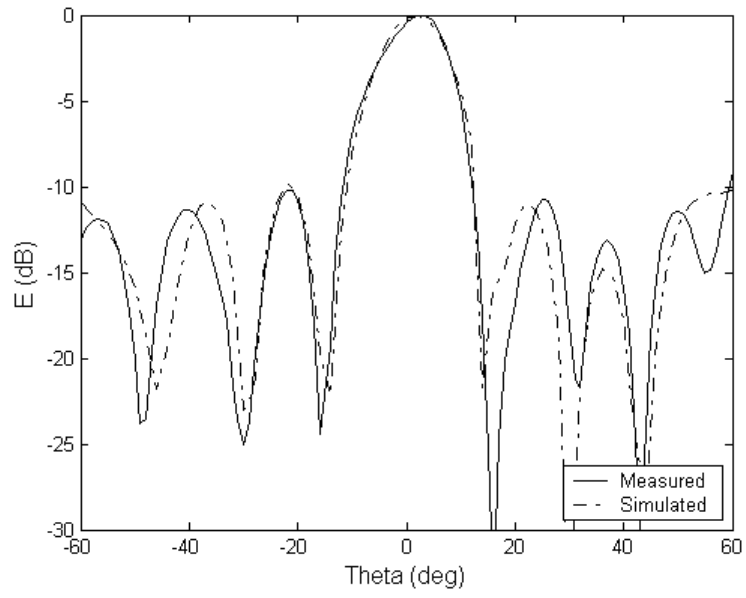


(b)

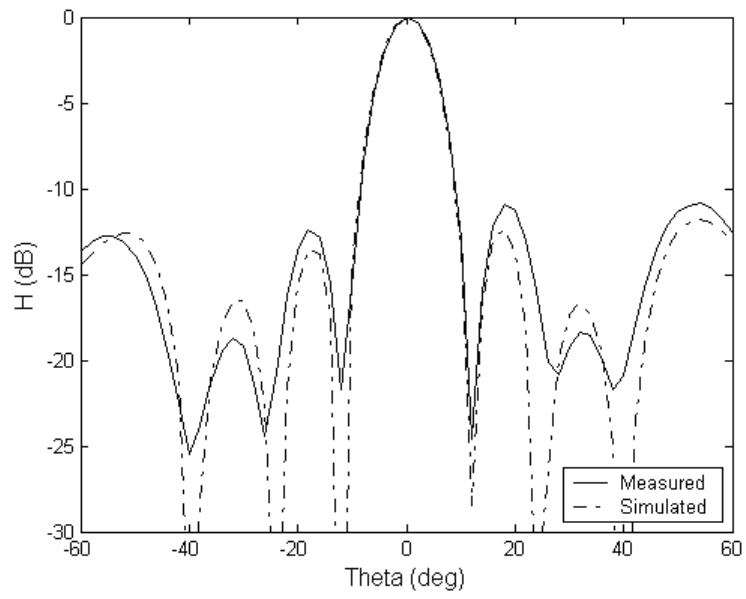


(c)

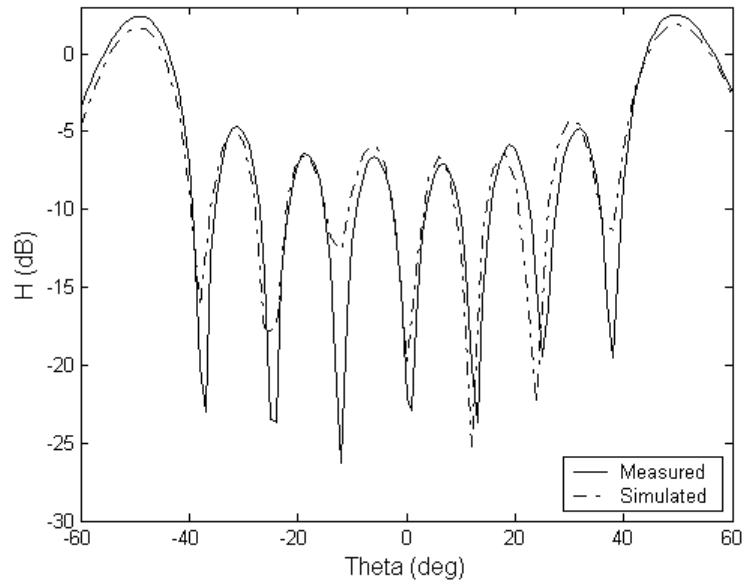
Fig.4.56: Radiation patterns of the 4 X 4 semi-circle probe-fed stub patch antenna array at 5.4 GHz. (a) Co-polarized pattern in the E-plane (b) Co-polarized pattern in the H-plane (c) Cross-polarized pattern in H-plane



(a)



(b)



(c)

Fig.4.57: Radiation patterns of the 4 X 4 semi-circle probe-fed stub patch antenna array at 7 GHz. (a) Co-polarized pattern in the E-plane (b) Co-polarized pattern in the H-plane (c) Cross-polarized pattern in the H-plane

#### 4.4.2 Two-element Linearly-polarized Array

##### 4.4.2.1 Antenna Geometry

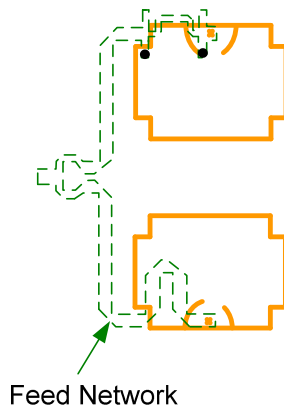


Fig.4.58: 2 X 1 linearly polarized array.

For some applications, it is required that the cross-polarization levels of the antennas

are low. It is possible to reduce the cross-polarization levels of a probe-fed patch antenna by using two elements that are positioned in a back-to-back configuration as shown in Fig.4.58. The two ports have to be excited exactly out of phase (i.e. a  $180^\circ$  phase difference). The resulting effect is that the co-polarized currents on the two resonant patches are aligned, but that the fields radiated by the cross-polarized currents, cancel out. The spacing between the antenna elements is 15 mm.

#### 4.4.2.2 Feed Network

The two-element array is excited by a feed network with its circuit schematic shown in Fig.4.59. The  $180^\circ$  broadband balun was designed to operate at a center frequency of 5.4 GHz. The balun structure comprises of a two-way equal power division cascaded by a non-coupled-line broadband  $180^\circ$  phase shifter as shown in Fig.4.58. The characteristics impedances of the microstripline are given as follows [111]:

$$\begin{aligned} Z_1 &= \sqrt{2}Z_0 \\ Z_2 &= 1.27Z_0 \\ Z_3 &= 1.61Z_0 \end{aligned} \quad (4.4)$$

Fig.4.60 shows the measured S-parameters results of the planar balun. The balun exhibits balanced output ports power distribution with deviation of  $\pm 0.4\text{dB}$  from 4 to 7.35 GHz. Fig.4.61 depicts the measured output ports phase difference. The relative average phase imbalance is about 6.5 degrees over a considerably wideband from 3GHz to 7.2 GHz. We observed that as the frequency increases, the losses increases as depicted in Fig 4.45.

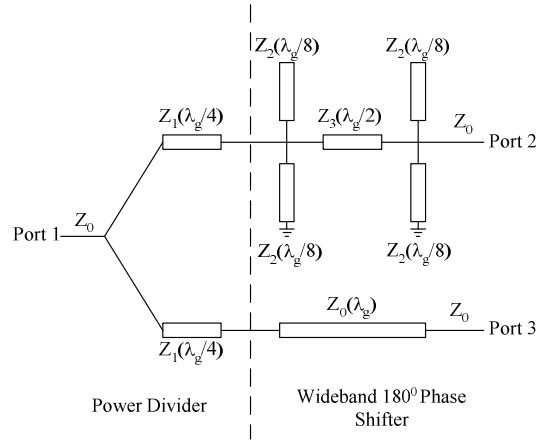


Fig.4.59: Circuit schematic of the planar balun.

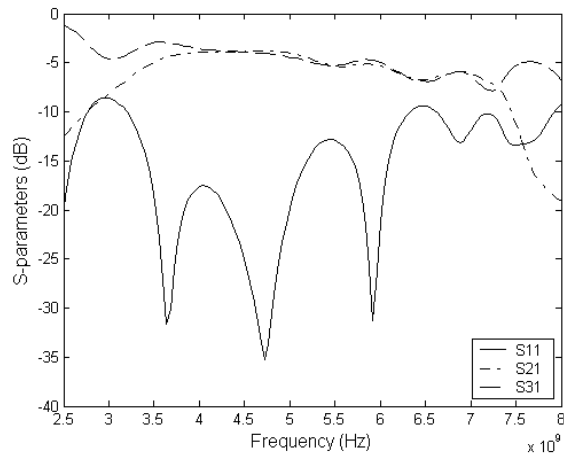


Fig.4.60: Measured output ports S-parameters of the planar balun.

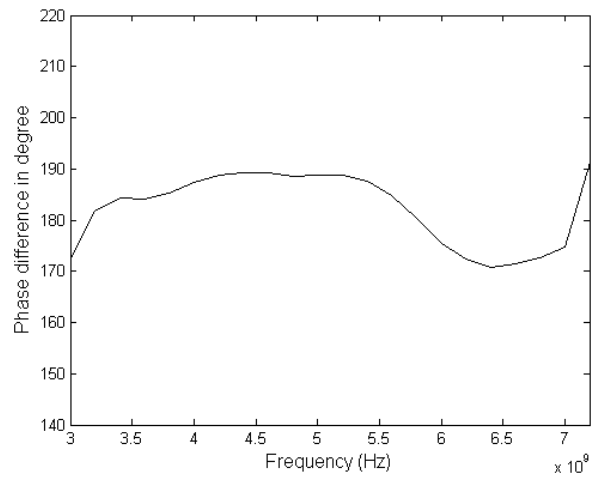


Fig.4.61: Measured phase difference between the output ports of the planar balun.

#### 4.4.2.3 Simulations and Measurements

The measured return loss of the array is depicted in Fig.4.62. A wide impedance bandwidth of approximately 66% is achieved. Fig.4.63 shows the measured and simulated radiation patterns at 5.4 GHz in the E-plane and H-plane respectively. Note that feed network is not included in the simulation. Generally there is a good agreement between the simulated and the measured radiation patterns. The cross-polar discrimination of this array is better than -15 dB. The measured broadside gain at 5.4 GHz is 9.25 dBi. The half-power beamwidth in the E-plane and H-plane are  $35.1^\circ$  and  $61^\circ$  respectively.

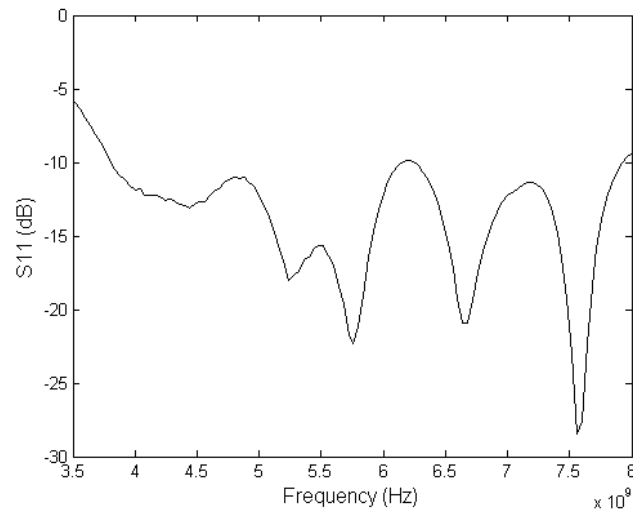
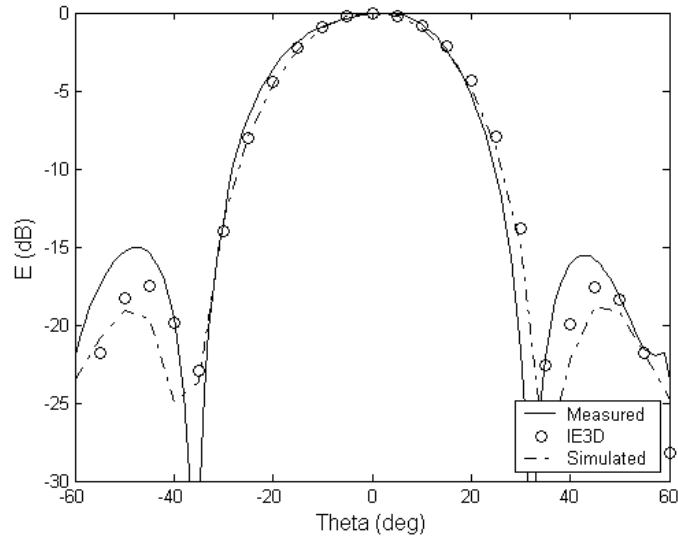
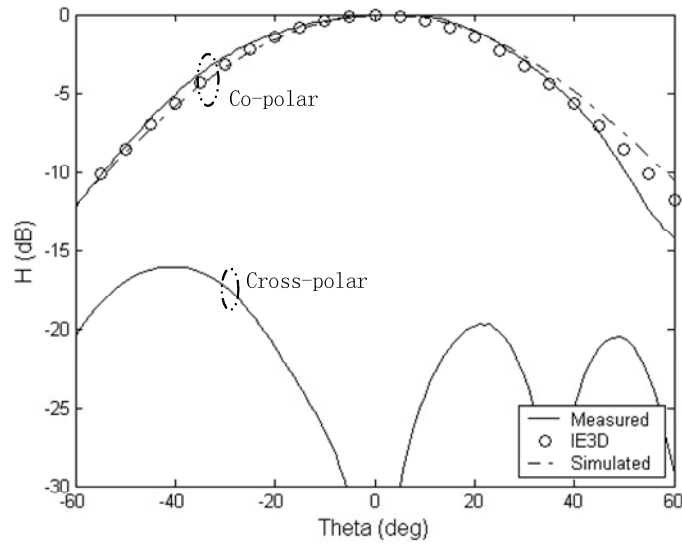


Fig.4.62: Measured return loss of the 2 X 1 linearly polarized array.



(a)



(b)

Fig.4.63: Radiation patterns of the 2 X 1 linearly polarized antenna array at 5.4 GHz. (a) E-plane (b) H-plane

#### 4.4.3 4 by 4 Linearly-polarized Array

In order to demonstrate that the technique to reduce the cross-polarized level can also be extended to the larger antenna array, the performance of a 4 by 4 linearly polarized antenna array is investigated and presented in this section. Since the radiation patterns

obtained from the proposed method have a good agreement with the measured ones, the performance of this array is predicted by the simulation only.

The 4 by 4 antenna array is shown in Fig.4.64. The dimensions of each array element, the spacings,  $G_x$  and  $G_y$  between the elements and the dielectric substrate used for the feeding networks are the same as that of the proposed 2 by 1 antenna array described in Section 4.4.2. The simulated radiation patterns in the E and H plane for 5.4GHz are shown in Fig.4.65. The cross-polarized levels are below -30 dB. The simulated broadside gain of the antenna at 5.4 GHz is 19.1 dBi. The half-power beamwidth in the E-plane and H-plane are  $17.3^\circ$  and  $12.9^\circ$  respectively.

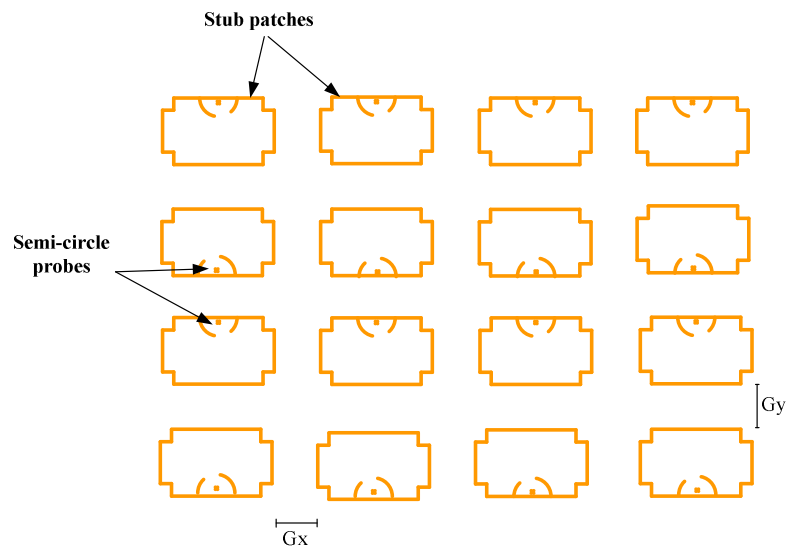
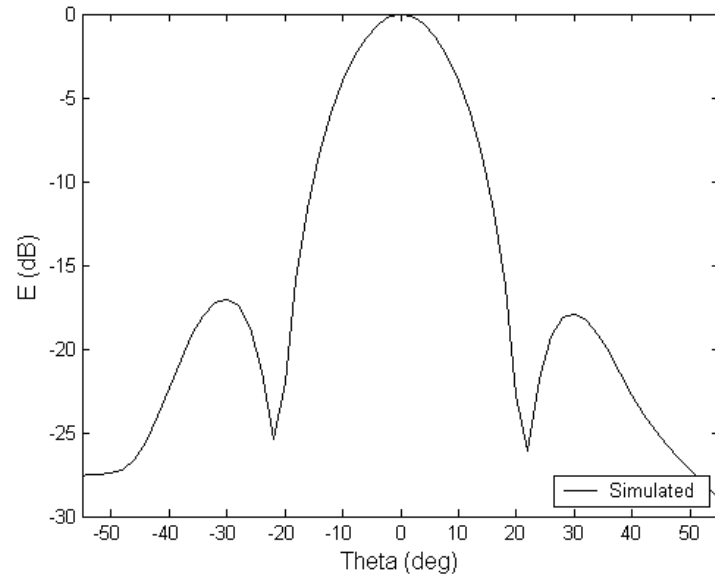
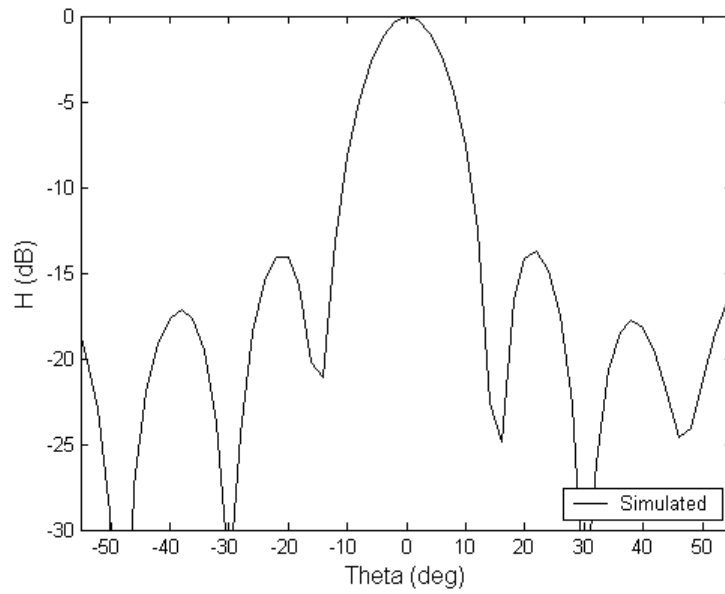


Fig.4.64: 4 X 4 linear polarized antenna array.





(a)



(b)

Fig.4.65: Radiation patterns of the 4 X 4 linear polarized antenna array at 5.4 GHz. (a) E-plane (b) H-plane

## 4.5 Conclusion

In this chapter, three wideband antennas for wireless LAN application have been developed. Wideband operations can be achieved by employing multiples resonance technique. A semi-circle probe is used to excite the antennas. The initial dimension of the semi-circle can be obtained from equations (4.1) to (4.3). The antenna elements are characterized in order to show how the various dimensions of the structure affect the impedance bandwidth of the antenna elements. It is shown that the length and the width of the added stubs are the two important parameters for controlling the impedance bandwidth of the semi-circle probe fed stub patch antenna. It is found through numerical simulations that the optimum length and width of the stub are  $0.24\lambda$  and  $0.07\lambda$  respectively. By modifying the rectangular patch antenna into a diamond patch, an impedance bandwidth of 47.9% is achieved. The slanted edge of the diamond-shaped antenna helps to introduce another resonance dip at 6 GHz. By further introducing four slots at the center of the slanted edges (flower-shaped patch antenna), we observe that this resonance dip is pushed outward to 7 GHz. Besides the flower-shaped patch antenna, it is also possible to cut pentagon slot at each corner of a rectangular patch (pentagonal-slot patch antenna) to achieve wideband operation. Among the three antennas, the pentagonal slot patch antenna gives the best performance. It is also shown how the stub patch antenna element can be used in two different applications.

## **CHAPTER 5      Conclusions and Future Work**

The main focus of the work presented in this thesis is the development of an efficient technique to accelerate the analysis of microstrip structures. Various novel wideband probe-fed microstrip patch antennas and arrays are then designed with the proposed method. This chapter discusses and summarizes the results of the research work described in the previous chapters. The major contributions of this work are reviewed and suggestions for future work are discussed.

### **5.1      Conclusions**

The multilayer Green's function, the method of moments and the computation of the antenna parameters have been discussed in Chapter 2. Three interpolation schemes, namely the radial basis function, the Cauchy method and the generalized pencil-of-function method (GPOF) are investigated to speed up the evaluation of the Green's function for large structure. GPOF is noted to be more accurate than the radial basis function and the Cauchy method when the number of interpolation points is small. To evaluate 500000 number of Green's functions, GPOF takes approximately 3.3 seconds while the direct computation of the closed-form Green's function takes about 3000 seconds.

Chapter 3 addresses the issue concerning excessive matrix size generated by the

conventional MoM when solving large microstrip problems. A new grouping concept called the macro-basis function with progressive method is presented to analyze large microstrip array. The method reduces the matrix size and in turn, leads to saving in computer storage and computational time when compared to conventional MoM. Through our numerical simulations, we find that for strong coupled structure the computed current give high error of more than 10% as compared with the conventional MoM. In order to remedy the problem, a new iterative refinement process is developed. If the number of iterative sweeps required is large, the computational time increases. Therefore, it is imperative to reduce the number of iterative sweeps. The initial current can be computed using either the macro-basis function with progressive method or the sub-domain multilevel approach. However, between the two methods, we find that the macro-basis function with progressive method gives a better convergence and its effectiveness in accelerating the convergence of the iterative procedure is demonstrated in the thesis. This chapter also addresses the improvement in the MoM matrix fill-in time with the help of multipole expansion via the adaptive integral method. The testing functions and the macro-basis function are translated to rectangular grid, allowing their interaction to be carried out in compressed representation. This also permits the use of fast Fourier transform to carry out the matrix-vector multiplication, leading to an improvement of around 56.5% in MoM fill-in time as compared to the macro-basis function with progressive method for a 1 by 14 series fed array with 3737 unknowns. The accuracy of the macro-basis function with progressive and adaptive integral method has been demonstrated through several examples, in which this technique is compared with a conventional MoM approach and measurements. For a 20 by 20 antenna array with 87780 unknowns, the proposed method is 98.4% faster than the commercial software,

IE3D.

As the bandwidth demand of modern wireless communication systems is expanding, it is necessary to use antennas that have wide impedance bandwidth. Various novel wideband probe-fed antennas were developed in Chapter 4. They are the semi-circle probe-fed stub antenna, semi-circle probe-fed flower-shaped antenna and semi-circle probe-fed pentagon-slot antenna. By adding a semi-circle patch on top of the vertical probe, the inherent inductance of the probe is compensated. It has been demonstrated that by using such a feeding mechanism on the polygonal patches, wide impedance bandwidth can be achieved. To our knowledge, at the time of the design, the proposed antennas have the largest bandwidth that can be obtained from the probe proximity-coupled technique. The measured impedance bandwidth of the stub patch antenna is 62.3% with a broadside gain of 6.36 dBi at 5.4 GHz. The 3 dB gain bandwidth is 39.2%. The wideband operation is achieved by introducing stubs at the sides of the rectangular patch. Similar impedance bandwidth performance can be achieved for the flower-shaped patch antenna. By modifying the rectangular patch antenna to a diamond-shaped antenna, an impedance bandwidth of 47.9% can be achieved. By further introducing the flower-shaped patch antenna, an impedance bandwidth of 63% is achieved. However, the 3 dB gain bandwidth is only 31.6%. Besides stub patch and flower-shaped patch antennas, wideband operation can also be achieved by cutting pentagonal slots at the four corners of the rectangular patch, thus increases its length, thereby exciting higher-order modes. This unique configuration can produce a wide impedance bandwidth of about 68.3%, a 3 dB gain bandwidth of 45.5% and a broadside gain of 7.07 dBi at 5.4 GHz. Among the three antennas, pentagonal slots patch antenna gives the best performance with the largest impedance

and gain bandwidth. Since the stub patch antenna has the simplest structure and the highest cross-polarized level at 5.4 GHz, it is used in array configuration. Two applications are addressed. The first application is for system in which polarization purity does not represent a constraint and the second application is for linearly polarized system. In the second application, it is important to reduce the cross-polarized levels of the array. This can be achieved by positioning two elements in a back-to-back configuration and the two ports have to be excited exactly out of phase.

## 5.2 Suggestions for Future Work

This thesis has provided a solution for the efficient simulation of planar structures that need a large number of unknowns to be accurately modelled. Besides, it has also introduced three novel wideband antennas using proximity coupled techniques. However, there are several possible improvements that can be carried out in addition to the developments presented. These new ideas that resulted from the work done in this thesis are discussed in the following paragraphs.

High-order sub-domain basis functions can be incorporated into MBF-PM method where MoM is implemented using curvilinear triangular patches or rectangular patches. High-order sub-domain basis function is used with the intention to reduce the number of unknowns.

With the widespread evolution of wireless communications, miniaturization for personal communications equipment has become one of the most fundamental

requirements. The size of the developed antenna elements is quite large. Hence there is a need to investigate miniaturization of the antenna elements. Compact microstrip antenna can be designed with substrate having higher dielectric constant. There is a need to look into methods to reduce the size of the antennas while maintaining its performance.

The use of smart antennas in small mobile terminals, such as notebooks or handheld computers, is restricted solely by the lack of space. Placing the individual radiators closer together aggravates the problem of mutual coupling between antenna ports which leads to highly distorted beam patterns and greatly reduced radiation efficiency. As such, there is a need to find a method to decouple and match an antenna array with reduced radiator separation so as to minimize the antenna array.

## References

- [1] S. Ooms and D. D. Zutter, "A New iterative diakoptics-Based Multilevel Moments method for Planar Circuits," *IEEE Trans. Microwave Theory and Techniques*, Vol. 46, No. 3, pp. 280-291, March 1998.
- [2] Umashankar, K.R., Nimmagadda, S., and Taflove, A., "Numerical analysis of electromagnetic scattering by electrically large objects using spatial decomposition technique," *IEEE Trans. Antennas and Propagation*, Vol. AP-40, pp.867-877, Aug 1992.
- [3] Chiu Chi Yuk. Impedance Bandwidth Broadening Techniques for Small Patch Antennas. PhD thesis. City University of Hong Kong, 2005.
- [4] R. S. Elliot. *Antenna Theory and Design*. Prentice-Hall, Inc., Englewood Cliffs. pp. 143-147, 1981
- [5] C. A. Balanis. *Antenna Theory: Analysis and Design*. Wiley, New York, second edition, 1997.
- [6] J. R. James and P. S. Hall. *Handbook of Microstrip Antennas*. Vols. 1 and 2. Peter Peregrinus, London, UK. 1989.
- [7] G. Kumar and K. C. Gupta, "Broad-Band Microstrip Antennas Using Additional Resonators Gap-Coupled to the Radiating Edges," *IEEE Trans. Antennas and Propagation*, Vol. AP-32, No. 12, pp 1375-1377, Dec 1984.
- [8] G. Kumar and K. C. Gupta, "Nonradiating Edges and Four Edges Gap-Coupled Multiple Resonator Broad-Band Microstrip Antennas," *IEEE*



- Trans. Antennas and Propagation, Vol. AP-33, No. 2, pp. 173-178, Feb 1985.
- [9] G. Kumar and K. C. Gupta, "Directly Coupled Multiple Resonator Wide-Band Microstrip Antennas," IEEE Trans. Antennas and Propagation, Vol. AP-33, No. 6, pp. 588-593, June 1985.
- [10] R. Q. Lee and K. F. Lee, "Experimental study of the Two-Layer Electromagnetically Coupled Rectangular Patch Antenna," IEEE Trans. Antennas and Propagation, Vol. AP-38, No. 8, pp. 1298-1302, August 1990.
- [11] T. M. Au and K. M. Luk, "Effect of Parasitic Element on the Characteristics of Microstrip Antennas," IEEE Trans. Antennas and Propagation, Vol. AP-39, No.8, pp. 1247-1251, August 1991.
- [12] H. Legay and L. Shafai, "New Stacked Microstrip Antenna with Large Bandwidth and High Gain," IEE Proc.-H, Microwaves, Antennas and Propagation, Vol. 141, No. 3, pp. 199-204, June 1994.
- [13] R. B. Waterhouse, "Design of Probe-Fed Stacked Patches," IEEE Trans. Antennas and Propagation, Vol. AP-47, No. 12, pp. 1780-1784, Dec 1999.
- [14] R. B. Waterhouse, "Design and Scan Performance of Large, Probe-Fed Stacked Microstrip Patch Array," IEEE Trans. Antennas and Propagation, Vol. AP-50, No. 6, pp. 893-895, June 2002.
- [15] T. Huynh and K. F. Lee, "Single-layer single-patch wideband microstrip antenna," Electronics Letters, Vol. 31, No. 16, pp. 1310-1312, August 1995.
- [16] K. F. Lee, K. M. Luk, K. F. Tong, Y. L. Yung and T. Huynh, "Experimental study of a two-element array of U-slot patches," Electronics Letters, Vol. 32, No. 5, pp. 418-420, Feb 1996.
- [17] K. F. Lee, K. M. Luk, K. F. Tong, S. M. Shum, T. Huynh and R. Q. Lee, "Experimental and simulation studies of the coaxially fed U-slot rectangular

- patch antenna,” IEE Proc., Microwaves, Antennas and Propagation, Vol. 144, No. 5, pp. 354-358, Oct 1997.
- [18] M. Clenet and L Shafai, “Multiple resonances and polarization of U-slot patch antenna,” Electronics Letters, Vol. 35, No. 2, pp.101-103, Jan 1999.
- [19] K. F. Tong, K. M. Luk, K. F. Lee and R. Q. Lee, “A Broad-Band U-slot Rectangular Patch Antenna on a Microwave Substrate,” IEEE Trans. Antennas and Propagation, Vol. AP-48, No. 6, pp. 954-960, June 2000.
- [20] Gh. Z. Rafi and L. Shafai, “Low-cross-polarization wideband V-slot microstrip antenna,” Microwave and Optical Technology Letters, Vol. 43, No. 1, pp. 44-47, 2004.
- [21] Gh. Z. Rafi and L.Shafai, “Wideband V-slotted diamond-shaped microstrip patch antenna,” Electronics Letters, Vol-40, pp.1166-1167, 2004
- [22] B. L. Ooi, Q. Shen, and M. S. Leong, “A Novel E-shaped Broadband Microstrip Patch Antenna,” Microwave and Optical Technology Letters, Vol. 27, No. 5, pp. 348-352, Dec 2000
- [23] Luk, K. M., et al., “Broadband Microstrip Antenna,” Electronics Letters, Vol. 34, pp. 1442-1443, 1998
- [24] Mak, C.L., K. F. Lee, and K. M. Luk, “A Novel Broadband Patch Antenna with a T-Shaped Probe,” IEE Proc. Microwaves, Antennas Propagation, Pt. H, Vol. 147, pp. 73-76, 2000.
- [25] A. A.Kishk, K. F. Lee, W. C. Mok and K. M. Luk, “A Wide-Band Small Size Microstrip Antenna Proximately Coupled to a Hook Shape Probe”, IEEE Trans. Antennas and Propagation, Vol. AP-52, No. 1, pp. 59-65, Jan 2004
- [26] H. W. Lai and K. M. Luk, “Design and study of wideband patch antenna fed by a meandering shaped probe,” IEEE Trans. Antennas and Propagation, Vol

54, pp 564-571, Feb 2006.

- [27] K.Kunz and R. Luebber. The finite difference time domain method for electromagnetics. CRC Press, 1993.
- [28] K.L. Shlager and J. B. Schneider. A selective survey of the finite-difference time-domain literature. IEEE Antennas and Propagation Magazine, 1995.
- [29] M. V. K. Chari and P. P. Silvester. Finite elements in electrical and magnetic field problems. John Wiley, 1980.
- [30] P. P. Silvester and R. L. Ferrari. Finite elements for electrical engineers. Cambridge University Press, second edition, 1990.
- [31] Williams F. Ames. Numerical methods for partial differential equation. Academic Press, second edition, 1977.
- [32] R. F. Harrington. Field computation by moment methods. Macmillan., Wiley-IEEE Press second edition, 1968.
- [33] J. R. Mosig. Numerical Methods for Microwave and Millimeter-Wave Passive Structures, chapter Integral equation techniques. New York: Wiley, 1988.
- [34] W. C. Chew, J. M. Jin, E. Michielssen and .J. M. Song. Fast and Efficient Algorithms in Computational Electromagnetics. Artech House, 2001.
- [35] D. M. Pozar and S. M. Voda, "A rigorous analysis of a microstrip feed patch antenna," IEEE Trans. Antennas and Propagation, Vol. 35, pp. 1343-1350, Dec. 1987.
- [36] D. M. Pozar, "Input impedance and mutual coupling of rectangular microstrip antennas," IEEE Trans. Antennas and Propagation, Vol. 30, pp. 1191-1196, Nov. 1982.
- [37] P. B. Katehi and N. G. Alexopoulos, "On the modeling of electromagnetically

- coupled microstrip antennas – The printed strip dipole,” IEEE Trans. Antennas and Propagation, Vol. 32, pp. 1179-1186, Nov. 1984.
- [38] J. R. Mosig, “Arbitrarily shaped microstrip structures and their analysis with a mixed potential integral equation,” IEEE Trans. Microwave Theory and Techniques, Vol. 36, pp. 314-323, Feb. 1988.
- [39] Y. L. Chow, J. J. Yang, D. G. Fang, and G. E. Howard, “A Closed-Form Spatial Green’s Function for the Thick Microstrip Substrate.” IEEE Trans. Microwave Theory and Techniques, Vol. 39, No. 3, pp. 588-592, March 1991
- [40] T. K. Sarkar, E. Arvas and S. M. Rao, “Application of FFT and the conjugate gradient method for the solution of electromagnetic radiation from electrically large and small conducting bodies,” IEEE Trans. Antennas and Propagation, Vol. 34, No. 5, pp. 635-640, May 1986.
- [41] R. F. Bloemenkamp and P. M. van den Berg, “A conjugate gradient FFT method for transient scattering by dielectric cylinders,” Proc. IEEE Antennas Propagation S. Int. Symp., Vol 2, pp 1374-1377, July1999.
- [42] R. Coifman, V. Rokhlin, and S. Wandzura, “The fast multipole method for the wave equation: A pedestrian prescription,” IEEE Antennas and Propagation Magazine, Vol. 35, No. 3, pp. 7-12, June 1993.
- [43] J. M. Song, C. C. Lu and W. C. Chew, “Multilevel fast multipole algorithm for electromagnetic scattering by large complex objects,” IEEE Trans. Antennas and Propagation, Vol. 45, No. 10, pp. 1488-1493, Oct 1997.
- [44] J. M. Song, F. Ling and J. M. Jin, “Multilevel fast multipole algorithm for analysis of large-scale microstrip structures,” IEEE Microwave and Guided Wave Letters, Vol 9, pp 508-510, Dec 1999.
- [45] J. M. Song and W. C. Chew, “Fast multipole method solution using parametric

- geometry,” *Microwave and Optical Technology Letters*, pp. 760-765, Nov. 1994.
- [46] E. Bleszynski, M. Bleszynski, and T. Jaroszewics, “AIM: adaptive integral method for solving large-scale electromagnetic scattering and radiation problems,” *Radio Sci.*, Vol. 31, pp. 1225-1251, Sept./Oct. 1996.
- [47] F. Ling, C. F. Wang, and J. M. Jin, “An efficient algorithm for analyzing large-scale microstrip structures using adaptive integral method combined with Discrete Complex-Image Method,” *IEEE Trans. Microwave Theory and Techniques*, Vol. 48, No. 5, pp. 832-839, May 2000.
- [48] J. M. Song, C. F. Wang, F. Ling and J. M. Jin, “Adaptive integral solution of combined field integral equation,” *Microwave and Optical Technology Letters*, Vol. 19, pp. 321-328, Nov. 1998.
- [49] C. F. Wang, F. Ling and J. M. Jin, “Application of adaptive integral method to scattering and radiation analysis of arbitrarily shaped planar structures,” *Journal of Electromagnetic Waves and Applications*, Vol. 12, pp. 1021-1038, Aug. 1998.
- [50] E. Suter and J. Mosig, “A subdomain multilevel approach for the MoM analysis of large planar antennas,” *Microwave and Optical Technology Letters*, Vol. 25, pp. 270-277, Aug.2000.
- [51] J. Parron, J. M. Rius and J. Romeu, “Analysis of a Sierpinski fractal patch antenna using the concept of macro-basis function,” *IEEE Antenna and Propagation Society International Symposium*, Vol 3, pp. 616-619, July 2001.
- [52] I. Stevanovic and J. R. Mosig, “Efficient evaluation of macro-basis function reaction terms in the subdomain multilevel approach,” *Microwave and Optical Technology Letters*, Vol. 42, No.2, pp. 138-143, July 20 2004.

- [53] C. Craeye, "New analysis method for finite periodic structures combining macro-basis functions and multipole approaches," *IEEE Antennas and Propagation Society International Symposium*, pp. 4103-4108, 2006.
- [54] C. Craeye, "A fast impedance and pattern computation scheme for finite antenna arrays," *IEEE Trans. Antennas and Propagation*, Vol. 54, No. 10, pp.867-877, Oct 2006.
- [55] W. B. Lu, T. J. Cui, Z. G. Qian and W. Hong, "Accurate Analysis of Large-Scale Periodic Structures Using an Efficient Sub-Entire-Domain Basis Function Method," *IEEE Trans. Antennas and Propagation*, Vol. 52, No. 11, pp. 3078-3085, Nov. 2004
- [56] Y. Hua and T. K. Sarkar, "Generalized Pencil-of-Function Method for Extracting Poles of an EM System from its Transient Response," *IEEE Trans. Antennas and Propagation*, Vol. 37, No. 2, pp. 229-234, Feb 1989.
- [57] K. Jain, T. K. Sarkar, and D. D. Weiner, "Rational modeling by pencil-of-function method," *IEEE Trans. Acoust., Speech, Signal Processing*, Vol. ASSP-31, No. 3, pp. 564-573, June 1983.
- [58] Y. C. Hon and X. Z. Mao, "A multiquadric interpolation method for solving initial value problems," *Scientific Comput.*, Vol. 12, No1, pp. 51-55, 1997.
- [59] H. G. Wang and C. H. Chan, "The Implementation of Multilevel Green's Function Interpolation Method for Full-Wave Electromagnetic Problems," *IEEE Trans. Antennas and Propagation*, Vol. 55, No. 5, pp 1348-1358, May 2007.
- [60] R. S. Adve, T. K. Sarkar, S. M. Rao, E. K. Miller and D. R. Pflug, "Application of the Cauchy Method for Extrapolating/ Interpolating Narrow-Band System Responses," *IEEE Trans. Microwave Theory and*

Techniques, Vol. 45, No. 5, pp. 837-845 May 1997.

- [61] S. F. Peik, R. R. Mansour and Y. Leonard Chow, "Multidimensional Cauchy Method and Adaptive Sampling for an Accurate Microwave Circuit Modeling," IEEE Trans. Microwave Theory and Techniques, Vol. 46. No. 12, pp. 2364-2371, Dec1998
- [62] Zeland Software, Inc., Std. IE3D version 11
- [63] K. A. Michalski and J. R. Mosig, "Multilayered Media Green's Functions in Integral Equation Formulations." IEEE Trans. Antennas and Propagation, Vol. 45, No. 3, pp. 508-519, March 1995
- [64] K. A. Michalski and D. Zheng, "Electromagnetic scattering and radiation by surfaces of arbitrary shape in layered media, Part 1: Theory," IEEE Trans. Antennas and Propagation, Vol. 38, pp. 335-334, Mar. 1990
- [65] D. Zheng, Radiation, scattering and guidance of electromagnetic fields by conducting objects of arbitrary shape in layered medium, PhD thesis, The University of Mississippi, 1988.
- [66] A. A. Kishk F. Alonso-Monferrer and A. W. Glisson, "Green's functions analysis of planar circuit in a two-layered grounded medium," IEEE Trans. Antennas and Propagation, Vol. 40, pp. 690-696, Jun. 1992.
- [67] K. A. Michalski, "On the dyadic Green's function for a grounded dielectric slab," Nat. Radio Sci. Meet. Dig., pp. 96, Boston, MA, June 1984.
- [68] T. Itoh, Numerical Techniques for Microwave and Millimeter-Wave Passive Structures. John Wiley, 1989.
- [69] J. R. Mosig and F. E. Gardiol. A dynamic radiation model for microstrip structures. Advances in Electronics and Electron Physics, Vol. 59, pp. 139-237, 1982.

- [70] J. R. Mosig and F. E. Gardiol, "Analytic and numerical techniques in the Green's function treatment of microstrip antennas and scatterers," IEE Proc., Part H: Microwaves, Optics and Antennas, Vol. 130, pp. 175-182, 1983.
- [71] W. C. Kuo and K. K. Mei, "Numerical approximations of the Sommerfeld integrals for fast convergence," Radio Sci., Vol 13, pp 407-415, May-Jun. 1978.
- [72] M. I. Aksun, "A robust approach for the derivation of closed-formed Green's functions," IEEE Trans. Microwave Theory and Techniques, Vol. 44, pp 651-658, May 1996.
- [73] P. B. Katehi and N. G. Alexopoulos, "Real axis integration of Sommerfeld integrals with applications to printed circuit antennas," J. Math. Phys., Vol. 24, pp. 527-533, Mar. 1983.
- [74] K. A. Michalski and C. M. Butler, "Evaluation of Sommerfeld integrals arising in the ground stake antenna problem," IEE Proc. Microwaves, Antennas and Propagation, Vol. 134, pp. 93-97, Feb. 1987.
- [75] D. M. Bubenik, "A practical method for the numerical evaluation of Sommerfeld integrals," IEEE Trans. Antennas and Propagation, No. 6, Vol. 25, pp. 904-906, Nov 1977.
- [76] F. Ling, "Discrete complex image method for Green's functions of general multilayer media," IEEE Microwave and Guided Wave Letters, Vol. 10 pp 400-402, Oct. 2000
- [77] F. Ling and J. M. Jin, "Discrete image method for Green's functions of general multilayer media," IEEE Microwave and Guided Wave Letters, Vol. 10, pp 400-402, Oct. 2000.



- [78] S. M. Rao, D. R. Wilton and A. W. Glisson, "Electromagnetic Scattering by Surfaces of Arbitrary Shape," *IEEE Trans. Antennas and Propagation*, Vol. 30, No. 3, pp. 409-418, May 1982
- [79] S. Makarov, "MoM Antenna Simulations with Matlab: RWG Basis Functions." *IEEE Antennas and Propagation Magazine*, Vol. 43, No. 5, pp. 100-107, October 2001
- [80] J.R. Mosig, D. Appl. Sc. and F.E. Gardiol, "General integral equation formulation for microstrip antennas and scatterers," *IEEE Proc. Microwaves, Antennas and Propagation, Part H*, Vol. 132, No. 7, pp. 424-432 Dec 1985.
- [81] D. C. Chang and J. X. Zhang, "Electromagnetic modeling of passive circuit elements in MMIC," *IEEE Trans. Microwave Theory and Techniques*, Vol. 40, pp. 1741-1747, Sep. 1992.
- [82] J. X. Zheng. *Electromagnetic Modeling of Microstrip Circuit Discontinuities and Antenna of Arbitrary Shape*. PhD thesis, University of Colorado, 1990.
- [83] Edwin K. L. Yeung, John C. Beal and Yahia M. M. Antar, "Multilayer Microstrip Structure Analysis with Matched Load Simulation," *IEEE Trans. Microwave Theory and Techniques*, vol. 43, No. 1, pp 143-149 Jan 1995.
- [84] Z. A. Maricevic and T. k. Sarkar, "Analysis and Measurements of arbitrary shaped open microstrip structures," *Progress in Electromagnetics Research Symposium 15*, pp 253-301, 1997.
- [85] Y. Leonard Chow and W. C. Tang, "3-D Green's Functions of Microstrip Separated Into Simpler Terms- Behavior, Mutual Interaction and Formulas of the Terms," *IEEE Trans. Microwave Theory and Techniques*, Vol. 49, No. 8, pp 1483-1491, Aug 2001.
- [86] F. Ling and J. M. Jin, "Scattering and radiation analysis of microstrip

- antennas using discrete complex image method and reciprocity theorem,”  
Microwave and Optical Technology Letters, Vol. 16, pp, 212-216, Nov. 1997
- [87] A. K. Bhattacharyya, “Long Rectangular Patch Antenna with a Single Feed.”,  
IEEE Trans. Antennas and Propagation Vol. 38, No. 7, pp 987-993, July 1990
- [88] M. Abramowitz, and I. A. Stegun, “Handbook of mathematical functions,”  
Dover Publications, inc., New York, 1964.
- [89] Schwering, F., N. N. Puri, and C. M. Butler, “Modified Diakoptic theory of  
antennas,” IEEE Trans. Antennas and Propagation, Vol. 34, pp. 1273-1281,  
Nov1986.
- [90] G. Goubau, N. N. Puri and F. Schwering, “Diakoptic theory of multielement  
antennas,” IEEE Trans. Antennas and Propagation, Vol. 30, pp. 15-26, Jan.  
1982.
- [91] G. E. Howard. Analysis of Large Microwave Integrated Circuits by the  
Multilevel Moment Method. PhD thesis. University of Waterloo, 1991.
- [92] T. Vaupei and T. F. Elbert, “Diakoptic Basis Function Grouping Techniques  
Applied to the Method of Moment Solution of (M) MIC-Structures,” Antennas  
and Propagation Society International Symposium, Vol. 2, pp 1059-1062, June  
2003
- [93] K. R. Umashankar and S. Nimmagadda, “Application of integral equation and  
method of moments for electrically very large scatterers using spatial  
decomposition technique,” IEEE AP-S Symposium Digest, Vol 1, pp 76-79,  
May1990.
- [94] Q. Ye and L. Shafai, “Performance of the progressive numerical method and its  
comparison with the modified spatial decomposition technique in solving  
large scattering problems.” IEE Proc. Microwave, Antennas and Propagation,

Vol. 145, No. 2, pp. 169-174, April 1998.

- [95] Q. Ye and L. Shafai, "Large Electromagnetic Scattering Computation Using Iterative Progressive Numerical Method." IEEE AP-S Symposium Digest, Vol. 2, pp 938-941, July 1996.
- [96] R. Mittra, J. F. Ma, E. Lucente and A. Monorchio, "CBMOM-An iteration free MoM approach for solving large multiscale EM radiation and scattering problems," IEEE Antennas and Propagation Society International Symposium and USNC/URSI Meeting, Session 51, Washington, DC, pp. 2-5, July 3-8 2005.
- [97] Kwon, S. J., K. Du, and R. Mittra, "Characteristic basis function method: A numerically efficient technique for analyzing microwave and RF circuits," Microwave and Optical Technology Letters, Vol. 38, No. 6, pp. 444-448, Sept. 2003.
- [98] Yeo, J., V. V. S. Prakash, and R. Mittra, "Efficient analysis of a class of microstrip antennas using the Characteristic basis function method (CBFM)," Microwave and Optical Technology Letters, Vol. 39, No.6, 456-464, Dec. 2003.
- [99] J. X. Wan, J. Lei and C. H. Liang, "An efficient analysis of large-scale periodic microstrip antenna arrays using the characteristic basis function method," Progress in Electromagnetics Research Symposium 50, pp. 61-81, 2005.
- [100] W. B. Lu, T. J. Cui, X. X. Yin, Z. G. Qian and W. Hong, "Fast algorithms for large-scale periodic structures using subentire domain basis functions," IEEE Trans. Antennas and Propagation, Vol. 53, No. 3, pp. 1154-1161, March. 2005
- [101] W. B. Lu, T. J. Cui, X. X. Yin, Z. G. Qian and W. Hong, "Acceleration of fast

- multipole method for large-scale periodic structures with finite sizes using sub-entire-domain basis functions,” *IEEE Trans. Antennas and Propagation*, Vol. 53, No.2, pp. 1154-1161, March. 2005
- [102] Robert A. Sainati. *CAD of Microstrip Antennas for Wireless Applications*. Artech House
- [103] ETSI EN 302 288-1 V1.1.1 (2005-01)
- [104] I. J. Bahl and P. Bhartia. *Microstrip Antennas*. Artech House, 1980.
- [105] Kirshning, M. R. H. Jansen, and N. H. L. Koster, “Accurate Model for Open-Ended Effect of Microstrip Lines,” *Electronics Letters* Vol. 17, No. 3, pp. 123-125, Feb. 1981
- [106] R. H. Clarke, “A statistical theory of mobile radio reception,” *Bell Syst. Tech. J.*, Vol. 47, pp. 957-1000, July/ Aug. 1968.
- [107] M. Manzini, A. Alu, F. Bilotti and L. Vegni, “Polygonal patch Antennas for Wireless Communications,” *IEEE Trans. Vehicular Technology*, Vol. 53, No. 5, pp. 1434-1440, Sept.2004.
- [108] M. Manzini, F. Bilotti, A. Alù, and L. Vegni, “Design of Broad-Band Polygonal Patch Antennas for Mobile Handsets,” *J. Electromagnetic Waves and Applications*, Vol.18, No. 1, pp. 61-72, 2004.
- [109] E. H. Newman and D. M. Pozar, “Electromagnetic modelling of composite wire and surface geometries,” *IEEE Trans. Antennas and Propagation*, Vol. AP-26, pp. 784-789, Nov.1978.
- [110] W. C. Chew and J. A. Kong, “Effects of Fringing Fields on the Capacitance of Circular Microstrip Disk,” *IEEE Trans. Microwave Theory and Techniques*, Vol. MTT-28, pp. 98-104., Feb.1980.
- [111] Z. Y. Zhang, Y. X. Guo, L. C. Ong and M. Y. W. Chia, “A new wideband

planar balun on a single-layer PCB,” IEEE Microwave and Wireless Components Letters., Vol. 15, No. 6, pp. 416-418, Jun. 2005.

- [112] S. Y. Eom, “Broadband  $180^\circ$  Bit Phase Shifter Using a  $\lambda/2$  Coupled Line and Parallel  $\lambda/8$  Stubs,” IEEE Microwave and Wireless Components Letters, Vol. 14, No. 5, May 2004.
- [113] J. Rogers and R. Bhatia, “A 6 to 20 GHz Planar Balun using a Wilkinson Divider and Lange Couplers,” IEEE MTT-S Digest 1991.
- [114] J. C. Rautio, “An investigation of microstrip conductor loss,” IEEE Microwave Magazine, Vol.1 No. 4, pp. 60-67, Dec 2000.
- [115] D. M. Dobkin. RF Engineering for Wireless Networks: Hardware, Antennas, and Propagation. Newnes; Pap/Cdr edition

## APPENDIX A Transmission Line Green's Function

### A.1 Transmission Line Green's Function

This appendix derived the functions  $V_i^p$ ,  $V_v^p$ ,  $I_i^p$  and  $I_v^p$  in the expression of the Green's function in equation (2.26) to equation (2.29) based on transmission line equation. The transmission line analog of the layered medium consists of a cascade connection of uniform transmission line sections, where section  $n$  with terminals at  $z_n$  and  $z_{n+1}$  has propagation constant  $k_{zn}^p$  and characteristic impedance  $Z_n^p$ . To find the TLGF's, we excite the transmission line network by unit strength voltage and current sources at  $z'$  in section  $n$  and compute the voltage and current at  $z$  in section  $m$ . The voltage and current source section is illustrated in Fig A.1 where  $\bar{\Gamma}_n$  and  $\bar{\Gamma}_{n-1}$  are the voltage reflection coefficients looking to the left and right, respectively out of the terminals of section  $n$ . Similarly,  $\bar{Z}_n$  and  $\bar{Z}_{n-1}$  are the input impedance looking to the left and right respectively out of the terminals.  $\bar{\Gamma}_k$  and  $\bar{\Gamma}_k$  are expressed as follows:

$$\begin{aligned}\bar{\Gamma}_k &= \frac{\bar{Z}_k - Z_{k+1}}{\bar{Z}_k + Z_{k+1}}, k = 1, 2, \dots, n, \\ \bar{\Gamma}_k &= \frac{\bar{Z}_k - Z_{k+1}}{\bar{Z}_k + Z_{k+1}}, k = 1, 2, \dots, n,\end{aligned}\tag{A.1}$$

where  $\bar{\Gamma}_0 \equiv 0 \equiv \bar{\Gamma}_{n+1}$ .

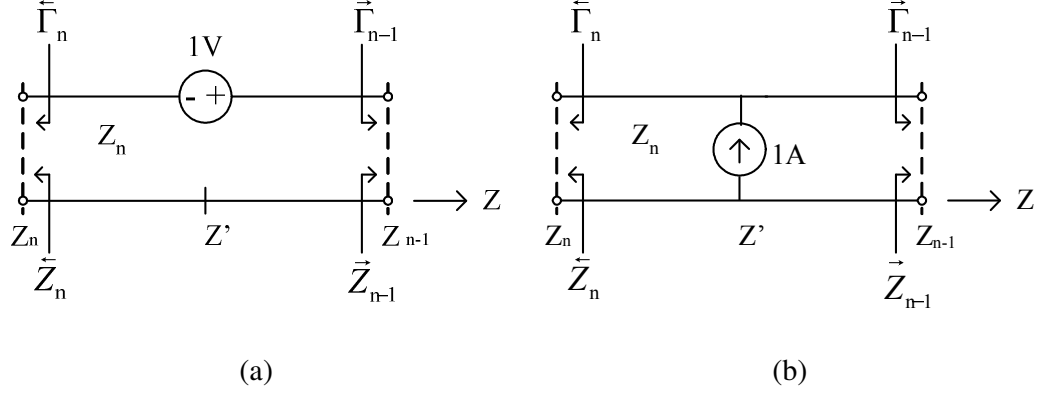


Fig A.1: (a) Voltage source (b) Current source in the  $i^{\text{th}}$  transmission-line section.

$\vec{Z}_k$  and  $\vec{Z}_k$  are expressed as follows:

$$\begin{aligned} \vec{Z}_k &= Z_k \frac{\vec{Z}_{k-1} + jZ_k \tan(kz_k(z_{k-1} - z_k))}{Z_k + j\vec{Z}_{k-1} \tan(kz_k(z_{k-1} - z_k))}, k = 1, 2, \dots, n \\ \vec{Z}_k &= Z_{k+1} \frac{\vec{Z}_{k+1} + jZ_{k+1} \tan(kz_{k+1}(z_k - z_{k+1}))}{Z_{k+1} + j\vec{Z}_{k+1} \tau_{k+1}}, k = n-1, n-2, \dots, 1 \end{aligned} \quad (\text{A.2})$$

where  $\vec{Z}_1 = Z_1$  and  $\vec{Z}_n = Z_{n+1}$

When the source and observation points are in the same section ( $n=m$ ),  $V_i^p$  is given

by

$$V_i^p(z|z') = \frac{Z_i}{2} \left[ e^{-jk_{zn}(z-z')} + \frac{1}{D} \begin{pmatrix} \vec{\Gamma}_{n-1} \vec{\Gamma}_n e^{-j2k_{zn}(z_{n-1}-z_n)} e^{-jk_{zn}(z-z')} \\ + \vec{\Gamma}_n e^{-jk_{zn}(z'+z-2z_n)} \\ + \vec{\Gamma}_{n-1} e^{-jk_{zn}(2z_{n-1}-(z'+z))} \\ + \vec{\Gamma}_{n-1} \vec{\Gamma}_n e^{-j2k_{zn}(z_{n-1}-z_n)} e^{jk_{zn}(z-z')} \end{pmatrix} \right], \quad (\text{A.3})$$

where  $D = 1 - \vec{\Gamma}_{n-1} \vec{\Gamma}_n e^{-j2k_{zn}(z_{n-1}-z_n)}$ .

From equation (2.23), we can derive  $I_i^p$  as

$$I_i^p(z|z') = \frac{1}{2} \left[ \pm e^{-jk_{zn}(z-z')} + \frac{1}{D} \begin{pmatrix} \bar{\Gamma}_{n-1} \bar{\Gamma}_n e^{-j2k_{zn}(z_{n-1}-z_n)} e^{-jk_{zn}(z-z')} \\ + \bar{\Gamma}_n e^{-jk_{zn}(z'+z-2z_n)} \\ - \bar{\Gamma}_{n-1} e^{-jk_{zn}(2z_{n-1}-(z'+z))} \\ - \bar{\Gamma}_{n-1} \bar{\Gamma}_n e^{-j2k_{zn}(z_{n-1}-z_n)} e^{jk_{zn}(z-z')} \end{pmatrix} \right]. \quad (A.4)$$

From the third equation of equation (2.23), we can derive  $V_v^p$

$$V_v^p(z|z') = \frac{1}{2} \left[ \pm e^{-jk_{zn}|z-z'|} + \frac{1}{D} \begin{pmatrix} \bar{\Gamma}_{n-1} \bar{\Gamma}_n e^{-j2k_{zn}(z_{n-1}-z_n)} e^{-jk_{zn}(z-z')} \\ - \bar{\Gamma}_n e^{-jk_{zn}(z'+z-2z_n)} \\ + \bar{\Gamma}_{n-1} e^{-jk_{zn}(2z_{n-1}-(z'+z))} \\ - \bar{\Gamma}_{n-1} \bar{\Gamma}_n e^{-j2k_{zn}(z_{n-1}-z_n)} e^{jk_{zn}(z-z')} \end{pmatrix} \right]. \quad (A.5)$$

Finally from the second equation of equation (2.23), we can derive  $I_v^p$  as

$$I_v^p(z|z') = \frac{Y^p}{2} \left[ e^{-jk_{zn}|z-z'|} + \frac{1}{D} \begin{pmatrix} \bar{\Gamma}_{n-1} \bar{\Gamma}_n e^{-j2k_{zn}(z_{n-1}-z_n)} e^{-jk_{zn}(z-z')} \\ - \bar{\Gamma}_n e^{-jk_{zn}(z'+z-2z_n)} \\ - \bar{\Gamma}_{n-1} e^{-jk_{zn}(2z_{n-1}-(z'+z))} \\ + \bar{\Gamma}_{n-1} \bar{\Gamma}_n e^{-j2k_{zn}(z_{n-1}-z_n)} e^{jk_{zn}(z-z')} \end{pmatrix} \right]. \quad (A.6)$$

The upper and lower signs in the equations pertain to  $z > z'$  and  $z < z'$ , respectively.

When the source section is above the observation section ( $m < n$ ), the voltage and current at  $z$  in section  $m$  can be derived recursively from those in section  $n$ . The final solution of  $V^p$  and  $I^p$  is

$$\begin{Bmatrix} V^p(z) \\ I^p(z) \end{Bmatrix} = V^p(z_n) \frac{\prod_{k=m+1}^{n-1} \bar{T}_k^p}{1 + \bar{\Gamma}_m^p e^{-j2k_{zm}^p(z_{m+1}-z_m)}} \times \begin{Bmatrix} \bar{\tau}_m^p(z) \\ \bar{y}_m^p(z) \end{Bmatrix} e^{-jk_{zm}^p(z_{m+1}-z)}, \quad (A.7)$$

where

$$\bar{T}_k^p = \frac{V^p(z_k)}{V^p(z_{k+1})} = \frac{(1 + \bar{\Gamma}_k^p) e^{-jk_{zk}^p(z_{k+1}-z_k)}}{1 + \bar{\Gamma}_k^p e^{-j2k_{zk}^p(z_{k+1}-z_k)}}, \quad (A.8)$$

$$\bar{\tau}_m^p(z) = \left[ 1 + \bar{\Gamma}_m^p e^{-j2k_{zm}^p(z-z_m)} \right], \quad (A.9)$$



$$\bar{y}_m^p(z) = -Y_m^p \left[ 1 - \bar{\Gamma}_m^p e^{-j2k_{zm}^p(z-z_m)} \right]. \quad (\text{A.10})$$

Equation (A.7) can be applied to any source type. Hence, if section n is excited by a unit-strength current source at  $z'$ , then  $V^p(z_n) = V_i^p(z_n | z')$ . If section n is excited by a unit-strength voltage source at  $z'$ , then  $V^p(z_n) = V_v^p(z_n | z')$ .

Analogous formulas may be developed for the case  $m > n$ , where  $z$  is outside the source section and  $z > z'$ . However this is hardly necessary because the reciprocity theorems allow one to interchange the source and field point locations.

## A.2 Single-Layer Green's Functions

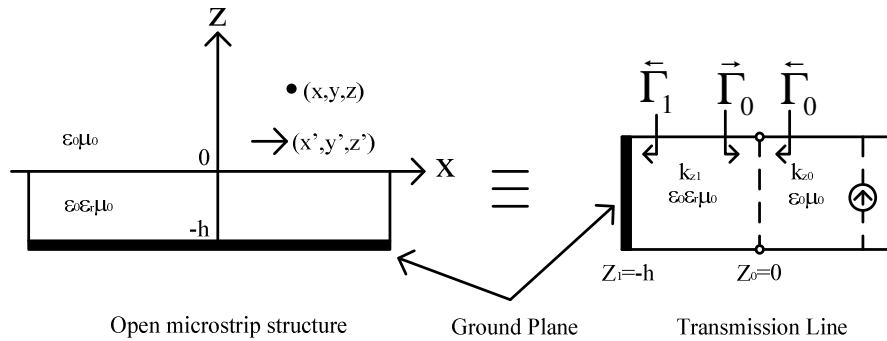


Fig A.2: Single-layer microstrip structure.

Using the formulation derived in Section A.1, one can easily determine the Green's function for a single layer. Consider an  $x$ -directed electric dipole of unit strength located above a microstrip substrate. Fig A.2 shows the open microstrip structure and the equivalent transmission line section with  $\bar{\Gamma}_0 = 0$ ,  $\bar{\Gamma}_1 = -1$ .

The spectral-domain potentials in the air region can be represented as follows:

$$\tilde{G}_A^{xx} = \frac{\mu_0}{4\pi} \frac{1}{j2k_{z0}} \left[ e^{-jk_{z0}(z-z')} + R_{TE} e^{-jk_{z0}(z+z')} \right], \quad (A.11)$$

$$\tilde{G}_q = \frac{1}{4\pi\epsilon_0} \frac{1}{j2k_{z0}} \left[ e^{-jk_{z0}(z-z')} + (R_{TE} + R_q) e^{-jk_{z0}(z+z')} \right], \quad (A.12)$$

where

$$R_{TE} = -\frac{r_{10}^{TE} + e^{-jk_{z1}h}}{1 + r_{10}^{TE} e^{-jk_{z1}h}}, \quad (A.13)$$

$$R_q = \frac{2k_{z0}^2 (1 - \epsilon_r)(1 - e^{-j4k_{z1}h})}{(k_{z1} + k_{z0})(k_{z1} + \epsilon_r k_{z0})(1 + r_{10}^{TE} e^{-j2k_{z1}h})(1 - r_{10}^{TM} e^{-j2k_{z1}h})}, \quad (A.14)$$

$$r_{10}^{TE} = \frac{k_{z1} - k_{z0}}{k_{z1} + k_{z0}}, \quad (A.15)$$

$$r_{10}^{TM} = \frac{k_{z1} - \epsilon_r k_{z0}}{k_{z1} + \epsilon_r k_{z0}}, \quad (A.16)$$

$$k_{z0}^2 + k_p^2 = k_0^2, \quad (A.17)$$

$$k_{z1}^2 + k_p^2 = \epsilon_r K_0^2. \quad (A.18)$$

## APPENDIX B Method of Averages

Let us consider the integral

$$I = \int_a^{\infty} \cos(\lambda\rho)f(\lambda)d\lambda, \quad (\text{B.1})$$

where  $f(\lambda)$  is a continuous function, having an asymptotic behavior of the form  $\lim_{\lambda \rightarrow \infty} f(\lambda) = c\lambda^\alpha$ . Above a certain value of the argument  $\lambda$ , the function  $f(\lambda)$  and all its derivatives have a constant sign. When  $\alpha > 0$ , the function  $f(\lambda)$  diverges at infinity. The infinite integration interval must obviously be bounded. Partial values can then be calculated numerically, defining  $I_m^1$  ( $m = 1, 2, \dots, M$ ) as

$$I_m^1 = \int_a^{\lambda_m} \cos(\lambda\rho)f(\lambda)d\lambda, m = 1, 2, \dots, M, \quad (\text{B.2})$$

where  $\lambda_m$  are the successive zeros of the oscillatory function  $\cos(\lambda\rho)$ , superior to the integration boundary  $a$ . The variation between the real value  $I$  of the integral and the approximations  $I_m^1$  is given by the value of the integral over  $[\lambda_m, \infty]$ . This value can be estimated, dividing the interval into an infinite number of subintervals, each having as its width one period of  $\cos(\lambda\rho)$ .

A new sequence  $I_m^2$  ( $m = 1, 2, \dots, M-1$ ) is defined by taking the average of two consecutive values of the sequence  $I_m^1$ , following the general expression:

$$I_m^{l+1} = \frac{1}{2} (I_m^l + I_{m+1}^l), l = 1, \dots, M-1, m = 1, \dots, M-1. \quad (\text{B.3})$$

Subsequence use of the average relation produces new sequence  $I_m^1$ . Taking into account the asymptotic behavior of  $f(\lambda)$ , the sequence  $I_m^1$  with  $l > \alpha + 1$  is the first one that will converge toward the real value of  $I$ . Successive sequences converge faster each time. The last sequence reduces to a single value  $I_1^M$  which will be closer to the true value than  $I_M^1$  in spite of the fact that no new evaluations of the integrand have been required. The final value  $I_1^M$  can be expressed directly in terms of the starting sequence  $I_M^1$  by

$$I_1^M = 2^{1-M} \sum_{m=1}^M \binom{M-1}{m-1} I_m^1. \quad (\text{B.4})$$

The average value algorithm can be applied to Bessel functions  $J_n(\lambda\rho)$ , defining the values  $\lambda_m$  as zeros of  $\cos(\lambda\rho - \pi/4 - n\pi/2)$ .